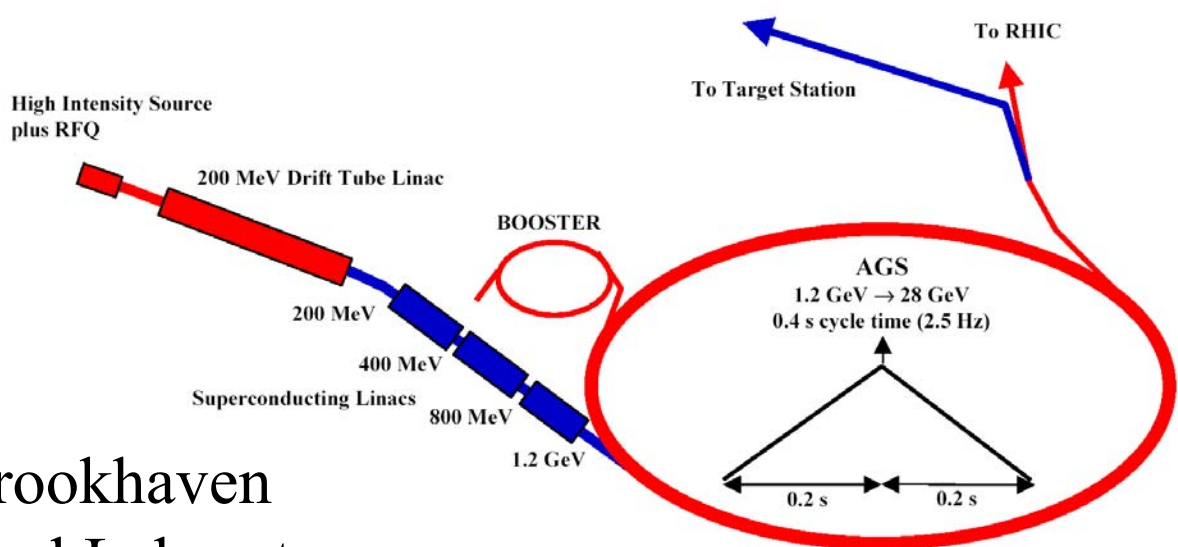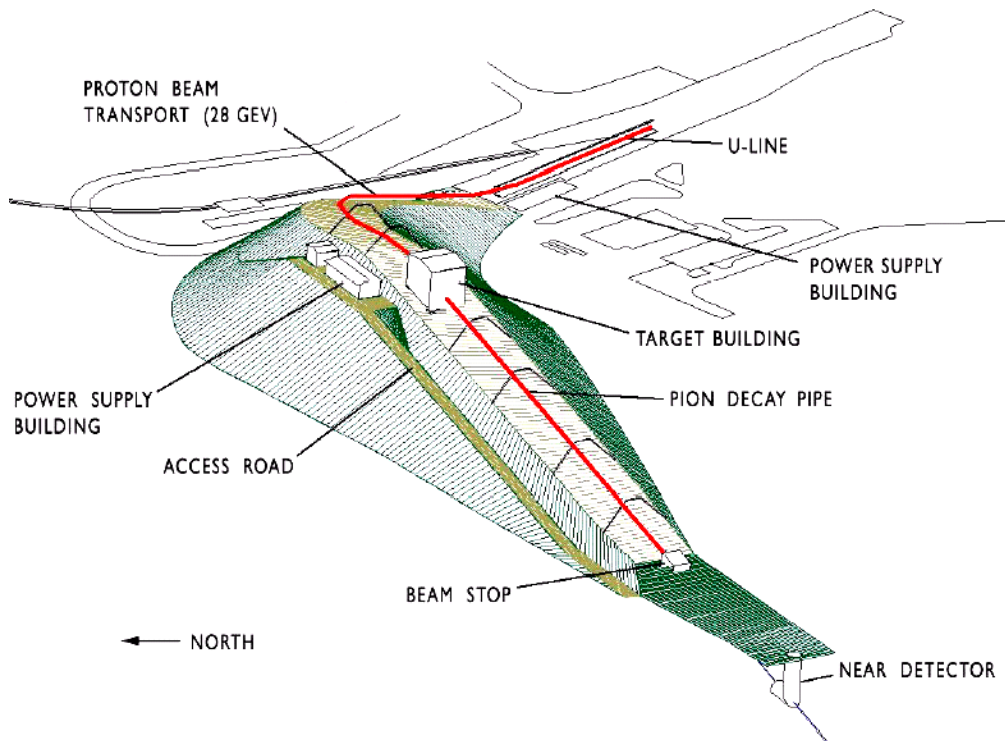# The AGS-Based Super Neutrino Beam Facility
Conceptual Design Report

Brookhaven
National Laboratory
Upton, NY 11973

8 October 2004

The AGS-Based Super Neutrino Beam Facility Conceptual Design Report

Editors: W. T. Weng, M. Diwan, and D. Raparia

Contributors and Participants

J. Alessi, D. Barton, D. Beavis, S. Bellavia, I. Ben-Zvi, J. Brennan, M. Diwan,
P. K. Feng, J. Gallardo, D. Gassner, R. Hahn, D. Hseuh, S.Kahn, H. Kirk,
Y. Y. Lee, E. Lessard,   D. Lowenstein,   H. Ludewig, K. Mirabella,
W. Marciano, I. Marneris, T. Nehring, C. Pearson, A. Pendzick,
P. Pile, D. Raparia, T. Roser, A. Ruggiero, N. P. Samios,
N. Simos, J. Sandberg, N. Tsoupas, J. Tuozzolo, B. Viren,
J. Beebe-Wang, J. Wei, W. T. Weng, N. Williams,
P. Yamin, K. C. Wu, A. Zaltsman,
S. Y. Zhang, Wu Zhang

This document contains figures in color. The figures should be viewed in color.

Contents

1 Physics Motivation and Overview of the Project

1.1 Neutrino Physics Goal and Potential for Discoveries

Measurements of solar and atmospheric neutrinos have provided strong evidence for non-zero neutrino masses and mixing of weak flavors among them [1, 2, 3]. Atmospheric results have been further strengthened by the K2K collaboration's accelerator based results [4]. The Solar neutrino results have been confirmed by the KamLAND collaboration in a reactor based experiment that has shown that the large mixing angle (LMA) solution is most likely the correct one [5]. Interpretation of the experimental results is based on oscillations of one neutrino flavor state, ν_e, ν_μ or ν_τ, into the others, and described quantum mechanically in terms of transitions between neutrino mass eigenstates, ν_1, ν_2 and ν_3. The mass differences involved in the transitions are measured to be approximately $\Delta m_{21}^2 \equiv |m(\nu_2)^2 - m(\nu_1)^2| = 8 \times 10^{-5} \text{eV}^2$ for the solar neutrinos and $\Delta m_{32}^2 \equiv |m(\nu_3)^2 - m(\nu_2)^2| = 2.5 \times 10^{-3} \text{eV}^2$ for the atmospheric neutrinos, with large mixing strengths, $\sin^2 \theta_{12}$ and $\sin^2 \theta_{23}$ in both cases.

The parameters are now sufficiently well-known that they open the possibility for a feasible accelerator based very long baseline experiment that can explore both Solar and Atmospheric oscillation parameters in a single experiment. The facilities required for this program are: 1) a 1 MW "Super Neutrino Beam" provided by an upgraded AGS proton driver accelerator at Brookhaven National Laboratory and 2) a 500 kT water Cherenkov detector, such as the UNO [6], or the 3M concept, located in a deep underground laboratory at a distance of more than 2000 km from BNL. In the absence of oscillations, one could collect $\sim$60000 events in a running period of $5 \times 10^7 sec$. In neutrino oscillation physics there are three measurements of primary interest that can be addressed with this kind of data. These are described below and analyzed in [7] and [8] in more detail; we use the parameter convention described in [1]:

(i) Definitive observation of oscillatory behavior in the ν_μ disappearance mode and precise determination of the oscillation parameters Δm_{32}^2 and $\sin^2 2\theta_{23}$.

(ii) Detection of the oscillation $\nu_\mu \rightarrow \nu_e$ in the appearance mode and measurement of the parameter $\sin^2 2\theta_{13}$. This will involve matter enhancement and allow measurement of the sign of Δm_{32}^2, i.e., which neutrino ν_3 or ν_2 is heavier.

(iii) Measurement of the CP violation parameter, δ_{CP}, in the neutrino sector.

For precise measurements of Δm_{32}^2 and $\sin^2 2\theta_{23}$, it is desirable to observe a pattern of multiple nodes in the energy spectrum of muon neutrinos. Since the cross section, Fermi motion, and nuclear effects limit the resolution of muon neutrino interactions below ~ 1 GeV, we need to utilize a wide band muon neutrino beam with energy range of 1-6 GeV and a distance of $\sim$2000 km to observe 3 or more oscillation nodes. See Fig. 1.1.

The appearance spectrum of electron neutrinos from the conversion $\nu_\mu \rightarrow \nu_e$ contains information about $\sin^2 2\theta_{13}$, δ_{CP}, Δm_{21}^2 and the ordering of neutrino masses through the matter effect (i.e. $(m_1 < m_2 < m_3)$ versus $(m_3 < m_1 < m_2)$). We showed in [7] that the effects of the various parameters can be separated using the broad-band 1-6 GeV beam and the $\sim$2000km distance. The matter effect causes the conversion probability to rise with energy

Oscillation Nodes for $\Delta m^2 = 0.0025$ eV^2
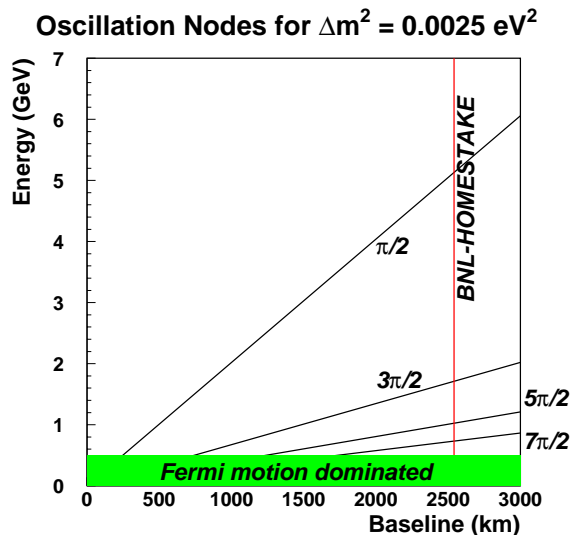
Figure 1.1: Oscillation nodes in energy versus distance from the source of neutrinos for $\Delta m^2_{32} = 0.0025 eV^2$. For muon type neutrinos threshold effects, nuclear effects, and the smallness of cross section limits us to making measurements with neutrinos > 500 MeV. Therefore, to obtain a signature of at least 3 oscillation nodes we must use neutrinos in the range of 1 to 6 GeV and a baseline of $> 2000\ km$.

and is mostly confined to energies > 3 GeV whereas the effects of δ_{CP} fall as $1/E$. In initial running, this energy dependence can be used to measure the value of δ_{CP} and $\sin^2 2\theta_{13}$ without taking data with anti-neutrinos. Once established the CP parameters can be measured with greater precision by running in the anti-neutrino mode.

Current and near term accelerator based experiments are focused on the atmospheric mass scale. Experiments using astrophysical sources such as solar neutrinos or atmospheric neutrinos are sensitive to either the solar or the atmospheric mass scale. The parameters are now known well enough ($\Delta m^2_{32} \sim 0.0025 eV^2$ and $\Delta m^2_{21} \sim 8 \times 10^{-5} eV^2$) [2, 5, 3] that it is possible to design a qualitatively different experiment that will have good sensitivity to both mass scales. The CP contribution is dependent on both atmospheric and solar Δm^2; it is also likely that such an experiment is necessary to uncover any new physics in neutrino mixing or interactions with matter. A next generation accelerator experiment with well understood, pure beams, sufficiently long baseline, and low energy wide band beam (1-5 GeV) could fill this role as we have described.

In this proposal we describe the accelerator upgrades needed to reach 1 MW of power at the AGS and the design of a wide-band neutrino beam that could be aimed at the distant detector. For the purposes of this proposal we have chosen the Homestake mine in Lead, South Dakota as the site for the underground detector, however any other equivalent site >2000 km from BNL in the West can be accommodated in our design.

The importance of both the super neutrino beam and the large underground detector to the national scientific enterprise has been unambiguously stressed in a number of recent re-

ports. The most important of these are 1) "Neutrinos and Beyond," by the Nation Research Council's Neutrino Facilities Assessment Committee in 2003 (http //books.nap.edu /books /0309087163 /html /70.html) and 2) the "Physics of the Universe" from the National Science and Technology Council, Committee on Science (http//www.ostp.gov/ html/ physicsofthe-universe2.pdf). The super neutrino beam and the large underground detector in combination enable a broad spectrum of physics: neutrino oscillations and CP violation, detection of nucleon decay, supernova, and other astrophysical neutrino sources. A thorough examination of this possibility, therefore, is imperative for particle and nuclear physics.

In the following, we show a specific implementation of the above project by upgrading the current BNL-AGS accelerator. All the enabling technologies for this program have been demonstrated in existing facilities. The accelerator upgrade and the beam project could enter the engineering design phase as soon as funding is made available.

1.2   Outline of the Project

After more than 40 years of operation, the AGS is still at the heart of the Brookhaven hadron accelerator complex. This system of accelerators presently comprises a 200 MeV linac for the pre-acceleration of high intensity and polarized protons, two Tandem Van der Graaffs for the pre-acceleration of heavy ion beams, a versatile Booster that allows for efficient injection of all three types of beams into the AGS and, most recently, the two RHIC collider rings that produce high luminosity heavy ion and polarized proton collisions. For several years now, the AGS has held the world intensity record with more than 7×10^{13} protons accelerated in a single pulse [9].

The requirements for the proton beam for the super neutrino beam are summarized in Table 1.1 and a schematic of the upgraded AGS is shown in Figure 1.2. Since the present number of protons per fill is already close to the required number, the upgrade is based on increasing the repetition rate and reducing beam losses (to avoid excessive shielding requirements and to maintain activation of the machine components at workable level). It is also important to preserve all the present capabilities of the AGS, in particular its role as injector to RHIC.

The AGS Booster was built not only to allow the injection of any species of heavy ion into the AGS but to allow a fourfold increase of the AGS intensity. It is one-quarter the circumference of the AGS with the same aperture. However, the accumulation of four Booster loads in the AGS takes about 0.6 s, and is therefore not well suited for high average beam power operation. To minimize the injection time to about 1 ms, a 1.2 GeV linac will be used instead. This linac consists of the existing warm linac of 200 MeV and a new superconducting linac of 1.0 GeV. The multi-turn H^- injection from a source of 30 mA and 720 μs pulse width is sufficient to accumulate 9 x 10^{13} particle per pulse in the AGS[10].

The minimum ramp time of the AGS to full energy is presently 0.5 s; this must be upgraded to 0.2 s to reach the required repetition rate of 2.5 Hz. The required upgrade of the AGS power supply, the rf system, and other rate dependent accelerator issues will be discussed in Chapter 3.

The design of the target/horn configuration is shown in Figure 1.3. The material selected for the proton target is a Carbon-Carbon composite. It is a 3-dimensional woven material that exhibits extremely low thermal expansion for temperatures up to 1000^0C; for higher

Table 1.1: Performance of the present and upgrade AGS.

	Present	Upgrade
Average Beam Power (MW)	0.14	1.0
Beam Energy (GeV)	24	28
Average Beam Current (μA)	6	36
Cycle Time (s)	2	0.4
Number of Protons per Fill	7.0×10^{13}	8.9×10^{13}
Number of Bunches per Fill	12	23
Protons per Bunch	5.8×10^{12}	3.87×10^{12}
Number of Injected Turns	190	240
Repetition Rate (Hz)	0.5	2.5
Linac Energy (MeV)	200	1200
Linac Average/Peak Current (mA)	20/30	21/28
Linac rms Emitt (π mm mr, nor)	2.0	1.0
Pulse Length (ms)	0.5	0.72
Chopping Rate	0.70	0.65

temperatures it responds like graphite. This property is important for greatly reducing the thermo-elastic stresses induced by the beam, thereby extending the life of the target.

The target consists of a 80 cm long cylindrical rod of 12 mm diameter. The target intercepts a 2 mm rms proton beam of 10^{14} protons/pulse. The total energy deposited as heat in the target is 7.3 kJ with peak temperature rise of about 280 °C. Heat will be removed from the target through forced convection of helium gas across its outside surface.

The extracted proton beam uses an existing beamline at the AGS, but is then directed to a target station atop a constructed earthen hill. The target is followed by a downward slopping pion decay channel. This vertical arrangement keeps the target and decay pipe well above the water table in this area. The 11.3 degrees slope aims the neutrino beam at a water Cerenkov neutrino detector to be located in the Homestake mine at Lead, South Dakota. A 3-dimensional view of the beam transport line, target station, and decay tunnel is provided in Figure 1.4.

To assist the reading of this report and enforce consistency across chapters, the design parameters of each subsystem are provided in Appendix A.

1.3   Beam Loss and Shielding

It is an accepted practice for high power proton facilities to keep the radiation loss below a few Watt/m. This will result in the activated radiation, after long period of operation, to be below 100 mrem/hour, a necessary condition for hands-on maintenance. The primary reasons for such uncontrolled beam losses are injection, transition crossing, and extraction. For this proposal, detailed simulations have been performed to assure that the beam losses are below the specified limit. For example, the simulation result shown in Table 4.2 indicates that the
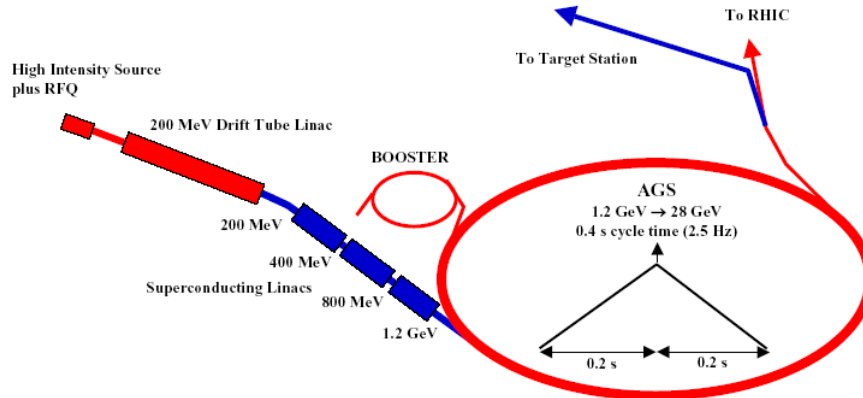
Figure 1.2: AGS proton driver layout.

loss at injection is about 1.6 W/m, a lower level than that of PSR and SNS.

A well-designed collimator system has to be provided to capture unavoidable stray particles at strategic positions in order to minimize uncontrolled losses around the accelerator. The allowable radiation levels at these collimation locations can be higher for two reasons: the collimators can stand higher radiation levels and they do not require regular maintenance; additional shielding can be provided at those isolated locations for radiation protection. If sufficient internal shielding is provided, there is no need for additional earth shielding on top of the AGS berm.

1.4   Modes of Operation

The physics reach outlined in references [7] and [8] is based on the AGS running for 5 years at 10^7 s per year. With 1 MW AGS at 2.5 Hz, this is equivalent to 2.3×10^{21} protons on the target. This can be accomplished in about 24 weeks of dedicated proton operation, or 30 weeks of parasitic operation in conjunction with RHIC heavy ion program.

There are three distinct periods for the AGS-RHIC accelerator complex within the span of this plan. The first one is the current mode of operation, in which we operate RHIC for heavy ion physics for about 25 weeks and for polarized proton physics for about 6 weeks. Typically, there is a long summer shutdown without operation for about 4 months.

The second period is when the RSVP program is in operation, some time after 2009. At that time, the AGS will run protons, in addition to serving as an injector for RHIC. The AGS proton run can be concurrent with the RHIC heavy ion run during collision periods. If RSVP operation is more than 25 weeks/year, we can also run the AGS in dedicated mode.

The third period of time is when the neutrino facility at the AGS comes into operation, some time after 2012 (assuming the upgrade project starts in 2007). Then the neutrino physics early runs will share yearly time with the RSVP runs. The BNL institutional plan calls for 37 weeks per year of RHIC operation. If we assume a 30 week run for heavy ion and a 7 week run
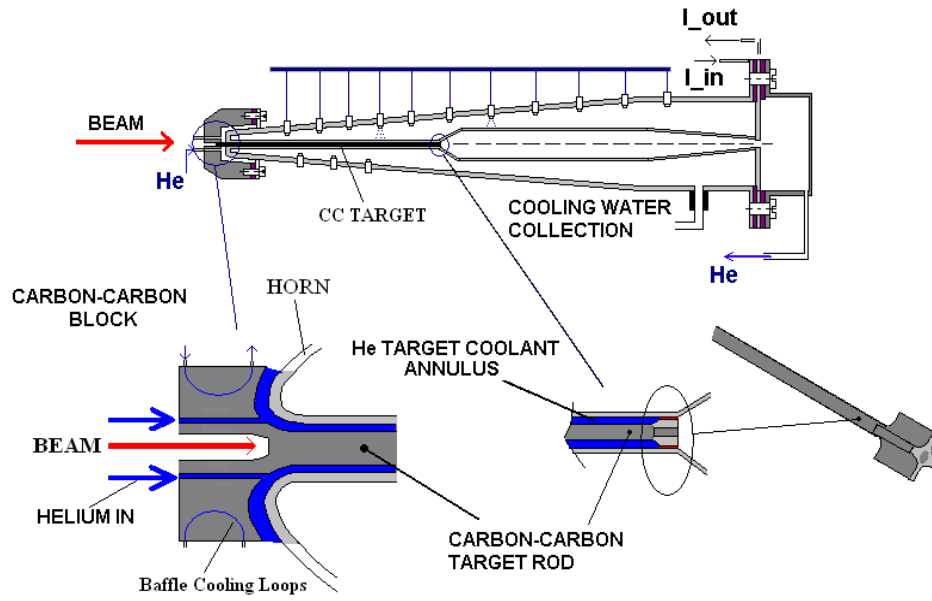
Figure 1.3: Conceptual arrangement of horn/target system including heat removal scheme
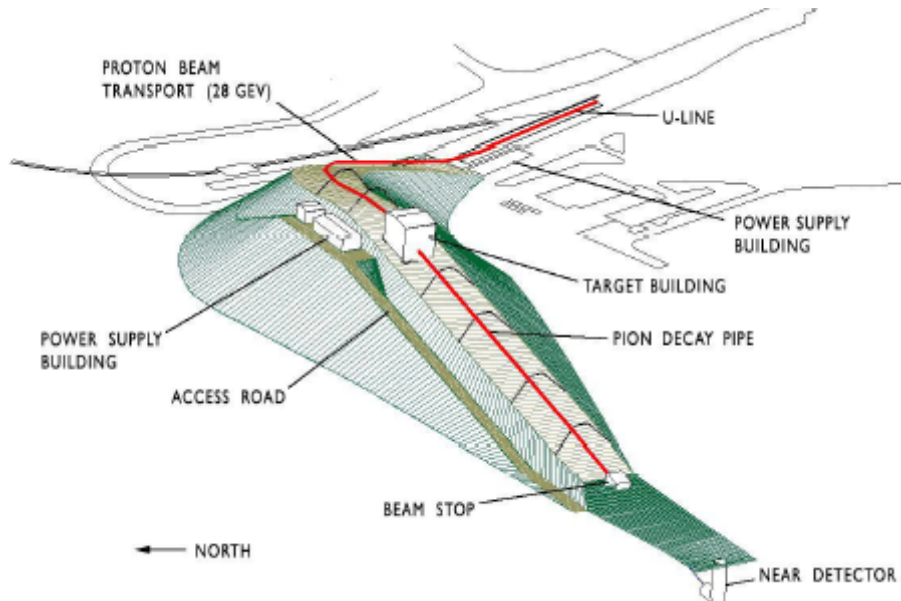
Figure 1.4: 3-dimensional view of the neutrino beamline. The beamline is shown without shielding on top of the beam-line magnets and the decay tunnel.

for polarized protons, then RSVP and neutrino can share the 85% time during RHIC heavy ion run. Or they can share time for additional dedicated proton operation of the AGS in the remaining 10 weeks, allowing 5 weeks of machine shutdown. When the RSVP physics run is completed, neutrino physics can take all the available proton time from the AGS.

1.5   Installation Strategy

Our estimate of the construction period of the neutrino facility is about five years. It is desirable and intended to complete the construction activities without interference with the regular RHIC and AGS physics operation. To achieve this goal, there are several provisions to be observed.

The first concern is the connection of the superconducting linac to the existing warm linac. As outlined in the last section, the annual proton linac operation for polarized protons and RSVP is no more than 30 weeks, leaving about 5 months time for construction without interfering with regular operations. We can use a one time 5 month break for the building reconfiguration, and the second 5 month break for equipment installation.

The second concern is the joining of the new SRF linac tunnel with the AGS tunnel. Here the construction time can be reduced to about 4 months which is still comfortable for tunnel connection and equipment installation in two year's time. This is not very different from the job carried out for the BAF line from the Booster in 1999 and 2000.

The third concern is the modifications of the main magnet power supply and the rf power source. Here we do not have the option of doing it in two shutdown periods, they have to be completed and put back to work during a single shutdown period. The additional requirement of both systems is that they have to be able to operate in a pulse-to-pulse convertible mode for both 0.3 Hz and 2.5 Hz AGS operation. Our estimate shows that this cannot be accomplished in a 4 month long shutdown period. We have to schedule the AGS and RHIC operation covering two fiscal years, back-to-back, with a single 7 to 8 month long shutdown period between operations. This has been done in the past during the RHIC construction time.

1.6   Further Improvements and Upgrade Options

This conceptual design is based on the requirement of a 1 MW AGS proton beam for neutrino production. There are many requests for delivering higher beam power in the future for expanded physics exploration, or even as the proton driver for a neutrino factory. The design approach described in this report is based on proven technology with credible results and affordable cost. We are continuously monitoring various new accelerator concepts for improvements either in technology or performance. These include linac, target/horn, and many beam dynamics issues. When the new concepts mature and are proven to be compatible with the project requirements, we will incorporate them into the final design and make commensurate changes in the WBS and cost estimate. Several possible upgrades to 2 MW and beyond are outlined below.

a. Increase the AGS repetition rate from 2.5 Hz to 5.0 Hz. This will bring the final beam power to 2 MW, assuming the same proton intensity per pulse.

b. Increase the AGS intensity to 1.8×10^{14} protons per pulse. This will bring the beam power to 2 MW at 2.5 Hz, or to 4 MW at 5.0 Hz. To make this option possible, the SRF linac energy has to be increased to be higher than 1.5 GeV to reduce the space charge effects in the AGS during injection time. A better transition crossing system also has to be implemented.

c. In this report, we add a 1 GeV superconducting linac to the existing 200 MeV warm linac to reach the required 1.2 GeV injection energy. We are currently working on an improved approach of replacing part of the warm linac with coupled cavity structure from 100 to 400 MeV, similar to what was done at FNAL in 1993, and then add additional a 1.1 GeV SCL to reach a final injection energy of 1.5 GeV. In this approach, the SCL can have only one frequency, 805 MHz, and one type of cavity and cryomodule design and the existing SNS high beta structure can be utilized. This improved linac design is discussed in Appendix B.

d. We are working on new geometries and techniques for focusing secondaries from a long target.

Other improvements to the neutrino beam characteristics are also under investigation. We will include in our design the possibility of delivering a 1 degree off-axis neutrino beam to the same far detector, by moving the target/horn system within the same decay tunnel. A new narrow band target/horn system could also be designed.

1.7   Summary of Cost Estimate and Schedule

The cost estimate of the AGS-Based super Neutrino beam Facility has been performed following the "bottoms up" approach. After the performance goals and physics design of the technical systems were completed, cognizant engineers who have built similar systems were assigned to prepare a cost estimate of sufficient detail, based on previous experience. Each estimate typically includes the cost of the detailed engineering design, procurement, manufacturing, testing and installation. Material and labor costs are captured as separate entries for each process.

Most of the cost numbers are based on BNL's recent experience in building RHIC, SNS ring, and LHC magnets. They also draw on extensive searches of price given in catalogs and on vendor's quotations. The Work Breakdown Structure (WBS) is given in Figure 9.1. All systems have been estimated by going down to the component and assembly level. From our past experience, both the manufacturing approaches and the cost estimates are consistent with good engineering practices and are credible.

The costs given reflect the "direct cost" of the item. In other words, estimates do not include G & A (lab overhead), and contingency. These cost elements are added to the direct cost following guidelines using standard estimating at BNL.

All the figures are in FY 2004 US Dollars. No inflation is included since the construction period is not known at this time.

The resultant total direct cost in FY04 dollars of the 1 MW AGS Super Neutrino Beam Facility, not including both near and main detectors, is $273.4 M. The preliminary total

estimated cost (TEC) is \$406.9 M in FY04 dollars, including contingency at 30%; BNL construction project overhead at 14.5%. Escalation cannot be estimated without a project start year. The summary spread sheet of the cost estimate down to WBS level 3 is given in Figure 9.2

It is estimated that three years of R & D are needed to build prototypes and complete a detailed engineering design that will reduce cost and improve operational reliability. The construction can start one year after the R & D start and will take 4.5 years of construction and 0.5 year of commissioning to prepare the facility for physics research operations. The total elapsed time for the project from beginning to finish is 6 years. The schedule time line for the project is given in Figure 9.3

2   Injector Linac

To provide 1 MW proton beam power, the AGS has to operate at 2.5 Hz with little time allowed for injection. The present injector consists of the 200 MeV room temperature linac and 1.5 GeV Booster. It takes about 0.6 s to inject four Booster pulses to fill the AGS, which is not suitable for the upgrade operation. If a 1.2 GeV linac is used instead, the injection time can be reduced to less than 1 ms, allowing the AGS to cycle at the desired rate of 2.5 Hz. A 1.2 GeV linac injection can simultaneously fulfill the requirements of keeping the space charge tune shift in the AGS to be less than 0.25 and the injection losses down for reliable operation.

The distance between the exit of the 200 MeV linac and the AGS injection point is about 130 m. Only a superconducting linac (SCL) with sufficiently high gradient can meet the requirement of acceleration to 1.2 GeV within that distance. The superconducting linac technology has been used in many electron accelerators, such as LEP, CEBAF, and Tesla. The SNS project has designed a 1.0 GeV proton SCL system with an accelerating gradient of about 18 MeV/m. The design of the new AGS injector linac follows closely that developed at SNS. This will substantially reduce the design cost and increase confidence in the design.

The project described corresponds to an average SCL beam current of 36 μA, that yields the required average beam power of 1 MW at the top energy of 28 GeV, including also a controlled beam loss of about 5% during multi-turn injection into the AGS. The average beam power in exit is 45 kW, considerably less than the 1-MW level of the equivalent 1.0-GeV SCL for the Spallation Neutron Source (SNS) [11]. Thus the concern about component activation by the induced radiation from uncontrolled beam losses is greatly reduced. The repetition rate of 2.5 beam pulses per second gives a beam intensity of 0.89 x 10^{14} protons accelerated per AGS cycle; this is about 30% higher than the intensity routinely obtained with the present injector. At the end of an injection phase that takes about 240 turns, the space-charge tune depression is $\Delta\nu = 0.2$, assuming a bunching factor (the ratio of beam peak current to average current), of 3. Also, with the normalized beam emittance of 100 π mm-mrad, the actual beam emittance at 1.2 GeV is $\varepsilon = 50 \pi$ mm-mrad. Obviously, the effective vertical acceptance of the AGS at injection needs to match the final beam emittance value. The SCL beam pulse length is 0.72 ms, and the beam duty cycle 0.18%.

The preliminary design of the SCL consists of three parts: (i) Low-Energy (LE), (ii) Medium Energy (ME), and (iii) High Energy (HE). A schematic view of the new injector is given in Figure 2.1. The actual location of the SCL on the BNL site is shown in Figure 2.2. The beam leaves the present room temperature linac at the energy of 200 MeV and, after a bend of 17.5 degrees, enters a new 130 m long tunnel, where the SCL is located, and joins the AGS beamline at the location of magnet C01. The design parameters of the SCL and the AGS are given in Table 2.1.

We are currently working on an improved approach of replacing part of the warm linac with coupled cavity structure from 100 to 400 MeV, similar to what was done at FNAL in 1993, and then add additional 1.1 GeV SCL to reach final injection energy of 1.5 GeV. In this approach, SCL can be with one frequency, 805 MHz, and one type of cavity and cryomodule design and the existing SNS high beta structure can be utilized. This improved linac design is discussed in Appendix B.
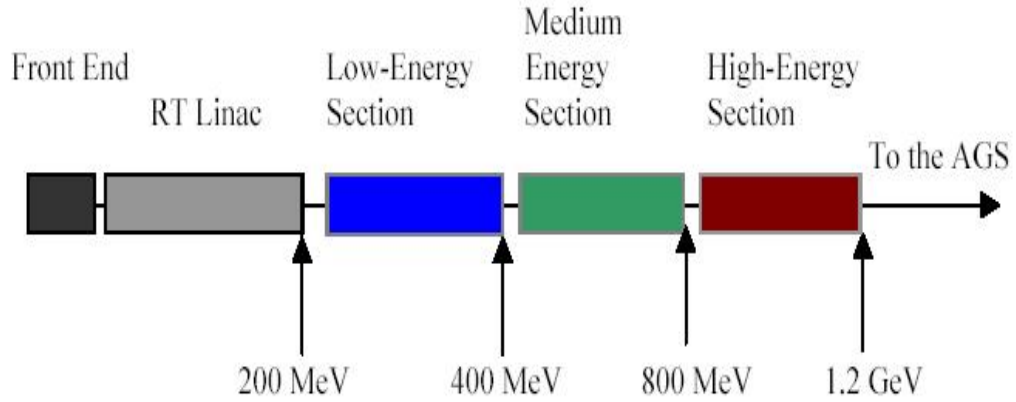
Figure 2.1: Layout of the 1.2-GeV superconducting linac injector for the AGS.

Table 2.1: Injector and AGS parameters for 1-MW upgrade (28 GeV).

Increm. Linac Ave. Power, kW	37.5
Kinetic Energy, GeV	1.2
β	0.8986
Momentum, GeV/c	1.92
Magnetic Rigidity, T-m	6.41
Repetition Rate, Hz	2.5
Linac No. of Protons / pulse	9.38×10^{13}
Linac Duty Cycle, %	0.179
AGS Circumference, m	807.076
Revol. Frequency, MHz	0.3338
Revolution Period, μs	2.996
Bending Radius, m	85.378
Injection Field, kG	0.7507
Injection Loss, %	5.0
Injected Protons per Turn	3.74×10^{11}
Norm. Emitt., π mm-mrad	100
Emittance, π mm-mrad	48.8
Space-Charge $\Delta\nu$	0.187
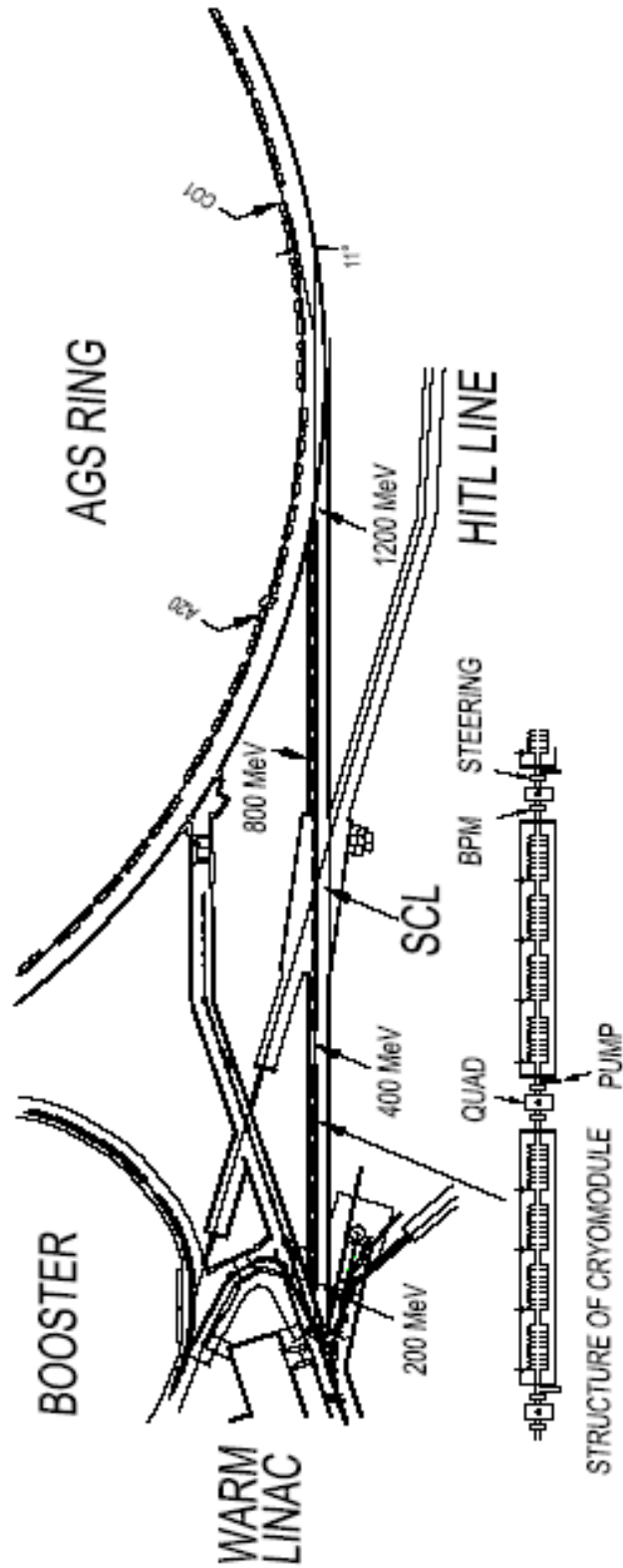
Figure 2.2: Layout of the superconducting linac.

2.1   Room Temperature Linac Upgrade

The Brookhaven 200 MeV H$^-$ linac typically operates $\sim$ 5000 hours/year in support of high intensity proton operation of the AGS, polarized protons for RHIC, and medical isotope production. Some nominal operating parameters of the linac are given in Table 2.2. A detailed description of the linac can be found in references [12] and [13]. One can see from this table that the present linac can meet all the requirements for beam current and repetition rate, duty factor except beam pulse width and transverse emittance. The required duty factor is less than the typical operating value. As will be discussed below, reconfiguration of 35 keV and 750 keV transport lines to achieve the desired emittance and upgraded power supplies for several systems to achieve the desired beam pulse width, will be required . However, since this upgrade is straightforward, the linac operation remains reliable, and there is room following this linac for the addition of a SCL; it was most cost effective to continue to use the full 200 MeV warm linac.

Table 2.2: Nominal operating parameters for the BNL linac.

Output Energy	200 MeV
Frequency	201.25 MHz
Repetition Rate	$\leq$ 10Hz
Beam Pulse Width	$\leq$ 500μs
Nominal Duty Factor	$\sim$ 0.3%
Output Beam Current	$\leq$ 35 mA
Output Emittance (rms, Normalized)	2 π mm mrad
Output Energy Spread (rms)	0.2%

      The front end of the linac is shown systematically in Figure 2.3. It starts with a magnetron H$^-$ ion source, which produces in excess of 80 mA H$^-$ beam at 35 keV. Following this, the low energy beam transport (LEBT) uses two magnetic solenoids to transport the H$^-$ beam $\sim$ 1 m and match it into an RFQ. The RFQ, operating at the linac frequency of 201.25 MHz, accelerates the beam from 35 keV to 750 keV. After the RFQ, the beam is transported $\sim$ 7 m to the linac. This medium energy beam transport (MEBT) includes 10 quadrupoles and 3 bunchers for beam matching into the linac, and a fast beam chopper which allows beam chopping with $\sim$ 10 ns rise and fall times. This chopper is a traveling wave structure, and the beam is chopped at a frequency to match into the Booster rf accelerating bucket at injection energy. A 201.25 MHz drift tube linac (DTL) accelerates the beam from 750 keV to 200 MeV. This linac has 9 cavities, each powered by a 5 MW peak power rf system. There are a total of 286 drift tubes, with a focusing electromagnetic quadrupole in each drift tube.

      As mentioned above, except for the (1) beam emittance and (2) beam pulse width, the present operation fulfills all requirements. A direct effect of linac beam emittance is the halo/tail generation in the circulating beam. Studies show the estimated halo/tail generation in the beam for present normalized rms emittance of linac beam is unacceptable (see Section 4.2.1). The most of the emittance growth is due to the fact present MEBT is rather long 7 m, with three bunchers, and by the time beam reaches the DTL is completely debunches and
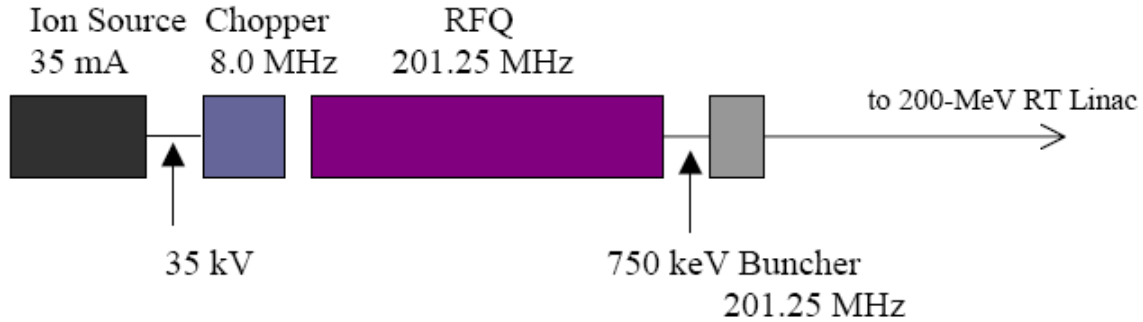
Figure 2.3: Layout of the front-end.

rebunches into the first tank of the DTL. Simulations show this causes the transverse emittance growth as well as a loss in beam current. To reduce the emittance growth various configuration of MEBT were considered. Our final choice is a short MEBT with three quadrupoles and two rebuncher cavities, which matches the beam into the DTL in both transverse and longitudinal plane and reduces the emittance growth by factor of five [14]. Due to space restriction, this configuration of the MEBT forces the chopper into the LEBT. Past experience has been that chopping in the LEBT did not work in the magnetic (solenoids) focusing system due to space charge and beam neutralization effects. The new proposed LEBT will be all electrostatic and uses a 90 degree spherical bend for polarized beam and straight section for the H^- beam.

Limitations in beam pulse width exist not due to mechanical limits on the ion source or linac, but rather as a result of limits in ion source power supplies, rf system power supplies, and pulsed transport line and tank quadrupole power supplies. Therefore, in order to serve as the injector to the SCL, the following improvements will be required:

1. The magnetron ion source discharge, extractor, and pulsed gas power supplies must be replaced by components with wider pulse capability.

2. On the 400 kW driver stage amplifier rf systems, one must increase the 4616 plate capacitor bank. This entails the purchase and installation of new 35 kV capacitors in the existing frame. The crowbar ignitrons and sockets must be replaced. Finally, we need to increase the size of the capacitors on grid power supplies.

3. In the rf modulator system, the capacitor bank has to be increased for the 4cw25000 anode supply, and the 8618 grid and cathode deck power supplies will need to be reworked

4. On the 5 MW rf system, we need to replace the 60 kV capacitor banks with banks having more capacity; again these can be installed within existing frames. The crowbar ignitrons and sockets have to be replaced for 100 kA tubes.

5. On the low level rf systems, all 400 watt solid state amplifiers will need replacement.

6. All pulsed transport line and tank quadrupoles supplies will have to be replaced with solid state units having wider pulse capabilities.

7. Reconfiguration of 750 keV beam line.

8. Three new quadrupoles and two rebuncher cavity for the 750 keV beam line.

9. All new electrostatic 35 keV beam line.

The above upgrades are all straightforward, and we are confident that the required performance can be achieved.

2.2 The Superconducting Linac(SCL)

2.2.1 Cavity and Cryomodule

Superconducting linac design involve determining following choices:

- Frequency

- Cavity velocity

- Number of cell per cavity

- Constant energy gain per cavity versus constant gradient

- Number of cavities per cryomodule

- Type of focusing lattice

Frequency of the linac depends on the expected longitudinal emittance at the injection energy and the availability of the technology. Our choice for frequency is 805 MHz in the low energy section same as the SNS value, since the injection energy and expected longitudinal emittance are similar to the SNS linac and is multiple of our linac frequency of 201.25 MHz. For medium and high energy sections we have chosen 1610 MHz to increase the average real state accelerating gradient in order to accommodate 1.0 GeV linac in 130 m length limited by our topology.

During the acceleration process from 200 MeV to 1.2 GeV, the particle β varies from 0.57 to 0.89. Ideally, the cavity design varies continuously with particle β, but this is unnecessary in the SC linac case. Study for the SNS shows that the two cavity groups ($\beta = 0.61$ and $\beta = 0.81$) are sufficient to accelerate up to 1.0 GeV. We have chosen $\beta = 0.615$ for low energy section same as SNS, but $\beta = 0.75$ for medium energy section and $\beta = 0.85$ for high energy section to make acceleration more efficient by reducing the variation in the transit time factor. Since the particle beta is not same as the cavity geometry beta throughout the acceleration, there is a phase slippage as the particle traverse the cavity. This slippage reduces the ideal possible energy gain and the transit time factor accounts for this effect.

Eight cells per cavity instead six cells per cavity results in a worse transit time factor, but reduces overall length of the accelerator since there are less inter-cavity spaces. Our choice is eight cells per cavity.

The maximum accelerating gradient in the SC cavity is determine by the achievable peak surface field. The chosen mode of operation is to operate each section of the SCL with the same energy increment. This requires the same axial field from one cryo-module to the next. To achieve this, and to compensate for the transit time variation from one cryo-module to next, it may be necessary to locally adjust the rf phase, taken here to be 30°. Also the coupling power may have to be adjusted according to the local transit time factor.

Four cavity per cryomodule were chosen for all three section, namely low energy, medium energy and high energy sections to minimize the overall length and maximize the regularities.

FODO lattice was chosen for the low energy section to reduce length of the warm insertion and, since the aperture in this section is 10 cm, aperture to beam size ratio remain larger than 6.5. Quadrupole doublets lattice is chosen for medium and high energy sections to maximize the aperture to beam size ratio since the aperture for 1610 MHz cavities is 5 cm.

2.2.2   Cell Design

The fundamental unit of the superconducting linac is the half-cell that determines the linac architecture and the beam dynamics. Figure 2.4 shows the geometrical view of the half-cell along the with definition of the cell parameters. Value of these parameters are given Table 2.3 and Figure 2.5 shows the SUPERFISH results for low, medium and high beta cavities. The peak surface electric and magnetic field is kept below 40 MV/m and 110 mT. These values are conservative since the typical values for TESLA cavities are about 55 MV/m and 125 mT for peak surface electric and magnetic field respectively.

2.2.3   Linac Architecture

A typical sequence of identical periods is shown in Figure 2.6. Each period consists of a cryo-module of length L_{cryo} with an insertion of length L_{ins}. The insertion is needed for the placement of focusing quadrupoles, vacuum pumps and valves, steering magnets, beam diagnostic devices, bellows, and flanges. It can be either at room temperature or in a cryostat. Here we assume that the insertions are at room temperature. The cryo-module includes M identical cavities, each of N identical cells, and each having a length NL_{cell}, where L_{cell} is the length of a cell. To avoid coupling by the leakage of the field, cavities are separated from each other by a sufficiently long drift space, d. An extra drift of length L_w may be added internally on both sides of the cryo-module to provide a transition between cold and warm regions. Thus, the length of a cryo-module is

$$L_{cryo} = MNL_{cell} + (M - 1)d + 2L_w. \tag{2.1}$$
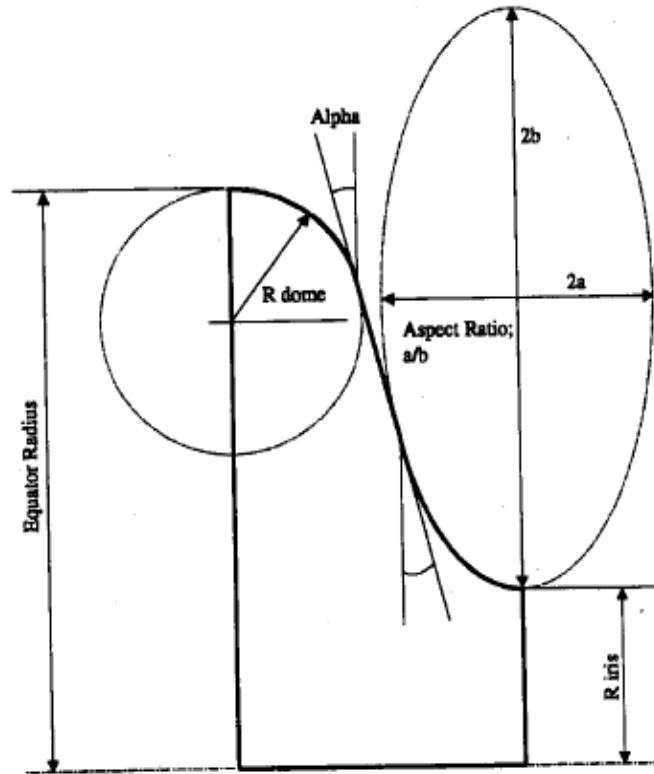
Figure 2.4: Reference geometry for the half-cells.

Table 2.3: Cell parameters

Section	Low Beta	Medium Beta	High Beta
Frequency (MHz)	805	1610	1610
Geometric Beta	0.615	0.755	0.851
Alpha (deg)	7	7	7
R iris (cm)	5	2.5	2.5
R dome (cm)	3.5	1.75	2.50
R equator (cm)	16.61	8.47	8.47
a/b	0.675	0.375	0.5
E peak (MV/m)	24.7	38.24	35.47
E0 (MV/m)	10.8	23.55	23.4
B max (mT)	60	107	87
Ep/E0	2.29	1.61	1.51
Bmax/Epeak (mT/MV/m)	2.05	2.81	2.44
Coupling (%)	~ 2	~ 2	~ 2
Lorentz Force Detuning Coef. (Hz/MV/m)	~ 2	~ 2	~ 2
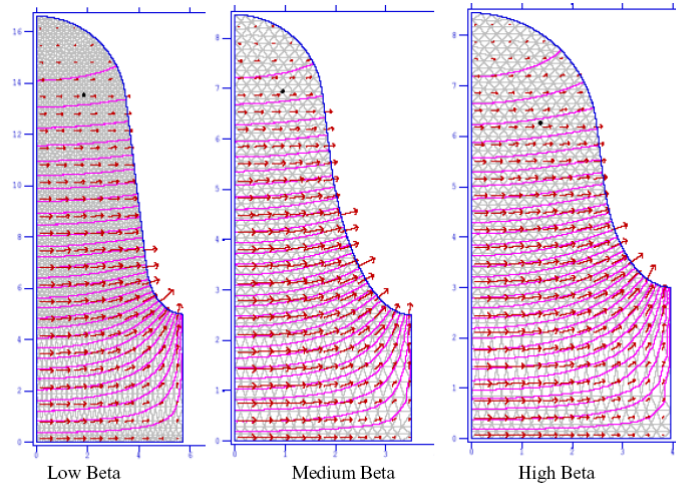
Figure 2.5: Superfish results for low, medium and high β half-cells.

There are two symmetric intervals: a minor one, between the two middle points A and B, as shown in Figure 2.6, that is the interval of a cavity of length $NL_{cell} + d$; and a major one, between the two middle points C and D, that defines the range of a period of total length $L_{cryo} + L_{ins}$. Thus, the topology of a period can be represented as a drift of length g, followed by M cavity intervals, and a final drift of length g, where

$$g = L_w + (L_{ins} - d)/2. \tag{2.2}$$

The choice of cryo-modules with identical geometry and with the same cavity/cell configuration is economical and convenient for construction. There is, nonetheless, a penalty due to the reduced transit-time-factors when a particle crosses cavity cells with length adjusted to a common central value β_0 that does not correspond to the particle's instantaneous velocity. To minimize this affect the SCL is divided into three sections, each designed around a different central value β_0, and with a different cavity/cell configuration. The cell length in a section is fixed to be

$$L_{cell} = \lambda \beta_0/2, \tag{2.3}$$

where λ is the rf wavelength. We adopted an operating frequency of 805 MHz for the LE-section of the SCL, and 1,610 MHz for the subsequent two sections, ME and HE. The choice of the large rf frequency in the last two sections has been dictated by the need to achieve as large an accelerating gradient as possible so the SCL would fit entirely within the available space. The major parameters of the three sections of the SCL are given in Tables 2.4 and 2.5.

Cryomodule

We have decided to have four cavities per cryomodule, based on the transverse and longitudinal phase advances(see Section 2.2.10). In addition to the active lengths of the accelerating cavities, the following length allowances were made for equipments along the beam line.
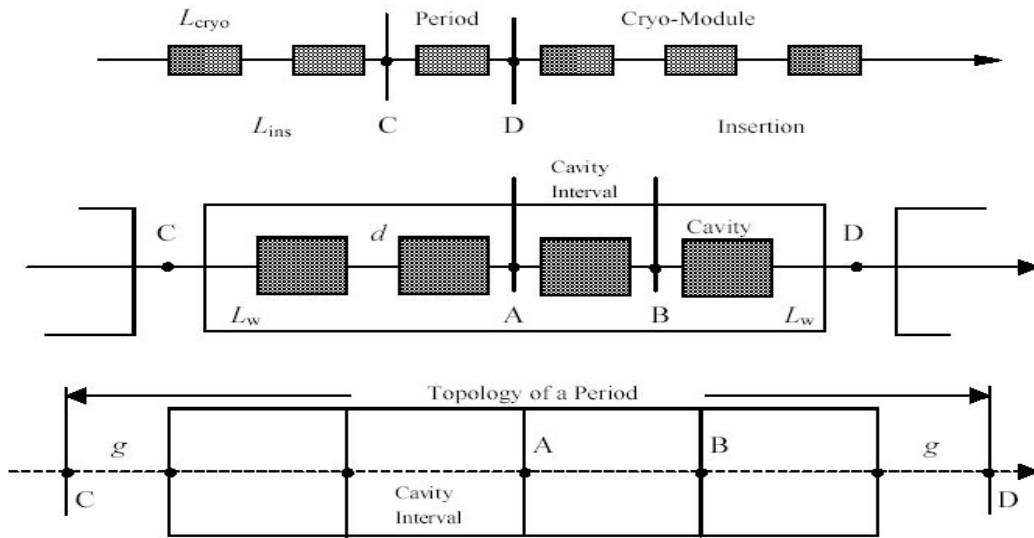
Figure 2.6: Configuration of a proton superconducting linear accelerator.

- Inter cavity space: 32 cm for 805 MHz, 16 cm for 1610 MHz

- Cold to warm transition: 30 cm

- Warm insertion: 100 cm for 805 MHz and 140 cm for 1610 MHz

Figure 2.7 shows the inter cavity space with the power coupler. There is not enough space for the HOM coupler.
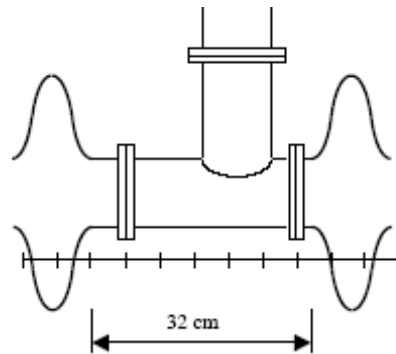
Figure 2.7: Inter cavity space

Warm Insertion

The linac beam line consists of the cryomodules and the warm sections. The warm section consist of 100/140 cm (805/1610 MHz) long spaces between the cryomodules that contains following beam line devices:

- Quadrupole magnets

- Horizontal and vertical steering dipoles

- Beam diagnostics

- Bellows

- A tee to accommodate a pumping port

- Two gate calves

Figure 2.8 shows the warm section with beam line devices
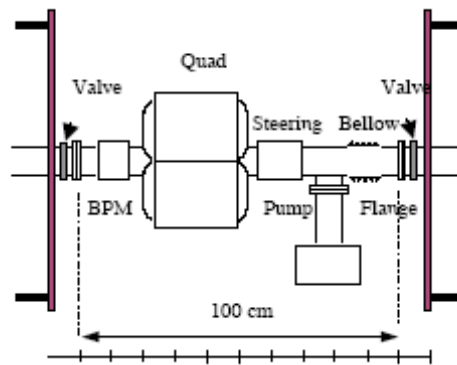
Figure 2.8: SCL warm section with beam line devices

SCL Length and Other Considerations

The length of the SCL depends on the average accelerating gradient. The local gradient has a maximum value that is limited by three causes: (1) The surface field limit, in the frequency range of interest between 805 and 1,610 MHz, is around 40 MV/m. For a realistic cell shape, we set a limit on the axial electric field to 15 MV/m at 805 MHz, and 30 MV/m at 1,610 MHz. (2) There is a limit on the peak power provided by rf couplers that we take here not to exceed 400 kW, including a contingency of 50% to avoid saturation effects. (3) To make the longitudinal motion stable, we can only apply an energy gain per cryo-module that is a relatively small fraction of the beam energy at the exit of the cryo-module. The conditions for stability of motion have been derived in reference [15]. There is one klystron feeding a single coupler to a single cavity. The total length of the SCL injector proper from end to end is about 130 m, including a 4.5-m long matching section between LE and ME sections. When averaged over the real estate, the actual acceleration rate is about 5 MeV/m in the LE section

and 10 MeV/m in the ME and HE sections. Efficiencies, defined as the ratio of beam power to required total AC power, is relatively high for a pulsed linac, ranging between 9 and 15%.

A superconducting linac is most advantageous for a continuous mode of operation (CW). There are two problems in the case of the pulsed-mode of operation. First, the pulsed thermal cycle introduces Lorentz forces that deform the cavity cells out of resonance. This can be controlled with a thick cavity wall strengthened on the outside by mechanical supports. Second, there is an appreciable period of time to fill the cavities with RF power before the maximum gradient is reached [15]. During the filling time, extra power is dissipated before the beam is injected into the linac. The extra amount of power required is the ratio of the filling time to the beam pulse length. The filling times are also shown in Table 2.5.

Table 2.4: General parameters of the SCL.

Linac Section	LE	ME	HE
Ave. *Incremental* Beam Power, kW	7.52	15.0	15.0
Average Beam Current, μA	36	36	36
Initial Kinetic Energy, MeV	200	400	800
Final Kinetic Energy, MeV	400	800	1200
Frequency, MHz	805	1610	1610
No. of Protons / Bunch x 10^8	8.70	8.70	8.70
Temperature, ^{o}K	2.1	2.1	2.1
Cells / Cavity	8	8	8
Cavities / Cryo-Module	4	4	4
Cavity Separation, cm	32.0	16.0	16.0
Cold-Warm Transition, cm	30	30	30
Cavity Internal Diameter, cm	10	5	5
Length of Warm Insertion, m	1.079	1.379	1.379
Accelerating Gradient, MeV/m	10.5	22.9	22.8
Ave. (real-estate) Gradient, MeV/m	**5.29**	**9.44**	**10.01**
Cavities / Klystron	1	1	1
No. of rf Couplers / Cavity	1	1	1
rf Phase Angle	30°	30°	30°
Method for Transverse Focusing	FODO	Doublets	Doublets
Betatron Phase Advance / FODO cell	90°	90°	90°
Norm. rms Emittance, π mm-mrad	0.8	0.9	1.0
rms Bunch Area, π ^{o}MeV (805 MHz)	0.5	0.5	0.

2.2.4   Radio Frequency Source

The SCL rf source system consists of the klystrons, power supplies, transmitters, circulators, waveguides and the beam control system. Low Energy (LE) section of the SCL will be

Table 2.5: Summary of the SCL design.

Linac Section	LE	ME	HE
Velocity, β: In	0.5662	0.7131	0.8418
Out	0.7131	0.8418	0.8986
Cell Reference β_0	**0.615**	**0.755**	**0.851**
Cell Length, cm	11.45	7.03	7.92
Total No. of Periods	6	9	8
Length of a Period, m	6.304	4.708	4.994
FODO-Cell Ampl. Func., β_Q, m	21.52	8.855	8.518
Total Length, m	37.82	42.38	39.96
Coupler rf Power, kW (*)	263	351	395
Energy Gain/Period, MeV	33.33	44.57	50.10
Total No. of Klystrons	24	36	32
Klystron Power, kW (*)	263	351	395
$Z_0 T_0^2$, ohm/m	378.2	570.0	724.2
Q_0 x 10^{10}	0.97	0.57	0.64
Transit Time Factor, T_0	0.785	0.785	0.785
Peak Axial Field, E_a, MV/m	13.4	29.1	29.0
Filling Time, ms	0.337	0.273	0.239
Ave. Dissipated Power, W	2	11	8
Ave. HOM-Power, W	0.2	0.5	0.4
Ave. Cryogenic Power, W	65	42	38
Ave. Beam Power, kW	7.52	15	15
Total Ave. rf Power, kW (*)	17	31	30
Ave. AC Power for rf, kW (*)	37	69	67
Ave. AC Power for Cryo., kW	46	30	27
Total Ave. AC Power, kW (*)	83	99	94
Efficiency, % (*)	9.05	15.21	16.08

(*) Including 50% rf power contingency.

operating at 805 MHz, while Medium Energy (ME) and High Energy (HE) at 1610 MHz. The basic rf source architecture will be the same for all three sections. Each cavity will be driven by a single klystron through the circulator. In most of the cases one transmitter will operate six klystrons; Two transmitters will be operated by a single power supply.
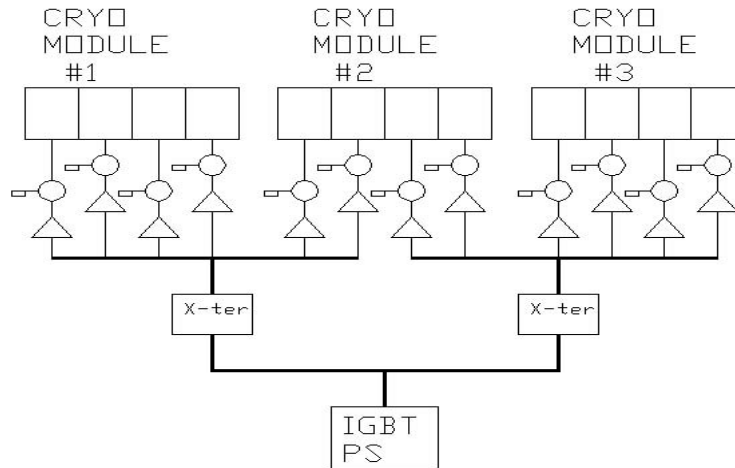
Figure 2.9: Radio frequency (rf) source architecture.

Klystrons for all three sections will be based on the SNS SCL CPI model VKP-8291A. This tube is rated for 550 kW peak, 50 kW average at 805 MHz. The 1.610 GHZ design uses the VKP-8291A electron gun and beam optics. The rf circuit would be scaled to twice the frequency, but the mechanical design approach would be the same.

Transmitters for the SCL klystrons will be the same as for the ORNL. Each unit will have it's own PLC controller, water cart and HV tank into which the klystron is fitted. Controls include the magnet power supplies, ion pump supply, rf amplifier and filament power supply.

Power supply to support the klystrons will also be based on the ORNL SNS design. It will be rated at 75 kV 140 Amps. To eliminate the need for the fast shutdown (crowbar protection) we intend to utilize IGBT technology.

Y junction circulators, rated at 550 kW pulsed power will be used to protect the klystron amplifiers.

The SC LINAC LLRF system will be based on the use of independent controllers for each LINAC cavity. The controllers will provide flexible closed loop amplitude and phase control of the cavity fields. The technology used will be FPGA / DSP based, making use of high speed, high accuracy ADCs and DACs to interface with the analog rf signals. Synchronization between controllers will be based on either a distributed rf reference or a distributed digital timing reference system.

2.2.5 Cryogenic System

There are 23 cryomodules consisting of three types of design for the Low, the Medium and the High Energy region in SCL. With total length of 130 m (approximately 40 m for each

region), it is hard to take advantage of long cryomodule such as the TESLA design. The SNS high beta design is selected as the baseline.

In SCL, each cryomodule consists of four cavities and each cavity consists of eight cells. There is a power coupler for each cavity. The cavities are to be immersed in a helium vessel operating at 2.1 K and 0.04 bar. The power couplers are to be cooled by 4.5 K helium flow at 3 bar. The heat shield is to be cooled between 30 and 50 K. Parameters and heat loads of a cryomodule are given in Table 2.6. In Table 2.6, the dynamic heat loads refer to additional heat input from rf operation.

Table 2.6: Parameters and heat loads of a cryomodule

	Low Energy	Medium Energy	High Energy
No. of cryomodule	6	9	8
No. of cavities per module	4	4	4
No. of cells per cavity	8	8	8
Length	5.46 m	3.49 m	3.77 m
2 K static heat load	28 W	28 W	28 W
2 K dynamic heat load	0.33 W	1.22 W	1.00 W
4.5 K load for couplers: static	0.2 g/s	0.2 g/s	0.2 g/s
4.5 K load for couplers: dynamic	0.1 g/s	0.1 g/s	0.1 g/s
Shield heat load including transfer Line	200 W	200 W	200 W

The cryogenic system is to be designed for providing cooling at 2.1, 4.5 and 50 K temperature levels. All 23 cryomodules are cooled in parallel as shown in Figure 2.10. The Helium refrigerator is located outside the tunnel and is connected to SCL by a set of transfer lines.

Flow schematic for cooling a cryomodule is given in Figure 2.11. Two end boxes are used for interfacing a cryomodule with the transfer lines. A 2 K subcooler heat exchanger is installed in one of the end box. Through the Transfer Line, cold helium at 4.5 K is provided to SCL. Majority of the 4.5 K helium transfer line is cooled to $\sim$ 3 K, counter flow heat exchange with the 2.1 K boil-off in the subcooler, before expanded into the helium vessel. A small portion of the 4.5 K helium is used to cool the Power Couplers. The refrigerator also provides 30 K helium flow to the shield. The shield return temperature is kept below 50 K.

Use of the 2 K subcooler simplifies the transfer line construction. Compared to the case without 2 K subcooler, one less line is needed. The thermodynamic efficiency is better because heat load in the supply line is absorbed at 4.5 K rather than at 2 K level. Bayonets and isolation valves are incorporated in the transfer lines. A cryomodule can be replaced without warmup of other modules. This feature increases cost of the distribution system. In the follow up study, trade off between cost and operation needs will be performed.
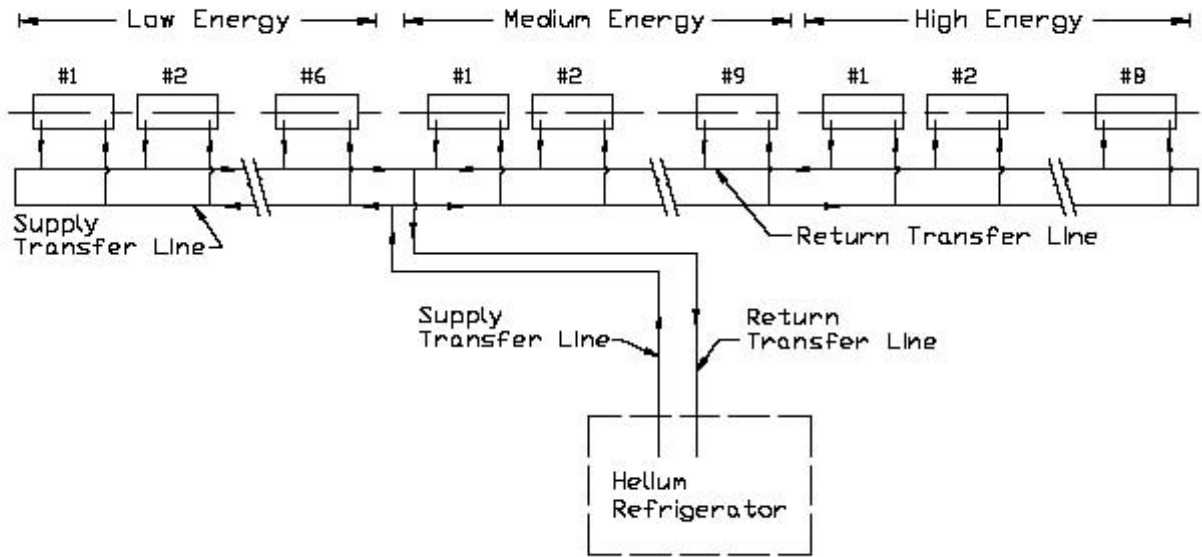
Figure 2.10: Cryogenic distribution system for AGS SCL.
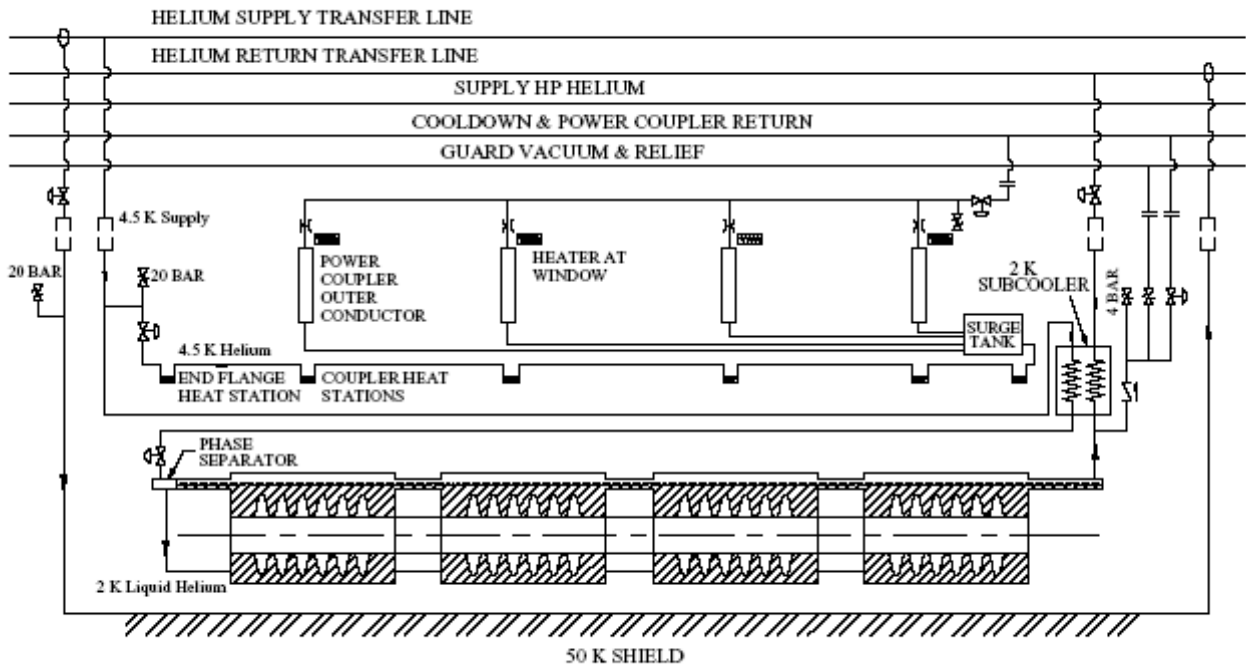
Figure 2.11: Flow schematic for cooling a cryomodule in AGS SCL.

Table 2.7: Refrigeration parameters.

23 Cryomodules	Primary	Secondary	Shield
Temperature	2.1 K	4.5 K	35 - 55 K
Pressure	0.04 bar	3.0 bar	$\sim$ 4bar
Static load	645 W	4.6 g/s	4,600 W
Dynamic load	21 W	2.3 g/s	0 W
Total load	666 W	6.9 g/s	4,600 W
Refrigerator Capacity	1,300 W	15 g/s	6,200 W
Margin	$\sim$ 100%	$\sim$ 100%	$\sim$ 35%

Total heat load and pressure requirement for SCL is given in Table 2.7. Baseline heat loads are extrapolated from the SNS published literature. Once actual experience on SNS becomes available, heat load values will be revised. In Table 2.7, the primary load refers to the 2 K heat load for cooling the cavities. The secondary load refers to the 4.5 K cooling for the power couplers. The shield heat load is for cooling the heat shield.

The static heat load consists of heat conduction and thermal radiation. The dynamic heat loads result from rf operation. In SCL, the 2 K dynamic load is relatively small due to its low duty cycle. The 4.5 K dynamic heat loads are assumed to be the same as those couplers in SNS.

In this report, capacity margin of the helium refrigerator is chosen to be the same as SNS. Once SNS is commissioned, these margins could be revised to more suitable values. Total equivalent capacity is 1,800 W at 2.1 K and equals about 60% that of the SNS refrigerator. Refrigerator configuration is expected to consist of a conventional 4 K cold box and a 2 K cold box with a 5 stage cold compressors. Redundancy and maintainability will be incorporated to achieve highest reliability.

2.2.6   Vacuum System

The SCL vacuum system consists of the cryomodules, the room temperature (RT) insertion sections and the interfaces to existing Linac and AGS. To minimize the H$^-$ stripping by the residual gas molecules, average pressure of 10^{-8} Torr is required for the SCL. The H$^-$ stripping cross section is proportional to $1/\beta^2$ and Z of the target gas [16]. The fraction of the beam loss per meter along SCL is estimated as shown Figure 2.12 for pressures of 1x10^{-8} Torr and 1x10^{-10} Torr (assuming a gas composition of 90% H$_2$ and 10% CO) and found to be of tens ppb and fraction of ppb, respectively; much less than the requirement of 1 watt/m. The beam line vacuum pressures in cryomodules are normally at 10^{-12} Torr owing to the large cryopumping provided by the 2° K surface. Pressure of $\leq$1x10^{-9} Torr is desirable in the RT sections to minimize gas migration and particulate contamination to the SC cavities, and will also have minimum H$^-$ stripping.
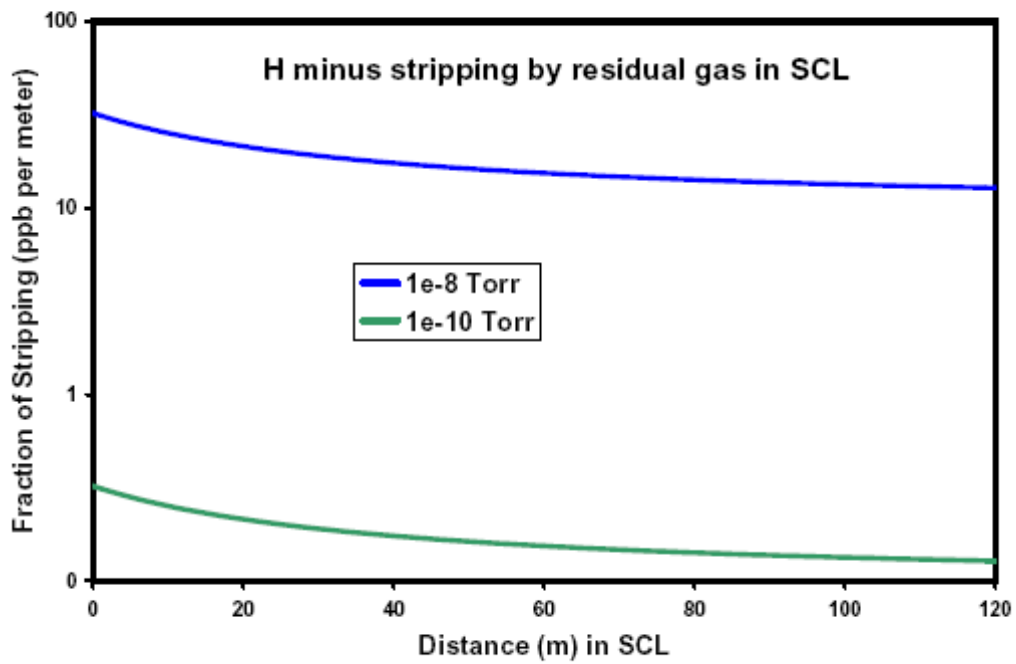
Figure 2.12: Estimated fractional beam loss per meter along the SCL.

The cryomodule beam vacuum will be instrumented with vacuum gauges and ion pumps to monitor and maintain the vacuum during initial conditioning and testing, and when the cavities are not cold. Each cryomodule can be isolated with all-metal gate valves at the warm-to-cold transitions. Relieve valve or burst disc will prevent the damage of cryomodules from catastrophic failure. To protect the high-power coupler window from multipacting and excessive RF loss, the coupler will be equipped with diagnostics for vacuum, temperature (infrared detector), and light (arc detector). Vacuum and light levels will be used to trip the rf in case of arcing. Roughing manifolds will connect several cryostats to turbopump stations to pump and maintain the insulating vacuum until the cavities are at the operating temperature of 2K. Additional portable turbopump stations will be used to pump those cryostats with significant helium leaks.

The RT insertion and matching sections between cryomodules will house the focusing and steering magnets, alignment, beam diagnostics, bellows, gate valves, and ports for vacuum gauges, ion pumps and roughing. The RT sections will be cleaned and in-situ baked to reduce the pressure to below 1×10^{-9} Torr, therefore minimizing contamination of the adjacent cavities.

Differential pump stations (DPS) at the entrance and exit of SCL are needed to create pressure differential between the 10^{-8} Torr RT Linac and AGS from the ultrahigh vacuum of SCL. These DPS consist of high-speed titanium sublimation pumps, sputter ion pumps, and electrostatic precipitators to prevent particulate migration and contamination to SCL cavities. The DPS should provide a factor of 1000 improvement in pressure from RT systems to SCL. Fast closing valves will be positioned at DPS to prevent catastrophic vacuum failure reaching the cavities.

A clean room facility for the preparation, assembly and testing of the SC cavities is highly desirable but not included in the baseline design, neither are the electro-chemical polishing facility and high temperature vacuum furnace for cleaning and annealing of the cavities.

Pirani and cold cathode gauges will be used throughout the SCL as primary vacuum measurement, and will be supplemented by the ion pump readouts. Cold cathode readings together with the arc detector will trip the rf in one millisecond to protect the high-power coupler windows. Portable residual gas analyzers will be used to analyze the gas composition when a problem arises. All the vacuum electronic devices will be located at the service buildings. These devices with local and remote capabilities can be operated through front panel switches and will communicate with the PLC based Control system through multi-drop serial communication network drops for remote monitoring and control. PLCs will provide the logic for the operation of the sector gate valves and other machine subsystems with hard wired I/O from the devices.

2.2.7   Magnet System

Magnets for SCL and it's transfer lines are included in Section 5.2.

2.2.8   Power Supply System

There is a total of 54 current regulated, dc power supplies interfaced with quad or dipole magnets. The magnet designs are based on magnets which have been built at Brookhaven in the past. The longest distance assumed from a power supply to a magnet and back is about 500 feet. Table 2.8 indicates the type and number of magnets interfaced with each power supply. Field magnet data as well as magnet voltage, current and cable, plus magnet resistance is indicated. The following power supplies are water cooled, thyristor controlled dc power supplies.

There are 49 power supplies rated at 50 volts, 550 amps and 1 power supply rated at 50 volts, 250 amps. All these power supplies are based on existing designs used as part of the recent commissioned Booster NSRL beam line. Further more we need 4 linear air cooled power supplies rated at 25 volts 25 amps. The design of these power supplies is based on the Spallation Neutron Source (SNS) correctors. The interface of all the power supplies to our controls will be a PSI/PSC system identical to the Booster NSRL and SNS control system.

2.2.9   Diagnostics System

Instrumentation has been selected to provide beam position and phase (BPM), intensity (BCM), shape & energy (BSM), profile, and loss (BLM) measurements with quantities shown in Table 2.9.

Beam Position Monitors

There will be micro-strip type BPM's installed at the quadrupoles throughout the SCL and transports. The signals will be down converted to a 50MHz intermediate frequency (IF) for processing. A sampled in-phase and quadrature-phase (I&Q) processing technique will be used to obtain amplitude and phase information from the IF signal. These will provide position measurements across the beam pipe radius with 1% accuracy and resolution of 0.1% aperture radius.

Beam Profile Monitors

Measuring transverse beam size and emittance is important for matching and as a tuning diagnostic. Typically carbon wire scanner systems are used to measure beam profiles, however due to concern about the possibility that carbon wire ablation, or broken wire fragments, could find their way into the superconducting cavities, a laser wire profile monitor system will be used at locations throughout the SCL. Advantages are that profiles can be measured during normal operations without reducing pulse widths, and there are no moving parts inside the vacuum system. We can expect to achieve accuracy of 1 part in 10,000 based on the experience with the system under development at the SNS SCL. There will be 13 profile measurement locations throughout the SCL, one after every other tank.

There will also be three plunging multiwire profile monitors in the transport between SCL and AGS. This semi-destructive measurement will allow transverse profile measurements as well as emittance information for each beam transfer to the AGS.

Table 2.8: Power supplies for linac and matching sections magnets

LOCATION	# PS	MAG. TYPE	# IN SERIES	MAX. FIELD (T-T/m)	MAG. VOLT. (V)	MAG. CURR. (A)	MAG. + CABLE RESIST. (OHMS)	PS VOLTS	PS AMPS
200 MeV to SCL	1	3D10	1	0.98 T	18.72	520	0.041	50	550
SCL to AGS	1	2.4D116	2	0.21 T	1.32	228	0.086	50	250
200 MeV to SCL	4	3Q8.6	1	3 T/m	2.2	22	0.42	25	25
SCL and SCL to AGS	48	4Q8	1	20.0 T/m	10	497	0.07	50	550

Table 2.9: Superconducting linac instrumentation quantities.

Device	SCL-Low	SCL-Med	SCL-High	Transport	Totals
BPM	8	9	8	6	31
BCM	2	1	1	1	5
BLM	17	20	18	12	67
Profile					
Laser wire	4	5	4		13
Multiwire				3	3
Screen				1	1
BSM	1				1

Beam Loss Monitors

In order to provide machine protection, allow "hands-on" maintenance, as well as a tool for tuning, the beam loss monitor system (BLM) will be critical for minimizing losses and optimizing efficiency. This system will be primarily based on argon-filled ion chambers with custom-built electronics packaged in VME modules. We will use the calibrated chamber designed at BNL for SNS with its improved response time and extended dynamic range. There will be 62 ion chambers distributed over the 180 m of transport from the DTL to AGS. They will be located primarily near the quadrupoles, acceleration tanks and dipoles.

The front-end electronics will provide three output signals, a wide-band signal for viewing losses with respect to time, a filtered signal for high resolution long term loss measurements, and a leaky integrator stage will provide a signal to a comparator with a programmable threshold which will feed the machine protect system in the event of a large loss. There will also be five neutron detectors which will utilized the same electronic signal processing.

Beam Current Monitors

The beam current monitor system will be based on fast current transformers (FCT) from Bergoz Instrumentation, and custom built electronics. There will be hardware included for system calibration. A total of five transformers will be installed: one upstream of the SCL, after each of the low, medium and high sections, and finally one before AGS injection.

Bunch Shape Monitor

A BSM will be installed between the 200 MeV bend and the first tank of the SCL to help tune matching characteristics. The longitudinal distribution of charge in the linac bunches is one of the most important beam parameters. The principle of the BSM is based on the coherent transformation of longitudinal distribution of the analyzed beam charge into spatial distribution of low energy secondary electrons through transverse rf modulation. The bunch shape monitor first developed at BNL, with further advancements made at INR and SNS will provide bunch shape, energy and energy spread measurements.

Screen & Electron Catcher

A remote controlled plunging phosphor screen will be monitored by a rad-hard video camera near the injection region. This will include neutral density filters to increase dynamic range. Its purpose is to help set up and diagnose injection.

An isolated electron catcher will collect the electrons stripped at the injection stripping foil. The current measured will be processed by custom electronics, and will generate a wideband signal for monitoring stripping efficiency and foil integrity.

2.2.10   SCL Beam Dynamics

Configuration

SCL configuration is shown in Table 2.10. The low-energy-section consists of six, 6.3 m long 90 degree FODO periods with energy gain of 33.3 MeV per period. The medium and high-energy-section consist of nine and eight 90 degree periods of length 4.7 and 4.9 m respectively. The quadrupole lengths used in these section are 30 cm long.

Table 2.10: Linac configuration

Linac Type	LE	ME	HE
Energy Range (MeV)	200-400	400-800	800-1200
Cell Geometric β	0.615	0.755	0.851
Lattice Type	FODO	Doublet	Doublet
Lattice Period (m)	6.304	4.708	4.994
Quadrupole Gradient(kG/cm)	0.15-.22	1-1.4	1.4-1.8
Energy gain/period (MeV)	33.33	44.57	50.10
RF Phase (degree)	-30	-30	-30

Matching into SCL

The beam from the present 200 MeV linac was matched in the SCL low energy section using four additional quadrupoles and one dipole (magnets described in Section 5.2), and one 805 MHz buncher. This matching section is achromatic. Figure 2.13 shows the TRANSPORT output.

Beam Stability

The peak beam current is similar to the SNS 35 mA, and simulations show there is no concern for space charge, beam breakup due to higher order modes in the cavity, etc. The emittance growth after 200 MeV is small for transverse and longitudinal planes. Table 2.11 shows the expected emittance along the linac. The various beam dynamics parameters are shown Figures 2.14 to 2.19.

1Neutrino Superbeam T9–SCL
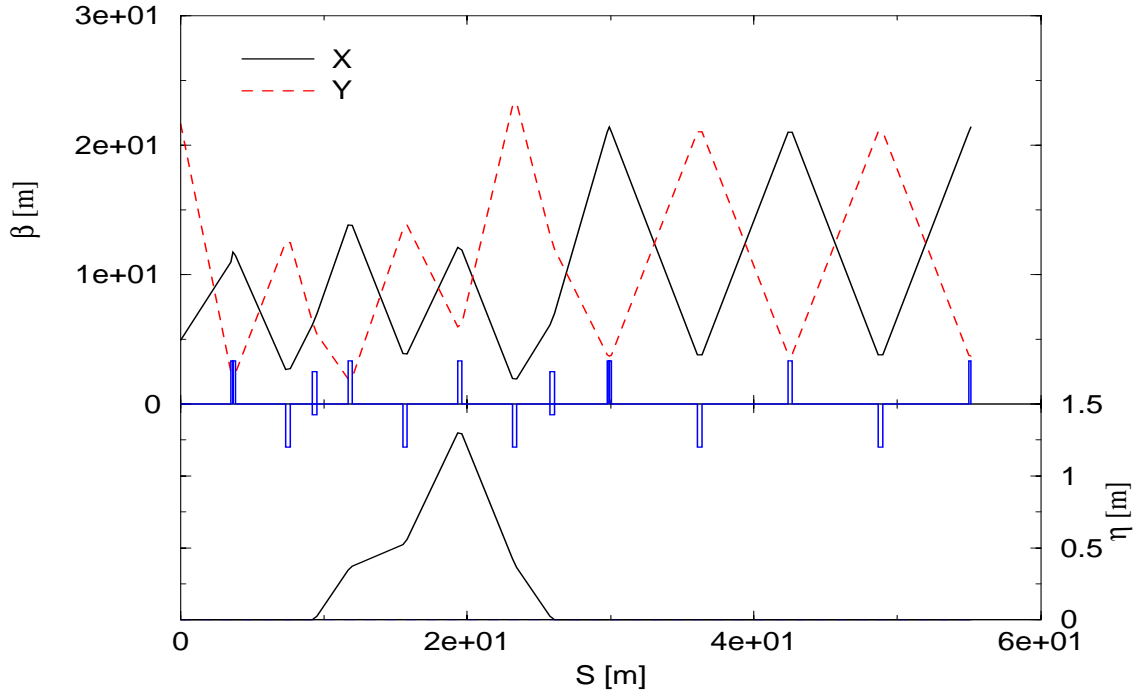
Time: Wed Jun 2 11:43:59 2004 Last file modify time: Wed Jun 2 11:43:55 2004

Figure 2.13: β and η functions along the 200 MeV linac to SCL.

Table 2.11: Expected transverse emittance through the linac

Energy	Present π mm mrad (rms,n)	AGS-SCL π mm mrad (rms,n)
35 keV	0.375(@80 mA)	0.3 (@50 mA)
200 MeV	2.0	0.6
1200 MeV		1.0
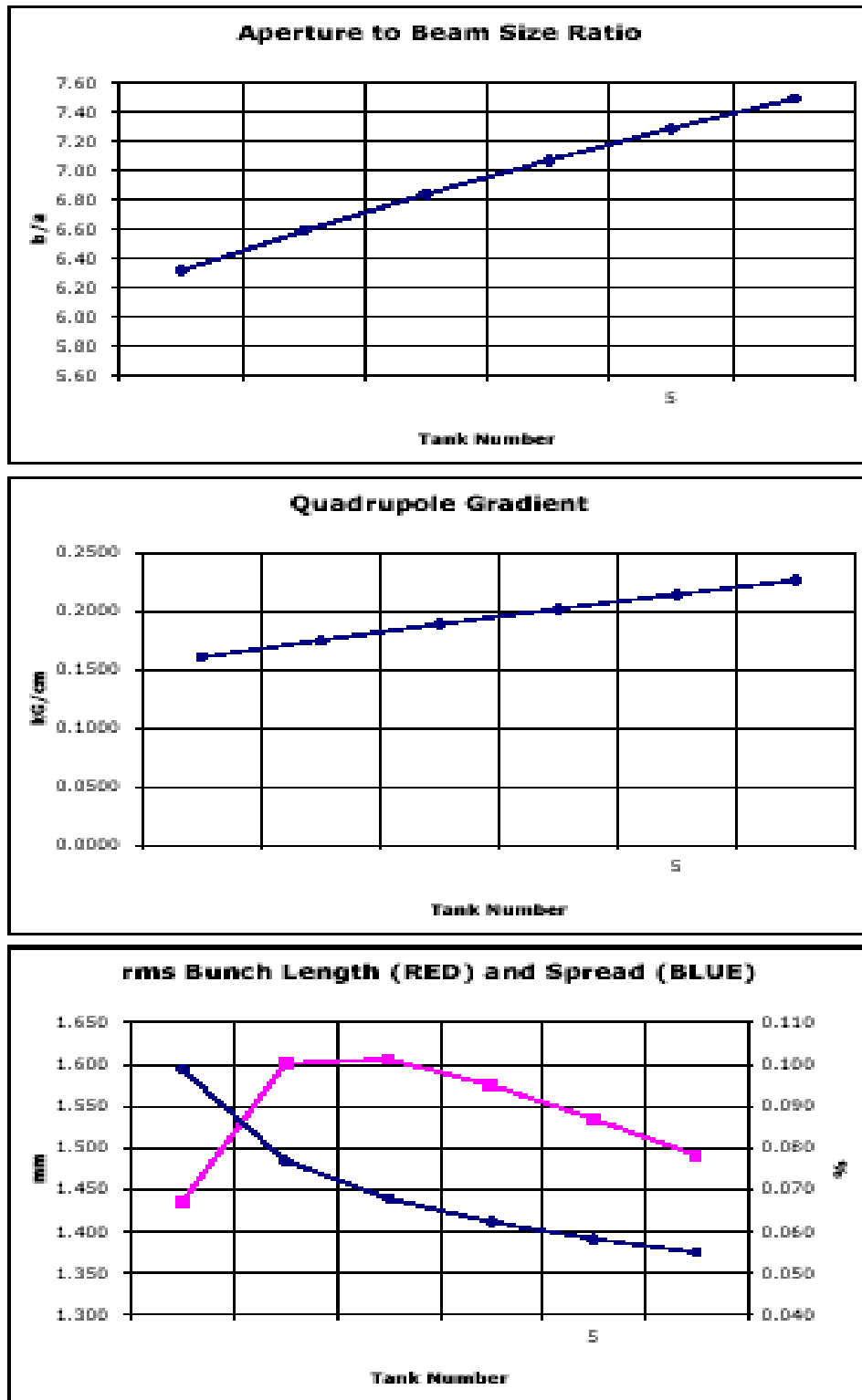
Figure 2.14: Plots of behavior vs. *period* (tank) number of LE section.
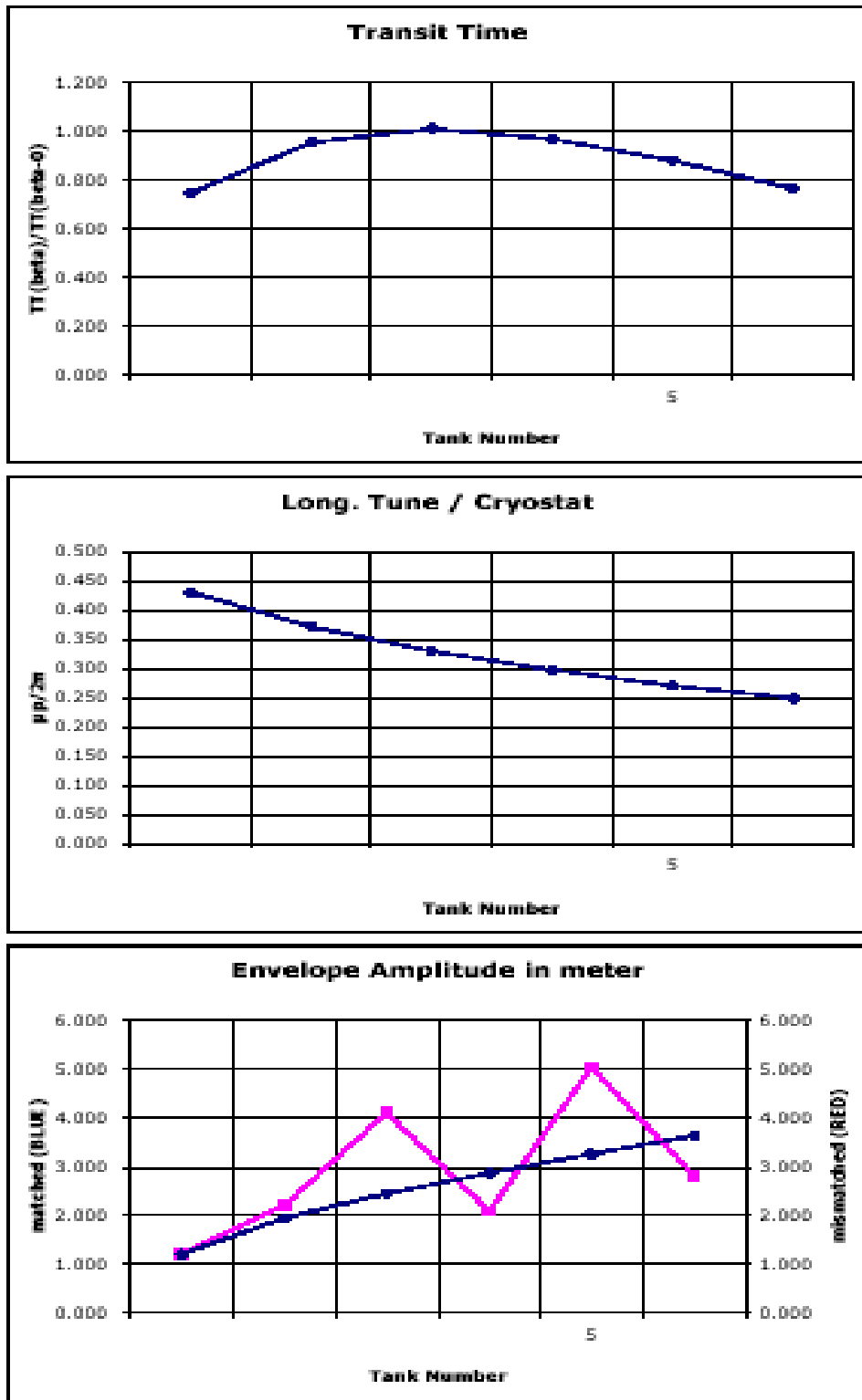
Figure 2.15: Plots of behavior vs. *period* (tank) number of LE section.
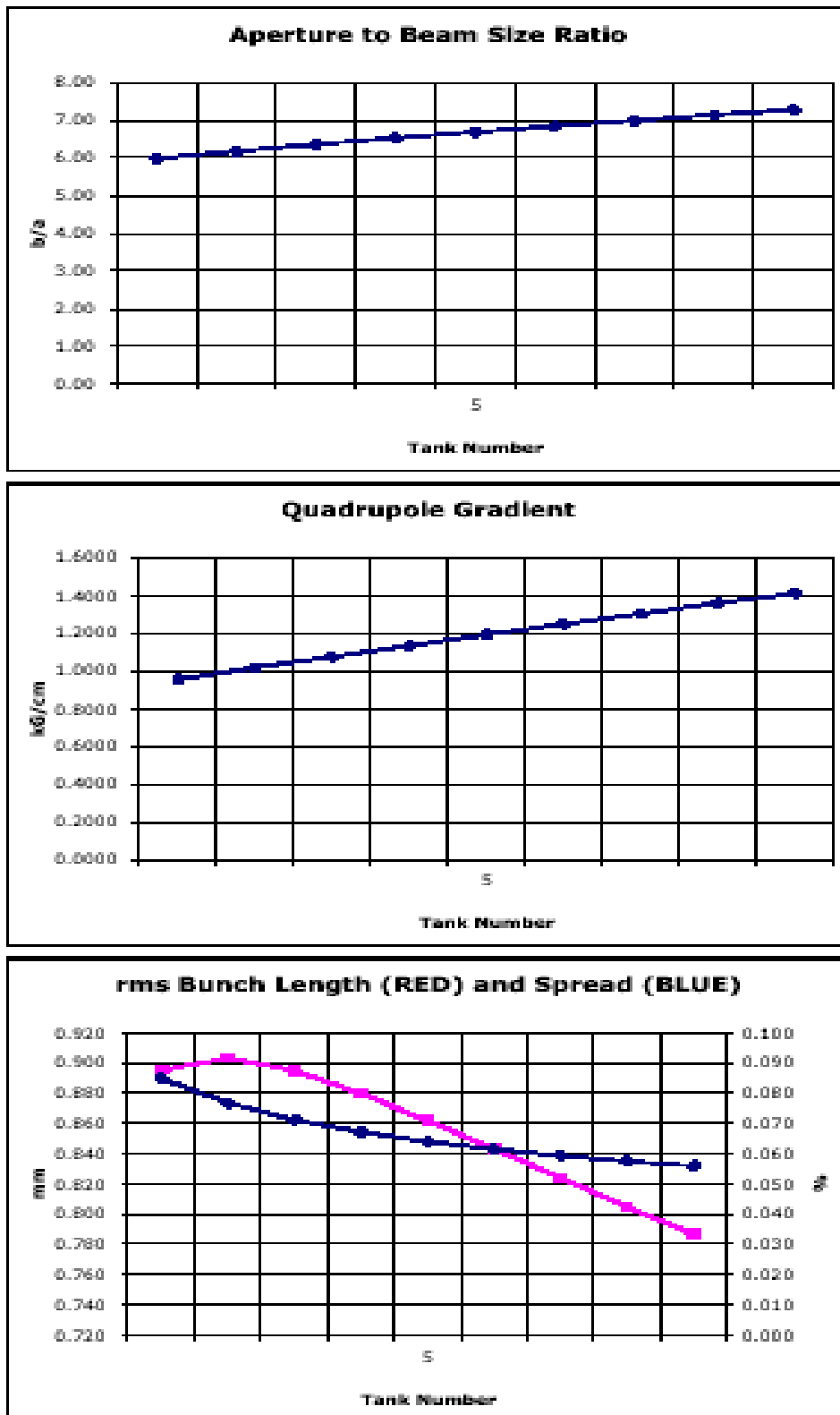
Figure 2.16: Plots of behavior vs. *period* (tank) number of ME section.
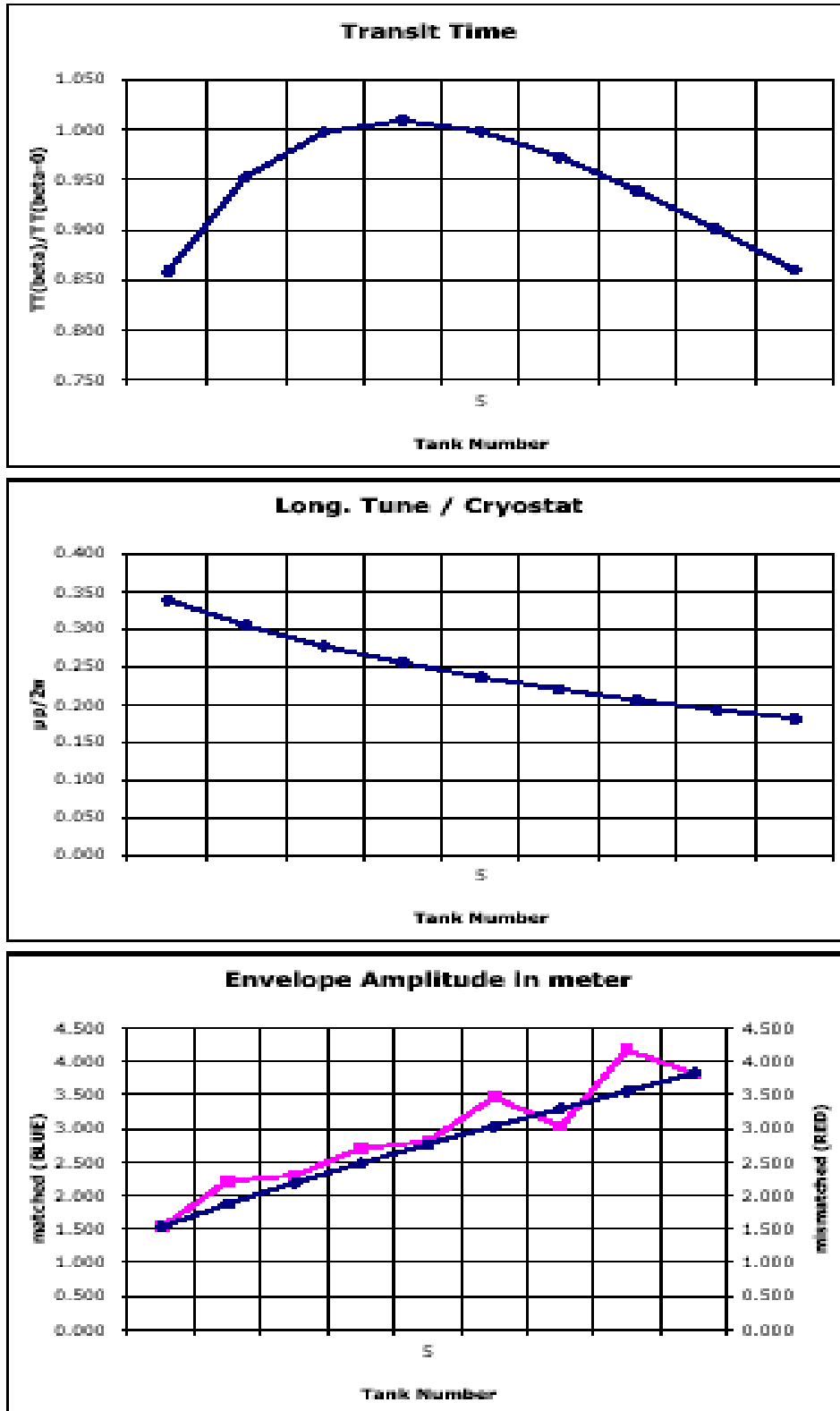
Figure 2.17: Plots of behavior vs. *period* (tank) number of ME section.
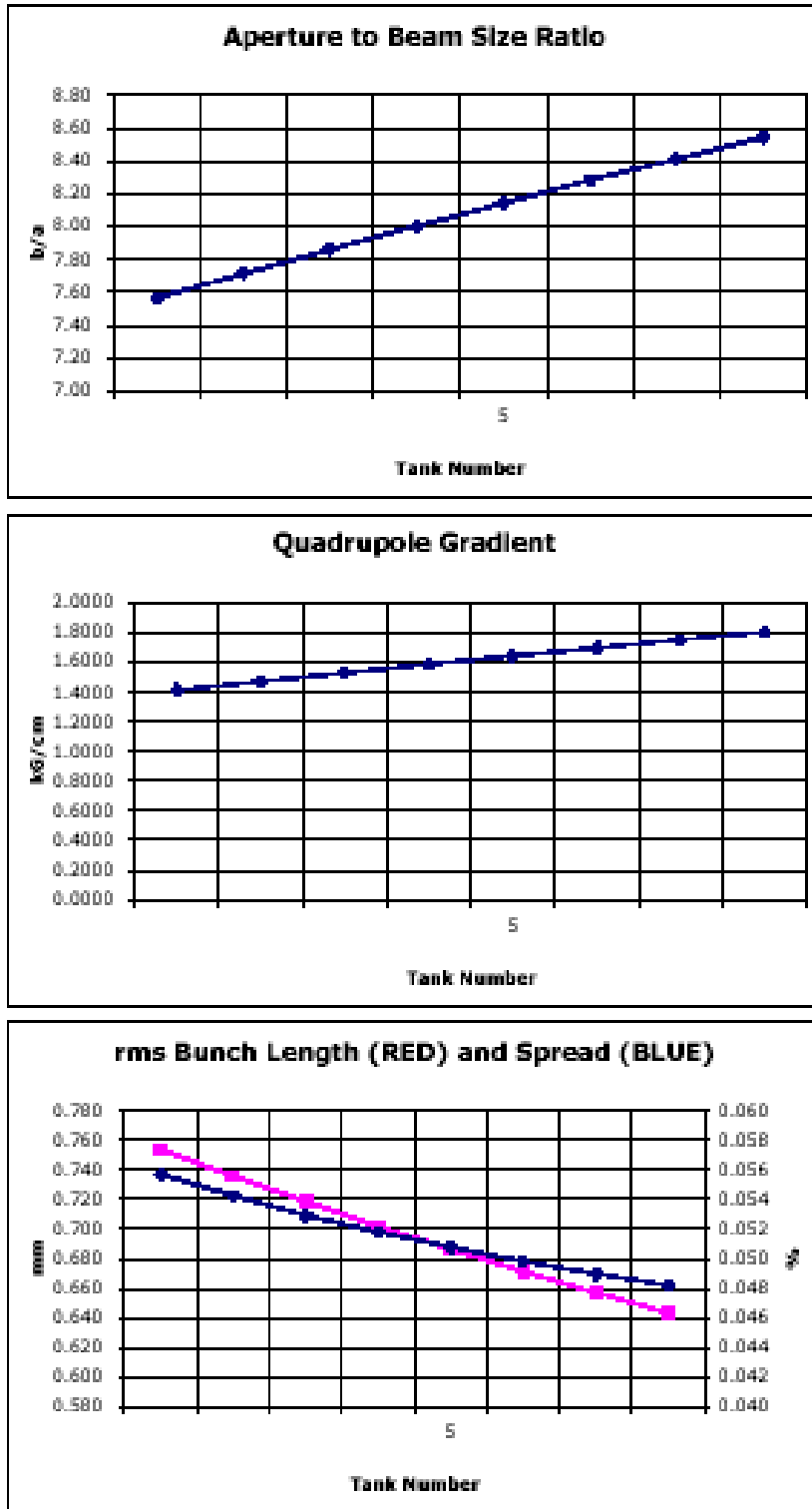
Figure 2.18: Plots of behavior vs. *period* (tank) number of HE section.
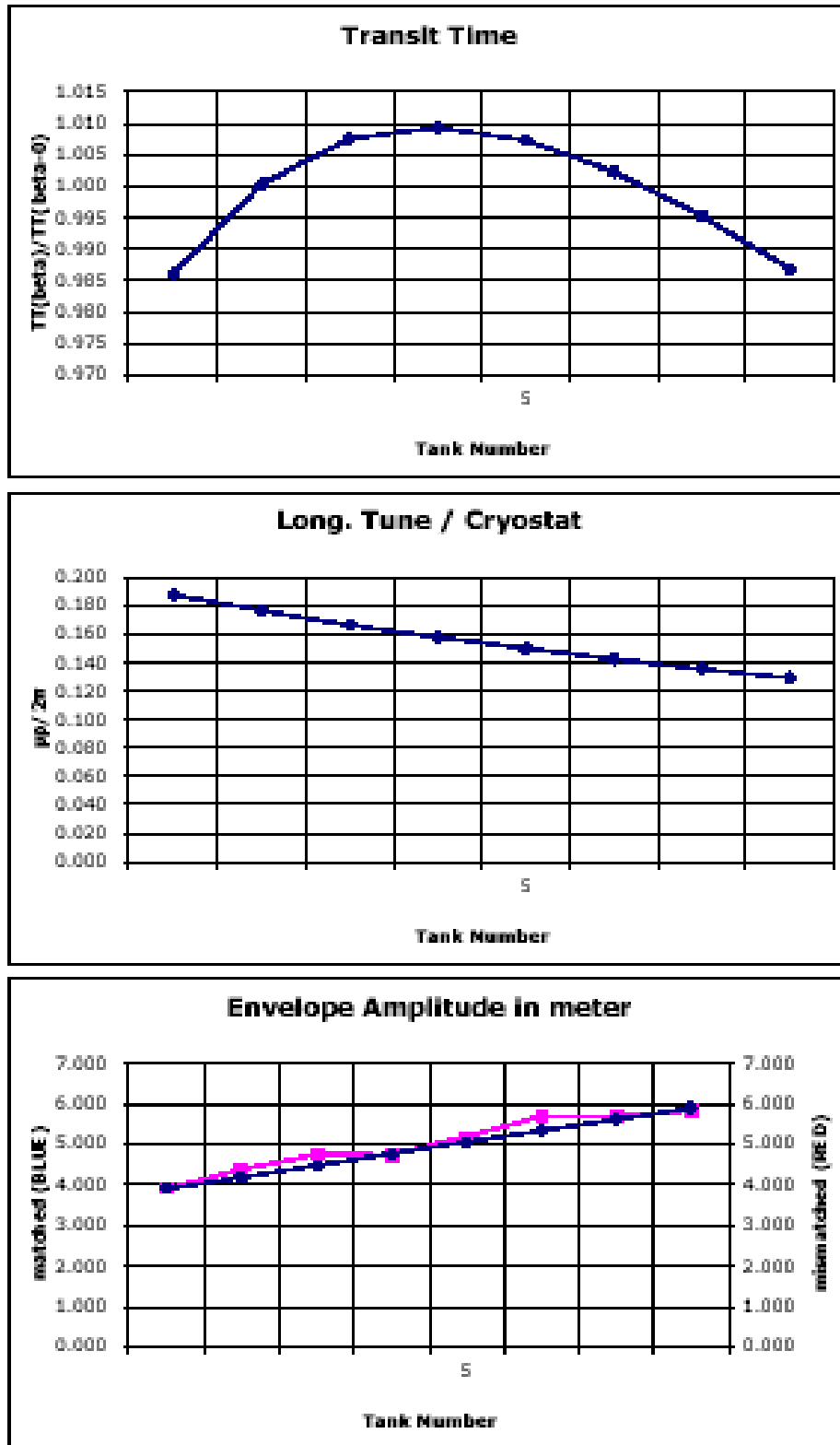
Figure 2.19: Plots of behavior vs. *period* (tank) number of HE section.

Tolerances

Based on the simulations and achieved tolerances at BNL and SNS, we limit the errors to the values shown in Table 2.12.

Table 2.12: Tolerances for the SCL

Quadrupole transverse displacement	0.1 mm
Quadrupole rotation	2.5 mrad
Quadrupole tilt	2.5 mrad
Quadrupole gradient error	0.25%
Cavity displacement	1 mm
Klystron amplitude error	0.5%
Klystron phase error	0.5 deg

The expected energy jitter due to klystron phase and amplitude error is about $\pm$ 2.5 MeV and phase jitter about $\pm$ 3.5 degrees. The expected transverse jitter due to drift tubes in the DTL is about 0.25 mm.

Beam Loss

Typical beam profile at 1000 MeV is shown in Figure 2.20 in units of rms radius. The maximum extent of the beam is about eleven σ. Figures 2.14 to 2.19. show the minimum ratio of the beam pipe size to the rms beam size is about six. The fractional part of the beam in six to eleven σ is about 1×10^{-4}, which will be lost in the SCL. The SCL beam power at 1200 MeV is 45 kW and about 130 m long, therefore the beam loss per meter is $\leq$ 0.04 Watts.

Negative ion stripping during transport along the SCL has been found to be very negligible, never exceeding a rate of 2 x 10^{-8} per ion. But the final 11° bend, before injection into the AGS, could be of concern. To control the rate of beam loss by stripping to a 10^{-5} level or less, the bending field should not exceed 1.25 kGauss over a total integrated bending length of 12 m.

Matching into the AGS

The Courant-Snyder parameters at the injection point are given in Section 4.1.2. A 30 m long transfer line consisting of eight quadrupoles and an eleven degree bend accomplishes the matching constraints. Because the beam power is only 45 kW and line aperture is more than 10 sigma, transverse collimation is not needed to maintain the losses less than 1 Watt/m. The matching section length is not enough for efficient momentum collimation and energy corrector cavity. Figure 2.21 shows the TRANSPORT output for this line.
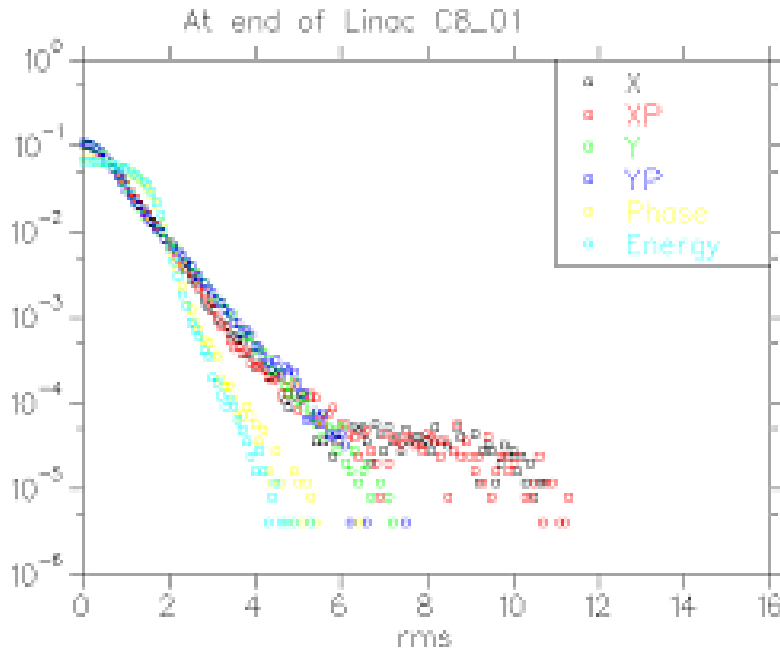
Figure 2.20: Typical beam profile at 1 GeV. X-axis shows the beam σ.
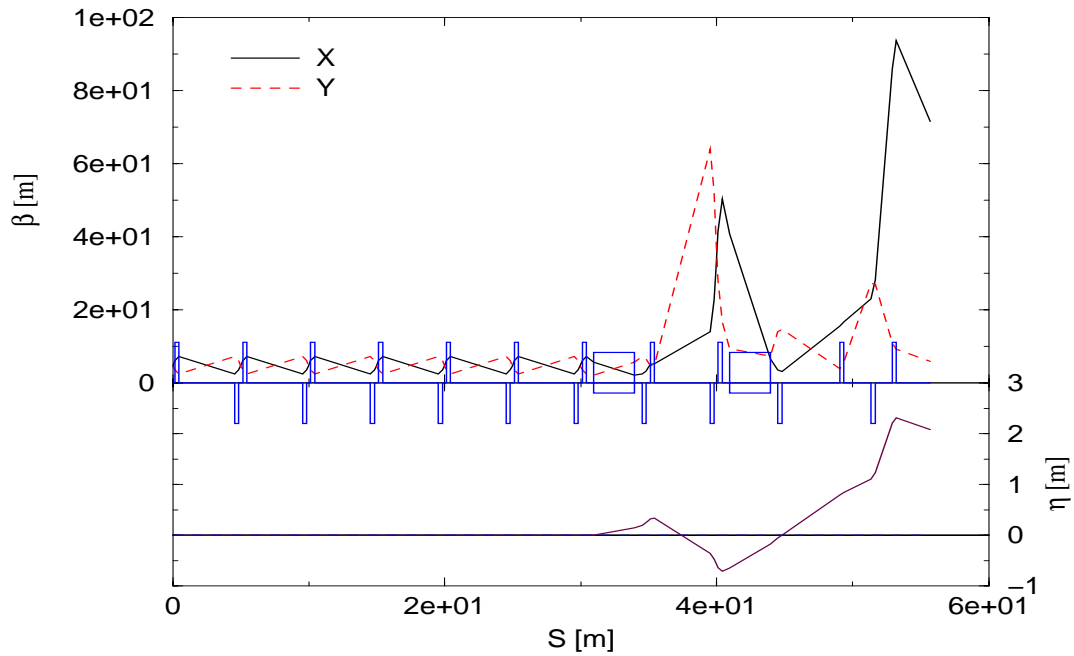
Figure 2.21: β and η functions along the SCL to AGS injection.

3   AGS Upgrade

3.1   Introduction

In its current operation, the AGS receives four batches of 1.5 GeV proton beam from the Booster synchrotron in about 0.5 second. The typical intensity achieved for slow extracted beam operation is about 70 TP (10^{12}). In the proposed AGS upgrade for the neutrino beam program, a new 1.2 GeV superconducting linac will be used as injector which can provide 89 TP proton with injection time of less than a ms. To provide 1 MW beam power for neutrino production, the AGS has to be cycled at 2.5 Hz, instead of 0.5 Hz. For this improved capability, several major upgrade of the AGS have to be implemented.

- First is the new direct injection from the SCL with H$^-$. stripping foil system.

- Second is the new main magnet power supply and its six-loop configuration for the powering of the lattice magnets.

- Third is the new rf accelerating cavity and its associated power switching system for doubling the accelerating voltage operated at 2.5 Hz.

- Fourth is the new single turn fast extraction system for beam delivery to the target.

- Fifth is the new collimation and radiation shielding system to keep the beam losses at an acceptable level.

Those systems and the associated accelerator physics calculations; such as: the transition crossing, the impedances and collective effects, and the H$^-$ injection and phase space paintings, are discussed in Chapters 3 and 4.

3.2   AGS Main Power Supply Upgrade

3.2.1   Present Mode of Operation

The present AGS Main Magnet Power Supply (MMPS) is a fully programmable 6000 A, $\pm$9000 V SCR power supply. A 9 MW Motor Generator (MG), made by Siemens, is a part of the main magnet power supply of the accelerator. The MG permits pulsing the main magnets up to 50 MW peak power, while the input power of the MG itself remains constant. The highest power into the MG ever utilized is 7 MW, that is, the maximum average power dissipated in the AGS magnets did never exceed 5 MW.

The AGS ring comprises 240 magnets connected in series. The total resistance, R, is 0.27 Ohms and the total inductance L is 0.75 H. There are 12 superperiods, A through L, of 20 magnets each.

Two stations of power supplies are each capable of delivering up to 4500 V and 6000 A. Every station consists of two power supplies connected in parallel. One power supply is a 12 pulse silicon controlled rectifier (SCR) type rated at $\pm$5000 volt, 6000 A unit (P type) that is typically used for fast ramping during acceleration and energy recovery. The other is a lower

voltage rated at $\pm$ 1000 V, 6000 A, 24 pulse unit (F type) that is used for flattop or slow ramping operation. The two stations are connected in series, with the magnet coils arranged to have a total resistance R/2 and a total inductance of L/2. The grounding of the power supply is done only in one place, in the middle of station 1 through a resistive network. With this grounding configuration, the maximum voltage to ground in the magnets will not exceed 2500 Volt. The magnets are tested to 3 kV to ground, prior to each startup of the AGS MMPS after long maintenance periods.

3.2.2   Super Neutrino Beam Mode of Operation

To cycle the AGS ring to 28 GeV at 2.5 pulses per second and with ramp time of 200 ms the magnet peak current is 5200 Amp and the peak voltage is 23 kV. Figure(3.1) displays the magnet current, voltage and peak power of a 2.5-Hz cycle. The total average power dissipated in the AGS magnets has been estimated to be 2.7 MW.

Existing ripple specifications are to be preserved, to run present flat top cycles and PPM modes as well as be able to run 2.5 Hz modes, in the future. To do this, and to limit the AGS coil voltage to ground to values around 2.5 kV, the AGS magnets will need to be divided into six sections, each powered similarly to the present half AGS power system as shown in Figure 3.2. We will have four additional P type stations of power supplies as one existing P station. Existing station I and II power supplies and MG set will be preserved. Every P type station will be rated at $\pm$ 5500 volts 6000 A, very similar to the present rating of the P type units. Bypass SCRs will be used across the 4 P type stations, to bypass these units based on load voltage requirements. Station 1 will be grounded as it is done presently and maximum voltage to ground of every section of magnets will not exceed 3200 volts.

3.2.3   The Motor Generator Requirements for 2.5 Hz

The peak power required for a 2.5 HZ mode of operation, is approximately 120 MW. The existing generator cannot provide such a power swing, since it is rated at only 50 MW peak power. One approach would be to purchase an additional 70 to 80 MW peak power motor/generator. The generator should be rated at a slip frequency of 2.5 HZ. This additional motor/generator would power the additional four P type stations of power supplies referenced above. The existing motor/generator would remain in place providing power to the existing station 1 and 2 power supplies.

3.2.4   The Inductor Storage Energy Approach

Another technique would be to store the additional energy needed in storage inductors. The existing motor/generator will remain in place powering the existing station 1 and 2 rectifiers. The additional energy will be stored in inductors driven by Silicon controlled rectifiers fed from the same input ac line, as the additional 4 Silicon controlled rectifiers (SCR) needed to power the AGS magnets for 2.5 Hz operation. Power flow from the ac line into the additional 4 Silicon controlled rectifiers and into Silicon controlled rectifiers powering the storage inductors are inverted images of each other. As a result the input power into these power supplies powering the magnets as well as the storage inductors would remain constant equal to the average power
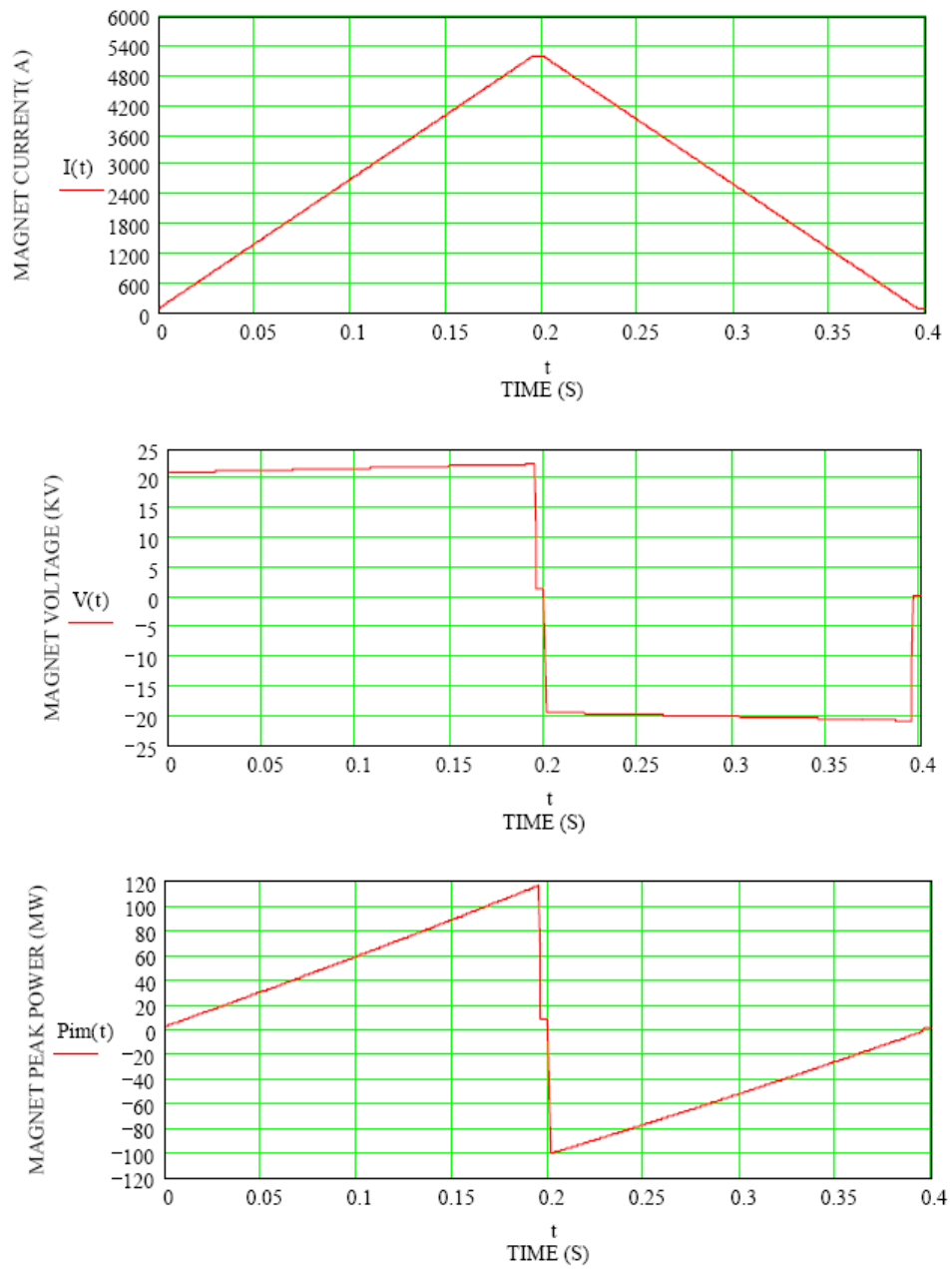
Figure 3.1: AGS magnet current, voltage and peak power for 2.5 Hz operation.
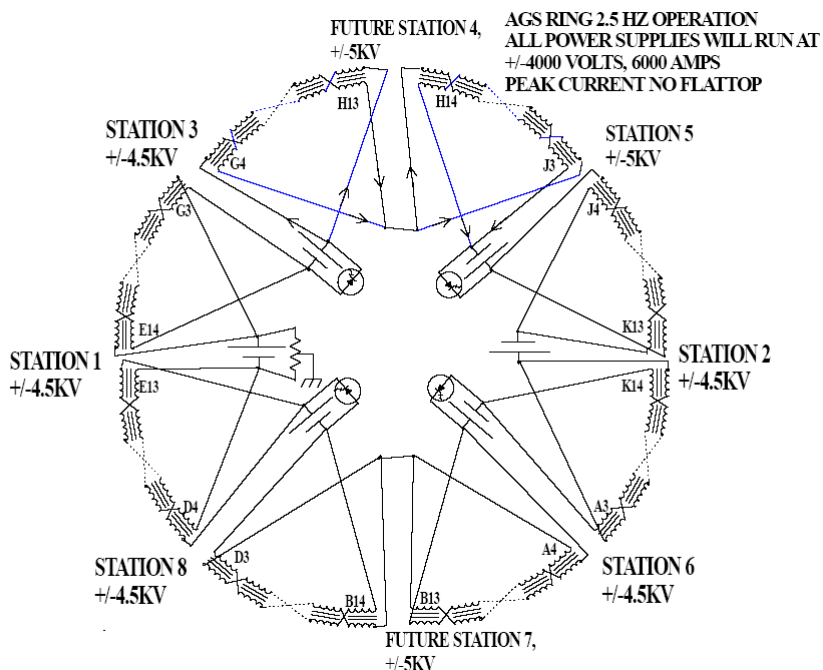
Figure 3.2: Schematic of power supply connections to the AGS magnets for 2.5 Hz operation.

losses in the magnets as well as the storage inductors. We need 5 SCR power supplies for 2.5 HZ operation, rated at about 8 kA, ± 4 kV. Each power supply drives a storage energy inductor. Each Inductor could be an air core toroid of 4.8 m outer diameter and 1.6 m coil diameter, with stored energy of 2 MJ, losses 600 kW and inductance of 0.063 H. The total average power into magnet power supplies as well as storage inductor power supplies would be around 5.7 MW. We need to optimize the inductor and it's topology and if possible reduce its losses and optimize the size and the weight of it. Figure 3.3 shows a block diagram of two SCR type of power supplies fed from the same input ac line, one powering a magnet and the other a storage inductor. Figure 3.4 shows the current, voltage and peak power of one out of the 5 SCR power supplies connected to storage inductors, while the magnet current is pulsing at 2.5 Hz as shown in Figure 3.1.

3.2.5   Control System

The controls of the existing power supplies will remain unchanged. (2 P bank regulators, 2 F bank regulators, 1 current regulator). There will be 4 voltage regulators for the additional 4 P type power supplies. All voltage references would be derived from the same MMPS computer program, except that they will be divided by 6. The current reference will be the same. The AGS MMPS computer program deriving these references, will be modified, to turn on, or off the bypass SCRs, based on maximum magnet voltage required. The bandwidth of the current loop must be 6 times faster than the present one, and a bandwidth of at least 10 to 20 Hz may be required. A bandwidth of 70 to 100 Hz should be sufficient for the voltage loops. Note that the present voltage loop bandwidth is 70 Hz. If the Inductor Storage Energy technique is
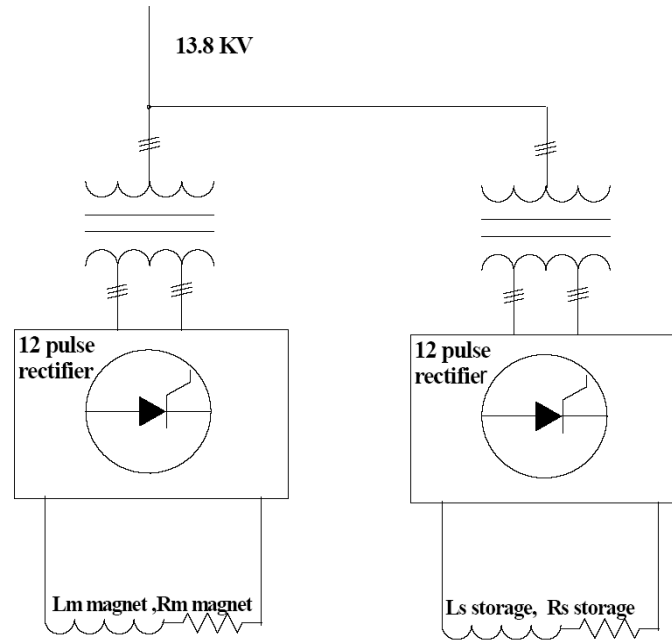
Figure 3.3: Inductor energy storage power supply configuration. Note there are 5 pairs of power supplies and 5 storage inductors for 2.5 Hz operation.

implemented, the 5 additional SCR power supplies would be current regulated with a current reference proportional to the inductor current as shown in Figure 3.4 The interlock system of every additional power supply will be very similar as the existing interlock system for the MMPS, which uses a programmable logic controller PLC system.

3.2.6 Real Estate

The new motor generator or the additional 5 power supplies driving inductors including the inductors, depending on which solution we will choose, are to be housed in new buildings west of the road going to bldg. 928 east of A10 house. An additional building is needed in the same area to house the new 4 P type power supplies and their controls. A new transformer yard is needed in the same area for the transformers of the 4 P type power supplies. We need to open 6 additional sleeves in the AGS ring and run trays with the power cables.

3.2.7 Commissioning

During summer shut downs, we can open 6 new penetrations in the AGS ring and disconnect the magnets in the same 6 locations. During the same period, we can install power cables from the magnets by the new feed-throughs and bring them outside the AGS ring to link boards where we can short them for normal operation. Construction of the new buildings can go on independently of operations. Construction of a new water cooling tower for the added
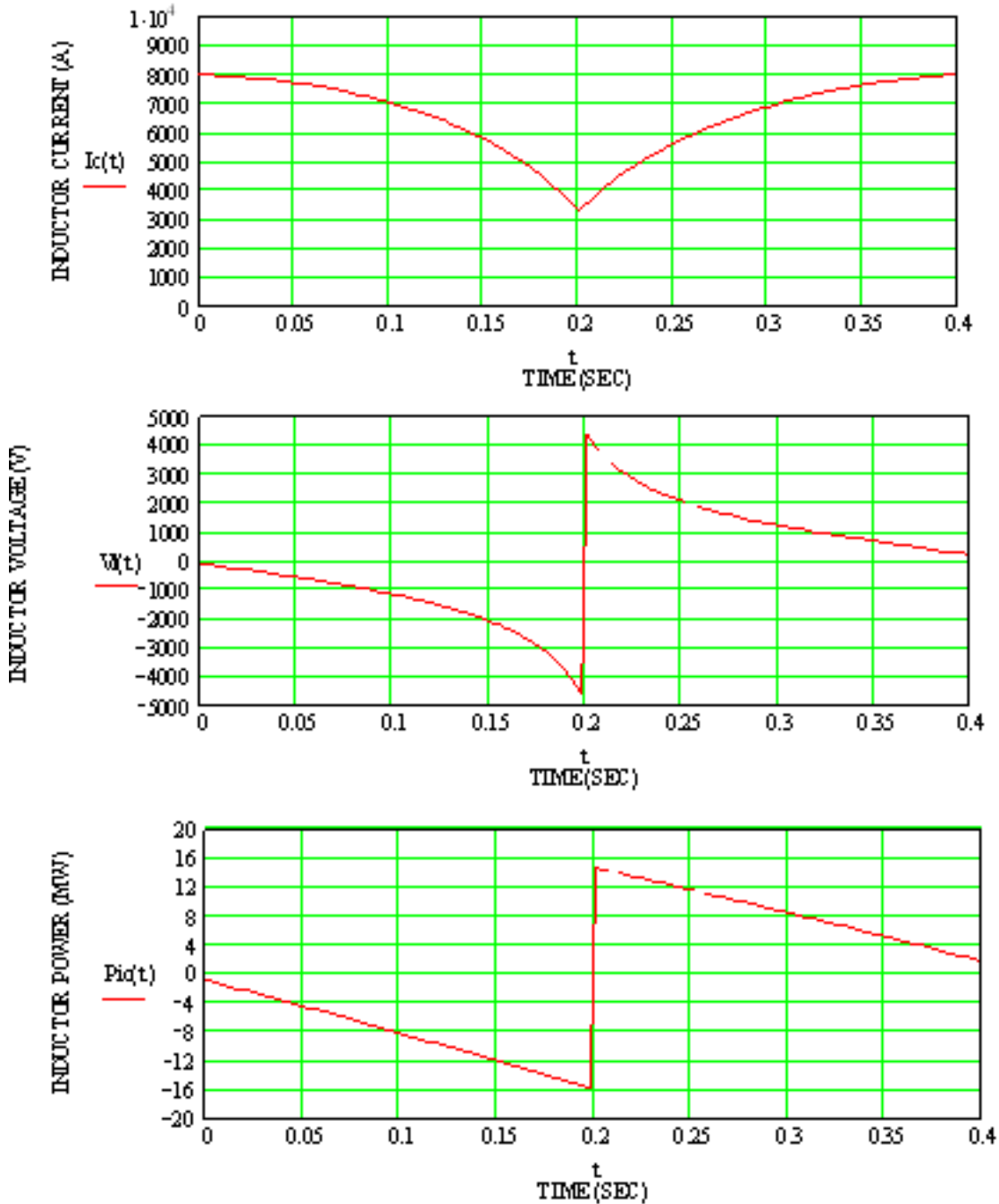
Figure 3.4: Storage inductor current, voltage and peak power for 2.5 Hz operation. Note there are 5 of these storage inductors for 2.5 Hz operation.

power supplies can go on independently of operations. Procurement and commissioning of the new power supplies/transformers/controls and new MG set could go on independently of operations. Final integration and commissioning would require the physics program to be off for 3 to 4 month.

3.3 AGS Radio Frequency System Upgrade

The rf system has to fulfill three major requirements: (1) provide 2.7 MW peak power to the beam, (2) supply 1 MV of accelerating voltage, (3) maintain capability of providing heavy ion beams as the RHIC injector. Of course the system must switch between 1-2 and 3 without equipment change.

More power amplifiers have to be installed. We can use the 10 existing power amplifiers and add only 10 more of the same design. They will be configured to drive two gaps each, as opposed to four gaps with the existing system. The DC power supplies need to deliver 25 A at 12 kV to make 300 kW. With 60% conversion efficiency this will give 180 kW of rf power, which is split between 80 kW for the ferrite dissipation (see below) and 100 kW for beam acceleration. The existing DC power supplies and the 300 kW tetrode power tube can fulfill these requirements if they drive just two gaps. The 10 new units can be copies of the existing design. The coupling to the cavity must be changed. The existing power amplifiers couple across the gap and therefore the full gap voltage appears at the tetrode plate. To reach 25 kV we will couple to one side of the gap and get a time two multiplication from the push-pull cavity configuration. In addition we will lower the capacitance at the gap (see below). This increases susceptibility to transient beam loading. On the other hand, the transient beam loading disturbance is much less with linac injection than with bunch-to-bucket from the Booster. The closed loop impedance of the cavities can be made sufficiently small be direct rf feedback. If we increase the feedback gain by 10 dB the effect to the reduced gap capacitance can be compensated. The extra feedback gain can be realized because of: 1. splitting the cavity into two two-gap units ameliorates the higher-order-mode problem that destabilizes the feedback, 2. new feedback driver amplifiers with higher current compliance will need to be built anyway to drive the tetrodes to higher power.

Peak voltage means increasing the gap voltage from 10 kV to 25 kV to make an average gradient of 33kV/m, since no extra insertion space is available on the AGS ring. The AGS Booster proton cavities are examples of this high gap voltage in an air-gaped ferrite cavity. They can operate at 22.5 kV and have been tested higher However, their average gradient is only 15 kV/m. The limit is given by the ferrite material. Above a certain threshold value of B_{rf} a ferrite becomes unstable and excessively lossy. The gap voltage at this $B_{rf,\max}$ is given by

$$V = -\frac{d}{dt}\int \omega B_{rf} dA = -\omega a l B_{rf,\max} \ln\left(\frac{b}{a}\right) \tag{3.1}$$

where: ω is the rf radian frequency and the variables a, b, and l are the inner and outer radii and length of the ferrite stack, respectively.

The only free parameter is ω. If we operate the rf system at the 24th harmonic of the revolution frequency ($\sim$9MHz) then the required voltage of 25 kV can be achieved with a safe value of $B_{rf,\max}$ of $\leq$ 20 mT. Two main consequences follow from the higher frequency. Firstly, the type of ferrite that is now used in the AGS will not do the job. The initial permeability is too high and given the minimum capacitance that would be found in a 25 kV gap structure the resonance frequency could not be as high a 9 MHz. Secondly, the heavy ion beams have an absolute requirement of a range of frequency sweep of 2.5:1. Gold ions come from the Booster at $\beta = 0.4$ and are accelerated to $\gamma = 10$. The Booster proton cavity ferrite (4M2) is suitable. The initial permeability is lower and we have measured this range of frequency change with 1300 Amp-truns of bias We have not observed instability in 4M2 even at this high bias value. Since the cavities need to be redesigned for the higher voltage gap, changing the ferrite is only small complication.

We still need a strategy to operate for RHIC with the different frequency range cavities. At injection from the Booster we have no problem because we already use harmonic 24 for bunch-to-bucket transfer and capture. However, after debunching and rebunching to make four bunches the existing harmonic cavity (KEK Finemet cavity) cannot give enough voltage to make the bunches short enough to fit into harmonic 24 buckets. An acceleration stage to an intermediate flattop would make this possible. The beam can then be captured in four buckets, with 20 buckets empty, and accelerated to top energy. The KEK cavity cannot operate at the higher frequency. A new rebunching cavity will be required and the intermediate flattop would complicate the acceleration cycle for heavy ions.

The next concern is the power dissipation in the ferrite and the mechanical stress that is created by the differential heating due to rf losses in the bulk material. We know from experience that below 300mW/cm^3 of dissipation the ferrites can be adequately cooled. The power density is also proportional to B_{rf}^2 and is given by

$$\frac{P}{V} = \frac{\omega B_{rf}^2}{2\mu_0(\mu Q)},\tag{3.2}$$

where: μQ is the quality factor of the ferrite.

The μQ product is a characteristic of the ferrite material and depends on the frequency and the B_{rf}. We have data on μQ for ferrite 4M2 (used the Booster and SNS ring) at 9 MHz and 20 mT. (Philips Components, Data Handbook MA03, 1997) The power dissipation is expected to be 775 mW/cm^3. This is the instantaneous power level but the rf cavities will be pulsed at 50 % duty cycle, implying 387 mW/cm^3. We can take advantage of the fact that as acceleration progresses the bucket area grows and it becomes possible to reduce the cavity voltage. If we let the synchronous phase angle go up to 45 degrees the voltage requirement is only 0.5 MV. Because this enters as the square (B_{rf}^2) the instantaneous dissipation drops to $\leq$ 100 mW/cm^3 and we can keep the time average value below the safe level. Although we have published data on 4M2 we have no practical experience with operating it at 9 MHz. In addition the rate of change of bias can affect ferrite behavior. We note these issues as important R&D subjects that must be examined thoroughly before a reliable design can be finalized.

3.4   Transition Crossing

The proton beam crosses the transition energy at $\gamma_T = 8.5$. During a non-adiabatic time $\pm T_c$, the beam may experience emittance growth and beam loss caused by chromatic non-linear mismatch, beam self-field mismatch, and beam instabilities [17]. Table 3.1 shows the main parameters pertaining to transition crossing in the AGS.

Table 3.1: Main parameters of the AGS for the super neutrino facility.

Parameter		Unit
Nominal transition energy, γ_T	8.5	
Acceleration rate, $\dot{\gamma}$	196.6	s^{-1}
Magnet ramp rate, $\dot{B}$	7.2	T/s
rf voltage, V_{rf}	1.0	MV
rf harmonic number, h	24	
rf synchronous phase, ϕ_s	0.52	radian
Number of proton per bunch	3.87×10^{12}	
Bunch area (95%)	$0.8 - 1.2$	eV·s
First-order non-linear compaction, α_1	2	
Transition energy with γ_T-jump, γ_T	9.5	
Transition jump amount, $\Delta\gamma_T$	± 0.5	
Transition jump time	< 1	ms
Momentum aperture (without transition jump)	2.4	%
Momentum aperture (With transition jump)	1.6	%
Typical fractional beam loss	0.2 - 3	%

In the absence of the transition jump, the characteristic non-adiabatic time

$$T_c = \pm \left(\frac{\pi E_s \beta_s^2 \gamma_T^3}{ZeV_{rf}|\cos\phi_s|\dot{\gamma}h\omega_s^2} \right)^{1/3} \qquad (3.3)$$

is about ± 0.87 ms, where E_s is the particle total energy, and ω_s is the angular revolution frequency. The non-linear time T_{nl}

$$T_{nl} = \pm \left| \alpha_1 + \frac{3\beta_s^2}{2} \right| \frac{\sqrt{6}\hat{\sigma}_{\Delta p/p}\gamma_T}{\dot{\gamma}} \qquad (3.4)$$

varies from about ± 1.6 to ± 1.9 ms, where the rms momentum spread reaches its design peak values $\hat{\sigma}_{\Delta p/p}$ of from 0.42% to 0.52% at transition for a proton bunch of 95% longitudinal phase-space area from 0.8 to 1.2 eV·s. The amount of beam longitudinal emittance growth due to the chromatic mismatch is proportional to the ratio T_{nl}/T_c. Upon transition crossing, the beam fills the entire momentum acceptance of about 2.4% (according to the measurement performed at AGS in 2004 [18]). The expected beam loss is up to 20% in the absence of the transition jump [19].

The longitudinal space-charge coupling impedance is given by

$$Z_{\|,sc}(n\omega_s)/n = -j\frac{g_0 Z_0}{2\beta_s\gamma^2},\tag{3.5}$$

where $Z_0 = (\epsilon_0 c)^{-1} = 377\ \Omega$, and $g_0 \approx 4$ is the geometric factor. Near transition, $\gamma \approx \gamma_T$, $Z_{\|,sc}/n \geq 10\ \Omega$ [20]. The effect of space-charge self force at transition is expected to be greatly compensated by the inductive coupling impedance of the machine that is independent of the beam energy.

It is necessary to use the transition jump method to effectively increase the rate of transition crossing [21, 22, 23]. The required amount of transition jump is $\Delta\gamma_T = \pm 0.5$ during a time of 1 ms or shorter. Such a jump effectively increases the crossing rate by more than a factor of 5 (Figure 3.5, [24]). The jump is realized by exciting a dispersion wave at harmonic 9 (near horizontal tune of 8.8) using 6 pulsed quadrupoles of alternating polarity, located at about 1.5 betatron period apart [23]. The peak current on the pulsed quadrupole is about 2.2 kA. During the γ_T-jump, the perturbation in the betatron tunes is small ($|\Delta\nu_{x,y}| < 0.03$). However, the maximum dispersion is increased by near a factor of 5 from 2.3 to 9.5 m (Fig. 3.7, [24]). The maximum β-function is increased by 20-30% (Fig. 3.6, [24]). Consequently, the momentum acceptance is reduced from 2.4% to 1.6%. Longitudinally, the lattice disruption caused by the γ_T-jump enhances the non-linear momentum compaction by more than a factor of 10. This enhancement effectively reduces the amount of transition jump at different momenta, as shown in Fig. 3.5. At the reduced momentum acceptance, the expected beam loss varies from about 0.2% for a 0.8 eV·s beam to about 3% for a 1.2 eV·s beam. Figure 3.9 shows the expected fractional beam loss upon transition crossing as a function of the initial (95%) longitudinal beam area. Near transition, the condition for machine hands-on maintenance of average loss of beam power of 1 W per meter corresponds to a fractional uncontrolled beam loss of 0.3% [25]. To meet this goal, the 95% bunch area needs to be below about 0.8 eV·s. Figure 3.8 shows the expected longitudinal phase space of the beam before, at, and after transition for an initial longitudinal (95%) bunch area of 0.8 eV·s in the presence of the transition jump using the computer codes TIBETAN [17].

3.5   Impedance and Collective Effects

For the AGS upgrade, mainly two types of impedance are of concern. The first type is the broadband impedance, which comes from the unshielded bellows, the chamber connections and steps, and the vacuum valves and pumping ports. The second type is the low frequency impedance, which has resonant modes in a few tens to several hundred MHz. The low frequency impedance mainly comes from the injection and extraction kickers. The ring longitudinal impedance, including also the resistive wall impedance, is depicted in Figure 3.10. At the low frequency, the wall impedance is dominant. From 10 MHz to 100 MHz, the contribution of the injection kicker can be noticed. The longitudinal impedance of the injection kicker comes from the flux leakage through the 1 mm copper sheet inserted in the window frame magnet. Above 100 MHz, the broadband impedance is dominant. Usually the impedance calculated from the machine devices is smaller than the measured one. A factor of 2 difference between the design, or calculated one from the machine devices, and the measured impedances
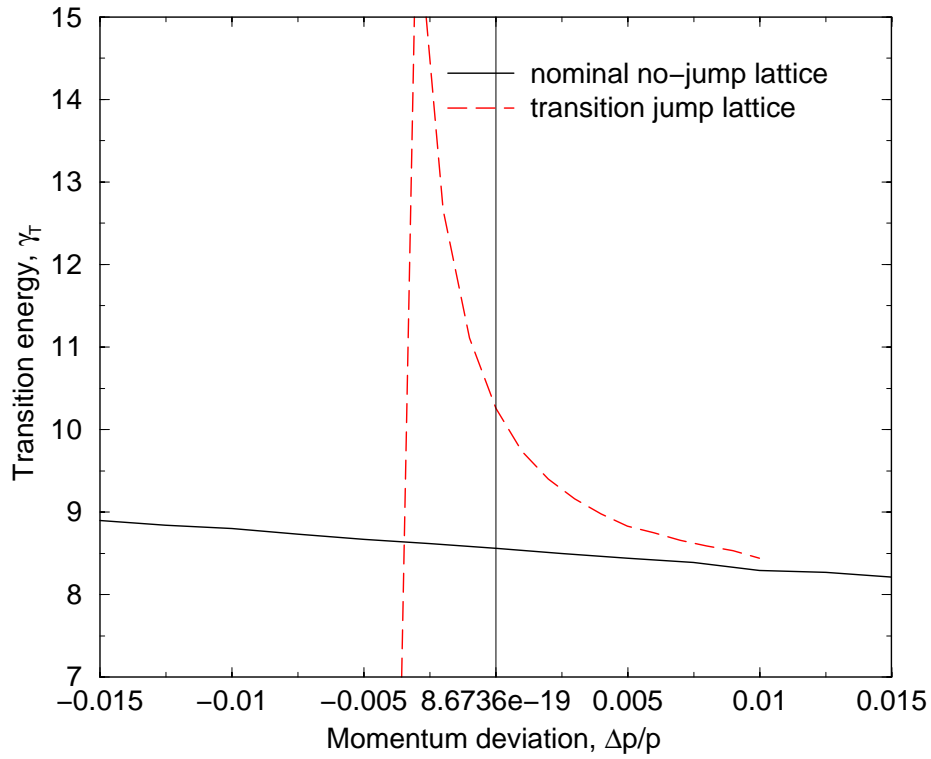
Figure 3.5: Dependence of transition energy on the momentum deviation in the AGS under nominal and γ_T-jump scenarios obtained with the computer code MAD.
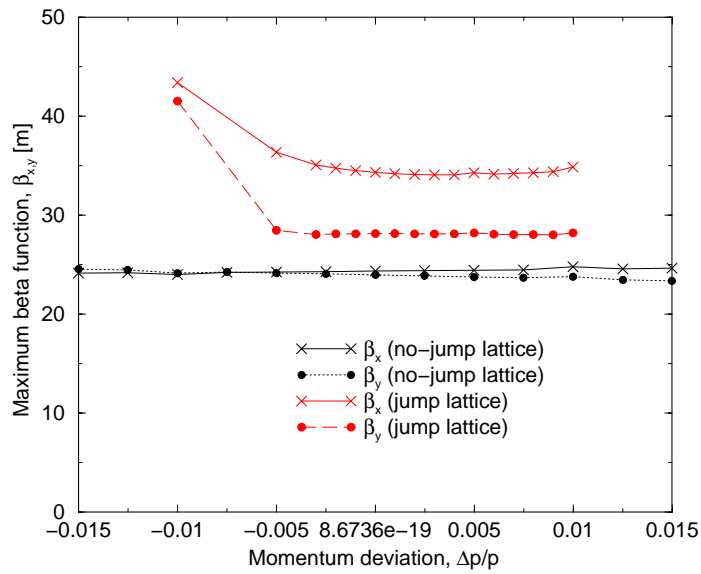
Figure 3.6: Dependence of β-function on the momentum deviation in the AGS under nominal and γ_T-jump scenarios obtained with the computer code MAD.
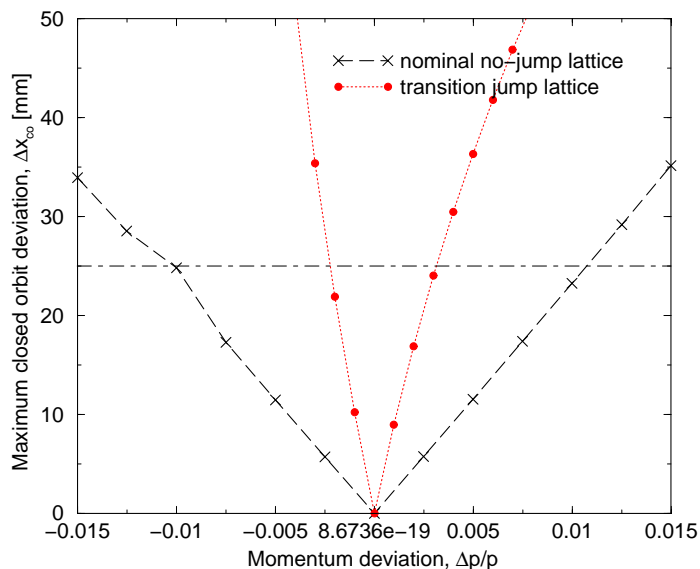
Figure 3.7: Dependence of the closed orbit on the momentum deviation in the AGS under nominal and γ_T-jump scenarios obtained with the computer code MAD.

has been observed at the RHIC, KEKB, and other machines. The transverse impedance is depicted in Figure 3.11. The upper panel shows the horizontal and the lower one the vertical impedances. The vertical impedance is larger mainly because of the smaller vertical size in the dipole chamber. Also, the injection kicker contributes mainly for horizontal impedance. The circulating beam is outside of the extraction kicker's C magnets unless immediately ready for extraction, therefore, the extraction kicker impedance is not included here. The concern of large impedance of the extraction kicker will be treated separately upon possible redesign of the kicker units. The beam instability consideration is focused on two aspects. These are, as usual for the AGS, at high energy, the longitudinal instability around transition, and the transverse instability above transition. The beam momentum spread at transition has to be less than 0.0075 because of the limited momentum aperture during the transition energy jump. With the transition jump, the slippage factor can be controlled to be greater than 0.0015. With a bunch rms length of 4 ns and the peak current of 60 A at transition, the longitudinal impedance needs to be less than 12 Ω to avoid longitudinal microwave instabilities. The measured AGS longitudinal impedance is about 30 Ω, which is not inconsistent with the one shown in Figure 3.10. All bellows in the AGS ring, total about 450, are unshielded. The chamber steps, including the connection from dipole to quadrupole, and the BPM housing, are not tapered. With limited effort of shielding and tapering, the AGS impedance can be reduced to about 12 Ω. In fact, if only the longitudinal microwave instabilities were of concern, a larger broadband impedance could be tolerated since the longitudinal space charge impedance of about 10 Ω at transition, which is capacitive, has the effect of cancelling the inductive broadband impedance. However, the transverse instability at the high energy is more serious, even with a broadband impedance of 12 Ω. In summary, since the intensity of
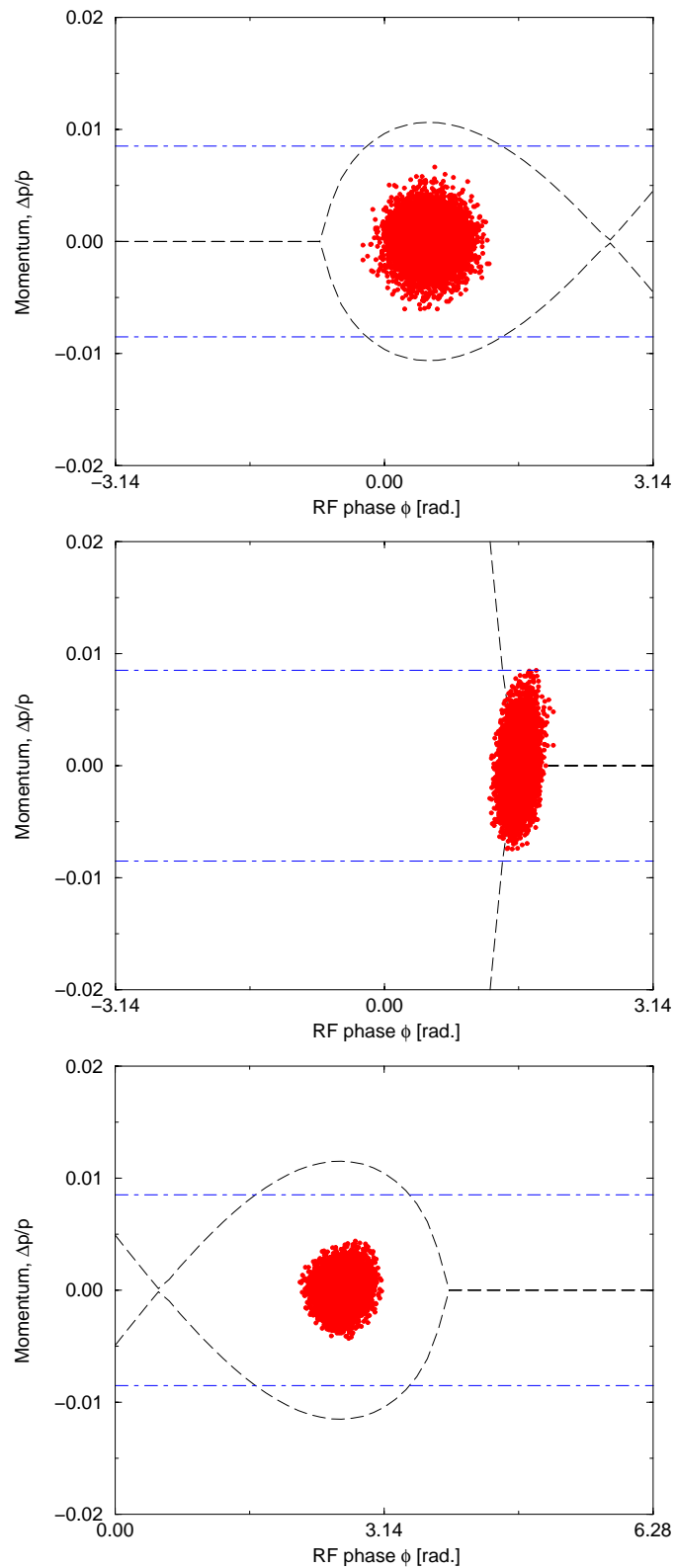
Figure 3.8: Longitudinal phase space of the proton beam before, at, and after crossing the transition energy in the AGS obtained with the computer code TIBETAN.
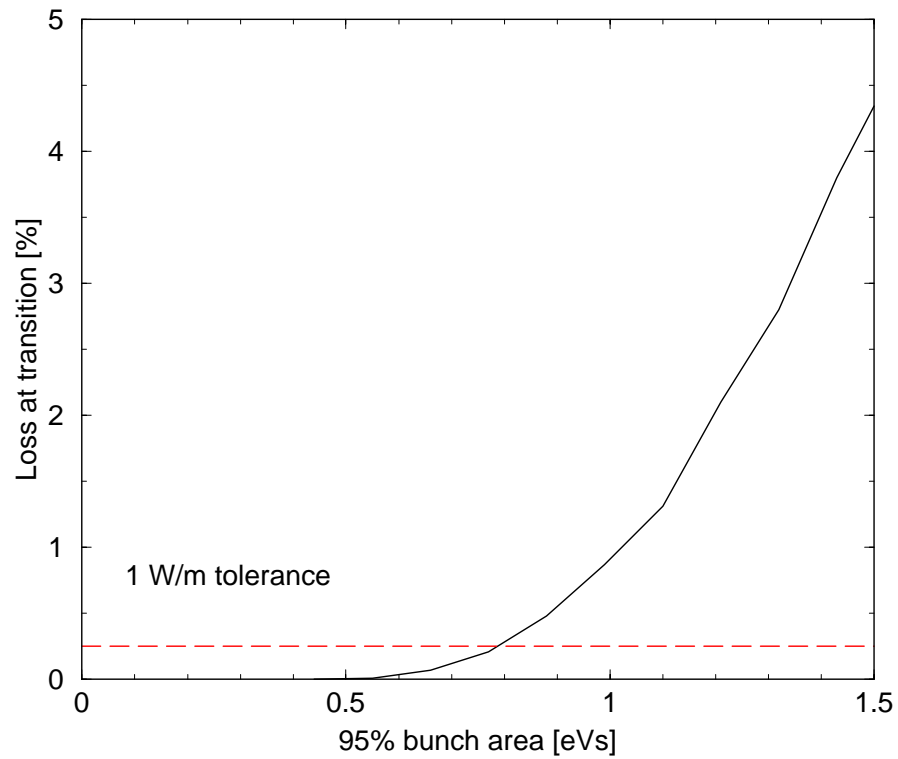
Figure 3.9: Expected fractional beam loss upon transition crossing as a function of the initial (95%) longitudinal beam area obtained with the computer code TIBETAN.

Longitudinal Impedance
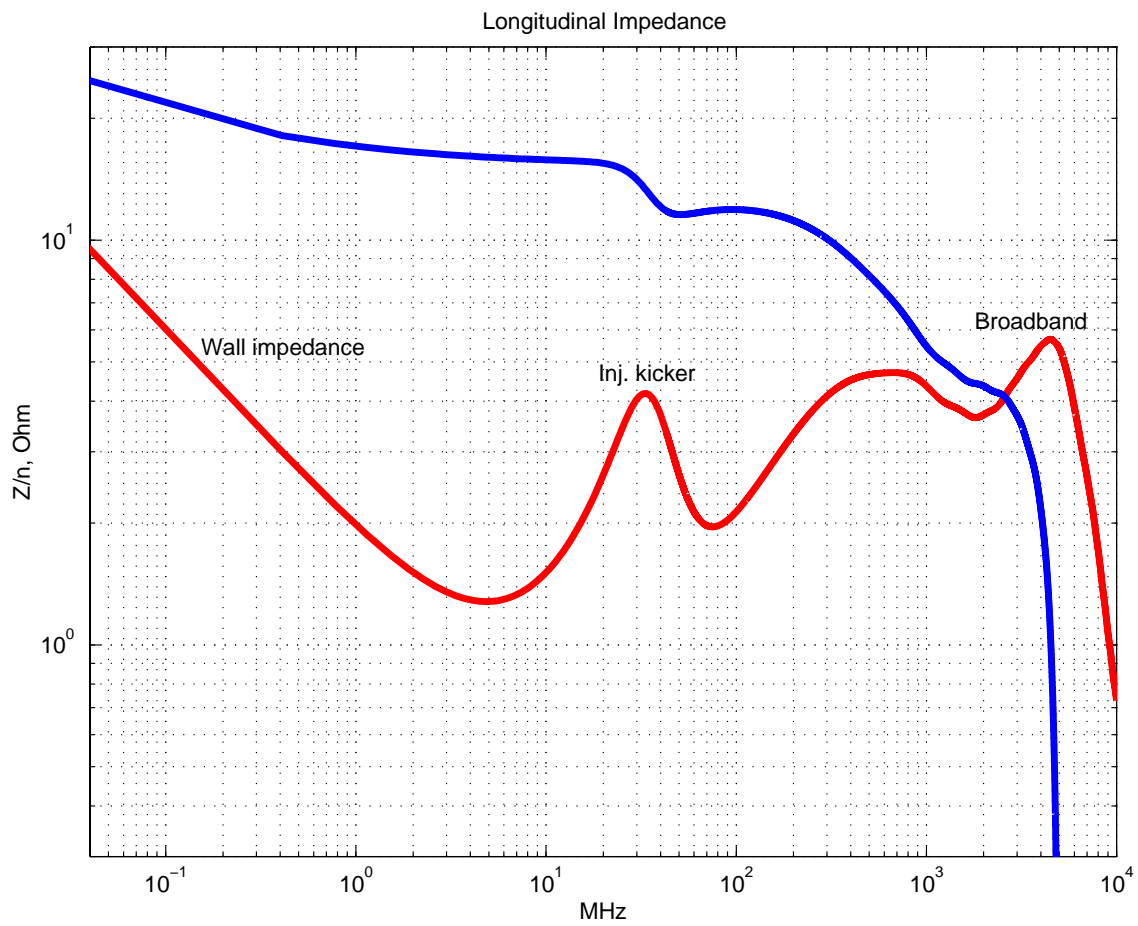
Figure 3.10: AGS longitudinal impedance. Blue line is for imaginary part, and red line is for real part of the impedance.
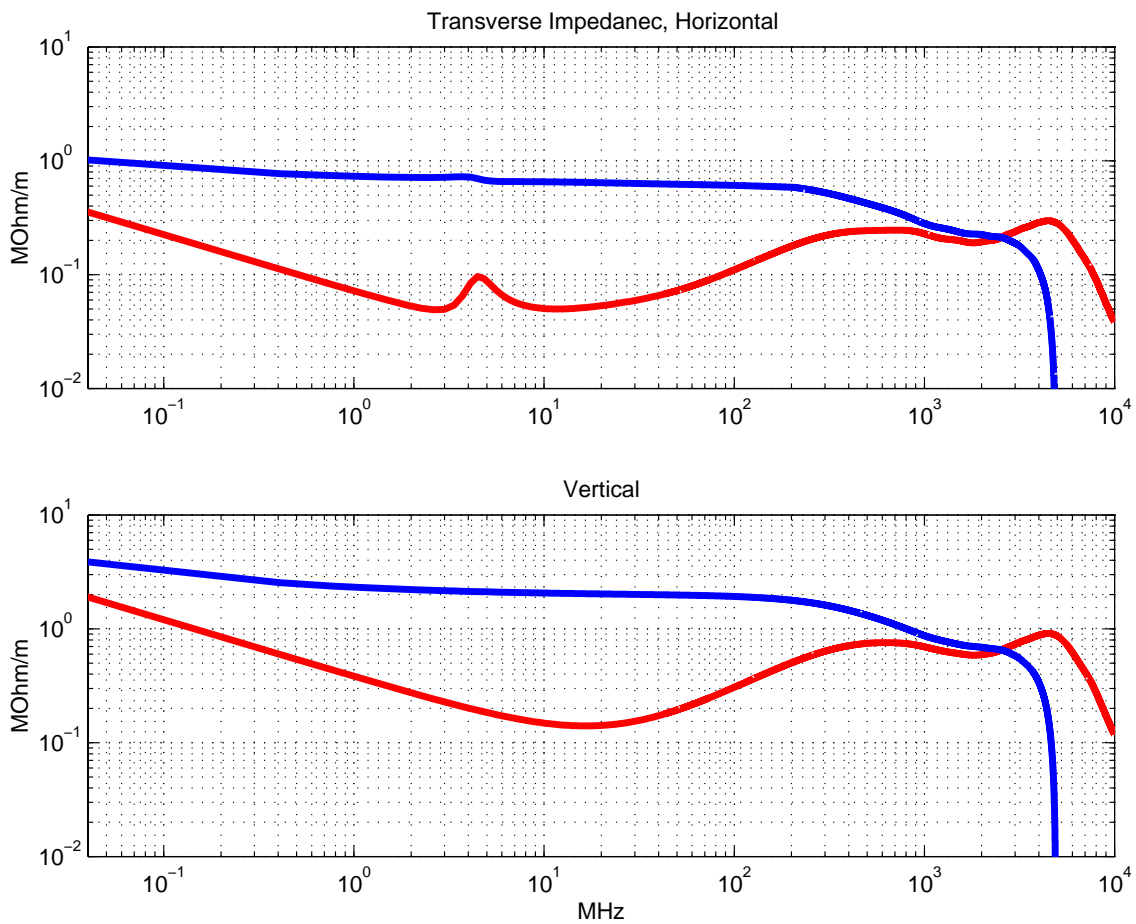
Figure 3.11: AGS transverse impedance. Blue line is for imaginary part, and red line is for real part of the impedance.

8.9×10^{13} is only marginally higher than the present 7.3×10^{13}, the beam instability during acceleration and transition crossing can be avoided.

3.6   Control System

3.6.1   Introduction

The discussion in this chapter addresses controls for all parts of the accelerator complex to be added or modified for the Super Neutrino Beam Facility. The fundamental premise of this conceptual design and cost estimate is that the RHIC controls architecture is a sound basis for scalable extensions to the new systems. The basic elements of the system comprise a networked family of front-end interfaces, mostly implemented in VME with CPUs running a real-time OS, connected via Ethernet to the AGS Main Control Room (MCR) console workstations and to central servers. Depending on the time-scale for this project, optimal technologies may change but experience shows that scope and costs estimated using this model should project favorably over the long term. Engineering activity will comprise hardware redesign/selection incorporating new technologies or dealing with parts obsolescence and the development of project-specific application software.

3.6.2   Distributed Services

Network

Inter-building network infrastructure consists of optical fiber with switched Ethernet to individual front-end nodes. 100Mbit Ethernet will suffice for many systems, but a Gigabit trunk will be desirable between the SCL and the AGS control center.

Timing and Links

Standard Linac and/or AGS Event Links and Real-Time Data Link will be delivered via fiber to all major equipment locations. Local distribution to individual equipment interfaces will be made via copper. Some engineering will be required for redesign of obsolescent modules.

Fast Beam Inhibit

A fast beam inhibit system will be required throughout the Linac and Transport areas of the project. It will be patterned after the present AGS and RHIC systems as upgraded to support RSVP. New software will be required to manage the more complex scope of system.

3.6.3   Front End Systems

Common elements

Standard interface infrastructure will comprise VME [or VME64] chassis, utility link interface, battery-backed SRAM, timing modules, remote power reset module, and terminal server

(cross-connect). Some engineering will be required for redesign of obsolescent units. Software support for an updated microprocessor will also be needed.

Power Supply systems

A dc reference and readback or function generator control with integrated digital waveform capture up to 10kHz will be provided as appropriate. State control and monitoring is provided via the same modules. A separate ADC is required for faster waveform clock-speed. Some engineering will be needed for redesign or new module selection, and database support.

Beam Diagnostic Systems

Most of the beam diagnostic interfaces will be patterned after existing AGS or RHIC systems, with some adaptation from PCI-based SNS systems to BNL-standard VME. Some engineering will be needed for new module selection, along with database, driver and interface software development.

Radio Frequency systems

The low-level rf system controls interface is at the VME backplane. This environment provides standard timing and a platform for custom DSP control modules that are included in the rf system scope, along with software effort for their support. Control of the high-power rf system equipment is implemented using networked PLCs that are likewise included in the rf system scope. Some Controls software effort will be provided for database support and console level application software.

Cryogenic system

Following the model of the RHIC cryogenic system, we have assumed that a commercial, PLC-based control system will be provided as part of the Cryo system scope. Some engineering will be required in the Controls area for database support and for software to provide access to cryogenics data for logging and correlation with accelerator performance.

Vacuum systems

Networked PLC interfaces have been included in the vacuum system scope. Server resources must be provided that apply standard time stamps to the data and export it using standard protocols. Engineering is required for database support and for software for data collection and alarms.

Facility systems

Existing systems will be extended for UPS, power and building temperature monitoring. Software engineering effort will be required for database and alarms.

3.6.4 Central Services

MCR Resources

The cost estimate includes funds to modernize console resources – workstations and comfort-display monitors for 2 consoles. Engineering is needed for database and several new console applications related to AGS injection, loss and beam-inhibit monitoring, and transport line set-up and tuning.

Server Resources

There will be a need for additional or modernized operations file server resources for Superbeam operations, machine archives and logs. Additional server resources will be provided for export of machine data to experiment clients. A GPS-based, standard time server will be provided for time standardization with the experiment systems.

Maintenance/Development Resources

Remote consoles – workstations and displays – will be needed to provide maintenance access in the new equipment locations. It will also be necessary to modernize some software development resources - developer workstations and software licenses.

4 AGS Injection and Extraction

For 1 MW AGS beam power, proton beam of $\sim$9x10^{13} protons at an energy of 28 GeV at a repetition rate of 2.5 Hz is required. 1.2 GeV H$^-$ ion from a superconducting linac (see Section 2.2) is chosen as the injection energy, and 28 GeV is chosen as the extraction energy.

4.1 H$^-$ Injection into the AGS

The plan view of the proposed injection area from the superconducting 1.2 GeV linac and the existing booster is shown in Figure 2.2 The injection point is in middle of the AGS C01 straight section and the linac beam enters through B19, B20 magnets and C01 magnets (see 4.1).

4.1.1 Issues for the 1.2 GeV H$^-$ Injection into the AGS

Beam loss in the injection process is one of the most important issue for a high power proton accelerator. We list below the relevant numbers we need to deal with in the proposed machine:

AGS beam power	1	MW
Injected beam power	43	kW
H$^-$ ions missing the foil power @2%	0.86	kW
H^o from stripping foil @2$\sim$10% *	0.86$\sim$4.3	kW
Stripped electron power	46	W

*This rate depends on the thickness of the stripping foil, and careful balance of the loss due to multiple scattering of the circulating beam and this loss is needed.

There are additional beam losses due to 1) nuclear scattering, 2) multiple Coulomb scattering and 3) energy loss and struggling as some part of the circulating protons traverse through the foil. An optimum thickness and size of the injection foil is needed to balance these losses against the aforementioned H$^-$ and H^o losses.

Although there is a potential issue about the excited H^o state stripping in the magnetic field downstream, the injection field of 0.63 kG is low enough to be ignored. The magnetic field of the injection line is limited to 2.5 kG to minimize the stripping of H$^-$.

In order to minimize the space charge related beam losses and instabilities, careful control of both transverse and longitudinal phase space is required; they will be described later in this chapter.

For an existing accelerator like AGS, retrofitting a controlled beam dump is difficult, and lost beam has to be dumped close to the machine vacuum chamber and magnets. The carbon is chosen as the material to dump the beam for its high thermal resiliency and short half life of the isotopes it produces. The range of the 1.2 GeV proton in the carbon is $\sim$430 g/cm^2 or $\sim$2 m of length. The carbon shall be encapsulated with thin metal and be water cooled to absorb the lost energy.

Heating of the vacuum chamber due to the stripped electrons has to be dealt with because the emittance of the electron beam is same as that of the beam in the linac.

4.1.2   Beam Parameters at the H$^-$ Injection Point

Many injection trajectories has been studied, and concluded that the best injection point is the center of the 2 feet straight section between C01 and C02 magnet longitudinally and 6 cm outside in the radial direction. The beam trajectory is shown in Figure 4.1. The injection is achieved without a septum magnet in the straight section B20. A straight section is chosen instead of a middle of the C01 magnet because of need of a foil changer. Since we have to use much thicker foil for the stripping efficiency and to accommodate somewhat brighter linac beam, the foil life will be considerably shorter than the ones presently at the AGS and the booster.

The H$^-$ missing the foil will hit the vacuum chamber about 58 inches downstream of the leading edge of the C02 magnet iron with 32 m-rad angle while the H^o from the foil hit at vacuum chamber flush with the upstream end of the C03 magnet iron with an angle of 35 m-rad. The H$^-$ loss point is particularly important because the full linac beam may go there in the case of the foil breakage, thus the system should be able to take few pulses of full linac beam.

We may modify the vacuum chamber to have steps to let these protons pass through the vacuum chamber with minimum energy loss and absorbed in the strategically placed carbon block.

The stripped electron goes through the fringe field of the C02 magnet and collected in the side of vacuum chamber. Here we place a water cooled copper block to absorb the heat.

Careful study has been performed for a possible orbit bump which could be produced around that point. The radial location and the direction (x,x') is traced back to the B19 straight section where the match into the linac beam is done.

The matching point x and x' are 46.2 cm outside and 81.5 m-rad. respect to the B19 straight section; the lattice parameters at both points are shown in Figure 4.1.

4.2   Multiturn Injection Simulations

4.2.1   Transverse Painting

For a high intensity proton accelerator, proper phase space distribution is a pre-requisite. A flexible method to paint the transverse phase space has been developed using programmable fast bump magnets.

The horizontal painting is achieved by 5 ferrite core bump magnets. Two magnets are located around quarter betatron wave length up and down stream of the injection point namely up and down stream of the B14 and C8 magnets. Since the 2 feet straight sections between main magnets are not long enough to install adequate ferrite magnet, two such straights are used to achieve necessary amplitude. The fifth ferrite magnet is used to correct any residual oscillation caused by this local bump. Those fast bump magnet shall be flexible to program either exponential or parabolic function of time with a time constant of 100 μs.
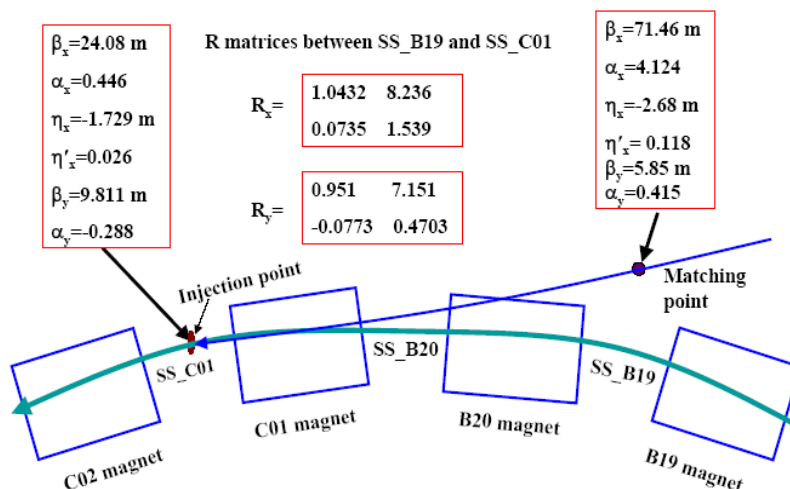
Figure 4.1: Beam parameters at the matching and injection sections.

Vertical painting will be accomplished by 3 fast bump magnets in the injection beam line. The horizontal painting is done by controlling the amplitude of the phase space displacements while vertical painting is accomplished by controlling the angle variable.

For high intensity proton accelerators, such as the upgraded AGS, there are very stringent limitations on uncontrolled beam losses. In this section, we present the estimate of emittance growth and uncontrolled beam losses as function of linac emittance by computer simulations.

All of the physical quantities used in the simulations (Table 4.1) are chosen according to realistic design specifications . Correlated Painting is chosen for injection into AGS, considering the available aperture at injection and beam halo/tail control. A significant effort has been made to optimize the injection painting. The optimized injection bump collapses as an exponential function of time with a time-constant of 0.1 ms. The initial foil-hit by each incident H^- is counted as three times to include the effects of two stripped electrons. The average foil thickness is assumed to be 300 μg/cm^2. In order to separate the effects of linac emittance from the other issues, the effects of space charge and magnet errors are not included in this study [26].

A direct effect of the linac beam emittance is the halo/tail generation in the circulating beam. Figure 4.2 shows the estimated halo/tail generation in the beam as a function of normalized rms emittance of the linac beam. Here, the Halo/tail generation is defined as the ratio of number of particles with emittance larger than the designed acceptance of 49 π mm-mrad to the total number of particles in the circulating beam.

From the results shown in Figure 4.2, it is clear that the correlated painting with the optimized injection bump, collapsing as an exponential function of time with a time-constant of 0.1 ms, gives the best final proton beam distribution in the upgraded AGS. The preferred linac emittance is about 1.5 π mm-mrad for acceptable injection losses.

Table 4.1: Simulation parameters.

Horizontal beta at the injection	28.0 m
Vertical beta at the injection	8.0 m
Horizontal emittance of injected beam	2π mm-mrad
Vertical emittance of injected beam	2π mm-mrad
Horizontal beam size at injection, σ_x	5.2293 mm
Vertical beam size at injection, σ_y	2.7952 mm
Horizontal Foil size (2.5 σ_x)	13.0731 mm
Vertical foil size (2.5 σ_y)	6.9878 mm
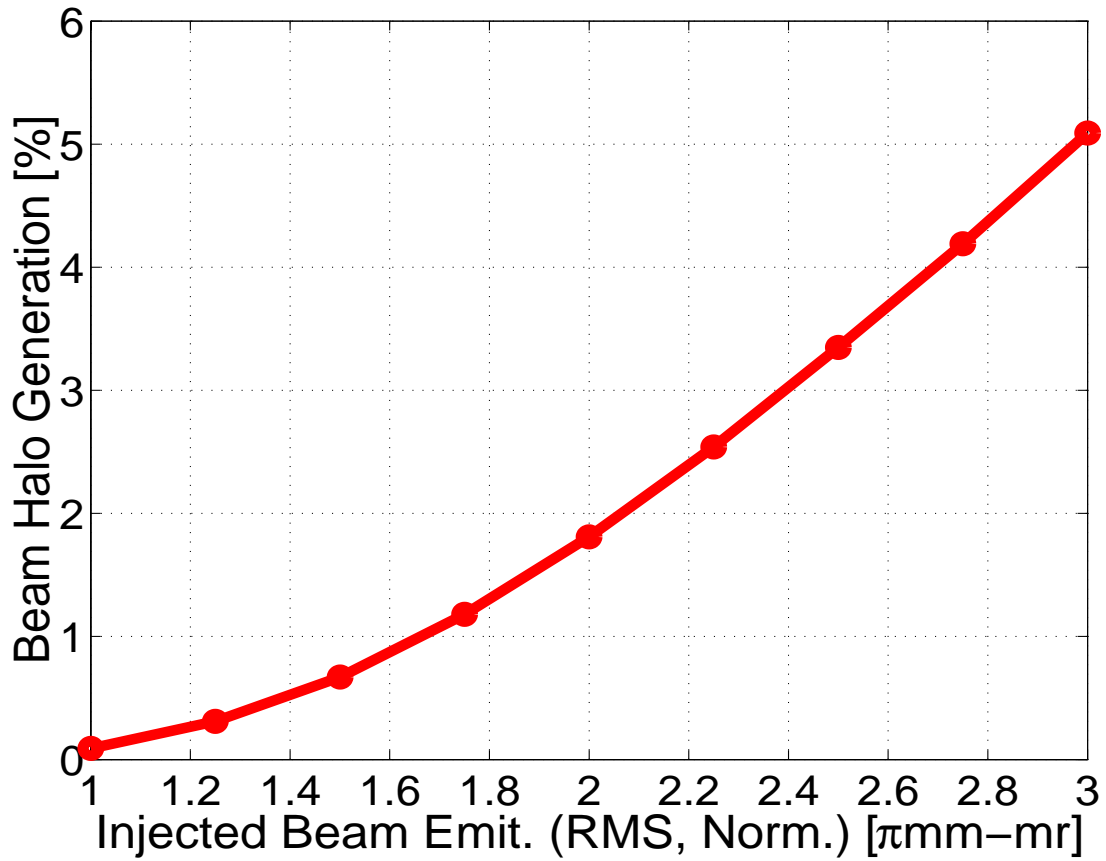
Figure 4.2: The estimated halo/tail generation in the circulating beam as functions of normalized rms emittance of injected beam.

Two methods have been considered to improve the H^- injection from the linac. One is to bring closer the RFQ immediately adjacent to the output of the ion source to reduce the emittance growth. In our estimate, this fact alone can reduce the linac output emittance from $2\ \pi$ mm-mrad to about $1\ \pi$ mm-mrad. Well-designed low level feedback system has to be provided to prevent further emittance growth in the high-energy section of the linac.

Another possible improvement is to introduce a second harmonics cavity for the AGS during injection time. It can effectively reduce the space charge tune shift by 30%. This will either reduce the resonance losses for the same intensity, or will allow for 30% more intensity to be accepted by the AGS.

4.2.2   Longitudinal Painting

The multiturn injection into the AGS is modeled after the SNS scheme. However, the repetition rate, and consequently the average beam power, is much lower in this case. The larger circumference of the AGS also reduces the number of foil traversals. Beam loss at injection into the AGS is estimated to be about 3% of controlled losses and 0.3% of uncontrolled losses. This is based on a comparison with the actual experience in the AGS Booster and the LANL PSR and the predicted losses at the SNS using the quantity $N_P/(\beta^2\gamma^3 A)$, which is proportional to the Laslett tune shift, as a scaling factor. This is summarized in Table 4.2. As can be seen, the predicted 3% beam loss is consistent with both the AGS Booster and the PSR experience and the SNS prediction.

Table 4.2: Comparison of H^- injection parameters

H^- Injection Parameters	AGS Booster	SNS	PSR	1 MW AGS
Beam Power, Linac Exit, kW	3	1000	80	43.2
Kinetic Energy, MeV	200	1000	800	1200
No. of Protons, N_P, 10^{12}	15	100	31	89
Vertical Acceptance, A, $\pi\mu m$	89	480	140	55
$\beta^2\gamma^3$	0.57	6.75	4.50	9.56
$N_P/(\beta^2\gamma^3 A)$, $10^{12}/\pi\mu m$	0.296	0.031	0.049	0.169
Total beam loss, %	5	0.1	0.3	3
Total Lost Beam Power, W	150	1000	240	1282
Circumference, m	202	248	90	807
Lost Beam Power per meter, W/m	0.8	4.0	2.7	1.6

Based on the linac exit parameters, the AGS multiturn injection parameters used in the simulations are summarized in Table 4.3. A relatively low rf voltage of 450 kV at injection is necessary to limit the bean momentum spread to be about 0.5%, and the longitudinal emittance to be 1.2 eVs per bunch. Such a small emittance is important to limit beam losses during transition crossing in the AGS.

A simulation of the 240 turns injection process is shown in Figure 4.3 . Larger chopping rate implies a longer bunch in the ring, and hence smaller space charge tune shift. Also, with

Table 4.3: AGS injection parameters used in the simulation.

Injection Turns	240
Repetition Rate, Hz	2.5
Pulse Length, ms	0.72
Chopping Rate, %	65
Linac Average/peak Current, mA	20/30
Linac Beam Momentum Spread	± 0.001
Linac Norm. 95% Emittance, $\pi\mu m$	12
AGS Injection RF Voltage, kV	450
Bunch Length in Ring, ns	85
Longitudinal Bunch Emittance , eVs	1.2
Beam Momentum Spread in Ring	± 0.005
Ring Norm. 95% Emittance, $\pi\mu m$	100

larger chopping rate, lower linac beam intensity is required. On the other hand, without the second harmonic rf, some dilution of the injected particles in the phase space is inevitable. It is noted that with the second harmonic rf, the SNS chopping rate is chosen to be 0.68. The choice of the chopping rate of 0.65 for the AGS injection is perhaps too large. The simulation indicates that the bunch shape is similar to the one at the PSR, with a noticeable sharper peak, however, a linac beam momentum ramping during the injection could improve this.

4.3 Extraction from AGS at 28.0 GeV

The present extraction scheme of G10 to H10 extraction is adequate for our purpose, and will be kept as it is. However, the fast kicker pulse forming network(PFN) should be upgraded to accommodate both RHIC transfer extraction and full one turn extraction of this high power beam.
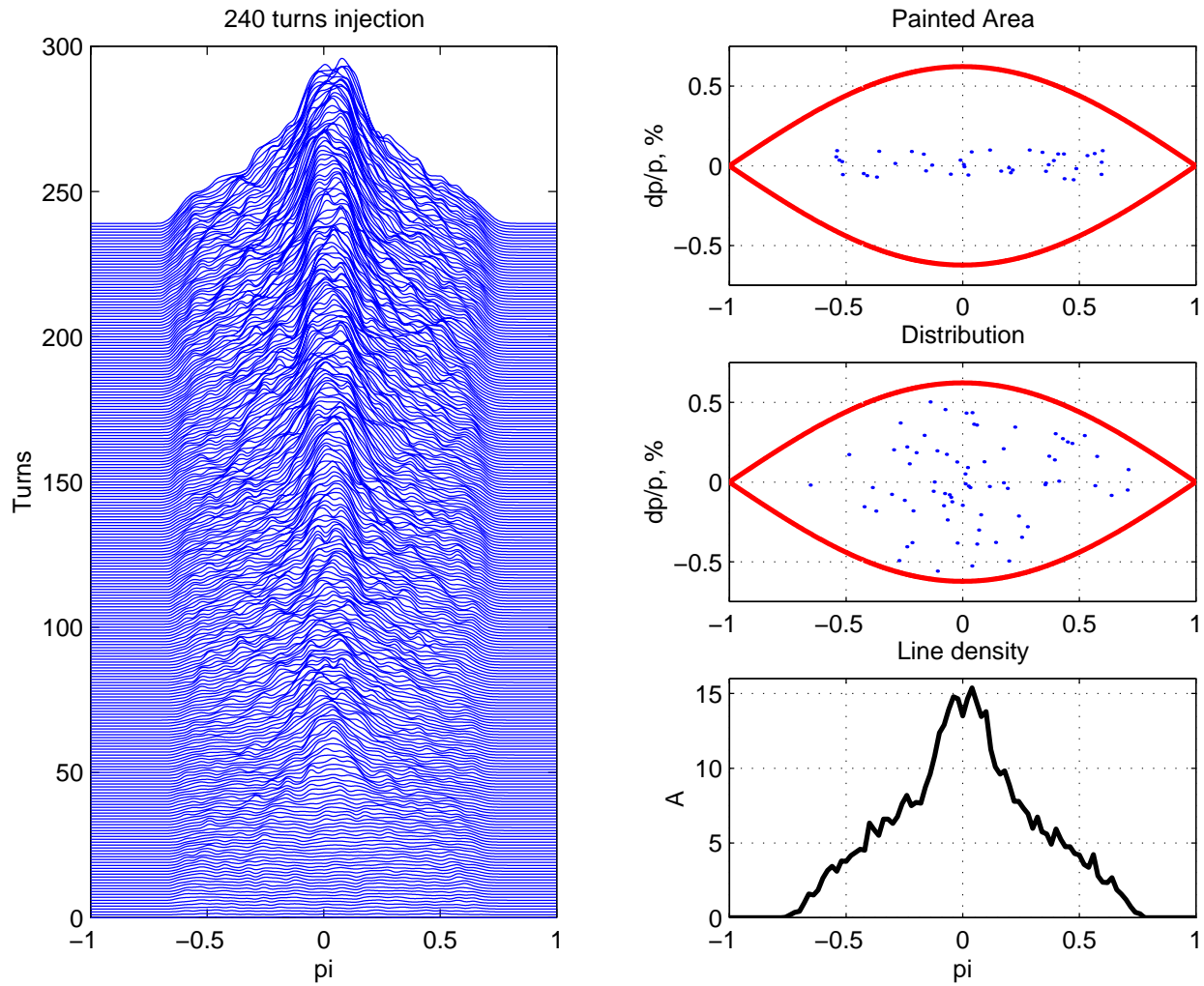
Figure 4.3: AGS injection simulation. The abscissa is phase.

5   Beam Transport to Target

5.1   Optics of the Beam Transport

The proton transport has been developed beginning at extraction from the AGS. The beam is assumed to have a 100 πmm-mr normalized emittance (95%) with beam correlations given by previous measurements. Beam transport optics from AGS fast extraction to the entrance to the U-line were taken from Tsoupas et al. [27]. The beam is transported $\sim$190 m from the AGS to the U-line spur using present RHIC transfer line magnets. The new superbeam transport begins at this point. The present plan is to direct the beam toward the Homestake mine in South Dakota. In order to do this the beam must be bent 68 degrees, 4 seconds to the west of the U-line direction and 11.26 degrees downward. BNL is located on an aquifer that is the sole-source for Suffolk county drinking water. With this in mind, a beam layout has been developed that takes the beam up and over a 42 m (beam height) hill to the production target and decay channel. This keeps the target, decay channel and beam dump at or above the present ground level and well above the Long Island water table. Figure 5.1 shows a plan view of the proposed layout while Figure 5.2 shows an elevation view of the beam on the hill. A cross section of the hill is shown in Figure 5.3.

The layout of the beam line is constrained by the RHIC tunnel and utilities on the north side, the NASA Radiobiology facility on the south side and the BNL site boundary on the west side. A beam layout was developed within these constraints and incorporates separate vertical and horizontal bends. The 17-degree vertical bend up begins near the end of the present U-line tunnel about 80 m from the beginning of the new transport. The 80 m drift before beginning the vertical bend up is necessary to avoid conflicts with the RHIC transfer line utilities and entrance labyrinths. A 17-degree angle was chosen based on what was estimated to be the maximum incline that technicians could comfortable work. This bend is followed by a 46 m drift to allow the beam to reach a height sufficient to allow, after a 68-degree horizontal bend and a vertical downward bend, a 200 m decay tunnel (target to dump) down the hill to a dump, keeping the front face of the dump at ground level. Although it might appear better to combine the vertical bend, drift and horizontal bend into one grand bend, this approach would push the beam dump (and potential near detector location) close to or beyond the BNL site boundary. Thus, the approach adopted calls for bending up before beginning the horizontal bend.

The optics design was constrained by the following considerations:

- The transport should be $\geq$99% free of beam loss

- To conserve power and reduce costs, use modest dipole fields ($\leq$15Kg)

- The horizontal bend plane is on the 17 degree vertical slope of the hill (avoids coupling)

- The vertical bend down toward Homestake is in the y-z plane defined by the beam at the completion of the horizontal bend (avoids coupling)

- Design should accommodate up to 28.5 GeV/c momentum.
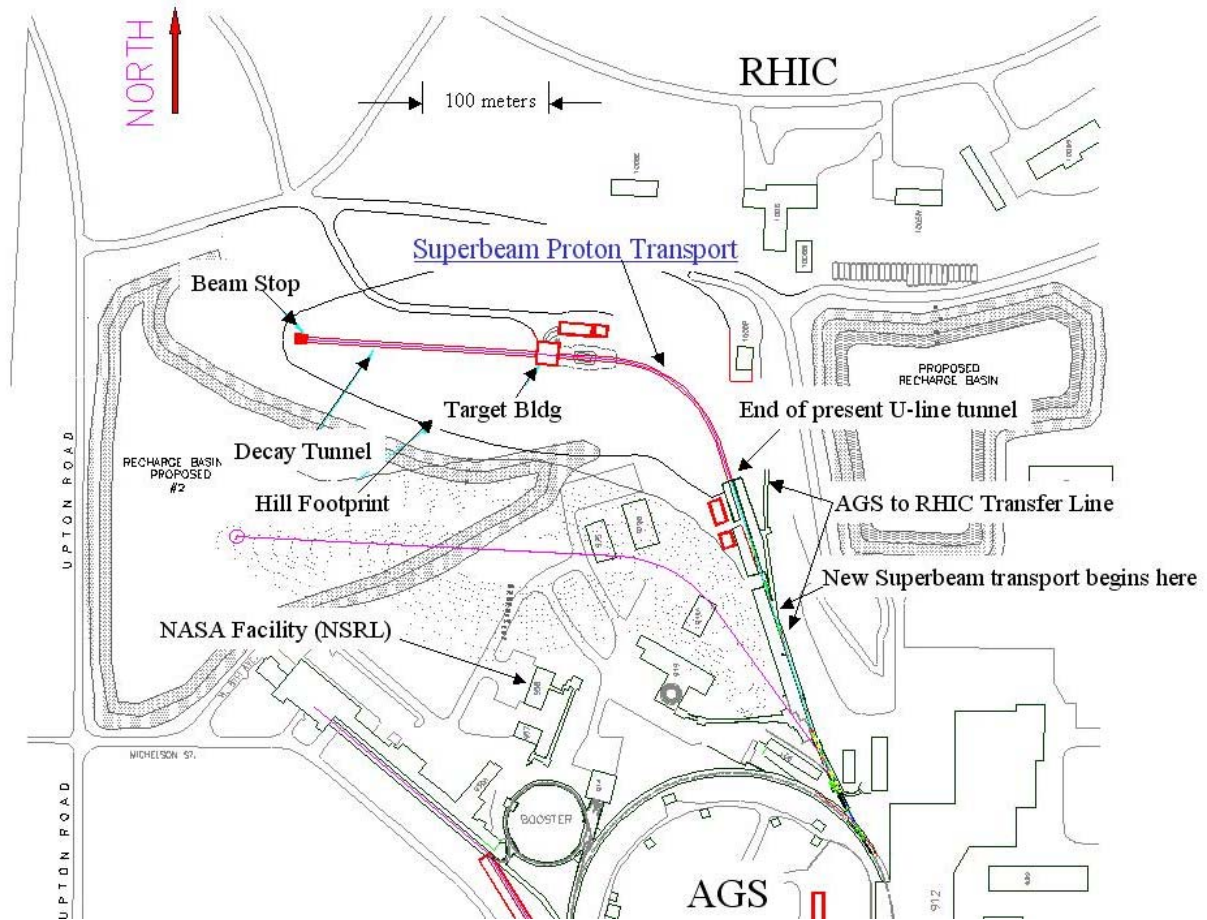
Figure 5.1: A plan view of the super neutrino beam facility at the AGS. The 1 MW proton beam will be taken from the existing extraction line (U-line) and continued on the upslope of the hill. The vertical and horizontal bending magnet are separate in this plan. The beam will be bent downwards at the top of the hill and directed toward Homestake.
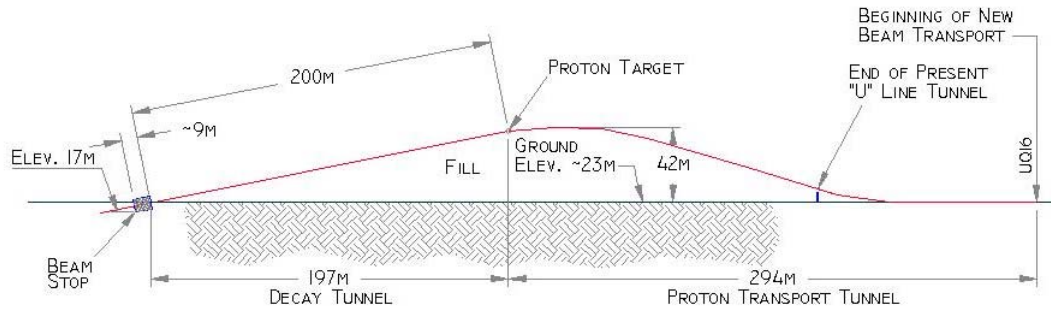
Figure 5.2: Elevation view of the neutrino beam line to Homestake, South Dakota. Distance is measured along the beam path.
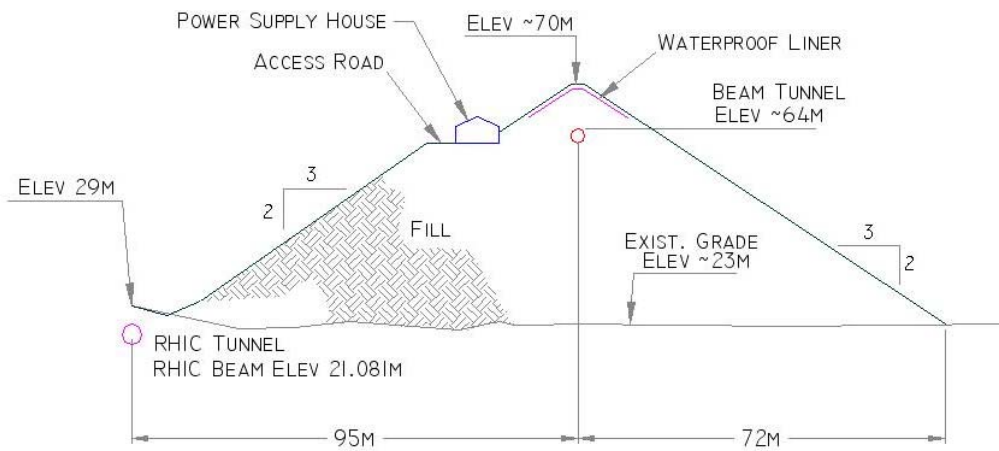
Figure 5.3: Hill cross section at target area.

- rms beam radius of ~ 2 mm at the pion production target.

In order to come out of the horizontal and final vertical bend with the beam heading toward Homestake the actual bend angles had to be adjusted to account for the fact that the bends are accomplished on the hill. The "ground level" horizontal and vertical angles, relative to the U-line beam direction, that point the beam toward Homestake are 68 and 11.3 degrees respectively. The required horizontal bend is 72.1 degrees followed by a 17.2 vertical bend down in the y-z plane defined by the beam as it exits the horizontal bend. Figure 5.4 shows x and y projections to the floor of the beam. Nineteen new quadrupoles, 34 new dipoles and 17 power supplies are needed for the beam transport described here. A breakdown of these elements is given in Table 5.1. In addition, several trim magnets will be used together with beam diagnostics devices to insure beam parameters and beam losses are kept within specifications.

The 6-sigma beam profile for the transport from the AGS to the superbeam dump is shown in Figure 5.5. It should be noted that a 10-sigma beam (167 π mm-mr normalized emittance) is transported without losses with this design. Both horizontal and vertical dispersion in the beam transport are easily controlled as can be seen in the figure. In fact, except for transport in the bends, the beam remains approximately achromatic (horizontal and vertical) all the way to the beam dump.

Figure 5.6 shows the 100 π mm-mr (6 sigma) Transport beam envelope in the target region with 6 sigma multiple scattering included in the 80 cm carbon-carbon target. The physical limits of a 1.2 cm diameter target are shown on the figure as well as the 2.5 cm exit aperture of the first horn. Note that >95% of the beam is contained within the target and beam loss on the first horn downstream end due to multiple scattering in the target is at the few % level. Final focus beam characteristics are controlled by a quadrupole doublet located between the end of horizontal and beginning of the vertical bend down and a quadrupole triplet located at the mid-point of the vertical bend.
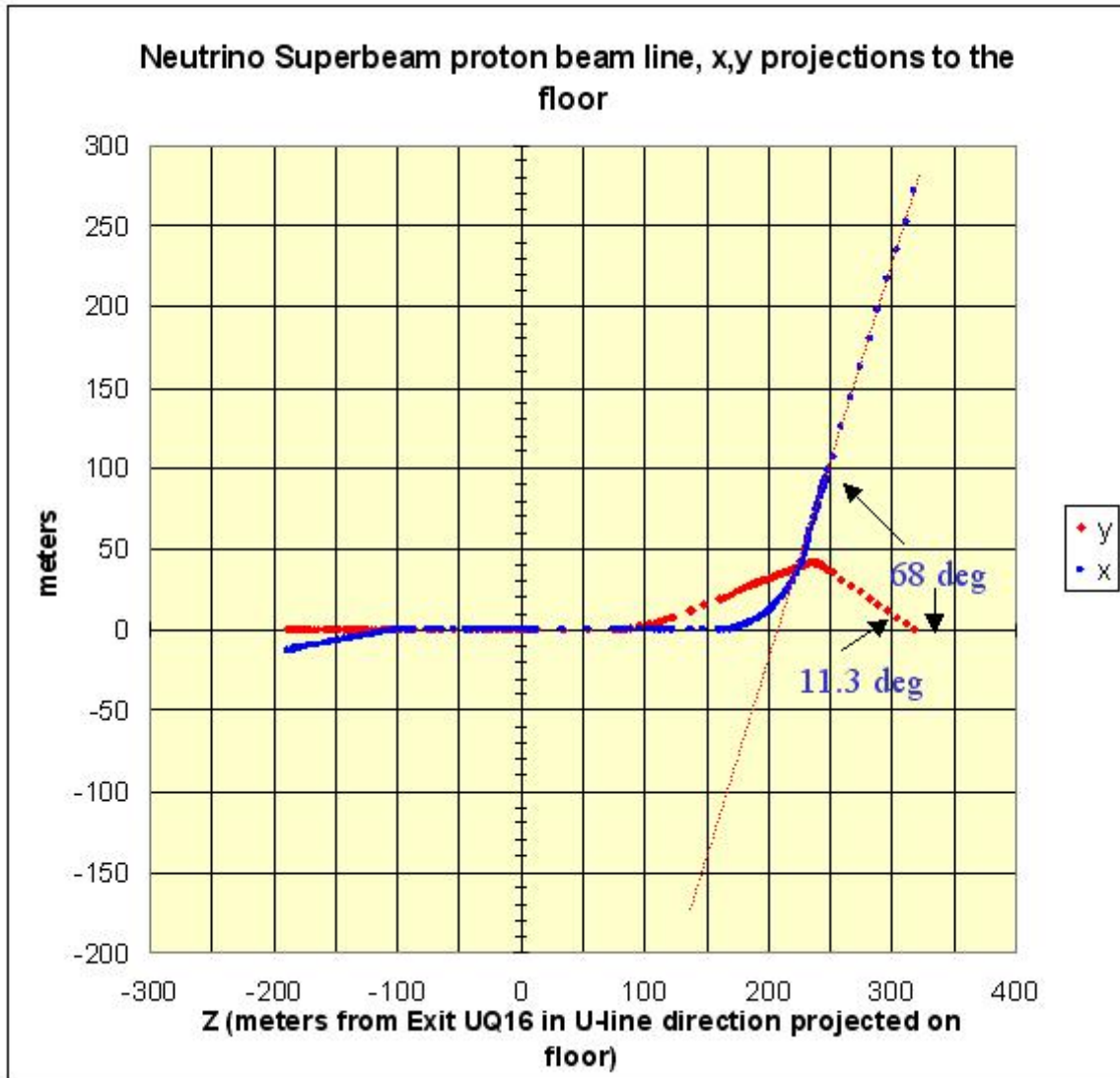
Figure 5.4: Superbeam proton transport x, y projections to the floor.

Table 5.1: New quadrupoles, dipoles and power supplies required in the AGS to target proton transport line.

New elements for the neutrino beam line (begin downstream of UQ16)						
		Gap/Dia. (cm)	Length (cm)	Number	Quads/dipoles in series	PS
Quads	4Q16	10.1	40.6	6	UQ25&30; UQ26&29; UQ27&28	3
	4Q24	10.1	61	7	UQ17-19;	5
	5Q36	12.7	91.4	1		1
	3Q36	7.6	91.4	4	UQ33&35	3
	3Q48	7.6	121.9	1		1
Dipoles	3D144	7.6	365.8	34	UP1-6; UD7-28; UP7-12	4
Trim Magnets				16		16
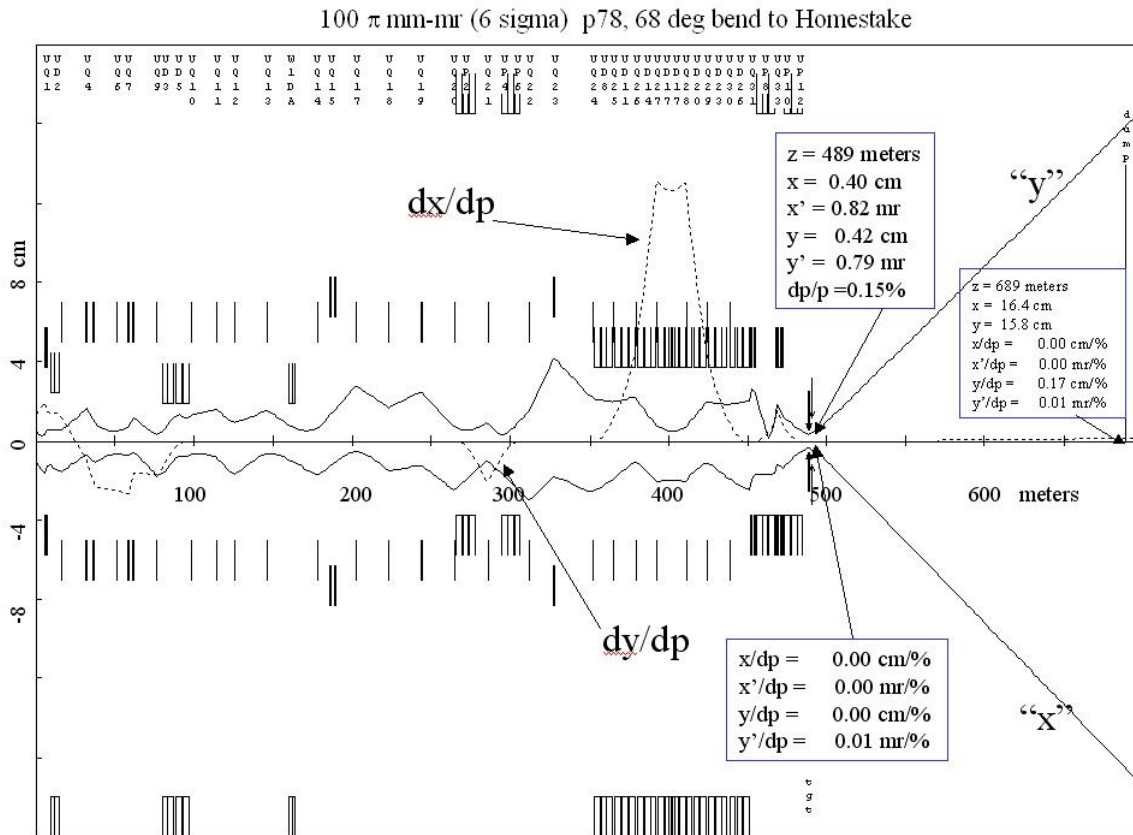
Figure 5.5: Beam transport from the AGS to the superbeam target and dump.
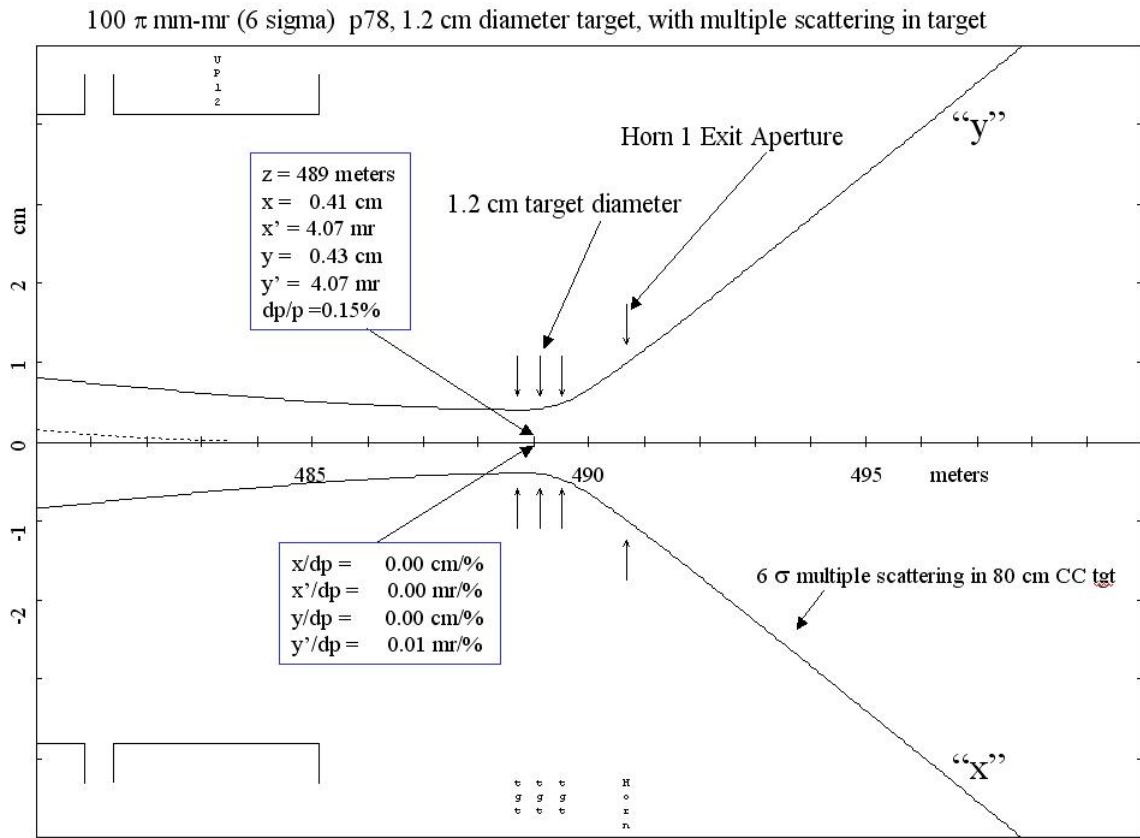
Figure 5.6: Beam transport from the AGS to the superbeam target area with multiple scattering in 80 cm CC target.

5.2 Magnets System

Scope

This section describes the dipole and quadrupole required for the superconducting Linac with its transport lines and for the transport of high energy protons from the U-line to the neutrino target.

Quantities and Performance Requirements

Table 5.2 provides a listing of the specifications for the dipole magnets required. Table 5.3 gives the specifications for the quadrupole magnets.

All of the magnets will designed to achieve the required field accuracy using 1006 quality steel plate that is heat treated prior to final machining. Using computer controlled numeric machine tools the steel cores will be machined to high accuracy and repeatability. The magnet pole tips will be machined to a tolerance of $\pm$ 0.02 mm. The dipole aperture and quadrupole pole positioning will be located to within $\pm$ 0.05 mm. Laminated cores will be used if it is cost effective for high quantity procurements. The magnets will be built so they can be "split" for easy installation of the coils and vacuum chambers. Bolted construction with accurate alignment pins will be used.

5.3 Power Supply System

There is a total of 17 current regulated, dc power supplies interfaced with quad or dipole magnets and 16 current regulated correction power supplies interfaced with vertical or horizontal correction magnets. The magnet designs are based on magnets which have been built at Brookhaven in the past. The beam transport line length is approximately 650 feet, but the longest distance from a power supply to a magnet and back is about 450 feet. These power supplies will be housed in two buildings located one at the beginning and one at the middle of the transport line. The following table indicates the type and number of magnets interfaced with each power supply. Field magnet data as well as magnet voltage, current and cable, plus magnet resistance is indicated. The following power supplies are water cooled, thyristor controlled dc power supplies. There are 2 power supplies rated at 160 volts, 32000 amps and 2 rated at 280 volts, 3200 amps, 10 rated at 30 volts, 550 amps, 2 rated at 50 volts, 550 amps, and 1 rated at 25 volts, 250 amps. All these power supplies are based on existing designs used as part of the recent commissioned Booster NSRL beam line. In addition we need 16-correction power supplies rated at $\pm$50 volts, $\pm$20 amps. These power supplies are air cooled, bipolar programmable current regulated supplies. The design is based on the Spallation Neutron Source (SNS) correctors. The interface of all the power supplies to our controls will be a PSI/PSC system identical to the Booster NSRL and SNS control system.

Table 5.2: Specifications for dipoles

DESIGNATION (in inches)	3D10	2.4D116	3D144	4D24
Location	200 MeV Linac to SCL	SCL to AGS Inj.	U-line to Target	U-line to Target
Quantity	1	2	34	16
# Power Supplies	1	1	4	16
Gap (m)	0.075	0.060	0.076	0.102
Pole Width (m)	0.300	0.150	0.153	0.250
Iron Length (m)	0.25	2.94	3.66	0.61
Magnetic Length (m)	0.30	3.00	3.73	0.71
Design Field (T)	0.98	0.21	1.55	0.20
Number of Coils	2	2	2	2
Turns per Coil	56	22	30	400
I required (A)	520	228	2730 - 3135	20
I max (A)	550	250	3200	20
Magnet resistance (Ω)	0.036	0.076	0.011	1.43
Power (kW)	4.88	1.98	51.3	0.60
Coil weight (lb)	161	155	2250	220
Steel weight (lb)	400	3000	21750	800
Construction	Plate	Plate	Plate or Laminations	Plate or Laminations

Table 5.3: Specifications for quadrupoles

DESIGNATION (in inches)	3Q8.6	4Q8	3Q36	3Q48	4Q16	4Q24	5Q36
Location	200 MeV Linac to SC Linac Line	200 MeV Linac to SC Linac Line	U-line to Target	U-line to Target	U-line to Target	U-line to Target	U-line to Target
Quantity	4	44	4	1	6	7	1
Power Supplies Req'd	4	44	3	1	3	5	1
Aperture (dia, m)	0.075	0.102	0.075	0.075	0.102	0.102	0.127
Iron Length (m)	0.22	0.20	0.91	1.22	0.41	0.61	0.61
Turns per Pole	76	40	32	40	26	38	44
Gradient (T/m)	3.0	20.0	30.6	36.1	13.6	20.6	6.1
Pole Tip Field (T)	0.11	1.00	1.15	1.35	.68	1.03	0.39
I Required (A)	22	497	536	505	519	538	222
I max (A)	25	550	550	550	550	550	250
Magnet Resistance(Ω)	0.099	0.020	0.019	0.022	0.020	0.037	0.044
Power (kW)	0.048	5.00	5.37	7.96	5.37	10.8	2.19
Coil Weight (lb)	43	91	474	675	90	167	200
Steel Weight (lb)	200	600	2000	2500	600	1000	1400
Construction	Plate	Plate or Laminated	Plate	Plate	Plate	Plate	Plate

Table 5.4: Beam transport power supplies.

LOCATION	# OF PS	MAGNET TYPE	# OF MAG-NETS IN SERIES PER PS	MAXIMUM FIELD PER MAGNET (T)	MAGNET CURRENT (A)	MAGNET PLUS CABLE RESISTANCE (Ω)	PS VOLTS	PS AMPS
AGS to Target	1	3D144	6	1.55	2730-3135	0.007*6+0.001 =0.043	160	3200
AGS to Target	1	3D144	6	1.55	2730-3135	0.007*6+0.001 =0.043	160	3200
AGS to Target	1	3D144	11	1.55	2730-3135	0.007*11+0.001 =0.078	280	3200
AGS to Target	1	3D144	11	1.55	2730-3135	0.007*11+0.001 =0.078	280	3200
AGS to Target	16	4D24	1	0.2	20	1.43+0.3 = 1.73	50	20
AGS to Target	3	4Q16	2	13.6	519	0.02*2+0.005 = 0.045	30	550
AGS to Target	1	5Q36	1	6.1	222	0.044+0.01 = 0.054	25	250
AGS to Target	2	3Q36	1	30.6	536	0.019+0.005 = 0.024	30	550
AGS to Target	1	3Q36	2	30.6	536	0.019*2+0.005 =0.043	30	550
AGS to Target	1	3Q48	1	36.1	505	0.022+0.005 = 0.027	30	550
AGS to Target	2	4Q24	2	20.6	538	0.037*2+0.005 =0.079	50	550
AGS to Target	3	4Q24	1	20.6	538	0.037+0.005 =0.042	30	550

5.4   Diagnostics System

A suite of beam diagnostics has been selected to monitor position (BPM), current (BCM), loss (BLM), profiles, and targeting parameters with quantities shown in Table 5.5. These will provide two functions: assure beam is accurately on target and directed towards the far target, and aid in the effort to keep any losses to an absolute minimum level. Since the C-AD has been providing facilities for fixed target programs for many years, similar types of all the devices described here already exist. Due to the unprecedented beam density, coupled with beam loss limitations, there will be increased requirements on precision, calibration and robustness.

The instrumentation designed for low intensity gold beams in the existing upstream 200m U-line will be upgraded to accommodate the high intensity beams.

Table 5.5: Transport and target instrumentation.

Device	Transport	Target	Totals
BPM	22	2	24
BCM	2		2
BLM			
Ion Chamber	40		40
Long cable	4		4
Profile			
Multiwire	10	2	12
Phosphor Screen		1	1
Target Station			
Telescope		1	1
Scintillator		1	1
Segmented IC's		1	1

Beam Position Monitors

These non-intercepting devices will provide data on every shot during normal operations. There will be 22 BPM's located primarily at the quadrupoles; they will be similar in design to the strip-line type presently used in the AGS to RHIC transport. The two just upstream of the target will have higher resolution to enhance the position measurement to improve targeting. The processing electronics will be custom built and have the capability of measuring single batch positions with sub-mm accuracy.

Beam Current Monitors

There will be two similar current monitors in the transport, one upstream and one down-stream, which will enable transport efficiency measurements with a few percent accuracy.

The beamline assemblies will be similar to the existing AGS to RHIC BCM's, and the toroids are commercially available from Bergoz. The signal processing electronics will provide single batch measurements and a calibration technique.

Beam Loss Monitors

In order to provide machine protection, allow "hands-on" maintenance, as well as a tool for tuning, the beam loss monitor system (BLM) will be critical for minimizing losses and optimizing efficiency. This system will be primarily based on argon-filled ion chambers with custom-built electronics packaged in VME modules. We will use the calibrated chamber designed at BNL for SNS with its improved response time and extended dynamic range. There will be 40 ion chambers distributed over the 300 m of transport from the existing U-line to target. They will be located primarily near the quadrupoles, and dipoles. Also, 4 additional 100' long gas filled heliax loss monitors will be installed to measure integrated losses in bends and transport sub-sections. The beam current monitors will be accurate to a few percent, but the loss monitors will be several orders more sensitive and will provide a primary means of troubleshooting.

Beam Profile Monitors

The profile monitors will be multi-wire type with 32 wires in each plane. They will operate on the principle of secondary emission from the 1mm spaced wires, which are spring tensioned and suspended on a frame. The device head is plunged into the vacuum chamber and beam path while data is taken. This semi-destructive measurement will provide two-dimensional profiles for each single batch, and will be located in the transport to allow emittance measurements. All of the multi-wires can be inserted for the same pulse to get a snapshot of the transport parameters. Since the existing U-line transport is instrumented for low intensity gold beams to RHIC, these 10 profile monitors will be installed throughout the 488m of transport between AGS and the target. The two multiwires just upstream of the target station will have closer wire spacing to increase the resolution to provide more accurate targeting. The design of the multiwire head at the target station and the choice of wire will require some study due to avoid breakage in this high intensity, small cross section beam. The multiwires' signals will be processed by Eurocrate integrator based electronics with remote gain control and will be of the standard design used throughout the C-AD facility. A multi-position phosphor screen will be installed just upstream of the target; the image will be viewed by a rad-hard video camera and processed in a frame grabber. High-resolution profiles can be acquired, as well as detailed halo measurements utilizing a screen with a hole in the center to increase low-end dynamic range.

Target Station Instrumentation

The target station instrumentation includes the downstream BPM's, multiwires, phosphor screen, which all are described above, and a telescope, scintillator, and segmented ion chambers. These will be designed to tolerate the expected high radiation fields, and will be easily removable for maintenance to allow access to change the target from the upstream side.

To help align the 2 mm(rms) beam on the target there will be an ion chamber mounted 1 m away at 90 degrees to the target in a telescope configuration. There will be a collimated path through the shielding which will allow signal measurement. Integrator signal processing will be used to generate data to be compared with measured beam position during transverse scans to optimize targeting.

There will also be a scintillator/PMT assembly with fast response time to provide a time of arrival trigger to other nearby systems. Downstream of the target, a horizontal and vertical array of ion chambers will be installed to measure profiles of the secondary particles generated at the target.

5.5   Vacuum System

The proton beam transport line from AGS to target will branch from AtR at U8. The transport line vacuum system will be similar to that of AtR in design. The vacuum requirement in the transport line is less stringent due to the single-passage nature, where the reliability of the system is more important. The vacuum level in the beam transport lines is to be $\sim 10^{-7}$ Torr or better and is for the reliable operation of the beam diagnostic equipment and for the lifetime of the sputter ion pumps. The pipes and chambers will be made of stainless steel for its good vacuum and mechanical properties and ease of fabrication. Conflat type flanges with metal seals will be used to join together the chambers and drift pipes. Inconel bellows will be used for its high resistance to radiation induced stress corrosion. Quick disconnect type of flange assemblies will be used in the regions with high radiation dosage to minimize the personnel exposure in the event of component replacement and maintenance. Remote-operable flange assembly fashioned after the recent development in SNS may be used in this region, it is not in the base line though due to its cost and complexity. Sputter ion pumps positioned every ten meter will be used to maintain high vacuum and to monitor the vacuum levels, supplemented by cold cathode and pirani vacuum gauges. PLC will be used to interlock of vacuum valves and protect AtR vacuum similar to that of other vacuum systems in C-A complex.

6 Target/Horn System

6.1 Optimization of the Neutrino Beam Spectrum

For this report we have performed extensive simulations to optimize the beam for the distance to Homestake (2540 km). The ideal beam for this distance will be a broadband beam that covers roughly the ~0.5 GeV to 7.0 GeV range. The $\nu_\mu \to \nu_e$ process through Δm_{21}^2 (solar oscillations) will generate a sizable effect at the lowest energies. The energy range $1-3$ GeV will be important for the detection of CP violation. The energy region $3-5$ GeV contains the first matter enhanced (for neutrinos with regular mass hierarchy) $\nu_\mu \to \nu_e$ oscillation maximum. Lastly, the energy region $6-7$ GeV is important for the ν_μ disappearance measurement.

The main issues in our beam design are:

1. Target material and dimensions.

2. Proton beam intensity and spot size.

3. Horn Geometry.

4. Target placement with respect to the first horn.

5. Horn field strength and momentum kick.

6. Second horn dimensions and placement.

7. Dimensions of the decay tunnel.

8. Vacuum in the decay tunnel.

9. Radiation issues and beam dump geometry.

10. Uncertainties in the flux due to meson production uncertainties.

Some of the above items are discussed below. Other issues are either discussed elsewhere or are still under investigation.

6.1.1 Target Materials and Dimensions

To obtain a broadband neutrino spectrum we have adapted the standard scheme of multiple parabolic horns, each one focuses a different pion momentum region. The main difficulty with this approach is that the lowest energy pions we need to capture and focus are approximately 1-2 GeV and come from a long target. Previous experiments at BNL, such as E734 used a water cooled, 1.5 interaction length copper target. A solid copper target will not survive the 1 MW intensity proton beam that we propose. Therefore, both new materials and new focusing geometries must be considered.

The two main issues in the target system design are the target material and the space available for cooling. If a dense and high Z material, such as Super-Invar, is used then the

spectrum will be approximately the same as a copper target. A better approach is to use graphite as the target material and modify the horn geometry to allow for a longer target.

The target system design is described in a separate section. Here we will only refer to some studies that justify our choices. Figures 6.1 and 6.2 show the spectra of π^+ and π^- that are produced from a two-interaction length target for various materials. For a conventional neutrino beam, the useful part of the pion spectrum is in the energy region above 2 GeV. For this reason, high-Z targets are no longer advantageous and low-Z targets are preferred.
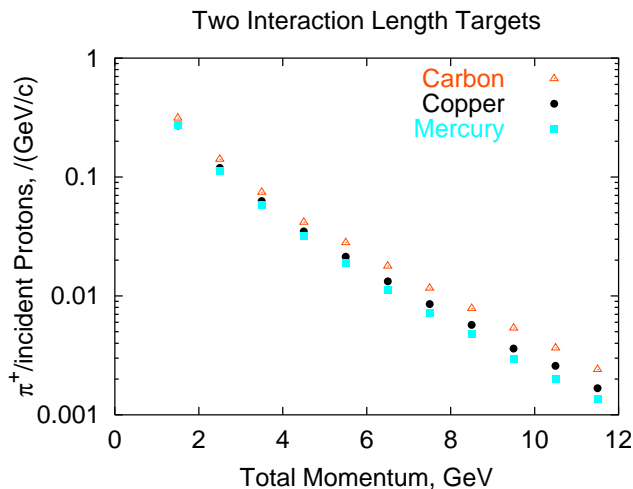
Figure 6.1: The number of π^+ per incident proton is shown as a function of its momentum for carbon, copper and mercury targets. The target is two interactions lengths long for each material.

In addition to maximizing the flux, the target/horn configuration must survive the thermal shock induced by the beam and the high current. Specifically, the target scheme must (a) ensure the removal of the deposited beam energy within the 400 ms period and (b) survive the thermally induced elastodynamic stresses that are expected to be comparable to the mechanical strength of most common materials. Similar concerns are valid for the horn, itself, which will be subjected to rapid heating and, as a result, high levels of thermal stress that will propagate through its volume. In order to satisfy the first requirement, several cooling scenarios are being investigated such as edge-cooling, forced helium cooling in the space between the target and the horn, and radiation cooling. All of these schemes present challenges stemming from integration with the horn in a limited space. To satisfy the second requirement, materials must be selected such that they can withstand and attenuate the thermal shock and be radiation resistant. To address this, low-Z carbon based materials such as graphite and carbon-carbon composites are being considered. Figure 6.18 shows the target mounted in the first horn into helium cooling system for the target and the water cooling manifold for the horn.

Two different forms of carbon, ATJ graphite and a carbon-carbon composite are considered as candidate target materials. These materials, while they have a lot of promise, present some challenges. The two types have been exposed to the AGS beam in the E951 experiment [33].
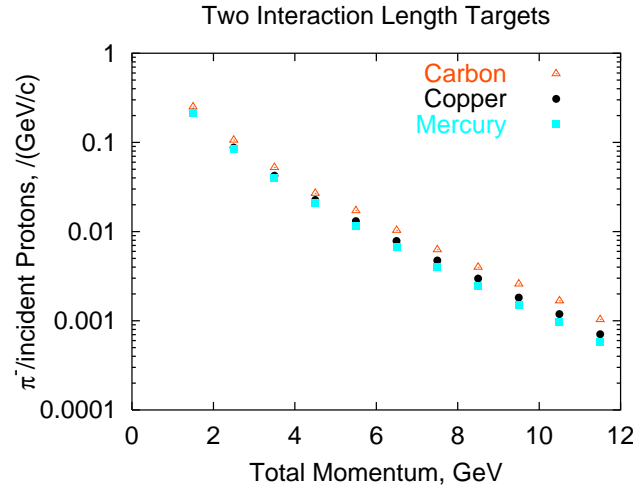
Figure 6.2: The number of π^- per incident proton is shown as a function of its momentum for carbon, copper and mercury targets. The target is two interactions lengths long for each material.

The carbon-carbon composite is a 3-D woven material that exhibits extremely low thermal expansion below 1000^oC and responds like graphite above that.

6.1.2 Proton Beam Spot Size

Preliminary studies on the feasibility of using carbon-based targets for this neutrino beam have been conducted. The thermal shock response and the survivability potential of the target were studied, utilizing the energy deposition estimates from MARS for 1 mm and 2 mm rms beam spots (corresponding to 3 mm and 6 mm radii of target). The total energy deposited on the target (and which needs to be removed between pulses) is 5.1 kJ for the 1 mm spot and 7.3 kJ for the 2 mm spot.

Since the 1 mm rms beam spot is the most serious case, it is examined in detail. For the 89 TP beam the peak energy density is of the order of 720 J/g. This is expected to lead to instantaneous temperature increases of $\sim 1000^\circ$C. A detailed finite-element analysis that involves both the horn and the target needs to be performed so the heat removal of the system can be optimized and, most importantly, so the thermal shock stresses can be computed. A material with a small thermal expansion should experience smaller thermal stresses. However, carbon-carbon composite materials exhibit an increasing thermal expansion at higher temperatures. This behavior of the material needs to be examined further. If the high temperature performance of this material is not satisfactory, a larger beam spot size could be used. From energy density considerations, a 2 mm rms beam spot would have a peak temperature rise per pulse that is less than a third of the 1 mm rms case. This would ensure that the material will be well within the safe zone. Cooling of the front-end is achieved by maintaining the temperature at the surface of the first 4 cm to 27^oC.

We examine the optimal geometry for high-energy pion production utilizing a carbon

target. In Figure 6.3 we see the result of varying the radius of a 1.5 interaction length (60 cm) long carbon target as we varied the proton beam radius. For this analysis the target radius was constrained to 3 times the proton beam rms radius. We note that although the total secondary pion production increases with radius, the desired high-energy portion of the production spectra is enhanced with smaller beam spot sizes. In Figure 6.4 we fix the beam/target radius at (2 mm/6 mm) and find that the production of 7-9 GeV pions increases with target length up to about 80 cm (2 interaction lengths) and then remains essentially constant up to 2 m.

We now explore the impact of bringing 89 TP protons/spill onto a carbon target. For this analysis we utilize MARS to calculate the energy deposition due to the hadronic showering within the target. We examine the two cases of 3 mm and 6 mm radius targets in Figure 6.5. We note the peak energy deposition density occurs near the entrance of the target and has the respective values of 700 and 200 J/g. As a figure of merit, 300 J/g is considered the danger regime where metal targets suffer damage due to the propagation of thermal generated pressure waves through the material. There is, however, evidence that carbon can withstand energy depositions in this regime. The best evidence to date comes from experience in the NUMI target development program. The NUMI carbon target is designed to expect 390 J/g peak energy deposition. A NUMI target test, performed in 1999, utilized a specially focused beam to produce energy depositions in the range of 400 to 1100 J/g without any external evidence of target breakup.
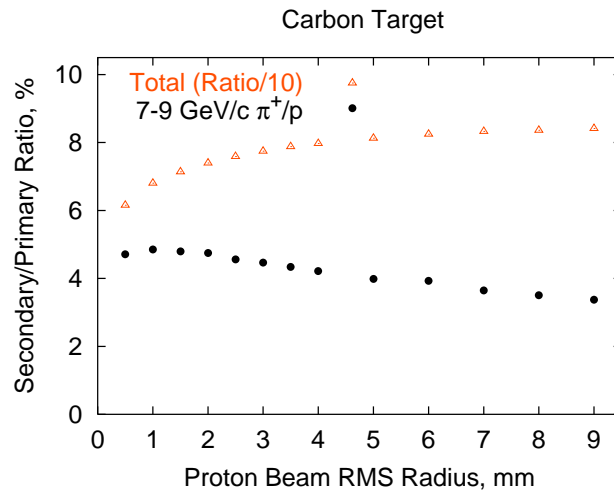
Figure 6.3: The ratio of the numbers secondaries to the number of primaries is shown as a function of rms beam radius. The target radius is assumed to be three times the rms beam radius and the target length is 1.5 interaction lengths.

The secondary particle shower resulting from the interaction of primary protons with the low-Z target will add to the transient heat load of the horn. This shower will be less significant for low-Z targets than for high-Z targets. However, its effect will be examined, and added to the Joule heat load.
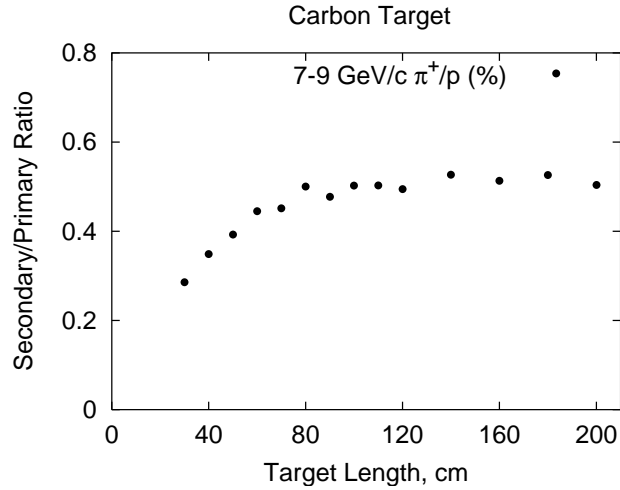
Figure 6.4: The ratio of the number of secondaries within a momentum cut of 7.9 GeV/c to the number of primaries is shown as a function of the target length for a target radius of 6 mm and a rms beam size of 2 mm.
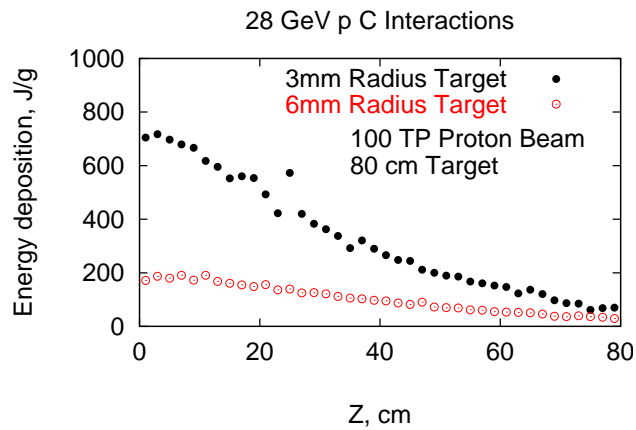
Figure 6.5: The energy deposition is shown as a function of target axial position for a 28 GeV 100 TP beam on a 80 cm carbon target for two different target radius.

There will be activation of the target and horn structure due to secondary and primary particles. This activation will be primarily due to Spallation products and neutrons generated in the secondary shower. The survival of the primary target in the radiation field needs to be examined. This can only be carried out experimentally using a prototypic proton beam on samples of the appropriate target material. The change in physical properties including, thermal expansion coefficient, elastic modulus, and yield strength, need to be examined as a function of proton fluence.

In the current option the target is an 80-cm long cylindrical rod with 12 mm diameter sizes. The 12 mm diameter target is chosen to intercept 100 TP, 2 mm rms proton beam.

There is a large ($\sim 50\%$) model dependent uncertainty on the neutrino flux at high energies (> 4 GeV). In particular the hadron production model in MARS gives lower flux than in GEANT [30]. This uncertainty could be reduced by on going experiments [31, 32, 33]. Higher total intensity or running time will reduce the physics impact of this uncertainty. We are also considering other ways (hadron hose [32]) to enhance the high energy flux.

6.1.3   Horn Geometry

The horn geometry is based on the idea of a thin parabolic magnetic lens for charged particles. The toroidal magnetic field (B in Telsa) from a sheet of current (I in kA) flowing along a beam axis can be expressed as

$$B[T] = 0.02\frac{I[kA]}{r[cm]} \tag{6.1}$$

where r is the radial distance from the beam axis. In the approximation of a thin lens (with thickness d as function of r) located far (distance x) from a point source of charged particles on the beam axis, the following condition focuses particles of momentum (p[GeV/c]) parallel to the beam axis:

$$0.3 \times 0.02\frac{I}{r} \times d = p \times \frac{r}{x} \tag{6.2}$$

Therefore, the shape of such a lens is described by:

$$d[cm] = r^2[cm] \times \frac{p[GeV/c]}{0.006 \times I[kA] \times x[cm]} \tag{6.3}$$

where both d and r are in cm.

Unfortunately, none of the approximations in the above formalism are useful for our purposes. The 1 MW carbon target has to be ~ 80 cm which correspond to two interaction length, and the horn needs to be placed around the target to provide sufficient solid angle of collection for momenta as low as 2 GeV/c. The horn geometry shown in Figure 6.6 is based on old designs from E734 and E889 [29, 28]. The design has three components: the first horn surrounds the target to capture particles in the 1 to 3 GeV/c region. The downstream part of the first horn has an approximate parabolic lens to collect particles in the 3-4 GeV/c region from the downstream part of the target. The second horn is placed ~ 8.3 m from the upstream end of the first horn to collect particles with momentum higher than 3-4 GeV/c. The shape of the horns has been studied by GEANT simulations. The important issues for the first horn are: (1) its opening after the target; (2) the thickness of the conductor on the inner wall of

the horn (2.5 mm of aluminum in the present design); (3) the length; (4) the shape of the parabolic lens at the downstream end. These issues need to be studied in greater detail by simulation. In particular, since any shape can now be manufactured by modern techniques, our design, which is partly influenced by old manufacturing constraints, could be made much closer to the ideal shape for focusing various momenta from different parts of the target.
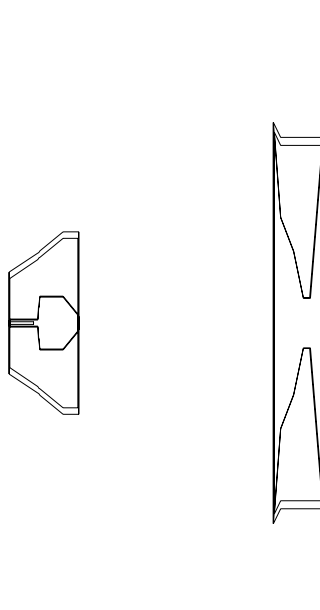
Figure 6.6: The horn geometry in the GEANT simulation. The vertical and horizontal scales are in the ratio of 1 to 13. The beam is incident from the left.

Figures 6.7 and 6.8 show the neutrino and antineutrino flux, respectively for 28 GeV protons using the target, horn, and 180 m long, 4 m diameter decay tunnel geometry to be described later. These spectra were obtained by a detailed GEANT 3.0 calculation which included the dimensions as well as materials of the target, the horn, and the decay tunnel. For this calculation we assumed air in the decay tunnel. Obviously a moderate improvement in the flux is expected with vacuum or helium in the tunnel. The decay tunnel dimensions are studied in a separate section below.

In the remaining part of this section we show our study of four important parameters of the geometry: (1) the distance between the two horns, (2) the placement of the target within the first horn, (3) the gap between the target and the horn conductor to allow for target cooling, (4) the current (or the field) in the horns. The most important quantity to optimize is the total flux of neutrinos. Nevertheless, it is important to understand the impact of any parameter choices on the shape of the spectrum. We performed these studies using PBEAM which is a fast Monte Carlo based program; it does not account for all scattering and multiple interaction effects.

Figure 6.9 shows the dependence of the total flux on the distance between the two horns. The current design is 8 m which is close to the optimal. A longer distance will cause a loss of flux at lower energies, but there is gain at higher energies. The introduction of a third horn
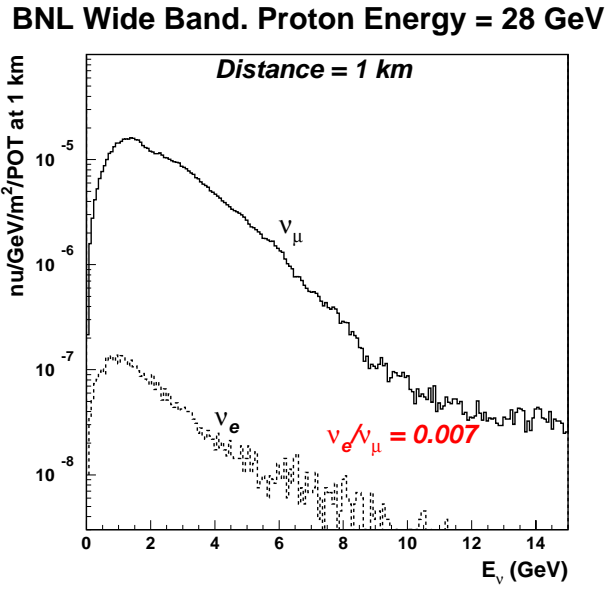
Figure 6.7: Wide band horn focused muon neutrino spectrum for 28 GeV protons on a graphite target.
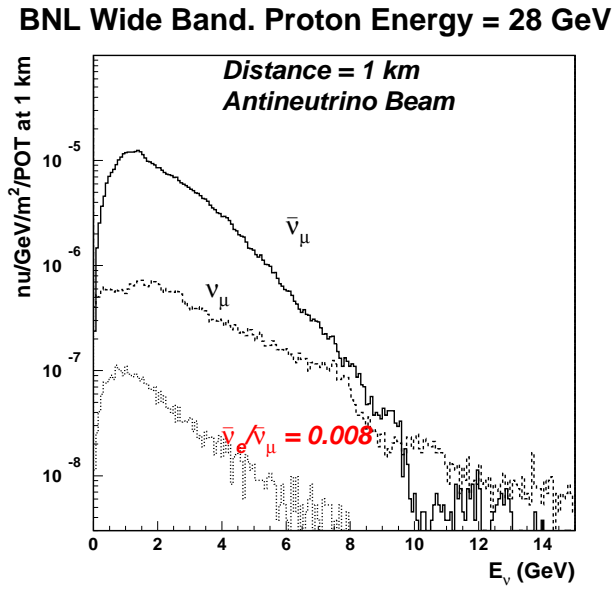
Figure 6.8: Wide band horn focused muon antineutrino spectrum for 28 GeV protons on a graphite target.

at 20 to 25 m distance will give a 10-20 % enhancement of flux above 4 GeV.
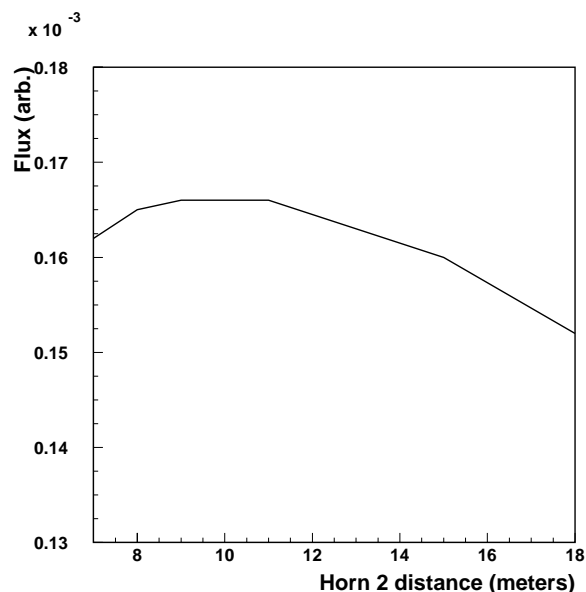
Figure 6.9: Total muon neutrino flux versus distance between the two horns.

Figure 6.10 shows the total flux versus the position of the target in the first horn. Target start position of 0 cm corresponds to placing the face of the target aligned with the face of the first horn. If the target is pulled outside the horn (Target Start < 0) then there is a considerable loss of flux. Target position 5 cm inside the horn is optimal in terms of total flux, but corresponds to slight reduction in the high energy flux, and about $\sim 5 - 10\%$ gain in the low energy (<1 GeV) flux.

An important design parameter is the gap between the 1.2 cm diameter target and the wall of the first horn. It is important to keep this gap narrow to collect low energy particles, however a narrow gap will limit the amount of coolant (either helium or water) that can be forced through it. In Figure 6.11 we have plotted the total flux versus the gap. The current design calls for a 3 mm gap. It is seen from this figure that a 5 mm gap might actually be optimum. However a closer examination of the spectrum shows that for the 5 mm gap there is about 6% loss of flux below 1 GeV. The gap and the strength of the magnetic field are closely coupled and will need to be studied in more detail.

The total flux is plotted against the current in the two horns in Figure 6.12. The flux can be increased considerably by increasing the horn current upto 400 kA. Increasing horn current beyond 500 kA will actually cause a loss of flux because pions below 4 GeV/c will start bending too much in the magnetic field. Based on past experience [28, 29], we assume that the horn current for both horns will be 250 kA. Significant flexibility in shaping the spectrum can be obtained if the two horns can be run at different currents using separate power supplies. These issues will be examined in more detail in the future.

There have been questions regarding the loss of pions (and thus neutrino flux) in the water
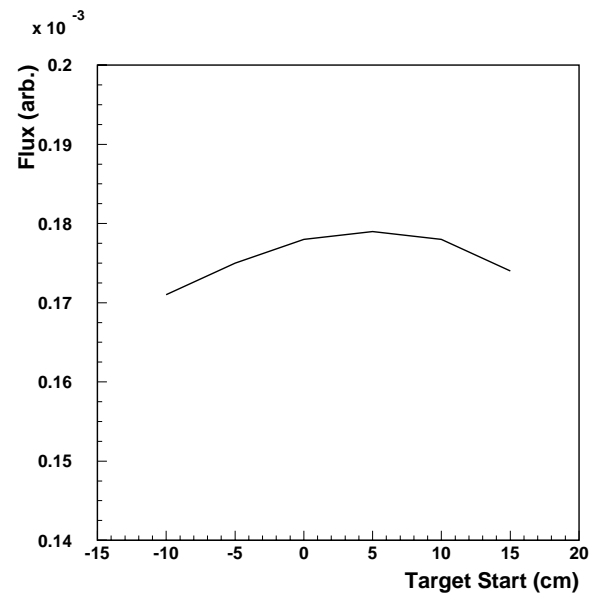
Figure 6.10: ν_μ total flux versus the position of the target in the first horn.
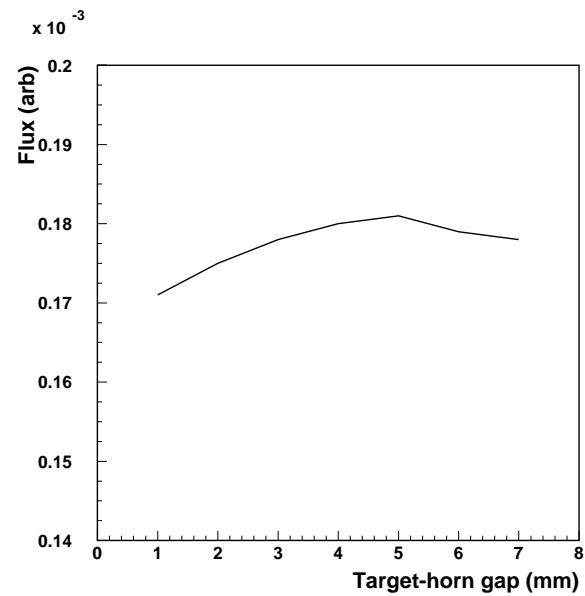
Figure 6.11: ν_μ total flux versus the gap between the target and the inner conductor of the first horn.

x 10^{-3}
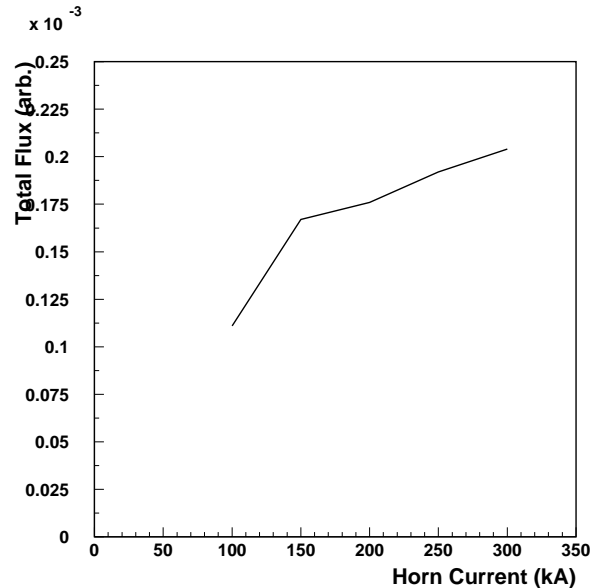
Figure 6.12: ν_μ total flux versus the current in the first horn and second horn.

used for cooling the first horn. The water flow needed to cool the horn is estimated to be 125 cm^3/s at a velocity of 2.5 m/s. If we assume that the horn is simply a pipe of length 2 m, then we find that the volume of water inside the horn at any given time is $\sim \frac{2.5\text{m/s}}{125\text{cm}^3\text{/s}} \times 2$ m $=$ 10 cm^3 which corresponds to 10 g. A large part of this water will be in vapor or steam form. An alternate calculation which estimate water film thickness based on viscosity yields 7 - 20 g. The pion flux out of the first horn is approximately uniformly distributed over 30 cm diameter opening. Therefore the water corresponds to approximately 2×10^{-4} additional interaction lengths. This will cause a negligible loss of flux compared to other effects. Nevertheless, there have been instances in the past (E734 running in 1983) when water accumulated at the bottom of the horn due to excessive initial flow rate or blockage in the drain. This should be guarded against to prevent flux loss.

6.1.4   Decay Tunnel

For our beam design we have assumed that the length of tunnel from the second horn to the beam dump is 180 m and the diameter is 4 m. These parameters can be further studied and optimized. The length of the tunnel influences the height of the hill that must be built and therefore the cost of the civil construction. Presently, a 180 m long tunnel appears to the maximum size that can be built with reasonable cost. Figures 6.13 and 6.14 shows the flux versus the radius of the tunnel and the length of tunnel. It can be seen that there is very little to be gained by making the tunnel radius larger than 2 m. And although one could continue to gain flux by making the tunnel longer, the cost of the civil construction of the hill is rising too fast (as approximately cube of the height of the hill) to make it practical.
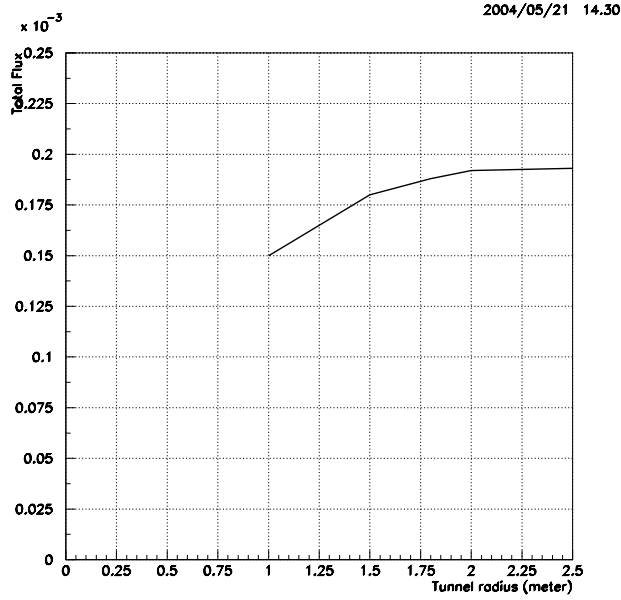
Figure 6.13: Flux in arbitrary units versus the radius of the decay tunnel. The decay tunnel was fixed to be 180 m long. We have chosen 2 m radius for our design.
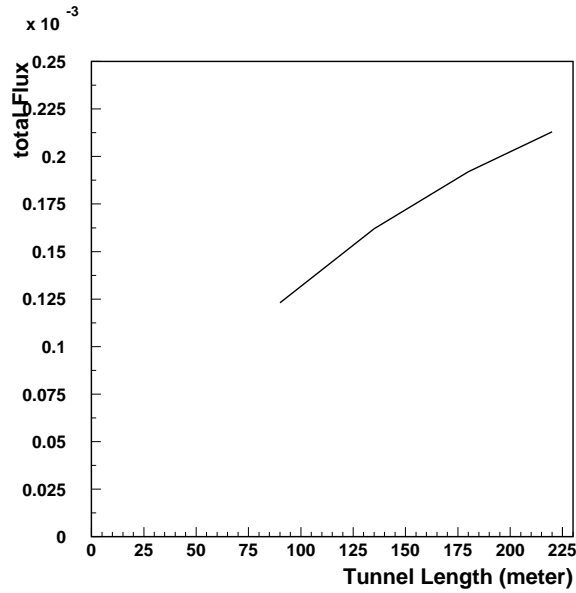
Figure 6.14: Flux in arbitrary units versus the length of the decay tunnel. The decay tunnel radius was fixed to be 2 m. We have chosen 180 m length for our design.

An important advantage of a 4 m diameter tunnel is that it will allow us to run with an off-axis beam. This could be accomplished by moving the target station and the horns horizontally by 1.3 m and then tilting the assembly by 1 deg. to point the beam axis towards the far corner of the 180 m long tunnel. This geometry is displayed in Figure 6.15. The neutrino beam spectrum (see Figure 6.16) obtained in this manner will have fewer high energy neutrinos and thus will reduce the neutral current background for the electron neutrino search.

There are many practical issues regarding 1 degree off-axis run. They are: (1) civil construction must allow for movement of target, horns and associated shielding (with total weight of about 1000 tons), (2) the proton beam transport on top of the hill must also be moved to aim the beam on the target, (3) the beam dump at the bottom of the hill must be sufficiently large to accommodate the beam striking it off-axis. Although these issues need to be solved for the 1 deg. off-axis running, the most important element is the diameter of the tunnel. The off-axis option is viable only if the diameter is 4 m or larger. We feel that this option is very important for the physics and do not want to rule it out at this stage.
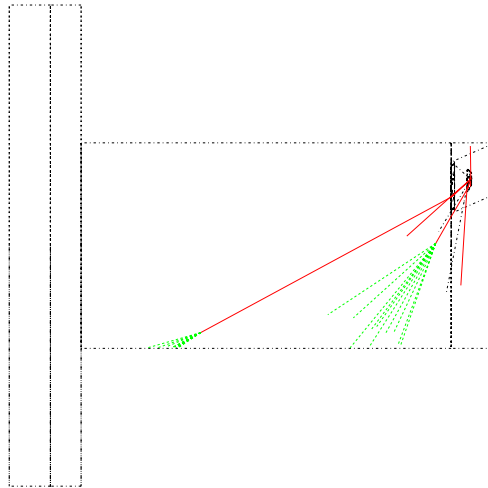
Figure 6.15: Geometry of horns and tunnel for 1 deg off-axis run. The target and horn station will be moved by 1.3 m and tilted to point into the downstream corner of the 4 m diameter tunnel to obtain approximately 1 deg off-axis spectrum.

If the decay tunnel is evacuated, there will be a window between the second horn and the tunnel. A steel window with 3 mm (1/8 inch) thickness will lead to about 3-5% loss of flux. The NUMI beamline will be using a Fe-Aluminum composite window to lower the amount of material in the center of the beamline to lower loss of flux. We could adapt the NUMI strategy. In case the decay volume is filled with helium the window can be much thinner. For any window, there will have to be active cooling to remove the energy deposited by the energy loss from pions. Detailed simulation work on the design of the window will be carried out as

BNL Proton Energy = 28 GeV
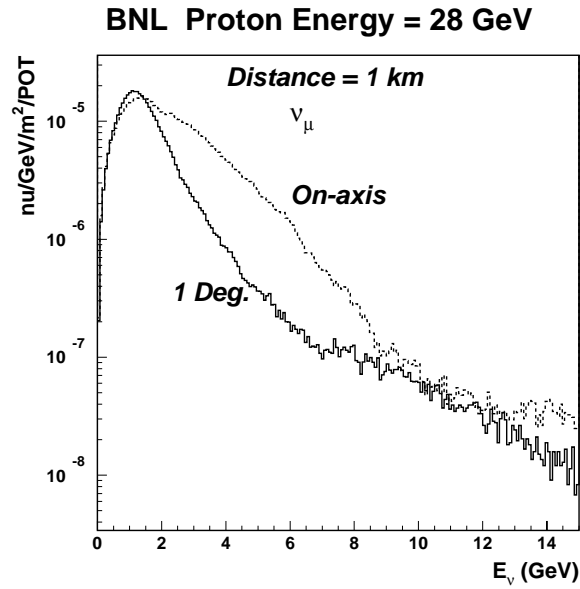
Figure 6.16: Off-axis horn focused muon neutrino spectrum for 28 GeV protons on a graphite target. The 1 deg off-axis spectrum obtained by the geometry in Figure 6.15 is compared to the on-axis spectrum.

28 GeV protons wide band beam
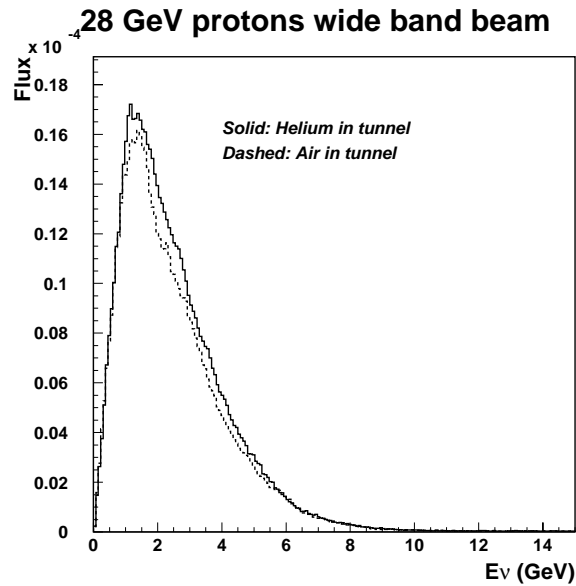
Figure 6.17: Muon neutrino spectrum for 28 GeV protons assuming helium (solid) in the tunnel versus air (dashed) in the tunnel.

we proceed with this project.

Further work on the optimization of this spectrum for the very long baseline experiment is ongoing. Further optimization focuses on enlarging the horns to accept more lower energy pions so that the flux near 0.5 GeV can be enhanced. We will also examine using the hadron hose [32] to capture more higher energy particles.

6.2   Description of the Integrated System

After an extensive evaluation of the graphite-based materials, carbon-carbon composite (CC) was selected as a target material both for its low-Z and thermo-mechanical properties [34]. Various aluminum-based materials are being considered for horn conductors, such as 3000-series and 6061-T6 aluminum, that low resistivity, high strength, resistance to corrosion and micro-cracking [35]. The baseline design parameters of the horn/target system are shown in Appendix A6.

In the process of designing the horn/target system the following key elements were closely considered:

- Heat generation and its removal from the target/horn system

- Target thermo-mechanical response to energetic, high intensity protons

- Irradiation and corrosion effects on target/horn materials

- Horn/target integration issues

Figure 6.18 is a conceptual description of the target and horn integrated system being considered in this study. The 12 mm diameter carbon-carbon composite target is fully inserted into the inner horn conductor allowing a 3 mm annular gap between the target and horn surfaces to allow coolant flow to remove the generated heat on the target and horn. After an extensive study on the coolant type and its compatibility with the rest of the system we have concluded that cooled, forced helium in the annular space will suffice to remove the heat generated in the target as well as a portion of the heat generated in the horn inner conductor. In the front of the target is a carbon-carbon beam "collimator" or baffle that has dual role: (1) it provides the upstream target support and includes the channels that will force the coolant flow into the annular space; (2) it plays the role of beam diffuser in the event the proton beam strays off the axis and thus protects the horn. The size of this baffle needs to be optimized to play that role effectively. The front end of the target will be maintained at low temperature, that will help in removing heat deposited on the target by conducting into the mass of the baffle. It is envisioned that the baffle/target arrangement will be a monolithic structure for system optimization. At the downstream end of the target a special design allows for the forced coolant to leave the horn neck-down section and provides a "simple support" for the target in the current design.

The horn, made out of aluminum alloy (Al-6061 T6 or Al-3000), has a diameter in its narrowest section of 18 mm while the thickness over that section is 2.5 mm. The thickness of the inner conductor reduces to ~ 1 mm downstream of the neck-down section to minimize the material in the pions path.

As shown in the schematic in Figure 6.18, the current supply and return take place at the downstream end of the horn. The baseline design calls for a 250 kA peak current to be achieved with a half-sine wave shape that has a base of 600 μs with a repetition rate of 2.5 Hz. The magnetic pressures and joule heating generated in the conductor are the main concern in the optimization of the horn conductor. While heat generated in the narrowest section of the horn will be partly removed by the fluid flowing in the annular space, the bulk of the heat
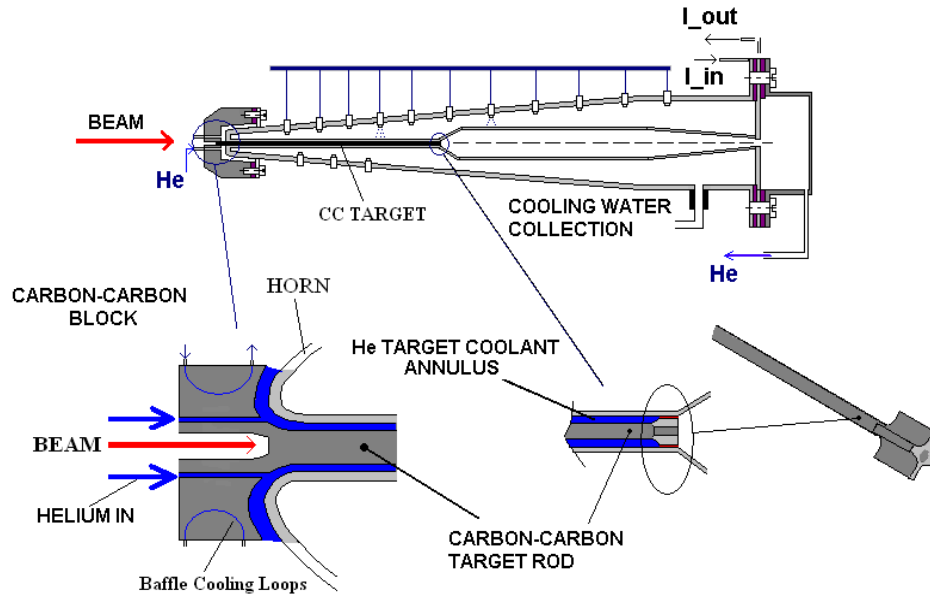
Figure 6.18: Conceptual arrangement of horn/target system including heat removal scheme

generated in the conductor by the flowing current has to be removed by the spraying water inside of the horn through a set of optimally positioned jets. Surface treatment/protection is of outmost importance to maximize the useful life of the aluminum material in that environment and is presently under experimental evaluation.

Also under consideration is a downstream thin window made of a thin layer of CC composite and whose role is to hold the target coolant in a closed loop system. This way the coolant is collected, cooled and returned to the target upstream to be re-injected into the annular space. The key issue with such window is the fact that it will intercept a significant portion of the incoming beam power ($\sim 80\%$) and may be subjected to significant thermo-mechanical stress conditions. In addition, the window will affect the neutrino spectrum, although being a low-Z (thus minimal interaction with secondary particles or generation from intercepting the beam protons) the problem of heating and beam interaction is minimized.

6.3   Target/Horn Heat Loads and Heat Removal Scheme

6.3.1   Target Heat Load

The energy deposited by a 28 GeV proton beam with intensity of 8.9×10^{13} protons per pulse and 2 mm rms on the 80 cm-long, 12 mm-diameter cylindrical target rod was estimated with the hadronic codes MARS and GEANT. Figure 6.18 depicts the energy distribution in both axial and radial directions. It can be seen that the peak energy is deposited at about 10 cm from the front end of the target. The appearance of fluctuations in the energy deposition

distribution is the result of the statistics that were used for this particular calculation. The integrated energy deposition per pulse is estimated to be about 7.3 kJ resulting in 18.25 kW for the 2.5 Hz operation. Such deposition leads to a temperature rise per pulse in the CC composite target of $\Delta T = 270^o$C.
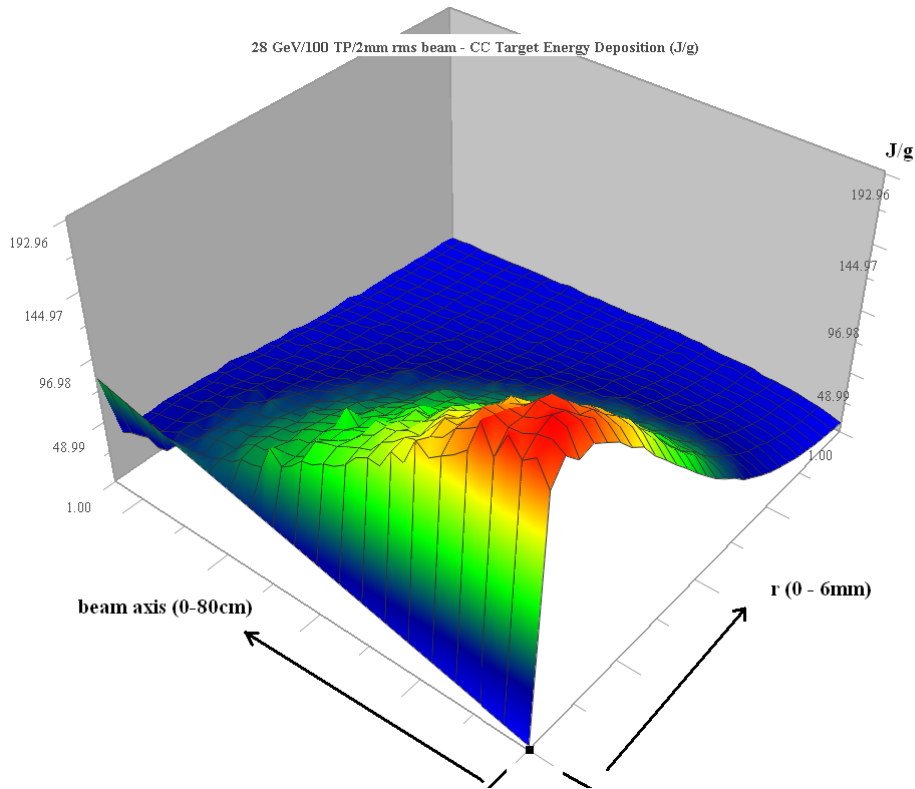
Figure 6.19: Energy deposition (J/g) in the 12 mm diameter CC composite target from a beam of 8.9×10^{13} proton intensity with 2 mm of rms beam size

As part of the design process, a number of cooling schemes have been considered for the integrated system of horn and target. Utilizing past experience on horn/target system performance we arrived at the current baseline scheme that calls for a de-coupling of the target from the horn with regards to their cooling and the use of helium as the fluid to remove the heat from the target.

Specifically, as shown in Figure 6.18, helium is forced past the surface of the CC target with sufficient velocity to ensure that the heat generated per beam pulse is removed before the next pulse arrives. The heat load in the horn comes from three different sources, namely, joule heating from the flowing current, energy deposition due to the proton beam interaction with the target, and heat by radiation from the surface of the CC target. While some of the heat in the horn will be removed by the flowing helium in the annulus, the bulk of the heat in horn conductors (inner & outer) will be removed by the spraying of cooling water over the inner horn surface. Since different mechanisms, namely heat convection, conduction and radiation between target and horn, will be at work, the heat balance of the overall system

as it reaches an operating temperature is addressed by using a comprehensive finite element model. Such detailed model will assist in the design of the overall system as well. As a first step, however, and in order to assess the heat removal capacity of surfaces in the system, a set of proof-of-principle estimates are presented that will indicate that the adopted scheme is feasible.

Given that the amount of heat transferred by radiation alone from the target to the horn is quite small, the primary mechanism is heat removal by forced convection of cold He in the annular space between the target and the horn. The key elements, in assessing how feasible such mechanism would be, are the operating temperature of the target, the temperature of the cooling fluid and the heat generation rate in the volume of the target that needs to be removed. These working parameters will establish, primarily, the mass flow rate and velocity of the coolant necessary to remove the generated heat. The heat removal via mass transport is given by

$$Q_m = m\ Cp\ dT_f \tag{6.4}$$

where m is the mass flow rate; C_p is specific heat of fluid at constant pressure; and dT_f is change in temperature of fluid.

Figure 6.20 shows how much heat can be removed as a function of mass flow rate, fluid pressure, and fluid temperature change. So that for approximately 18 kW of heat removal, at 5 atmospheres operating pressure and a fluid delta T of 200 °C. The mass flow rate is approximately 20 g/s.
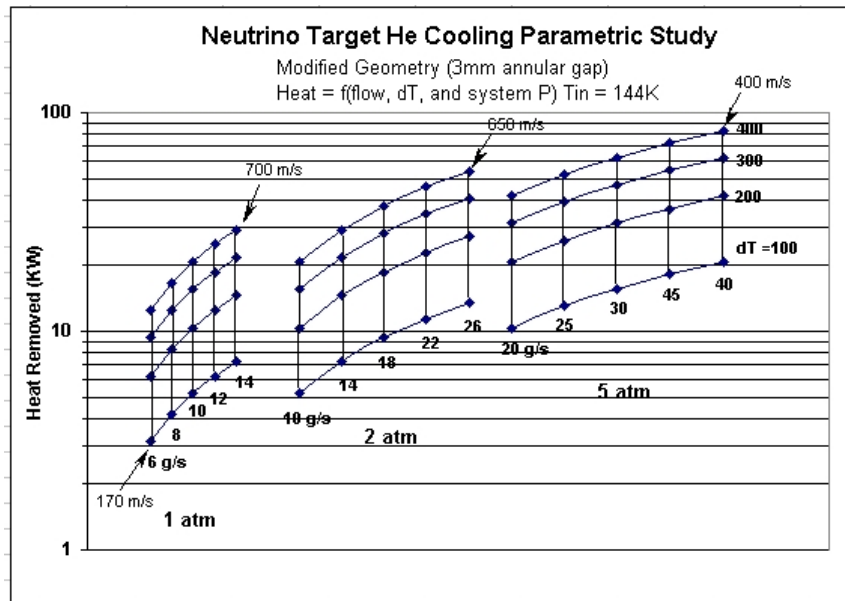
Figure 6.20: Heat removal via mass transport of helium gas.

This heat removed by mass transport must be exactly equal to the heat removed via convection,which is giving by

$$Qc = h_f AdT \tag{6.5}$$

where the h_f is the convection heat transfer coefficient; A is surface area; dT is difference between the bulk fluid and the hot surface temperature.

The heat transfer coefficient associated with the annular space with hydraulic diameter, d_h = 4A/P_w = 0.006 m is estimated based on turbulent flow in smooth tubes using the relation [36]:

$$N_u = 0.023 \ (R_e)^{0.8} \ (P_r)^{0.3} \tag{6.6}$$

where Re is $\rho V d_h / \mu$; ρ is density; V is Velocity; μ isdynamic viscosity; Pr is Prandtl number = $C_p \mu /K$ = 0.71; K is thermal conductivity and Nu is the Nusselt number. They are related to the heat transfer coefficient by

$$N_u = h_f \ \ d_h / \ k \tag{6.7}$$

where k = 0.16 W/m-K, and h_f is the convection heat transfer coefficient.

Thus, for the 20 g/s flow rate, an average density of 0.7 kg/m^3 (at 5 atmospheres pressure) and the annular flow area of 1.4 x 10^{-4} m^2, the velocity of the fluid is v = 200 m/s. The average dynamic viscosity is 2.3 x10^{-5} kg/m-s, so that R_e = 3.6 x10^4 and the Nusselt number is calculated to be

$$N_u = 92$$

thus the convection heat transfer coefficient

$$h_f = 2450 \ W/m^{2\circ}C$$

Thus for the energy balance to be maintained,

$$Q_m = Q_c$$
$$h_f \ A \ dT = m \ C_p dT_f = 18 \ kW$$

The target surface temperature can be calculated based on a surface area of 0.075 m^2

$$dT = 100 \ ^\circ C$$

That is, the average temperature of the target surface is 100 °C higher than the bulk fluid temperature.

Detailed Finite Element Analysis

A more detailed analysis was performed to determine the thermal-hydraulic behavior of the helium gas in the target-horn annular region and the target surface temperature profile. A helium gas coolant flow of 22 g/s at 10 atmospheres was used, since this was a typical value for a commercially available helium compressor, these parameters are stringent than those calculated in the previous subsection. Figure 6.21 shows the temperature profile from this FEA model. The Helium gas properties resulting from this model are shown in Figures 6.22 and 6.23.

The helium pressure and flow are achieved by the use of a rotary screw helium compressor combined with a helium-to-water heat exchanger to remove the heat created via compression and another helium-to-water heat exchanger to remove the heat picked up from cooling the target and horn. Figure 6.23 shows an industrial compressor that can supply the appropriate flows and pressures.
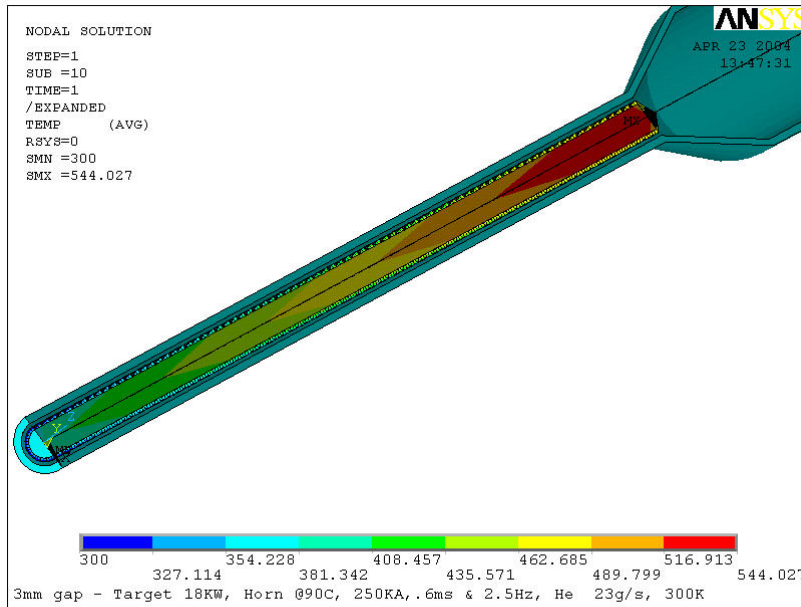
Figure 6.21: Target-horn temperature profile.
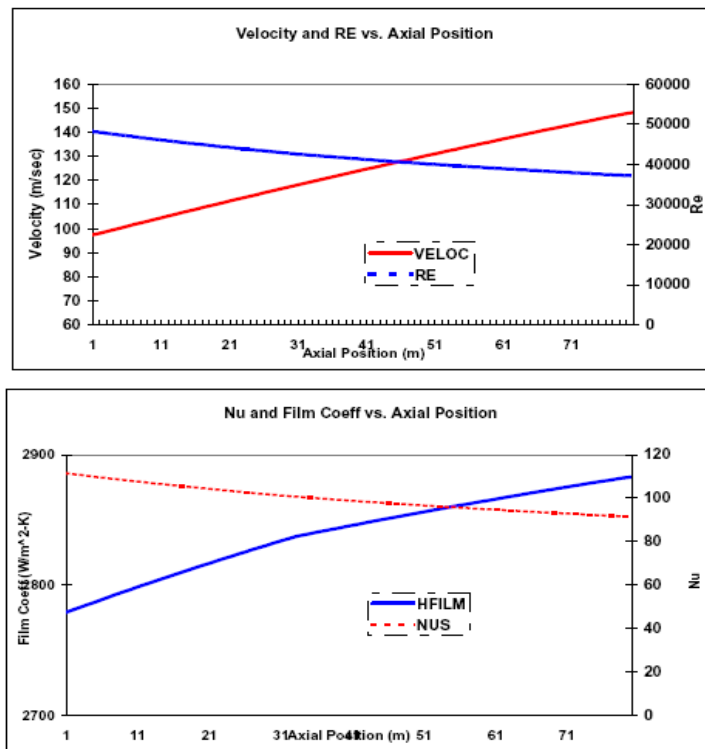
Figure 6.22: Helium thermal-hydraulic properties within target-horn annular region.
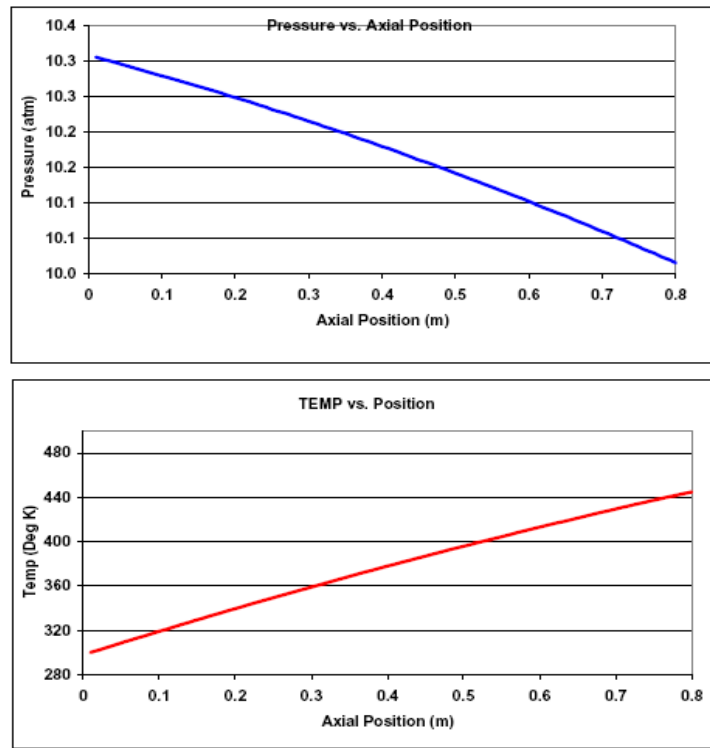
Figure 6.23: Helium thermal-hydraulic properties within target-horn annular region.
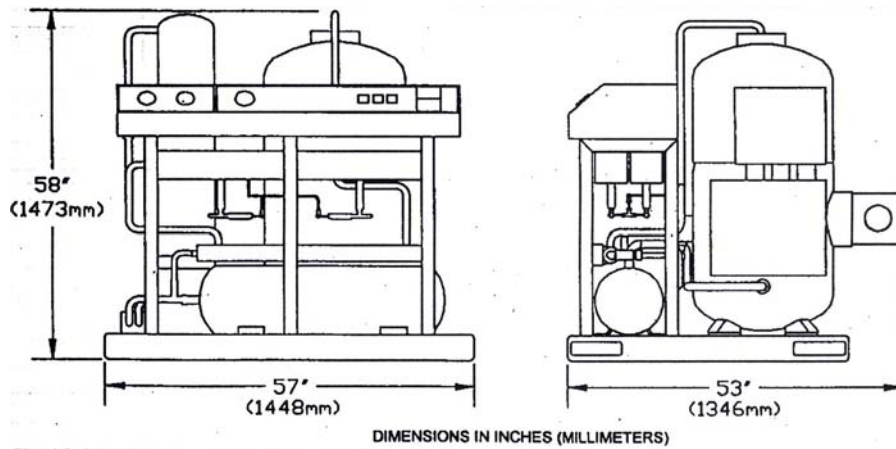
Figure 6.24: 110 kW helium compressor

6.3.2   Horn Heat Loads

Gamma-Ray Heating Estimate

The energy deposited on the inner horn conductor from gamma-rays and secondary particles that are generated from the proton beam interaction with the target has been estimated using the codes MARS [30] and MCNPx [38]. The total energy has been estimated to be of the order of 10.3 kW.

Joule Heating Estimate

Joule heating from the electron flow is the primary heat load in the horn. The peak current is I = 250 kA and is achieved with a half-sine wave shape that has a base of 600 μs with a repetition rate of 2.5 Hz. This pulse period is equivalent to approximately 830 Hz. The thickness of the inner conductor (2.5 mm) is smaller than the calculated skin depth for this frequency, so that the current will flow throughout the cross-sectional area. To estimate the joule heat load in the horn inner conductor, an idealized half-sine current pulse was used with a half-period of 600 μs. Using the resistivity of aluminum $\rho = 4.2 \text{x} 10^{-6}$ Ohm-cm, and the inner conductor geometry, it is estimated that approximately 29 kW will be deposited into the horn. Figure 6.25 shows the summary portion of the calculation.

For Proposed BNL Neutrino Superbeam: 250 KA

							$I^2 R$	
Current Peak =	2.50E+05	amps						
Current duration =	6.00E-04	seconds	as half sinewave					
thus, frequency, f =	833.33	Hz						
Duty cycle =	2.5	Hz		0.7	(RMS of sinewave)			
ρ_{al} =	4.2	μohm-cm						
t_s =	0.4807	cm						

Section	Davg	t_{wall} or t_s	A_{sd}	L	R_{ac}		$I^2 R$	
	(cm)	(cm)	(cm2)	(cm)	μohm			
1	2.05	0.25	1.610	80	208.7		13695	
2	4.15	0.25	3.259	10	12.9		846	
3	6.25	0.25	4.909	80	68.4		4492	
4	1.45	0.25	1.139	40	147.5		9681	
					437.5	μohms total AC R	28714	Watts

Thus, the total Power into horn from Joule Heating =   28.71 KWatts

Figure 6.25: Joule heating of inner horn.

Heat Load from Target Radiation

The CC target will be operating at a slightly higher temperatures than those of the horn (an operating CC target temperature of $\sim$250 ^oC has been selected based on the approximate calculation of sub-section 6.3.1 and FEA results). A small amount of heat will radiate from the target surface to the surface of the horn over the neck-down section. Assuming that the surface temperature of the aluminum is maintained at $\sim$90^oC with the help of the coolant

spray on the side of the inner horn conductor that does not see the target (a safe temperature for aluminum in the presence of water), then the radiating heat flux can be estimated from the relation:

$$\frac{q_{CC->Al}}{A_{CC}} = \frac{\sigma\left[T_{CC}^4 - T_{Al}^4\right]}{\frac{1}{\varepsilon_{CC}} + \frac{A_{CC}}{A_{Al}}\left(\frac{1}{\varepsilon_{Al}} - 1\right)} \tag{6.8}$$

where, $\sigma = 5.669 \times 10^{-8}$ W/m^2-K^4, $\varepsilon_{cc} = 0.98$ and $\varepsilon_{Al} = 0.09$ and A$_{CC}$ is the target area.

Based on the above parameters, the heat flux from the target surface is approximately q/A$_{CC}$ = 400 W/m^2 and the total heat transfer from the target to the horn inner conductor q = 400A$_{CC}$ = 13 W. As seen, the amount of heat exchanged by radiation heat transfer is quite low.

Heat Removal using RAW Spray on Inner Horn Conductor

We plan to remove the heat over the entire inner surface as well as the energy deposited throughout the horn from beam-target interaction by spraying water through special nozzles that penetrate the outer conductor. While this approach has been used extensively to cool horns in the past (and in many instances to cool the target as well through conduction across the horn inner conductor), there are some issues associated with such approach, namely, the potential acceleration of corrosion of the aluminum surface coming in contact with water and the fatigue failure through propagation of surface cracks plus the fact that water within the horn will be in the path of pions beam. The attempt to maintain the aluminum surface temperature, when in contact with water, below 100° C (based on experience from the reactor industry [?]) in an attempt to extend the life of the horn, results in larger quantities of water being sprayed against the conductor inner surface.

To estimate the required spraying capacity, attention is again focused on the inner conductor which will experience higher joule heating and gamma-ray heating. Assuming that the spraying jets are positioned in such a way that the entire inner surface experiences forced flow (resembling a cylinder in cross-flow), the following forced convection relations apply,

$$Nu_D = 0.3 + \frac{0.62 Re_D^{1/2}\, \mathrm{Pr}^{1/3}}{\left[1 + (0.4/\,\mathrm{Pr})^{2/3}\right]^{1/4}}\left[1 + \left(\frac{Re_D}{282000}\right)^{5/8}\right]^{4/5} \tag{6.9}$$

where, $Nu_D = h_f D/k$ is the Nusselt number and h_f is the effective convection heat transfer coefficient.

Assuming that the water jets force a flow with a free velocity of U = 2.5 m/s at a temperature of T$_{water}$ = 20 °C and that the conductor surface is maintained at a temperature of T$_{wall}$ = 80 °C, the parameters in the above formula have values: Reynolds number $Re_D = U_f D_e/\nu$ = 87963, Pr = 3.6, ν = 0.0054 cm^2/s and k = 0.645 W/m-K.

Substitution into the above relation leads to,

$$Nu_D = h_f D/k = 367 \tag{6.10}$$

And to an effective convection heat transfer coefficient of: $h_f = 12485\ W/m^2 - K$.

By relating the heat flux from the conductor surface to the convective heat transfer,

$$q/A = h \ (T_{wall} - T_{water}) \ W/m^2 \qquad (6.11)$$

the heat transferred through the surface area A is q = 38.5 kW. This cooling scenario can satisfy the needs for removing the heat from the inner surface of the conductor.

6.4   Target and Horn Material Selection

6.4.1   Target

The baseline material for the experiment is a special Carbon-Carbon composite. It is a 3-D weaved material and exhibits extremely low thermal expansion for temperatures up to 1000 °C while for higher temperatures it behaves like typical graphite. Its thermal expansion behavior is significant in the sense that the thermo-elastic stresses induced by intercepting the beam will be quite small and thus extending the life of the target. The Table 6.1 lists the variation of expansion as a function of temperature.

Table 6.1: Thermal expansion data for a 3-D fine weave Carbon-Carbon composite

Temp.	% elongation
23 °C	0%
200 °C	-0.023%
400 °C	-0.028%
600 °C	-0.020%
800 °C	0%
1000 °C	0.040%
1200 °C	0.084%
1600 °C	0.190%
2000 °C	0.310%
2300 °C	0.405%

In addition to the low thermal expansion the material is stronger than typical graphite reaching compressive strength $\geq$ 120 MPa.

Experience with this material has been acquired as a result of the BNL E951 experiment and its use in the SNS charge exchange foils. Figure 6.26 depicts axial strains. These are experimental results from actual proton beam tests conducted at the BNL AGS using 24 GeV protons and intensities of 3 to 4 x10^{12} protons per pulse.

The long-term behavior of this special material in an irradiation environment is not known. It is anticipated, however, that during the R&D phase the effects of irradiation to be studied experimentally.
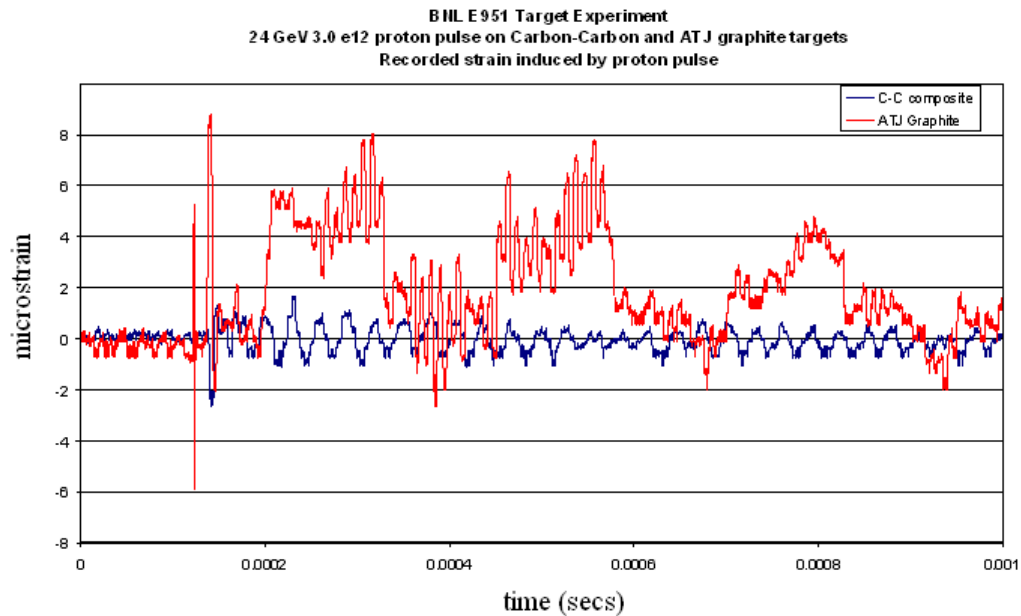
Figure 6.26: Experimental results of CC and graphite responding to 24 GeV proton beam

6.4.2 Horn

Figure 6.18 depicts the first of the two focusing horns made of aluminum and with a thickness in the neck-down section of the conductor is 2.5 mm. The radius of the inner conductor for the following calculations was assumed to be 9 mm.

6.5 Conceptual Design of the Horn Power Supply

The main objectives of the horn [34] power supply design is to achieve an output pulse amplitude of 250 kA, a pulse flat top of 2.5 μs or longer with a 1% flatness and pulse to pulse repeatability, and a repetition rate of 2.5 pulses per second.

Most commonly used scheme is the capacitor discharge type [39, 40, 41, 42]. In this type of circuit, a capacitor bank stores the energy, and a main discharge switch release the energy to the load through transmission lines. For very long distant transmission, pulsed transformers have been added into the KEK design and CNGS horn system. The horn as an electrical load is usually being described as an inductor in series with a resistor. Discrete parameters of inductance and resistance are also used to formulate the short length, low impedance transmission lines when associated with low bandwidth pulse. Hence, the circuit can be simplified as a RLC discharge circuit.

The pulse rise time, T_r, is usually approximated by the quarter period of sine wave. For a lossless LC oscillation circuit, this can be determined by the equation $T_r = \frac{\pi}{2}\sqrt{LC}$, and the load current is given by

$$I(t) = V_o\sqrt{\frac{C}{L}}\sin(\frac{1}{\sqrt{LC}}t). \tag{6.12}$$

The maximum current amplitude is $I_{\max} = V_o\sqrt{\frac{C}{L}}$ for lossless LC circuit.

In the case of critical damped RLC circuit, $R = 2\sqrt{L/C}$ and

$$I(t) = \frac{V_o}{L}t\,e^{-\frac{R}{2L}t}. \tag{6.13}$$

The maximum output current can be determined by

$$I_{\max}(t = \frac{2L}{R}) = V_o\sqrt{\frac{C}{L}}\,e^{-1}, \tag{6.14}$$

and the current rise time is $T_r = \frac{2L}{R} = \sqrt{LC}$.

Compare two cases, for a given L, C and charging voltage V_o, the output current of the critical damped one has peak amplitude of 0.3679 of the lossless one. To reach the same maximum output current, the initial voltage of the critical damped circuit has to be 2.7183 times of the lossless one. It implies that, for the critical damped one, the energy stored in the capacitor bank as well as the charging power has to be 7.389 times larger.

In the high current path, the resistance caused voltage drop and energy dissipation are critical factors to be considered. The cooling system for heat removal from the effective resistor, and the additional charging power required to make up the resistive dissipation can be very costly. Hence the low circuit resistance is preferred.

6.5.1 Effective Resistance and Skin Effect

The load and transmission line resistance varies with frequency due to skin effect. For any given material, the skin depth δ_s is inverse proportional to the square root of the frequency f, and the effective resistance R_{eff} is proportional to the oscillating frequency. Here

$$\delta_s = \frac{1}{\sqrt{\pi\, f\, \mu_R\, \mu_o \sigma}}, \tag{6.15}$$

and

$$R_{eff} = \frac{l}{\sigma\, b\, \delta_s}, \tag{6.16}$$

where l is the conductor length and b is the conductor width. The material's conductivity, relative permeability, and the free space permeability are described by σ, μ_R, and μ_o, respectively.

One can see that slower frequency leads to lower effective resistance. The other factors associated with effective resistance are the length, width, and permeability and material conductivity. For non-magnetic material, the relative permeability is close to unit. The switching device on-state resistance and hardware connection joints resistance also contribute to the total resistance.

In summary, the lower effective resistance can be achieved by using:

1. Lower frequency, higher skin depth;

2. Wider conductor width;

3. Shorter conductor length;

4. Higher conductivity material;

5. Lower switch on-state resistance; and

6. Lower connection joint resistance.

6.5.2   Inductance Issues

The total inductance includes the horn inductance, transmission line inductance, series inductance of the capacitor, switch inductance, and circuit loop stray inductance. The external inductance depends on the inductor geometry and material permeability. The internal inductance has frequency dependence. The voltage across the inductor is defined as $V_L(t) = L\frac{dI(t)}{dt}$. Hence, the larger inductor and faster current rate of change requires higher voltage.

For a lossless circuit, the total inductive energy shall be equal to the total capacitive energy storage, i.e.

$$\frac{1}{2}\,L\,I^2 = \frac{1}{2}\,C\,V^2. \tag{6.17}$$

Therefore, we have that the higher the inductance and current, the higher the capacitance and its initial voltage.

For a reasonable design, the total inductance shall be kept as low as possible, and the current rise time shall be chosen to accommodate the device operating voltage.

6.5.3   Principle Design Example

Let us consider a system with overall inductance of 2.5 μH, a total resistance of 2 mΩ, and a capacitor bank of 16 mF. If the initial capacitor voltage is 4000 Volts, the peak output current amplitude is about 288 kA with 314 μs rise time.
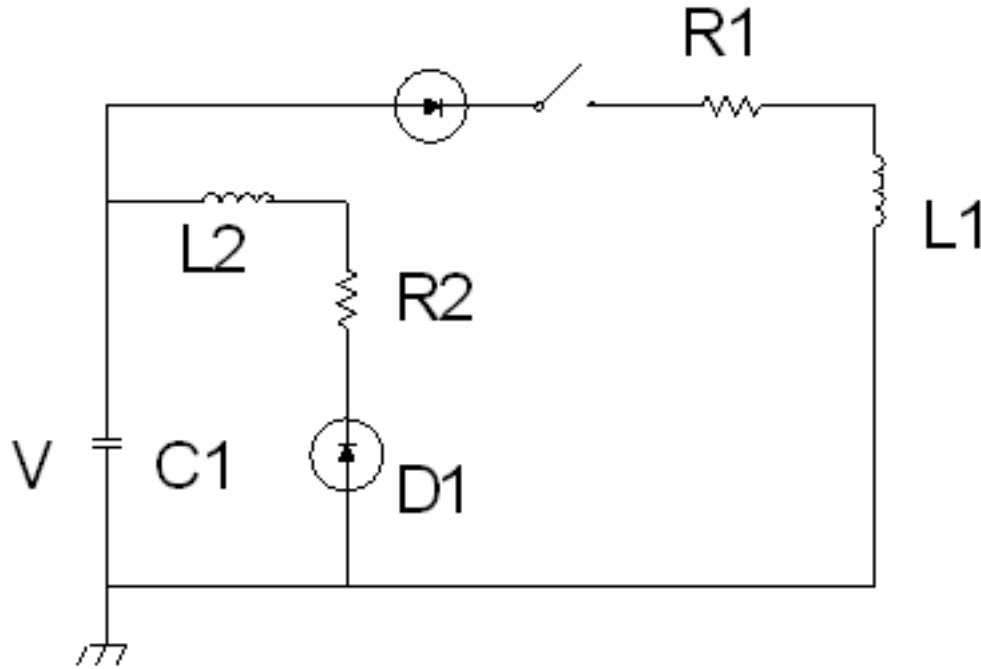
Figure 6.27: Simplified circuit diagram.

The stored energy in the capacitor is 128 kJ. For 2.5 Hz pulse repetition rate, the minimum charging power supply is 320 kW.

For the 3000-series aluminum being considered in the horn mechanical design, the material skin depth is 0.06525 cm at 25 kHz. Derive from it, we have the skin depth is 0.3574 cm at 833 Hz.

The parameters used in this example are rough estimates based on similar systems, as listed on Table 6.2. The resistance used in the example is tight for the chosen frequency. If higher resistance has to be used, then the voltage and capacitance have to be increased.

6.5.4   Major Components

The major components of this system include:

1. Charging Power Supply;

2. Capacitor Bank;

3. Discharge Switch;

Table 6.2: The parameter used here based on similar systems.

	Pulse				Cap.	Induct.				Resist.					Rep.
	Curr.	Volt.	Tr	10% Width		Horn #1	Horn #2	Stray	Tot.	Horn #1	Horn #2	Stray	Tot.	Rev. Dump	Rate
	kA	kV	μS	μS	mF	nH	nH	nH	nH	μΩ	μΩ	μΩ	μΩ	μΩ	Hz
AGS Narr. Band	240	12.44	58	350	0.850	462	567	635	**1664**				**9600**	5000	
AGS Wide Band	285	10.98	58	350	1.116				**1198**				**7500**	5000	
Mini Boone	170	5.35	143		1.500	680		660	**1340**	230		770	**1000**		5
NuMi	205	0.97	2600		900.	689	510	1208	**2407**	270	71	690	**1031**		0.53
CERN	300	7.275	81		1.075	420		200	**620**	128		200	**328**		75
Pulser with Output Transformer															
KEK	250	4.702	3000		6.000	1030				210					0.5
CNGS	150	7.21	4300		4.008	2150				405					2 pul./6s, 50ms apart
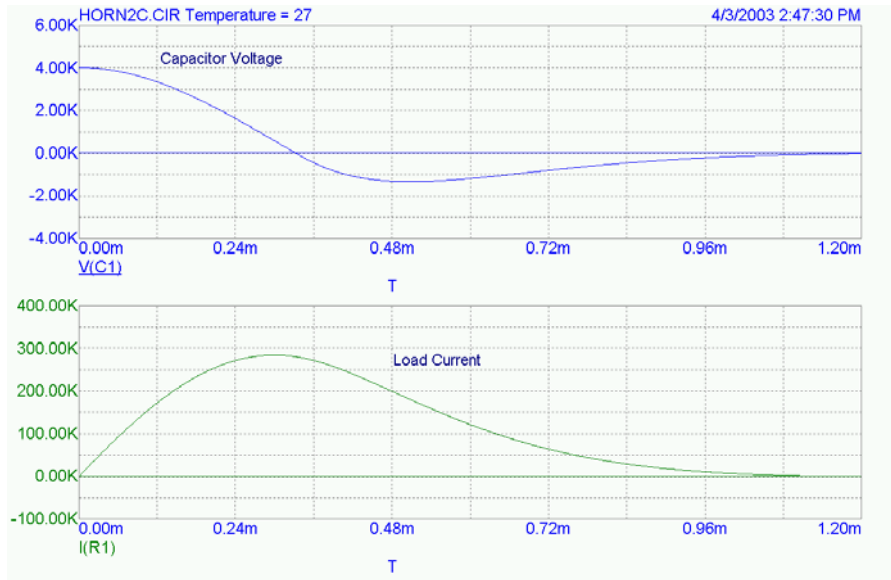
Figure 6.28: Circuit simulation with V=4000, C1=16 mF, R1= 2 m Ω, L1=2.5 μH, L2=0.1 μH, R2=7.5 mΩ.

4. Reverse Diode;

5. Transmission Line.

In this design, Self-Healing capacitors are being considered for the fault tolerance, and increased reliability. This type of capacitor is usually rated under a few kilo-volts. Multiple capacitor cells have to be used to divide capacitor bank into smaller units with lower stored energy per cell for safety concerns.

The discharge switch in favor is the light triggered thyristor. The newest in this category is the EUPEC T2563N80. The advantage of this device is its high voltage rating of 8000 V, high forward current rating of 5600 A rms, and 63 kA surge current. Multiple thyristors have to be used in parallel to carry the 250 kA pulse current.

This thyristor features light triggered gate structure. It eliminates the high voltage isolation trigger transformers normally used in conventional thyristors, and improves the high voltage hold-off and the noise immunity. Large reverse diodes are available from the same company.

The trend of new designs is to use solid-state switch, which has much longer lifetime compared to gas discharge switches. The very high current capability required in this system limits the selection to thyristor types for its high power rating per single unit and cost effectiveness.

The traditionally used ignitron is mercury vapor filled device. With rapid advancement of solid state devices, it is being replaced by thyristors. Other solid state devices, such as IGBT and MOSFET are limited by their current capability.

The transmission line being considered is similar to FERMI NuMI [43] design for its ultra low resistance.

The design options of high voltage, high current pulsed system are often limited by the industry development and available components. In this case, the preferred operating voltage is under 5 kV. The total resistance shall be kept to less than or around 2 mΩ.

6.6   Alignment Requirements and Tolerances

In order to have confidence that the flux of neutrinos is known at the far detector site the beam, target and horns must be positioned and oriented within certain tolerances. The criteria that is being used is that the worst acceptable flux variation at the far detector should be less than 5% from alignment uncertainties. There are approximately twenty parameters that can be varied in positioning the beam, the target relative to the horn, and each of the horns. Since any of these variables can be randomly misaligned any single variable would have a $1^1/_4$% rms variation. We can allow some of the parameters to exceed this $1^1/_4$% variation since other parameters would be able to come under this tolerance. Based on this a tolerance of 2.5% variation has been set for each of the variables. This criteria is less stringent than that which was used for the NuMI beam line. The NuMI criteria accepted a worst flux variation of 2% in any 1 GeV bin from 1-80 GeV. This yields an error for positioning the beam, target and horn to be 0.5 mm for NuMI. Since the BNL-Homestake wideband oscillation experiment expects to see more than one oscillation peak, it is less sensitive to a precise knowledge of the neutrino flux as the NuMI experiment is.

The PBEAM[44] program that was used for the NuMI alignment study was used to evaluate the flux at our far and near detector locations for a beam, target, and horn configuration. This program uses event weighting techniques for fast simulations allowing the generation of million event statistical samples for each configuration. The program produces $\pi^\pm$, $K^\pm$ and K^0 from the target and tracks these particles through the horn focusing system and decay tunnel. A weight is assigned for the particles produced from the meson decays corresponding to the probability that particle reaches the detector. The PBEAM program does not handle cascade decays such as the $\pi \rightarrow \mu \rightarrow \nu_e$ decay, which is an important source of the ν_e background for the lower energy BNL spectrum. The target production spectrum that is observed in PBEAM is not the same as that which comes from GEANT. PBEAM does not produce as many high energy mesons as GEANT does, however this may not be critical since the analysis looks at ratios of perturbed to unperturbed distributions. Table 6.3 shows the parameters that were used to describe the target-horn system for the alignment study. These parameters vary slightly from the current baseline values.

In the analysis each of the following variables was varied one at a time and the flux was calculated at the near and far detector positions:

- Vary x, y, θ_x, θ_y of the beam on the target.

- Vary x, y, θ_x, θ_y of the target relative to horn 1.

- Vary x, y, θ_x, θ_y of the position of the horn 1 plus target ensemble.

Table 6.3: Parameters used to describe the beam, target, and horn for the alignment analysis.

Parameter	Value
Beam Momentum	28 GeV/c
Beam rms Radial Size	1.0 mm
Target Material	Carbon
Target Density	1.7 g/cm^3
Target Length	80 cm
Target Radius	3 mm
Horn 1 Length	2.17 m
Horn 1 Inner Radius	7 mm
Horn 1 Upstream Position	0 m
Horn 2 Length	1.5 m
Horn 2 Inner Radius	32-44 cm
Horn 2 Upstream Position	8.5 m
Horn Current	250 kA

- Vary x, y, θ_x, θ_y of horn 2.

- Vary the horn current.

The ratio of the perturbed distribution to the unperturbed is calculated and fitted to a polynomial. (Fitting the distribution smoothes out the ratio). The largest variation in the distribution is used to determine the tolerance of that particular variable. Table 6.4 shows the allowable tolerances for the positioning and orientation of the beam, target and horns.

Table 6.4: Proposed positioning tolerances for the neutrino beam elements.

Variable	Proposed Tolerance
Beam Position	1.5 mm
Beam Angle	3 mr
Target Position	1 mm
Target Angle	3.7 mr
Horn 1 Position	1.7 mm
Horn 1 Angle	3.5 mr
Horn 2 Position	3.5 mm
Horn 2 Angle	7.0 mr

The target position and angle tolerances are given with respect to the position and angle of horn 1 since it is inside of it. The angle tolerances are given in milli-radians. They can be stated as tolerances of the relative position of the downstream part with respect to the

upstream part. The listed angular tolerances are consistent with (slightly larger) positioning each end of the element with the corresponding positioning tolerance.

These tolerances should be easy to achieve initially. There is a concern as to whether the neutrino beam elements will stay within these tolerances over time since the hill might settle after the alignment is made. If the positioning of the beam elements are monitored during a running period, a corrections to the determination of the flux can be made at the far detector. Active repositioning of the beam elements need not be made during a run. They can be repositioned during long shutdown periods if necessary. An optical system of measuring fiducial markers on both ends of the neutrino beam line elements during the run will be necessary.

There are several factors to consider when addressing the alignment issues on a project of this scope. The purpose of this paper is to point out these factors and ponder options available as to how one could go about solving them.

We have a good understanding of where we are on the face of the earth. In the late 1970's and early 1980's the National Geodetic Survey sent a crew of surveyors to BNL to establish control lines for the ISA project. The beam line they tied in is the same one to be used for the transport to the proposed Neutrino Super Beam. We have also tied four reference points to the HARN (High Accuracy Reference Network) while working with the NYSDOT and the National Geodetic Survey, using equipment that was purchased for ground water monitoring here at BNL. That equipment is now under the control of the Survey and Alignment Group. With upgrades to this equipment and additional observation epochs a local set of monuments will be set on and around the proposed construction for alignment purposes, these will become the primary monuments that will be observed during the building of the beam line and the be used to provide reference data to the alignment of the target, horns and transport beam equipment.

NOAA and the NGS have in place a Continuously Operating Reference Station (CORS) System throughout the United States. It is set up such that over the internet one can input data from GPS receivers and the location of that antenna will be computed and results given back to the requester in a few minutes. This is the way to pinpoint long base lines with precise knowledge at each end. The NGS should become a consultant in the planning and data reduction for these initial epochs of control work so that a clear understanding of the project goals can be met. They understand the effects of gravity, astro-geodetic deflections and the world geodetic system.

Where do we point the target and horns? Understanding where the detector is has a host of alignment issues that need to be addressed. The site, once fixed, will probably be in a mine deep beneath the surface of the earth. This will need to be defined so that one can do the necessary computations to establish the azimuth and vertical angle to place the target and horn. The Department of Geomatics Engineering from the University of Calgary performed a survey through the 710 m deep mine shaft using a HG Honeywell 2001 Inertial Navigation System for the detector location for the NuMI Project located 735 km from Fermilab.

Once a clear understanding of where we are and where we want to point the target and horns to is obtained we must provide a mechanism that will allow us to do just that. Due to

environmental issues the tunnel must initially be raised 50 m above the present tunnel height, this will require a few million cubic yards of dirt to be piled up to form the base of the tunnel. Settlement will take place and it will have to be monitored during the construction process. Every attempt to minimize the effect of settlement on the transport beam line and the target – horn enclosure should be taken seriously. Remote targets from the target – horn strong back will be brought out the top or side of the shielding so that they might be monitored for position, a minimum of four targets on each component so that roll and pitch of the object can be determined will be necessary. Jacks place beneath the strong back will be actuated to bring the targets to there ideal location. This ideal location will be established from observations on the primary monuments placed around the project site. We will also monitor the transport line by observing at least two preferably three SWIC locations. This can be done by supplying the alignment group with a vista to a pre-aligned retro reflector mounted on the SWIC's, so they it can be observed by a total station. This quick check will let us know that the beam line is OK or that it needs adjusting.

7   Conventional Construction

There are five new or modified conventional facilities needed to support the upgrade of the AGS complex for the Neutrino Super Beam.

1. A new superconducting LINAC tunnel, klystron gallery and cryogenic service building with associated mechanical and electrical utilities.

2. A new AGS motor-generator building and rectifier building with associated mechanical and electrical utilities.

3. Modifications to Building 929 to accommodate the new rf equipment associated with the AGS ring modification and expansion of the existing transformer yard to power the new AGS rf equipment.

4. Extension of the existing proton transport tunnel to a new neutrino target building including two new service buildings and mechanical and electrical utilities.

5. A new decay tunnel and relocation of the existing beam dump.

Our design approach is to:

- Model each of these facilities where possible, after a proven existing design, taking operations and serviceability into account. Value engineering will be performed as these designs matured.

- Minimize the effect on the RHIC running schedule by:

   1. Fully utilizing RHIC shutdown periods for construction.
   2. Stage the construction of the superconducting LINAC such that the connection to existing machines can be done during a single shutdown period.
   3. Install a shield wall in the existing beam transport line such that the new proton transport line can be built independently of RHIC operations.

- Minimize the environmental impact by:

   1. Construction of high radiation areas well above the water table.
   2. Integrate D&D issues in the design phase.
   3. Utilizing rainwater barriers over potential soil activation areas.
   4. Utilizing modular shielding in the target area.
   5. Integrating activated water and beam monitoring in the design.
   6. Providing controls for potential activated soils during demolition process.
   7. Maximizing the use of on-site soils.

- Control critical tolerances by:

October 8, 2004

1. Characterizing existing and imported soil parameters.

2. Maintaining stringent compaction requirements for the hill soil.

3. Requiring maximum hill settlement time before tunnel construction begins.

4. Allowing for active monitoring and re-alignment of critical components.

- Provide upgrades to existing BNL infrastructure consistent with Project needs:

  1. Providing a new BNL site power distribution.

  2. Upgrading the storm water management system.

  3. Providing new access roads.

- Meet all DOE, BNL, and Industrial design standards.

7.1 Superconducting Linac/Klystron Gallery

Description

This area consists of three major structures: the Superconducting Linac Tunnel (SCL), the Klystron Gallery, and the support building which houses the cryogenic equipment, pump room, control console and racks. The Superconducting linac tunnel connects the existing linac to the AGS ring. The klystron gallery is located above the SCL tunnel. Located midway between the SCL and klystron buildings, the support building provides access and services to both structures. The existing BLIP facility will have to be removed and the activated soil will be disposed. The area of the SCL, klystron gallery and support building are 7200 sq. ft., 23100 sq. ft., and 3600 sq. ft. respectively. Other items associated with this area include: one substation unit, roadways, a cooling tower and retaining walls. A cross section sketch of the SCL and klystron gallery is shown in Figure 7.1.

Design Basis

The present SNS superconducting linac design was used as the basis for the initial sizing of these facilities and for the determination of the required shielding. The design was modified to reflect the operational concerns and construction constraints of the AGS super beam facility.

Cost Basis

The cost estimate was developed utilizing the per unit cost method from the standard estimating guides. Costs to dispose of contaminated soil and for construction delays to match the RHIC shutdown periods were included.
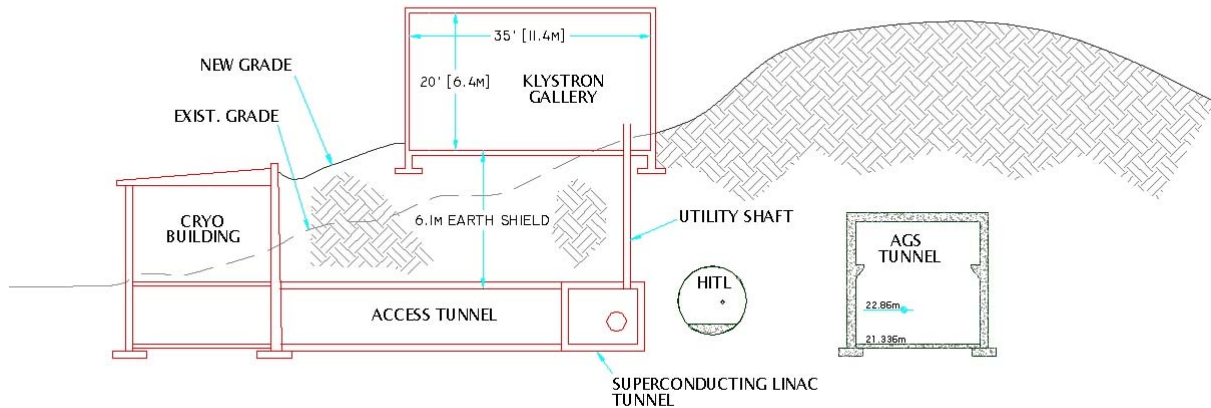
Figure 7.1: Cross section - superconducting linac, klystron gallery, cryogenic area and access tunnel

7.2   AGS Main Magnet Power Supply

Description

The new AGS main magnet power supply facility consists of the motor generator building and rectifier building plus supporting mechanical spaces. The motor-generator building houses the M-G set, provides a lay down area and a bridge crane rated for all the components. Below the M-G deck, mechanical equipment space is provided. Adjacent to the M-G room lies a rectifier room and control room. Above and below the rectifier and control rooms, mechanical equipment spaces are provided. Other items associated with this area include a substation area with multiple transformers and switching equipment, an oil retention pit for the transformer area, a cooling tower and pump system, cable trenches across roads, sleeves penetrating the AGS berm to bring the power into the AGS tunnel, and the concrete pedestal for the M-G set. Figures 7.2 and 7.3 show the plan view and cross section view of the motor generator set and power supply building.

Design Basis

The present AGS motor-generator complex was used as the design basis which was appropriately scaled for this project. Features such as a fully rated overhead crane and a roll-up access door to the building were included to enhance the inspection, maintenance and repair of the MG set.

Cost Basis

The cost estimate was developed using the per unit method from standard estimating guides along with a vendor quote for the crane. The cost also includes the substation, mechanical equipment, and provisions for the electrical distribution.
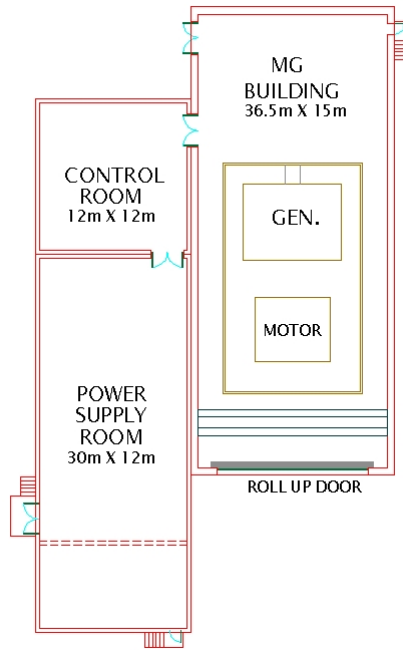
Figure 7.2: Plan view – motor-generator set and power supply Building
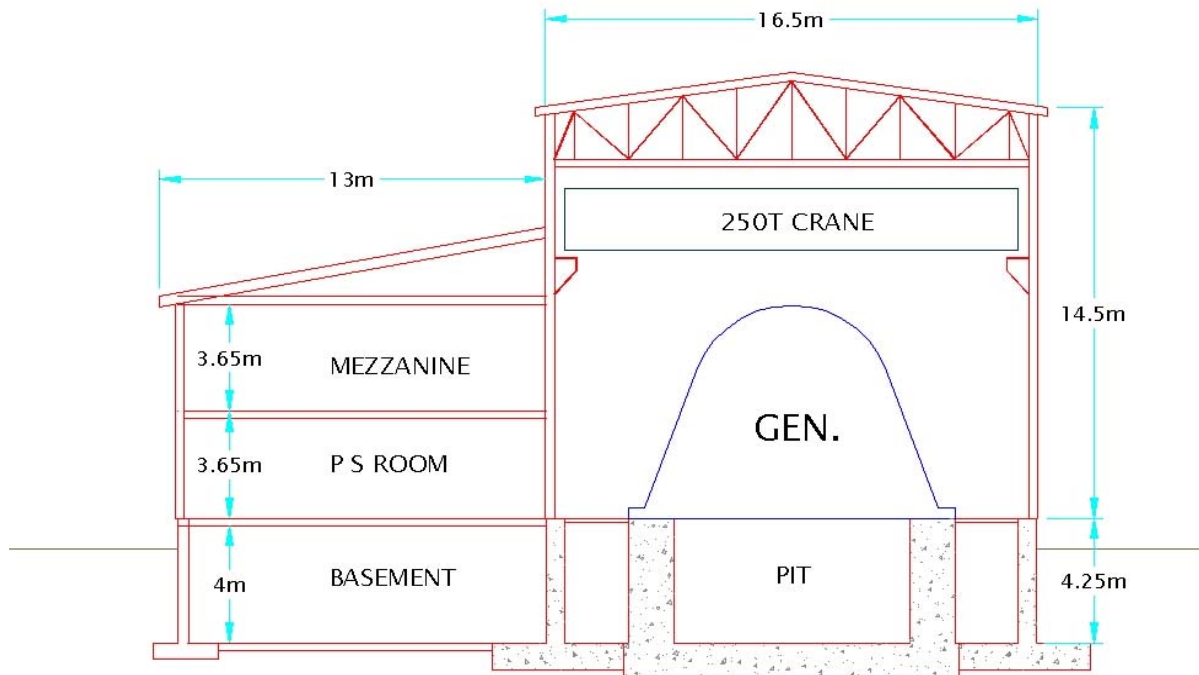
Figure 7.3: Cross section – motor-generator set and power supply Building

7.3 Building 929 Upgrade for AGS RF System

Description

The old AGS rf building is renovated for the new rf equipment providing proper air conditioning, fire protecting, etc. The area also provides an expanded transformer yard. The new rf equipment duplicates the present setup doubling the power delivered to the AGS rf equipment. Associated cable trays and trenches need to be installed to distribute the increased rf power.

Design Basis

The present rf system facilities were used for the design basis. The spacial and power requirements were doubled.

Cost Basis

The cost estimate was developed using the per unit method from the standard estimating guides. Costs were included substation mechanical equipment and provisions for the electrical distribution.

7.4 UtT Transport and Target Area

Description

The conventional construction for the extension of the existing "U" line beam transport consists of:

- Upgrading the shielding over the "U" line.

- Extending the proton beam transport tunnel approximately 300 m while increasing the beam elevation along a 50 m high hill.

- Providing two service buildings for power supplies and mechanical equipment.

- Installing a 3.5 MW cooling tower and pumping systems.

- Constructing the Target Building that houses the target, horns, horn power supply and related equipment.

The shielding over the existing "U" line will be upgraded with the addition of approximately 3 m of earth in certain areas and a waterproof liner throughout. This will bring the existing "U" line shielding up to the specifications for the new beam transport.

The beam transport tunnel will be extended approximately 300m, increasing in elevation, while bending ∼68 degrees West then down 11.3 degrees in order to match the bearing to Homestake, South Dakota. The resulting hill and beam transport arrangement, including the new and existing transport elements are illustrated in Figure 7.4.
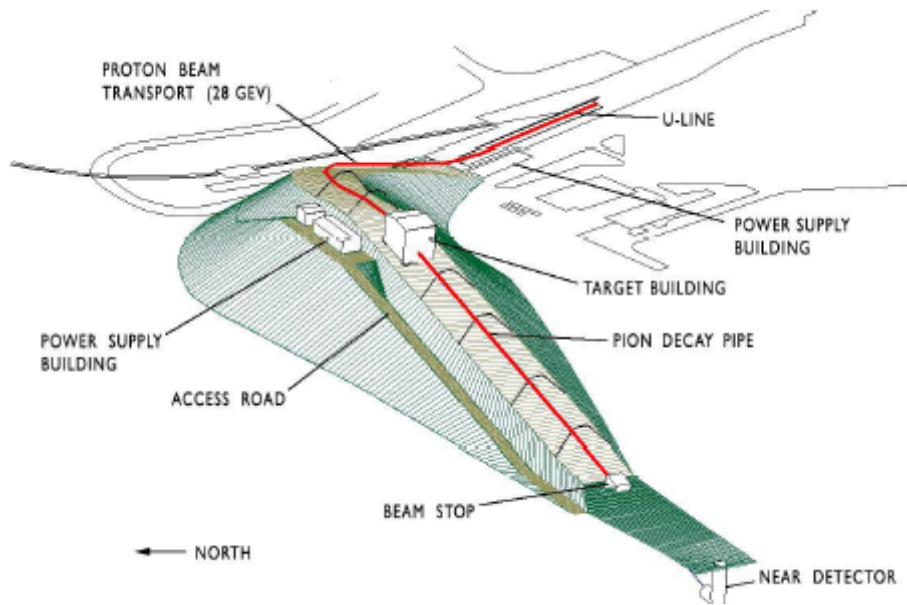
Figure 7.4: Aerial view – transport line, target building, decay tunnel and near detector

The vertical beam geometry results in a hill 50 m high at the apex of the proton beam. This geometry was chosen in order to avoid the irradiation of soil close to the Long Island water table keeping the beam dump above the water table, together with the impermeable rainwater barriers to avoid the rainwater penetration of irradiated soil, is consistent with present groundwater protection practices at BNL. A vertical profile and a cross-section of the hill is shown in Figures 7.5 and 7.6 respectively.
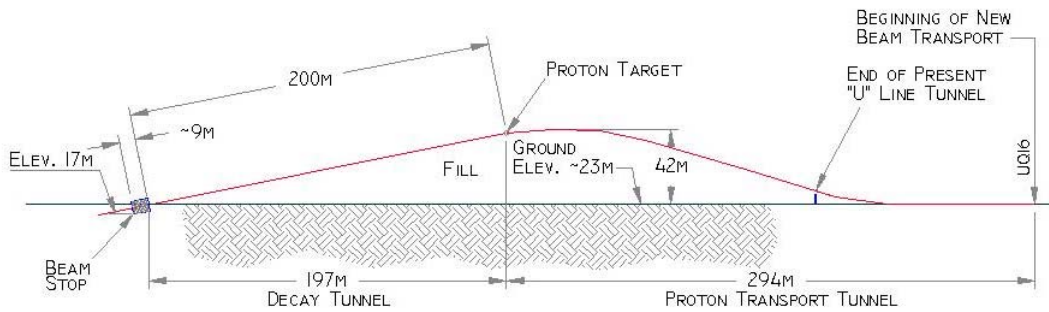
Figure 7.5: Elevation view of the neutrino beam line directed towards Homestake, South Dakota. Distance is measured along the beam path.
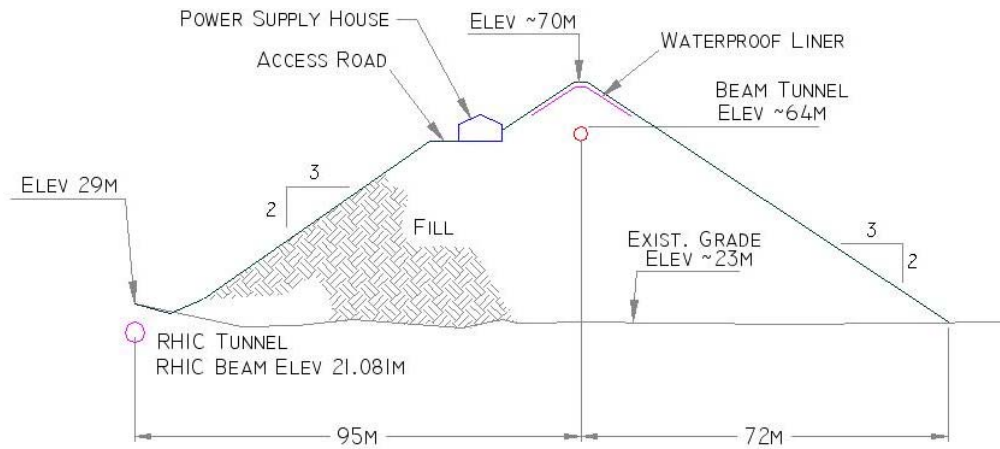
Figure 7.6: Cross section – hill and beam tunnel

The hill construction will consist of clearing the land, relocating utilities, and removing soils not meeting the required load bearing criteria. Approximately 1,400,000 cubic yards of sand fill will be placed forming the hill necessary for groundwater protection. Approximately 75% of the fill will come from new storm water recharge basins in this area.

The sand fill will be placed in 12" lifts and highly compacted in order to reduce settlement. The fill will be placed early in the project allowing it to settle for many years before re-excavaton for placement of the tunnel. Approximately 300m of 3 m diameter tunnel, overburdened with 6 m of fill, will be required for proton transport. A waterproof liners will be installed below the surface of the overburden to insure rainwater does not penetrate areas of potentially radioactive soil .

Access to the tunnel will be provided at the beginning of the vertical rise and near the target area. Equipment transport up and down the slope will be facilitated by use of a motorized railway. The access at the base of the slope will contain a shield wall that will allow RHIC running during construction of the proton transport.

Two power supply/utility buildings will be provided, one located low near the existing beam line, the other located high near the target area. These buildings will house power distribution systems, power supplies, water pumping systems, instrumentation and controls for the beam line.

The cooling water system will use a 3.5 MW cooling tower for primary heat rejection with four isolated, closed loop cooling systems for:

- All transport magnets ($\sim$2.6 MW)

- Two power supply areas ($\sim$.5 MW)

- Horn cooling ($\sim$.4 MW)

Each system will contain redundant pumps, a heat exchanger, a full flow filter and a side stream deionizer capable of maintaining the system at 2-5 megohm-cm. The system controls will be PLC based and be capable of monitoring and reacting to water leaks if they occur.

Design Basis

The hill and tunnel design are based on experience in building portions of the RHIC tunnel where the tunnel was placed on compacted fill and the settlement was both calculated and measured. The water cooling system and power supply building designs are based on the existing RHIC beam transport system with improvements gained from RHIC operation experiences, such as, air conditioning the power supply areas and tighter controls on the water system parameters.

Cost Basis

The cost was developed using the standard per unit cost for fill and experience in earth moving projects at BNL. Tunnel costs were escalated from previous tunnel construction at BNL. A conservative approach was taken with costs of construction material due to present volatility in the market.

7.5   Target Area

Description

The target facility will be a high bay building with a stepped foundation and an overhead crane of sufficient capacity to handle the largest load of approximately 50 tons. It will include the proton target, horn, horn power supply and water cooling system. A shielded storage area will be provided for radioactive component storage and repair. Modular concrete and steel shielding will provide radiation shielding. Access to the horn vault for installation and removal of the horns is accomplished by removing the modular shielding overhead. Present plans call for hanging the horns from shielded supports with the ability to survey and connect or disconnect the horns from above the shield. Figure 7.8 shows a plan view of the target building.

Design Basis

The design was based on existing high bay experimental buildings at BNL with reduced loads delivered to the soil to reduce settlement. Portable shielding was used to absorb radiation in order to reduce future D&D costs and provide flexibility in the design. The hanging shields were based on the design for many high intensity accelerator complexes, the most recent being the 1.5 MW "RTBT" line at the Spallation Neutron Source (SNS).

Cost Basis
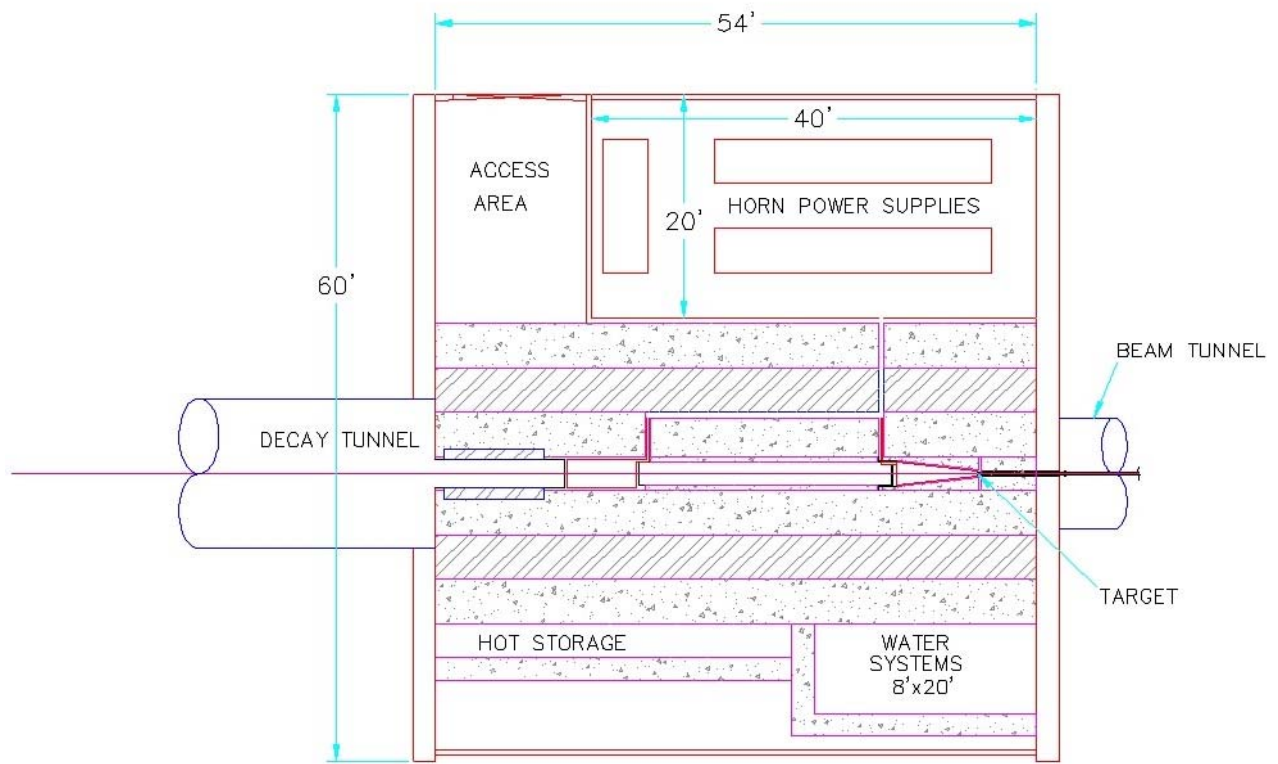
Figure 7.7: Plan view – target building

The costs were based on per unit costs from standard estimating guides and recent experience in the purchase of portable radiation shielding. The hanging shield costs were taken from the SNS shield costs.
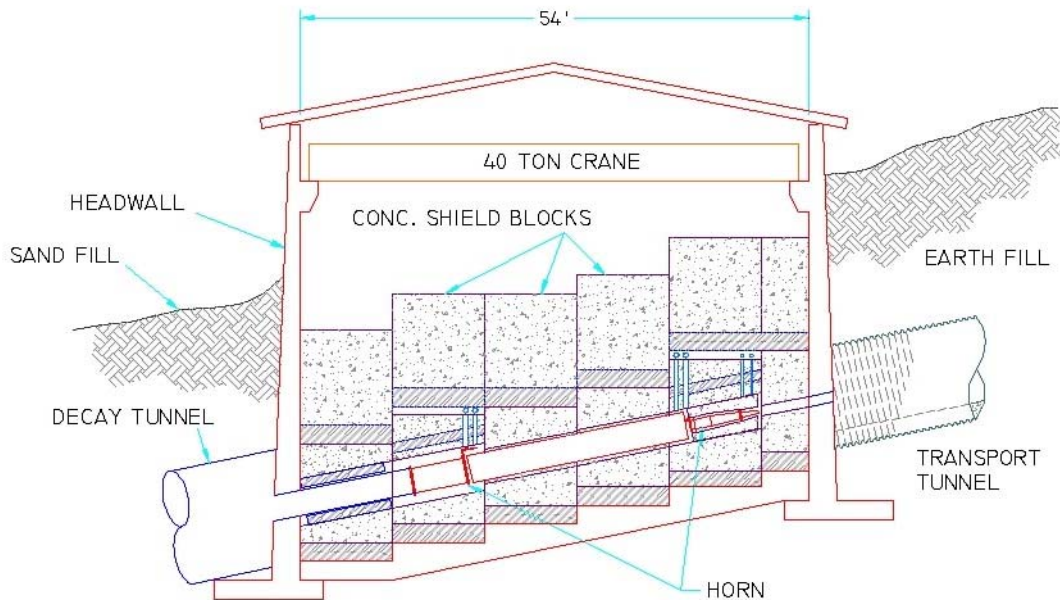
Figure 7.8: Cross section – target building

7.6　Decay Tunnel

Description

The decay tunnel will be a 4 m diameter steel tube, 185 m long, with seal and welded joints. There will be a thin window at each end and the contained volume purged with helium gas. Access to the windows is from above in the target area and at the beam stop. There will be no utilities or access to the decay tunnel between helium windows. The tunnel will be overburdened with 9 m of earth fill with a waterproof liner installed approximately 0.6 m below the surface. This will insure no rainwater can penetrate the potentially radioactive earth around the tunnel.

Design Basis
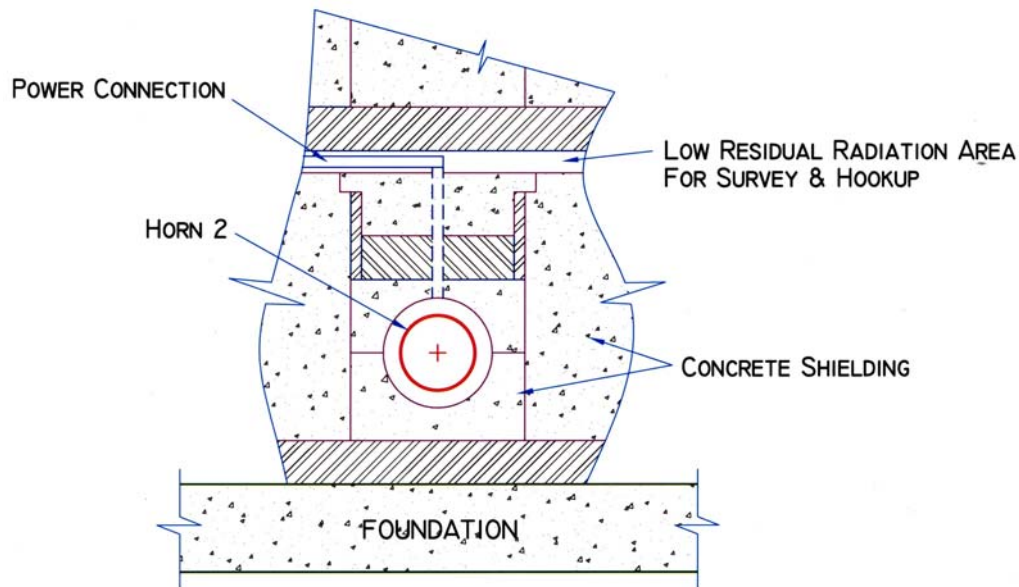
Figure 7.9: Cross section - horn and shielding

The decay tunnel design was provided by a manufacturer of underground tunnels using 3/16 rolled steel plate, structurally reinforced on the outside. The tunnel will be pre-assembled at the manufacturer and shipped in 13m lengths, with the final field assembly at BNL.

Cost Basis

The costs were provided by the manufacturer with installation costs estimated using per unit costs from estimating guides.

7.7   Beam Stop

Description

The beam stop will be approximately 9 m wide x 9 m high x 9 m long. It will have a stepped foundation to approximate the 11.3 degree vertical angle. The lowest portion of the stop will be approximately 3 m above the ground water table. The beam stop will mainly consist of existing steel plate from the decommissioned neutrino beam stop, overburdened with 4 m of soil. A waterproof liner will be placed 0.2 m below the surface of the soil to insure rainwater can not penetrate the beam stop. Access to the downstream helium window and front face of the beam stop will be provided from above. Simulations were carried out to predict the temperatures and stresses on the front face of the beam stop and the appropriate materials chosen. It is presently assumed that cooling of the upstream portion is necessary and temperature interlocks are required.

Design Basis

The present proton beam stop in the neutrino beam line was used as a design basis for this design with the appropriate scaling for beam flux distribution and intensity.

Cost Basis

Experience in moving shielding for the present RHIC experiments was used in estimating the labor costs for relocation. Concrete work was estimated using standard per unit estimating guides.

7.8   Utilities

7.8.1   Civil/Mechanical

Description

Civil / mechanical utilities include storm water management, sanitary, and potable water. These will be integrated into the existing BNL infrastructure.

Recharge basins / storm water system - The construction of the new hill will divide the present storm water system. To construct the hill, new recharge basins will need to be excavated. This will provide the necessary drainage for this portion of the site. A new capture system and piping will be required to handle the runoff from the hill.

Sanitary -new sanitary lines will be brought to the new neutrino facilities. Existing sanitary lines will be relocated to avoid interfere with the new tunnels. The majority of these interferences are located by linac and booster facilities. Some interferences may exist by the new transfer line/berm.

Potable Water - Potable water will be brought the new Neutrino facilities. Potable piping to several areas of RHIC will have to be relocated to maintain proper water supply. Areas affected include Building 1000P, Building 1008B, and the secondary source to RHIC's inner ring road piping.

Design Basis

The design is based on standard engineering practices.

Cost Basis

The estimate was developed utilizing standard per unit method from standard estimating guides.

7.8.2   Electrical

Description

To meet the increased power demand, new electrical equipment and feeds will be installed. At the 69 kV level, the tie line between the Temple Place substation and 5th Avenue substation will have to be upgraded from 77 MVA to 120 MVA. A new 20 MVA, 69 to 13.8 kV transformer (No.9), will be located in the future bay at Fifth Avenue substation. The new, associated 15

kV switchgear will be located in the existing substation house, Building 638. A new overhead line will be installed to bring the power from Fifth Avenue Substation, Building 638 to the new unit substations located near the new Target Building, the beginning of the beam transport tunnel and the superconducting linac / klystron gallery. A new, 13.8 kV, underground feeder needs to be installed from Temple Place Substation to the new motor-generator substation. Several existing 2.4 kV feeders in the vicinity of the new superconducting linac will have to be relocated. 13.8 kV feeders located near building 1000P and the new motor-generator will have to be relocated. Communications ductbanks will be provided to the various areas. Table 7.1 shows the preliminary apparent power requirements.

Table 7.1: Preliminary power requirements

Location	Conventional Power (kVA)	Experimental Power (kVA)	Total Power (kVA)
Superconducting Linac	550	8000	8550
AGS MMPS	650	6300	6950
RF Upgrade	275	3000	3275
Lower Power House	150	2150	2300
Upper Power House	150	2450	2600
Total Power (kVA)	1775	21,900	23,675

Design Basis

The design is based on standard engineering practices.

Cost basis

The estimate was developed utilizing standard per unit method from standard estimating guides.

7.9 Radiation Shielding

The conceptual shielding design for the Super Neutrino Beam meets the necessary standards for radiation protection and provides a basis for the initial cost estimates for the project. The design has been developed using existing reports, calculations, and simple analytical techniques to scale to the proposed facilities for the proton transport, target station, decay tunnel, and beam stop. More detailed modeling will be conducted when the design of the various components is more mature. The shielding has been designed to:

- Meet standards for chronic exposure to people at the adjacent areas and off-site.

- Prevent contamination of the ground water.

- Reduce direct exposure sufficiently so that personnel can service equipment at the facility during beam operations.

A brief description of the methods and assumptions used will be given in this section.

7.9.1 Source Terms

The shielding design requires estimations of the source terms and their locations. Logically, the Super Neutrino Beam breaks into four simple areas, proton transport from the AGS to the target station, target station, decay tunnel, and the beam stop. The proton beam transport is expected to have an integrated loss of 0.1% with less than 0.03% lost in any one location. The target station has been designed assuming 100% of the beam interacts in the target. It is assumed that no beam interacts with the helium in the decay tunnel. In reality, approximately 1% of the incident beam will survive the target and interact in the helium. 20% of the beam will survive the target and strike the beam dump.

An MCNPX calculation by A. Stevens [45] has been used to estimate the initial radiation pattern in the near shield. The calculation assumed that the 25 GeV proton beam struck an iron target 1 m long and 3 cm in radius. This target was placed in a tunnel with a 1.5 m radius and surrounded by soil. The initial radiation pattern has then been compared to the analytical techniques of Tesch[46] and discussed by A.H. Sullivan[47]. The analytical formulas compare well to the MCNPX results overestimating the dose by 2.4. The formulas provide a simple method to estimate the transverse shielding. This method was used for the beam transport, target station, and decay tunnel. The results from the MCNPX simulations for the proton beam on the carbon-carbon target [48] was extrapolated using the same formulas.

The beam stop was designed by using an existing design[49] of a 29 GeV beam dump in the AGS slow beam area. Analytical techniques were then used to extrapolated were necessary.

7.9.2 Ground Water Protection

The interaction of high-energy protons will create radioactive products in the surrounding shield. It is important that these radioactive products are not transported to the water table. The BNL standard[50] requires that the design of this facility prevent radioactive products in the groundwater from exceeding 5% of the drinking water standard. The use

of modular concrete and steel shielding for the entire project is cost prohibitive. Most of the facility will have an earthen shield. Modular shielding will be used at the locations of highest loss and when possible to reduce the amount of radioactive products created in the surrounding soil. The design standard allows for the use of approved capping materials to prevent created radioactive products from being transported by rainwater to the water table. Caps constructed of geomembranes or concrete will be used to meet the BNL standard for groundwater protection.

^{22}Na is the radioactive isotope that will determine the design of the cap which protects the groundwater. Based on the transport model used in the BNL standard, the cap must prevent rainwater from leaching the soil where the amount created ^{22}Na in a year exceeds 1.05×10^6 ^{22}Na atoms/cc. This corresponds to a neutron flux (E$\geq$20 MeV) of 9.4×10^{-13} neutrons/cm^2 per incident proton.

It is assumed that the proton transport has a maximum local chronic loss of 0.03% of the beam. The membrane has been placed at 5.5 m from the tunnel wall giving a factor of 5 more reduction than required by the standard. The membrane is covered with 0.6 m of earth.

It is assumed that 100% of the beam interacts at the target station. If it were sited inside a tunnel shielded by dirt the liner would need to be greater than 9 m from the target. The total amount of activation in the soil would be substantial. It was decided that the target area should have the shield constructed from modular steel and concrete blocks. The target area shield will have a thickness equivalent to 0.6 m of steel and 4.3 m of heavy concrete. The target area will be inside a building. The concrete floor will prevent rainwater from leaching activation products from the soil underneath the target station. The roof of the target building will prevent rainwater from entering the concrete and steel shielding. Additional shielding will be placed underneath the target and horns to reduce the activation of soil underneath the concrete floor.

The decay tunnel has been designed with the membrane 8.5 m from the tunnel wall. The membrane will have 0.6 m of soil overburden. At this stage of the design it was decide to be conservative in the estimate for the decay region. It is expected when the final design of the target area is complete that the membrane can be closer to the tunnel and the berm thickness can be decreased.

The beam dump is constructed from plates of steel. The dimensions of the steel were chosen to reduce the neutron flux sufficiently such that the activation of the soil in contact with the edges of the steel satisfies the BNL standard. The iron beam dump has a radius of 9 m and a length of 9.2 m. The concentration of ^{22}Na at the back of the steel is 0.004 of the standard with 100% of the beam striking the beam dump. The water cap for the decay tunnel will be extended over the beam dump. This is necessary to prevent water from percolating through the beam dump.

There are four monitoring wells planned for the Super Neutrino Beam area. The beam dump, decay tunnel, target station, and proton transport will each have an appropriately sited monitoring well. In addition, existing wells will monitor the portion of the proton transport, which is close to the AGS.

7.9.3   Sky Shine

Dose to adjacent facilities can occur due to leakage of neutrons through the shielding. The dose to people in the adjacent facilities is calculated using the sky shine formulation discussed by A.H. Sullivan[47]. The exposure at a location more than 100 m from the source is given by:

$$H = 70(H_0 A) \exp(-R/600)/(R^2), \tag{7.1}$$

where H is the dose rate in mrem/hr, $H_0 A$ is the integrated dose through the berm in rem-m^2 per hour, and R is the distance from the source to the occupied location in meters.

The limits are established by integrating the exposure over a year of operation. In addition occupancy factors can be used were appropriate. Five locations were examined for the yearly exposure from the super neutrino beam. The assumptions on occupancy and exposure limits are given in the Table 7.2

Table 7.2: Occupancy and exposure limits.

Location	Occupancy hours/week	Occupancy per work hour	Facility limit mrem/yr
Off-Site	168	1	5
Linac	40	1	100
Blip	40	0.25	25
BAF	40	0.25	25
Bldg. 1005	40	1	25
Bldg. 1006	40	1	100
Bldg. 1008	40	1	100

Based on these occupancy assumptions the exposure limit for off-site is the most stringent for all loss locations except the transport tunnel. Bldg. 1006 sets the upper limit for losses in the transport line due to its close proximity. The total potential dose to off-site is 0.2 mrem/yr. The potential dose to personnel in Bldg. 1006 is 4 mrem/yr.

7.9.4   Direct Exposure

Dose rates external to the shielding will typically be less than a few mrem/hr under normal operating conditions. The highest localized dose rates occur at the target building and are less than 60 mrem/hr . Barriers, postings and procedures will control access to the shielding. Abnormal operating conditions can cause substantial increases in the dose rates. Elements, which can cause abnormal conditions, will be monitored and a fast beam interrupt will limit the duration of the abnormal condition. Radiation detectors will be distributed along the facility to prevent personnel exposure and limit fault conditions. A dual PLC based access control system will prevent access to the transport tunnel, except under allowed conditions.

8 ESSH

8.1 Purpose of the ESHQ Chapter

The purpose of this chapter is to briefly describe the rigorous safety and environmental protection activities associated with the Super Neutrino Project that will be completed prior to commencement of construction, commissioning and operations.

8.2 Review of ESH Issues Associated with the Conceptual Design

The Super Neutrino project requires the construction of a super-conducting linac, an upgraded motor-generator set for the AGS, modifications to the AGS Ring shielding and rainwater-barriers, a new transport line off the existing U-line, a new target hall, a pion-decay region, and two new power supply buildings. Additionally, construction of a 50-m high hill and relocation of existing utilities and roads are planned.

The proposed location of the super-conducting linac (SCL) on the BNL site is at the end of the existing 200 MeV linac. The beam will leave the existing Linac at the energy of 200 MeV and, after a bend of 17.5 degrees, will enter a new 130 m long tunnel where the SCL is located, and will join the AGS ring at the location of magnet C01. The location of the SCL is within a zone of previously disturbed land. In order to protect groundwater from activated soil a waterproof liner will be installed approximately 0.6 m below the surface, and extend several meters on each side of the SCL.

Although the average power will not be higher than currently used, the peak power required is approximately 110 MW, exceeding the 50 MW rating of the existing Siemens motor generator. A new motor generator capable of providing 100 MW will be installed.

While the average power of the AGS ring will increase, routine proton beam loss will be maintained at the existing levels because of improvements in beam control. The 1 MW upgrades of the AGS will require the C-A Department to reduce the fractional beam losses by the same amount as the beam power is increased. The beam losses will be reduced by about a factor of ten ($\sim 10\%$ to $\sim 1\%$). Thus only a modest increase of shielding for the AGS is required and more important the activation of the AGS is kept at the present level, which allows for hands on maintenance. Some shielding may be added near hatches and the fan houses to minimize fault levels of radiation. If there is an incident the beam will also be shut-off within one pulse, which will be ten times faster than present capability. The maximum dose oduring a failure under the newer capability is about the same as today. This requires new chipmunk area radiation monitors to be installed.

In order to protect groundwater from activated soil, a waterproof liner will be installed approximately 0.6 m below the surface, and extend about 9 m on each side of the AGS ring.

The proton beam will be extracted from the AGS and will use part of the RHIC beam transport line before exiting the decommissioned neutrino beam-line tunnel in a northerly direction and at an upward angle of approximately 13.8 degrees. The beam will bend towards

the west by approximately 68.5 degrees, then down a total of 25.1 degrees to the proton target. The only major new radiation source will be at the target-horn station and appropriate shielding will be employed at that location.

A large flux of secondary particles, pions and kaons, will be created in the collision of extracted proton beam with the carbon-carbon target. A magnetic horn is used to focus these secondary particles. The horn is a coaxial magnetic lens which has high angular and momentum acceptance. After creation and focusing, the pions will decay in flight to a neutrino and to a muon. A 200-m pion-decay region will follow the target with the residual secondary beam entering the beam stop at 11.26 degrees to the horizontal. The on-site near detector facility, which detects neutrinos, will be located 285 m from the target, 21 m below ground level. It is noted that neutrinos interact weakly with matter and will not activate the ground or the groundwater.

The long decay tunnel and the steep incline results in a hill 50 m high at its apex. This geometry provides for the neutrino beam's 11.3-degree entry into the earth and avoids the potential irradiation of soil by stray protons or neutrons close to the Long Island water table. An impermeable rain-water barrier will be installed to prevent rain-water penetration of potentially irradiated soil, which is consistent with present ground-water protection practices at BNL.

Existing utilities and roads will be relocated and approximately 726,350 cubic meters of sand will be required to form the hill. The sand fill will be placed in 0.3 m lifts and compacted to 98% of its maximum density. The fill will be placed early in the project allowing it to settle for several years before re-excavation for placement of the tunnel. Approximately 330 m of 3-m diameter tunnel, overburdened with at least 6.0 m of fill will be required for proton transport. The impermeable rain-water barrier will be installed 0.6 m below the surface of the overburden.

Two power supply/utility buildings will be provided, one located near the existing beam line, the other located near the target area. These buildings will house power distribution systems, power supplies, water pumping systems, instrumentation and controls for the beam line. These are similar to the power supply/utility buildings already in use at the Collider-Accelerator complex.

In general, electrical power will be distributed around the site at 13.8 kV. Substations units will transform the power into convenient voltages, typically 480 and 208/120 volts. Electrical power is divided into two major categories: conventional and experimental. Conventional power encompasses building power for lighting and convenience power for heating, ventilation, air conditioning, and miscellaneous equipment. Although there are no safety critical power needs, emergency power will be provided as required for smooth operations. Experimental power feeds all the power supplies for magnets and associated equipment such as cooling-water pumps and cooling towers. All electric power distribution designs will follow the requirements of the National Electrical Code and industry standards.

The cooling water system will use a 3.5 MW cooling tower for primary heat rejection with four isolated, closed loop cooling systems for:

- All transport magnets

- Two power supply areas

• Horn cooling

Each system will contain redundant pumps, a heat exchanger, a full-flow filter and a side-stream deionizer. The system controls will be PLC based and be capable of monitoring and reacting to water leaks if they occur. All tritiated water systems will be in compliance with Suffolk County Article 12 requirements. Groundwater monitoring wells will be provided to insure compliance with all Local, State and Federal ground water protection requirements.

The target area will include the proton target, horns, horn power-supply and water-cooling system. A shielded storage area will be provided for radioactive component storage and repair. Modular concrete and steel shielding will provide radiation shielding. Access to the horn vault for installation and removal of the horns will be accomplished by removing the modular shielding. Present plans call for hanging the horns from shielded supports with the ability to survey and connect or disconnect the horns from above the shield in a relatively low residual-radiation environment. The design of this area, as well as all areas, will incorporate the as-low-as-reasonably-achievable (ALARA) radiation protection principles. A collimator downstream of horn #2, will be installed to intercept a portion of the off-axis beam that would otherwise interact in the soil along the decay tunnel.

The decay tunnel will be a 4-m diameter steel tube that is 185-m long with seal welded joints. There will be a thin helium window at the downstream end of horn #2 and a helium window at the upstream end of the beam stop. The contained volume will be purged with helium gas. The beam is designed so that it will not interact with air to create airborne radioactivity. Access to the upstream window will be provided through the target area. There will be no utilities or access to the decay tunnel between helium windows. The tunnel will be overburdened with 9 m of earth fill with a waterproof liner installed approximately 0.6 m below the surface, extending 9 m on each side of the tunnel. This liner will prevent groundwater contamination since some soil will be activated by beam.

The beam stop will be approximately 7-m wide, 7-m high and 9-m long. It will have a stepped foundation to approximate the 11.3-degree downward angle. The lowest portion of the beam stop will be approximately 3 m above the ground water table. The stop will consist mainly of existing steel plate from the decommissioned neutrino beam line that was built at the AGS in the 1960's, and it will be overburdened with 4 m of soil. A waterproof liner will be placed 0.6 m below the surface of the soil to prevent rainwater from penetrating the beam stop area.

The shielding policy for AGS Super Neutrino Beam Facility is the same as that for the rest of the Collider-Accelerator facilities since the accelerator, beam-line, target and support buildings are to be the responsibility of the Department. Specifically, the Collider-Accelerator Department's Radiation Safety Committee will review facility-shielding configurations to assure that the shielding has been designed to:

• Prevent contamination of the ground water

• Limit annual site-boundary dose equivalent to less than 5 mrem

• Limit annual on-site dose equivalent to inadvertently exposed people in non-Collider-Accelerator Department facilities to less than 25 mrem

- Limit dose equivalent to any area where access is not controlled to less than 20 mrem during a fault event

- Limit the dose equivalent rate to radiation-workers in continuously occupied locations to ALARA but in no case would it be greater than 0.5 mrem in one hour or 20 mrem in one week

- Limit the annual dose equivalent to radiation workers where occupancy is not continuous to ALARA, but in no case would it exceed 1000 mrem.

In addition to review and approval by the Radiation Safety Committee, final shield drawings must be approved by the Radiation Safety Committee Chair or the ESHQ Associate Chair. Shield drawings are verified by comparing the drawing to the actual configuration. Radiation surveys and fault studies are conducted after the shield has been constructed in order to verify the adequacy of the shield configuration. The fault study methodology that is used to verify the adequacy of shielding is proscribed and controlled by Collider-Accelerator Department procedures.

Significant environmental aspects of the Super Neutrino Project project include:

- Wetlands

- Sole Source Aquifer

- Excavation

- Chemical Storage/Use

- Liquid Effluent

- Hazardous Waste

- Radioactive Waste

- Radiation Exposures

- New or Modified Federal/State Permits

- Public Controversy

While the proposed action would not have a direct affect on wetlands, portions of the area of effect would be within one-half mile of New York State designated freshwater wetlands. Therefore, BNL would submit an application for permit under the Wild, Scenic and Recreational River Systems Act to the New York State Department of Environmental Conservation (NYSDEC).

Although BNL is situated over a Sole Source Aquifer, operation of these accelerator facilities should not affect the aquifer. This would include discharges to the BNL sanitary and storm water systems. The BNL Standards Based Management System Subject Area "Liquid Effluents" provides requirements related to discharges. Work planning, experimental review,

and Tier I safety inspections are three examples of several methods used to ensure hazardous effluents would not make their way into the sanitary waste-stream or storm-water discharges.

Excavation would be required to install the new buildings and the new piping associated with SCL, the proton transport tunnel, target area, decay tunnel, detector and cooling tower. Excavation would be limited to the area immediately adjacent to the buildings and the piping route. Standard construction techniques, such as silt-fences and/or straw-bales, would be used to control runoff during excavation. Excavated areas associated with piping would be backfilled and returned to grade.

Routine operation and maintenance actions associated with the accelerator facilities would involve the use of chemicals or compounds, generally in small quantities. BNL's Chemical Management System would track the quantity, location, owner and storage of any chemical inventory.

Any discharges associated with the proposed action, including cooling-tower effluent, would be managed according to the BNL Standards Based Management System Subject Area "Liquid Effluents".

Routine operation and maintenance actions associated with the accelerator facilities would result in a small amount of hazardous wastes being generated, primarily cleaning compounds. The total volume generated would not be expected to exceed a few tens of cubic feet per year and would not constitute a significant increase to Collider-Accelerator Department total estimates. All hazardous wastes would be managed in accordance with established BNL procedures and subject areas. Work planning, experimental review, and Tier I safety inspections are three examples of several methods for ensuring wastes are minimized and controlled.

Routine operation and maintenance actions associated with the accelerator facility would result in a moderate amount of radioactive waste being generated. The total volume generated would not be expected to exceed a few hundred cubic feet per year and would not constitute a significant increase to Collider-Accelerator Department total estimates. All radioactive wastes would be managed in accordance with established BNL procedures and subject areas. Work planning, experimental review, and Tier I safety inspections are three examples of several methods for ensuring wastes are minimized and controlled.

Routine operation and maintenance actions associated with the accelerator facilities would result in low-level radiation exposures to workers. Interlocks, access controls, training and procedure administration would be used to minimize exposures and employ ALARA principles.

Because portions of the affected area are within the one-half mile corridor of the Peconic River and are proximate to wetlands, BNL would submit to the New York State Department of Environmental Conservation an application for permit under the Wild, Scenic and Recreational River Systems Act. Depending on the disposition of the cooling-tower's discharge, the existing New York State Pollutant Discharge Elimination System (SPDES) permit would be revised as necessary. The proposed cooling system for the beam line would be a closed-loop de-ionized water system using ion exchange beds that would be removed for regeneration or disposal by a contractor off-site. At the proposed beam currents and energies induced activity would be expected in the cooling water that is used in closed-looped systems. This water would be collected and handled according to approved waste practices. Discharge of radioactive water or contaminants to the ground or to the sanitary system would be neither planned nor expected from the cooling systems. The closed-loop cooling system would be connected

to a cooling tower via a heat exchanger. Cooling-tower waters would be treated either with ozone or with biocides and rust inhibitors, and would meet all SPDES effluent limits.

Several issues may be controversial and include: 1) the potential to contaminate groundwater, 2) the visual impact of the proton beam line and target hill, 3) sky-shine radiation and 4) the underground off-site neutrino beam. In order to ensure activated soil shielding is protected from rainwater, impermeable caps will be installed over the low energy linac, superconducting linac, AGS ring, proton beam-line, decay tunnel and beam stop. Groundwater monitoring of the affected areas will be performed to ensure the integrity of the caps. In order to lessen the visual impact of the hill, the area will be re-vegetated as soon as practicable. Sky-shine radiation from the target area at the top of the hill, which may extend about 1000 m if unabated, will be greatly reduced by applying appropriately thick shielding over the target. The fourth issue, which is the creation of an underground offsite neutrino beam, will require a campaign to educate stakeholders and the nearby community about the neutrino and its infrequent interaction with matter.

8.3   ESHQ Plans for Construction

All requests for goods or services will be processed through a formal and well-documented system of review to incorporate any special environmental, safety and health (ES&H) requirements of the contractor or vendor. BNL will review the proposed contract scope of work using **Work Planning and Control for Experiments and Operations** Subject Area. The drawings for the Super Neutrino Project will be sent to the BNL's Safety and Health Services Division for review by the appropriate ES&H disciplines.

C-AD will define the scope of work with sufficient detail to provide reviewers and support personnel with a clear understanding of what is needed, expected, and required. This will include the type of work to be performed, location of work, defined contract limit lines, allowed access routes, and any sensitive or vulnerable Laboratory operations or infrastructure that may be impacted by this work.

The C-AD will ensure that facility hazards are characterized and inventoried specific to the expected location and activities.

The C-AD will ensure that minimum ES&H competency requirements for contractors are detailed and provided to the Procurement & Property Management Division (PPM). PPM will include those requirements in the bid and contract documents to qualify contractors for award. Competency requirements will be consistent with the project, facility and job to be performed.

Candidates for contract award will be required to submit the following:

Comprehensive Corporate Environmental, Safety and Health Program - Candidates for contract award must submit an acceptable Corporate Health and Safety Program to be considered for award. This program must be sufficiently detailed to clearly define ES&H responsibility, accountability, and authority of the company's employees for the intended work to be performed and the hazards to be encountered. They should include: Policy Statement, Personnel Duties (Inspection, Reporting, Accident/Incident Investigation, and Enforcement) Training, and Communication.

Performance History - Injury/Illness reports for the previous three years (OSHA 200 logs, or Insurance C-2 loss runs), Experience Modification Rates (EMR), Incidence Rates, and Days Away, Restricted and Transferred (DART) must be submitted in order to be considered for award. EMR, Incidence Rate, and DART Days must be equal to or better than industry average for award consideration. Exceptions may be allowed where candidates can prove that the causes of the higher than average rates have been, and will be rectified. Environmental compliance record for the latest 5-year period must be submitted.

Complex or Hazardous Activities - For projects involving complex or hazardous activities, submission of equivalent project experience, hazard-specific management programs, resumes and related work histories of field and supervisory personnel will be required. Examples of complex or hazardous activities include: Work in radiological areas, radiological construction work, working at heights, hoisting and rigging operations, excavation, working in confined spaces, exposure to sources of hazardous energy, exposure to vehicular movement, exposure to hazardous materials, demolition, or site clearing. In addition, copies of any required certifications, registrations or applicable County, State, or Federal Permits must be submitted. Examples include hazardous waste operations, asbestos, lead, and dewatering permits.

Administration - Personnel responsibilities will include the obligation to obey the safe working practices for their trade, the frequency and scope of inspections for deficiencies, corrective actions to be taken, reporting of accidents, injuries, near-misses, spills, and leaks.

Enforcement, Reporting, and Evaluation - Corrective action will be clearly defined with abatement and punitive actions outlined. The reporting and record-keeping process will be outlined with specific responsibilities for notifying owner, contractor, and regulatory personnel, documenting the deficiency and its abatement. A process for periodic evaluation and improvement of the program shall be included in the Corporate Safety Program.

Project Environmental Safety and Health Plan - The Contractor will be required to submit a project safety plan that complies with the requirements of the Federal Acquisition Regulations, BNL SBMS Requirements and 29 CFR 1926 Safety and Health Regulations for Construction. The plan will address the following:

- A Contractor/Vendor employee or designee shall be identified in writing as having responsibility for safety and health compliance at the project site.

- A Contractor/Vendor employee or designee shall be identified in writing as having responsibility for safety and health compliance over a particular hazardous activity.

- In addition to the Corporate ES&H Program requirements, specific hazard prevention and control programs will be included in the plan for routine, complex, and hazardous activities.

- Prime contractors shall award subcontracts based upon the evaluation criteria used to award prime contracts. Subcontractors shall comply with the Prime contractor's safety program, unless their own is more stringent.

- The plan will describe a process for ensuring that each employee entering the worksite receives initial worksite safety and health orientation and continued safety and health

training addressing the hazards associated with the work and the measures necessary to control or eliminate the hazards. Weekly "Tool Box" safety and health training will be conducted and documented for the duration of the project.

- A process for documenting accidents, injuries, illnesses, near-misses, and inspection results will be clearly outlined.

- Safe working practices shall be outlined for the hazards to be encountered. Punitive consequences for failure to follow safe working practices shall be commensurate with the severity of the violation, and shall include dismissal for serious or repeat violations.

- A written program including a company policy statement, prohibited activities, supervisor and employee responsibilities, enforcement actions, consequences for violations, on-going drug free awareness training, intervention procedures, employee assistance options.

- A list of BNL-specific permits, permissions, requirements, and instructions that are to be supplied to the contractor by BNL or its representative will be included in the plan.

The C-AD will ensure only authorized contractor personnel are allowed on the Laboratory property to perform work under the terms of their contract. They shall carry current BNL issued gate passes, identification badges, or be escorted by an authorized Laboratory employee. To obtain access, contractor employees must have received BNL site-specific training or be assigned an escort.

Materials to be disposed-of, recycled or otherwise reused either on or off-site, shall pass through the vehicle radiation monitor in the presence of a Radiological Control Technician or equivalent.

Job sites will be inspected with sufficient frequency to accurately assess compliance with ES&H obligations, and to identify any weaknesses in the contractor's ES&H management of the site. Violations of ES&H requirements shall be cause for a work interruption on that portion of the work, and may be grounds for a Stop Work Order for the entire project. Inspections will be documented.

The C-AD will make periodic inspections to verify project ES&H performance is consistent with contractual obligations. The frequency of inspections shall be adequate to represent the effectiveness of the contractor's ability to manage the job safely.

During periods of active construction, the contractor will be required to conduct daily inspection of the worksite to identify hazards and instances of noncompliance with project ES&H requirements. Records will be kept of all daily inspections. Records will be kept of hazards and the corrective actions taken.

Imminent danger, or failure to adequately correct identified safety deficiencies in a timely manner will be cause for a Stop Work Order to be issued on part or the entire project. The Stop Work Order can only be lifted when the contractor has prevented or controlled the identified hazards, and corrected the ES&H management system deficiencies that allowed them to occur.

All accidents, injuries, illnesses, environmental hazards, imminent danger, and near-misses will be reported to the appropriate BNL authority immediately. Investigation and reporting will be in compliance with BNL SBMS requirements.

Fire, accidents involving injury, illness or property damage, injury or illness of unknown origin, any quantity of pollutant dropped anywhere, the suspicion or discovery of munitions will require immediate notification of BNL Emergency Services (x911).

Contractor employees will be required to maintain current permits for the activities being performed at the jobsite.

ES&H performance data will be collected during each phase of the project and summarized at the end. Data shall rank the seriousness of the violations, the responsiveness of the contractor, and the effectiveness of the contractors ES&H management system. The C-AD will forward this data to the Procurement & Property Management Division on a timely basis throughout the project life, and at project closeout. The Procurement & Property Management Division uses this data to qualify organizations for award of future contracts.

8.4 ESHQ Plans for Commissioning, Operations and Decommissioning

The Collider-Accelerator Department (C-AD) will identify hazards and associated on-site and off-site impacts to the workers, the public and the environment from the Super Neutrino Project facilities for both normal operations and credible accidents. Although C-AD will not list and describe every hazard at the Super Neutrino Project facilities, sufficient detail will be provided to ensure that C-AD has performed a comprehensive hazard and risk analysis. The amount of descriptive material and analysis will be related to both the complexity of the facility and the nature and magnitude of the hazards. In addition, C-AD will provide an understanding of radiation risks to the workers, the public and the environment.

The C-AD will provide appropriate documentation and detailed description of engineered controls, such as interlocks and physical barriers, and administrative measures, such as training, taken to eliminate, control or mitigate hazards from operation. We will demonstrate that controls are sufficient to satisfy requirements and manage identified conditions associated with hazards. C-AD will document the methods used to mitigate the hazards to the extent prescribed by applicable requirements, codes or consensus standards.

The C-AD will describe the Department management organization, and the function and location of each Super Neutrino Project facility in addition to details of major components and their operation. The descriptions will be of sufficient depth and breadth that a reviewer familiar with accelerator operations but unfamiliar with a particular Super Neutrino Project site can readily identify potential hazards and populations or environments at risk.

The ESHQ analysis will address the hazards of the entire system of facilities within the purview of the Super Neutrino Project operations. It will cover facilities such as injectors, accelerators, experimental halls, experiments and their associated targets.

The ESHQ analysis will follow the generally accepted principles that include:

1. A description of the function of the integrated the Super Neutrino Project facilities and

the protection afforded the public and worker's health and safety, and the protection of the environment.

2. An overview of the results and conclusions of the ESHQ analysis including a description of the comprehensiveness of the safety analysis and appropriateness of Accelerator Safety Envelope.

3. A review of the land, water, air and wildlife environment within which the Super Neutrino Project facilities operate, individual facility characteristics that are safety-related and the methods to be used to operate the accelerators, the beam-lines and the experiments. The following items will be addressed:

   - Site geography, seismology, meteorology, hydrology, demography and adjacent facilities that may affect or may be affected by the Super Neutrino Project
   - Design criteria and as-built characteristics for components with safety-significant functions
   - Features that minimize the presence of hazardous environments such as those that ensure radiation exposures are kept ALARA during operation and maintenance
   - BNL and C-AD organizational and management structures and a delineation of responsibilities for safety, health and environmental protection
   - The function of engineered and administrative controls both for routine operation and for emergency conditions
   - Critical operational procedures to prevent or mitigate accidents
   - Design criteria and characteristics of experimental equipment, systems and components having safety-significant functions

4. The safety analysis, including the systematic methods used to identify and mitigate hazards and risks, will be documented. Hazardous materials, energy sources and potential sources of environmental pollution including radiological hazards will be characterized and quantified. Coupled with the identification of hazards will be a description of the controls that are employed for their mitigation. The description of controls will include discussion of credible challenges and estimates of consequences in the event of corresponding failure. A discussion of the risk to workers, the public and the environment from radiation will be included. In addition, the methods to ensure radiation exposures are kept ALARA during operation, maintenance and facility modification will be described.

5. An Accelerator Safety Envelope will be developed for the Super Neutrino Project and will consist of the engineered and administrative bounding conditions within which the BNL and C-AD will operate the Super Neutrino Project facilities.

6. A quality assurance program will be applied at the Super Neutrino Project, focusing upon activities that influence protection of the worker, the public and the environment.

7. A decommissioning and decontamination plan will be developed. A description of structural and internal features of the Super Neutrino Project facilities, which facilitate decommissioning and decontamination, will be provided. Waste management of radiological and hazardous material generation from routine operations and from the decommissioning and decontamination operation will be addressed.

9   Cost Estimate and Schedule

9.1   Methodology of the Cost Estimate

The cost estimate of the AGS-Based Super Neutrino Beam Facility has been performed following the "bottoms up" approach. After the performance goals and physics design of the technical systems are completed, cognizant engineers who have built similar systems were assigned to prepare a cost estimate of sufficient detail, based on previous experience. Each estimate typically includes the cost of the detailed engineering design, procurement, manufacturing, testing and inspection and installation. Engineering, material and labor costs are captured as separate entries for each estimated item.

Most of the cost numbers are based on BNL's recent experience in building RHIC, SNS ring, and LHC magnets. They also draw on extensive searches of price given in catalogs and on vendor's quotations. The Work Breakdown Structure (WBS) is given in Figure 9.1. All systems have been estimated by going down to the component and assembly level. From our past experience, both the manufacturing approaches and the cost estimates are consistent with good engineering practices and are credible.

For example, our cost estimate for the superconduction linac system follows closely the experiences of the SNS, including the material cost of Niobium, fabrication and cleaning process, and finally testing and measurement. In summary, one cryomodule costs about \$4 M which includes \$1.0 M for the cryostat and \$3.0 M for the 4 cavities each with 6 cells.

The cost base for the conventional facilities comes from many-year experience with the RHIC project and the recently completed NASA Space Radiation Facility. For example, the physical enclosure of a 12 foot cylindrical tunnel of the beam transport line is about 2000 dollars per foot, and that of the support building of about \$250 to 500 per square foot. Additional consideration has been given to special requirements for stability and environment control, if so warranted.

For the target and horn system, we draw on the experiences of BNL neutrino programs in the 1980s, plus the K2K of KEK and NuMI of FNAL experiments, resulting in the estimate of a target system of about \$400 K and cost a for the mechanical components for two horns of about \$600 K, and that of two power supplies which can provide 250 KA current for 2.5 μs pulse width every 0.4 s of about \$2.9 M.

The cost given reflects the direct cost of the item. In other words, the estimates do not include G & A (lab overhead), and contingency. These cost elements are added to the direct cost following guidelines using standard estimating rules at BNL.

The detailed cost estimates of all systems are built up from WBS level 5, or below and have been thoroughly reviewed by in-house experts. A cost book with all the back-up material and sources of estimate has been assembled and can be reviewed and updated as new information becomes available. In this roll-up, 30% for contingency, across the board for technical systems, has been used. We are currently working on a detailed cost and resource-loading exercise, with a realistic construction schedule and funding profile built-in, to address the manpower estimates and system-specific contingency requirements on an annual basis. The final bottoms-up estimate, including a bottoms-up contingency, will be available in mid-2005, as well as design improvements currently under study.

All the figures are in FY 2004 US Dollars. No inflation is included since the construction period is not known at this time.

9.2   Summary of the Cost Estimate

A preliminary estimate of the direct cost of the BNL Super Neutrino Beam Facility, summarized at level 3 and up in a spread sheet format is given as Figure 9.2.

The resultant total direct cost of the 1 MW AGS super Neutrino Beam facility, is $ 273.4 M. The preliminary total estimated cost (TEC) is $406.9 M in FY04 dollars, including a contingency of 30% on all items plus the BNL construction project G&A overhead applied at 14.5%. The cost escalation factor cannot be estimated without a project start year.

9.3   Construction Schedule

It is estimated that three years of R & D are needed to build prototypes and perform detailed engineering designs to reduce cost and improve operational reliability. The construction can start a year after the R& D start and will take 4.5 years of construction and 0.5 year of commissioning to get this facility ready for physics research. The planned schedule is represented in Figure 9.3, where FY1 represents the first year of project approval. The total elapsed time of the project is about 6 years.

Work Breakdown Structure

1.0 BNL Neutrino Superbeam Facility

1.1 The Linac System

1.1.1 Front End and RT Linac Upgrade

1.1.2 SCL Accelerating Cavity System

1.1.3 SCL RF Source

1.1.4 SCL Cryogenic System

1.1.5 SCL Vacuum System

1.1.6 SCL Instrumentation

1.1.7 SCL Magnet and Power Supply System

1.2 The AGS Upgrade

1.2.1 AGS Main Magnet Power Supply

1.2.2 AGS RF System Upgrade

1.2.3 AGS Injection/Extraction

1.2.4 Beam Transport to Target

1.2.5 Control System

1.3 The Target and Horn System

1.3.1 The Target System

1.3.2 The Horn System

1.3.3 Shielding and Remote Handling

1.3.4 Target & Horn Physics Support

1.4 The Conventional Facility

1.4.1 Linac Tunnel/Klystron Gallery

1.4.2 AGS Power Supply Building

1.4.3 Beam Transport and Target Area

1.4.4 The Decay Tunnel and Beam Stop

1.4.5 Site Utilities and Road

1.4.6 Modifications for AGS RF System

1.5 ES&H

1.5.1 ES&H

1.5.2 Access Controls

1.6 Project Support

1.6.1 Project Management

1.6.2 Technical Support

1.6.3 Project Controls

2.0 The Beam Monitoring

2.1 The Near Detector Facility

2.2 The Near Detector

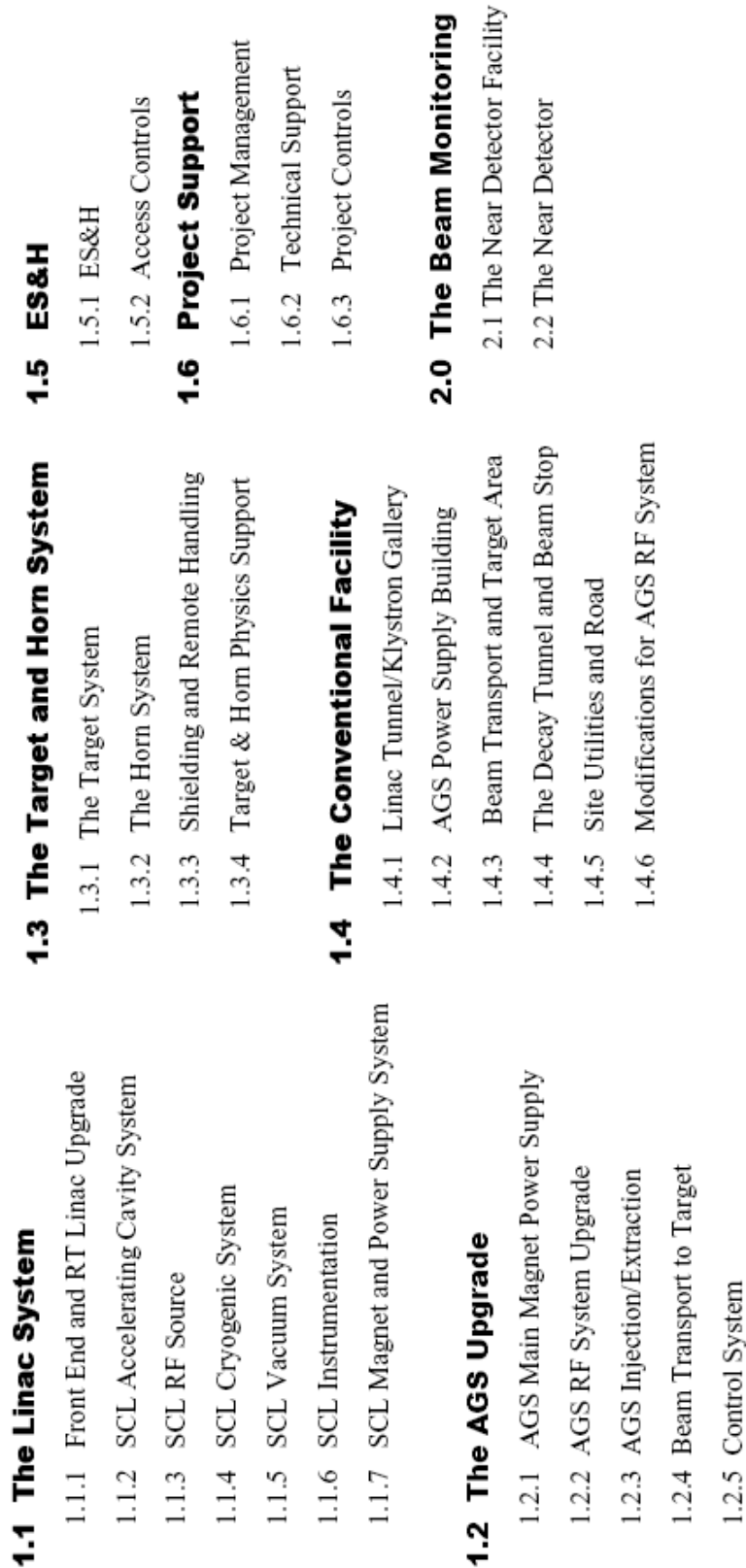Figure 9.1: Work breakdown structure.

Cost Estimate of the AGS Super Neutrino Beam Facility
Construction Phase - Direct FY04 Dollars

1.0 AGS Super Neutrino Beam Facility	EDIA	M&S	Labor	Total
1.1 The Linac System	**6,879,116**	**98,556,970**	**16,783,762**	**122,219,848**
1.1.1 Front End and RT Linac Upgrade	313,000	2,383,000	856,000	3,552,000
1.1.2 SCL Accelerating Cavity System	954,240	22,254,200	11,040,000	34,248,440
1.1.3 SCL RF Source	3,620,988	51,668,800	402,332	55,692,120
1.1.4 SCL Cryogenic System	370,000	13,700,000	2,200,000	16,270,000
1.1.5 SCL Vacuum System	641,598	3,474,570	1,148,378	5,264,546
1.1.6 SCL Instrumentation	460,957	1,390,400	409,061	2,260,418
1.1.7 SCL Magnet and Power Supply	518,332	3,686,000	727,991	4,932,324
1.2 The AGS Upgrade	**10,496,245**	**53,619,159**	**6,472,590**	**70,587,994**
1.2.1 AGS Main Magnet Power Supply	503,959	28,200,000	1,342,337	30,046,296
1.2.2 AGS RF System Upgrade	6,082,625	9,850,000	675,847	16,608,472
1.2.3 AGS Injection/Extraction	644,000	6,437,066	1,668,330	8,749,396
1.2.4 Beam Transport to Target	1,636,771	7,852,241	2,637,290	12,126,302
1.2.5 Control System	1,628,890	1,279,852	148,786	3,057,528
1.3 The Target and Horn System	**664,742**	**3,417,152**	**1,208,338**	**5,290,232**
1.3.1 The Target System	127,008	229,284	50,130	406,422
1.3.2 The Horn System	454,524	2,358,568	656,224	3,469,316
1.3.3 Shielding and Remote Handling	83,210	809,300	125,300	1,017,810
1.3.4 Target & Horn Physics Support	0	20,000	376,684	396,684
1.4 The Conventional Facility	**7,550,300**	**60,090,300**	**1,210,700**	**68,851,300**
1.4.1 Linac Tunnel/Klystron Gallery	2,253,000	11,529,000	230,000	14,012,000
1.4.2 AGS Power Supply Building	2,024,000	13,347,000	432,000	15,803,000
1.4.3 Beam Transport and Target Area	1,674,300	25,091,000	172,500	26,937,800
1.4.4 The Decay Tunnel and Beam Stop	184,000	1,225,300	115,200	1,524,500
1.4.5 Site Utilities & Roads	1,088,000	6,820,000	140,000	8,048,000
1.4.6 Modifications for AGS RF System	327,000	2,078,000	121,000	2,526,000
1.5 ES&H	**104,652**	**275,211**	**437,355**	**817,218**
1.5.1 ES&H	20,000	105,000	270,000	395,000
1.5.2 Access Controls,	84,652	170,211	167,355	422,218
1.6 Project Support	**1,148,681**	**384,109**	**4,096,963**	**5,629,753**
1.6.1 Project Management	0	100,000	1,178,000	1,278,000
1.6.2 Technical Support	1,148,681	214,109	2,146,963	3,509,753
1.6.3 Project Controls	0	70,000	772,000	842,000
AGS Super Neutrino Beam Facility Project Total	**26,843,736**	**216,342,901**	**30,209,709**	**273,396,345**

Figure 9.2: Cost estimate of the AGS Neutrino Superbeam Facility
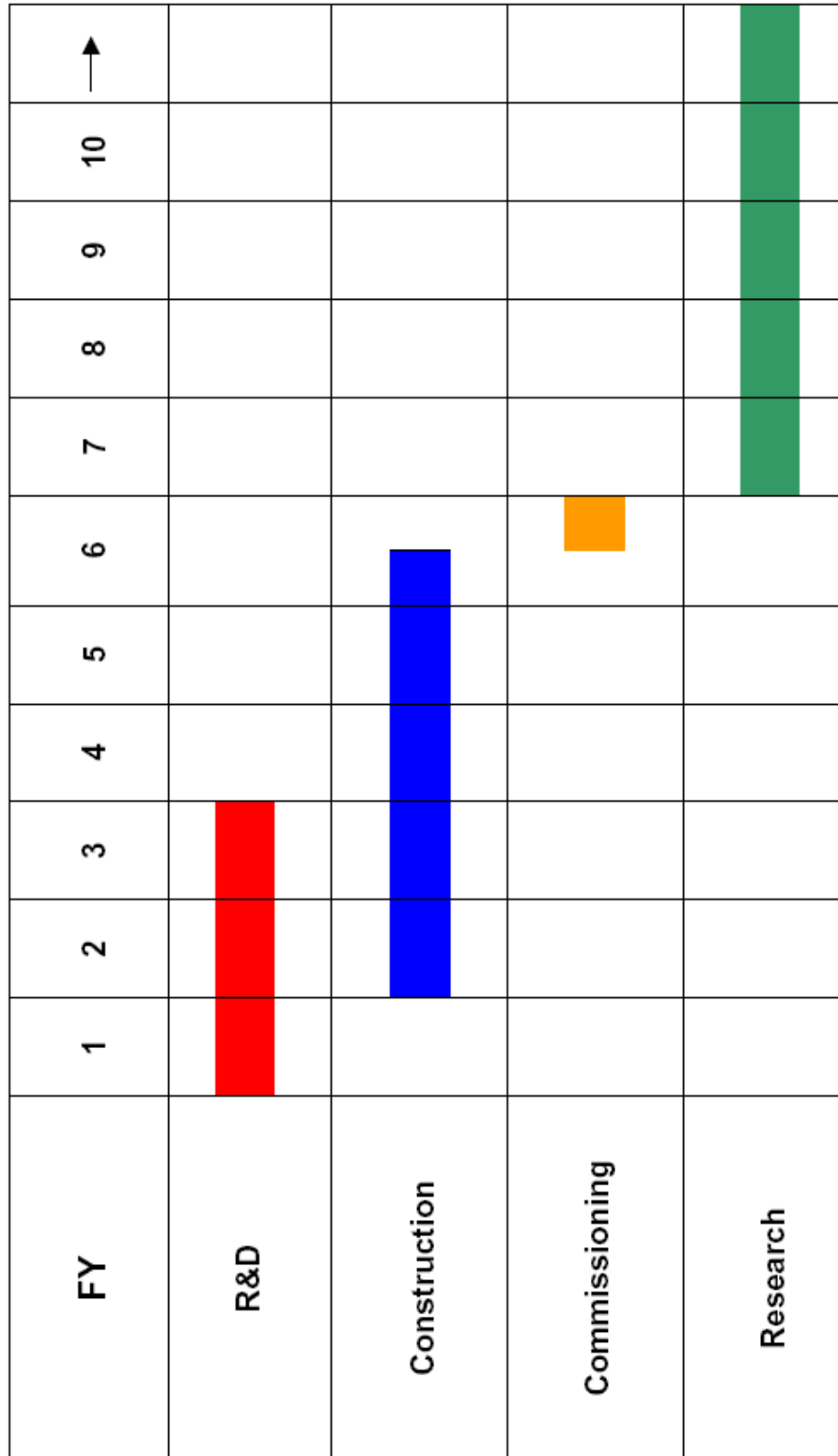
Figure 9.3: Construction schedule .

A   Appendix A: Design Parameters

A.1   Facility Level Parameters

Table A.1: Facility level parameters.

Proton Beam Energy	28 GeV
Protons per Pulse	8.9×10^{13}
Average Beam Current	36.0 (35.7)μA
Repetition Rate	2.5 Hz
Pulse Length	2.58 μs
Number of Bunches	23
Protons per Bunch	3.87×10^{12}
AGS Circumference	807.1 m
Bunch Length	87 (18)ns
Bunch Spacing (Gap)	37(95) ns
Extraction Gap	205 ns
Average Beam Power	1 MW
Normalized Emittance-X	100 π mm-mrad
Normalized Emittance-Y	100 π mm-mrad
Longitudinal Emittance	8-1.2 (1.6) eV-s
Energy Spread ($\Delta E/E$)	0.0039
Target Material	carbon-carbon
Target Radius	6.0 mm
Target Length	80 cm
Beam Size on Target	2 mm (rms)
Beam Elevation at Target	43 m
Decay Tunnel Length	200 m
Beam Dump Length	9 m
Physics Time per Year	10^7 s/year
Number of Protons on Target	2.2×10^{21} p/year

October 8, 2004

A.2   Front End and Warm Linac Parameters

Table A.2: Front end and warm linac parameters.

Energy of Warm Linac	200 MeV
Normalized Horizontal Emittance (rms)	1.0 π mm-mrad
Normalized Vertical Emittance (rms)	1.0 π mm-mrad
Longitudinal Emittance (rms)	0.125 MeV-deg
Macro-Pulse Average Current	21 mA
Macro-Pulse Peak Current	28 mA
Repetition Rate	2.5 Hz
Pulse Length	720 μs
Chopping Rate	65 %
Energy Spread ($\Delta E/E$)	0.00081
Energy Jitter($\delta E/E$)	0.0012

A.3   Superconducting Linac Parameters

Table A.3: Superconducting linac parameters

Linac Section	LE	ME	HE
Kinetic Energy Initial/Final, MeV	200/400	400/800	800/1200
Frequency, MHz	805	1610	1610
No. of Protons / Bunch x 10^8	8.70	8.70	8.70
Temperature, ^{o}K	2.1	2.1	2.1
Cells / Cavity	8	8	8
Cavities / Cryo-Module	4	4	4
Cavity Separation, cm	32.0	16.0	16.0
Cold-Warm Transition, cm	30	30	30
Cavity Internal Diameter, cm	10	5	5
Cell Reference β_0	0.615	0.755	0.851
Cell Length, cm	11.45	7.03	7.92
Length of Warm Insertion, m	1.079	1.379	1.379
Total No. of Periods	6	9	8
Length of a period, m	6.304	4.708	4.994
Total Length, m	37.82	42.38	39.96
Cavities / Klystron	1	1	1
No. of rf Couplers / Cavity	1	1	1
Coupler rf Power, kW (*)	263	351	395
Total No. of Klystrons	24	36	32
$Z_0T_0^2$, ohm/m	378.2	570.0	724.2
Q_0 x 10^{10}	0.97	0.57	0.64
Peak Axial Field, E_a, MV/m	13.4	29.1	29.0
Ave. Dissipated Power, W	2	11	8
Ave. HOM-Power, W	0.2	0.5	0.4
Ave. Cryogenic Power, W	65	42	38
Total Ave. RF Power, kW (*)	17	31	30
Norm. rms Emittance, π mm-mrad	0.8	0.9	1.0
rms Bunch Area, π ^{o}MeV (805 MHz)	0.5	0.5	0.5

(*) Including 50% rf power contingency.

A.4   AGS Parameters

Table A.4: AGS parameters.

Injection Kinetic Energy	1.2 GeV
Extraction Energy	28 GeV
Number of Injection Turns	240
Stripping Efficiency	98%
Beam Dump	25 kW
Electron Collection	25 Watts
Number of Protons/pulse	8.9×10^{13}
Harmonic Number	24
Filled Bucket	23
Repetition Rate	2.5 Hz
Strip Foil	carbon-carbon 300 μg /cm^2
rf Frequency at Injection	8.0 MHz
rf Frequency at Extraction	8.9 MHz
Peak rf Voltage	1.0 MV
Transition Gamma	8.5
Horizontal Tune	8.7
Vertical Tune	8.9
Beta Maximum	22.5 m
Beta Minimum	11.5 m
Horizontal Aperture	7 cm
Vertical Aperture	10 cm
AGS Dipole Resistance	0.27 Ω
AGS Dipole Inductance	0.78 Henries
Dipole Magnet Average Power	130 MW
Power Supply Voltage	$\pm$ 30 kV
Power Supply Current	5500 A
Max. Magnet Voltage to Ground	3.3 kV

A.5 Beam Transport Parameters

Table A.5: Beam transport parameters

Length (AGS to Target)	488 m
Lattice	FODO
Final Focus	Doublet
Beam Size (Radius) on Target	2 mm (rms)
Beam Position Tolerance at Target	1.5 mm
Beam Angle Tolerance at Target	3 mr
Dispersion at Target; H, V	0,0

A.6   Target/Horn Parameters

Table A.6: Target/Horn parameters

Target Material	carbon-carbon
Target Diameter	1.2 cm
Target Length	80 cm
Horn Inner Radius	9 mm
Beam size (radius) on target	2 mm (rms)
Horn Smallest Radius	6 mm
Horn Large Radius	61 mm
Horn Inner Conductor Thickness	2.5 mm
Horn Minimum Thickness	1 mm
Horn Length	217 cm
Horn Current	250 kA
Repetition Rate	2.5 Hz
Power Supply Wave Form	Sinusoidal, base width 1.20 ms

A.7 Decay Tunnel and Shielding Parameters

Table A.7: The decay tunnel and shielding parameters.

Transport Tunnel Radius	1.5 m
Shielding of Transport Tunnel	6 m
Decay Tunnel Radius	2 m
Decay Tunnel Length	200 m
Beam Dump Material	Steel
Beam Dump Length	9 m
Shielding of Target Bldg.	0.6 m Steel and 4.3 m of Heavy Concrete
Shielding of Decay Tunnel	9 m Soil

A.8   Conventional Facilities and Target Hill Parameters

Table A.8: Conventional facilities and target hill parameters.

The Linac Tunnel Length	130 m
Linac Tunnel Diameter	3 m
Klystron Gallery Length	130 m
Klystron Gallery Dimension	22 m x 12 m (W*H)
SRF Testing and Assembly Building	12 m x 36 m
Shielding of Linac Tunnel	3 m Soil
Linac Service Building	12 m x 22 m
New Beam Transport Tunnel	300 m
Beam Transport Tunnel Diameter	3 m
Shielding of Beam Transport Tunnel	6 m Soil
Beam Transport Service Buildings	2x(250 m^2)
Beam Elevation at Target	43 m
Target Hill Height	52 m
Target Hill Base Width	146 m
UP Hill Length to Target	310 m
Down Hill Length from Target	200 m
Target Service Building	16.5 m x 15 m
Electrical Substation	6100 KVA
Water Cooling Capacity	3.5 MW
Service Road	250 m

B   Appendix B:Alternate Injector Linac Design

B.1   Introduction

The design presented in Section 2 has a limitation for the future energy upgrade due to limited space (130 m) and also requires major R&D efforts for developing 1610 MHz cavity, power couplers, and cryomodules, which require much shorter warm to cold transition region compared to SNS cryomodules. An alternate design (see Figure B.1) is considered for the injector linac:

- Upgrade the 200 MeV linac to 400 MeV, based on the FERMILAB upgrade which was successfully completed in 1993; some BNL staff had participated in its activities. [55].

- Use the SNS high beta cryomodules [57] to 1.2 GeV or higher energies in the 130 m space.
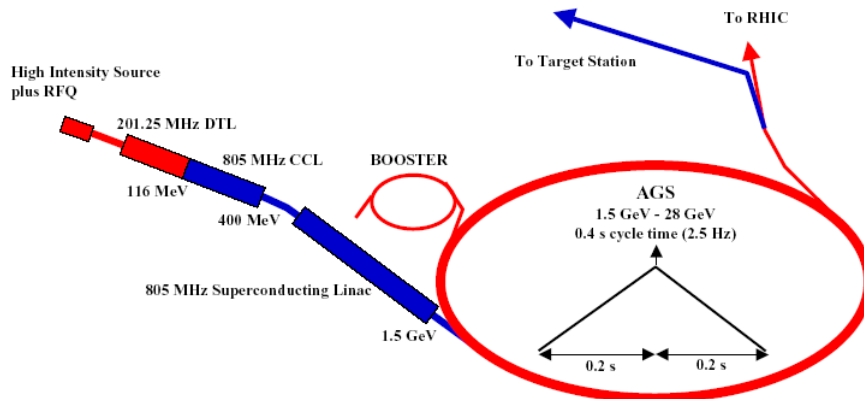

Figure B.1: AGS proton driver layout for alternate injector linac design.

The Fermilab 200 MeV linac was upgraded to 400 MeV by replacing last four DTL tanks with seven 805 MHz coupled cavity linac (CCL) modules[55]. These seven CCL modules fit within the existing linac tunnel enclosure, since the length of the CCL modules including the transition section is about 3 m shorter than the last four DTL tanks. Since 1993, the Fermilab linac has successfully accelerated a peak current of 50 mA with pulse length of 50 μs at repetition rate of 15 Hz. The average accelerating gradient in the CCL is 7.5 MV/m, which is about four times higher than LAMPF at Los Alamos. The peak surface field is 37 MV/m, which is 1.35 kilpatrick. Each module has 4 sections and each section has 16 cells. Each module is driven by a 12 MW klystron. There is a 16-cell buncher cavity just downstream of DTL Tank 5, a 4-cell vernier cavity between the buncher and the first accelerating module. The focusing lattice is FODO with quadrupole gradient of approximately 20 T/m.

Figure B.2: Fermilab linac after upgrade in the tunnel.

The SNS high beta module is 7.891 m long (including the warm section) and has 4 sections of 6 cells. The geometric beta for these modules is 0.81. The design accelerating field (E_0) is about 22.8 MV/m (E_0T=15.9 MV/m), 21 modules will accelerate H^- from 387 MeV to 1300 MeV. At present, cavity testing at JLAB [58] show that the accelerating gradient of 30 MV/m (E_0T=21 MV/m) has been achieved.
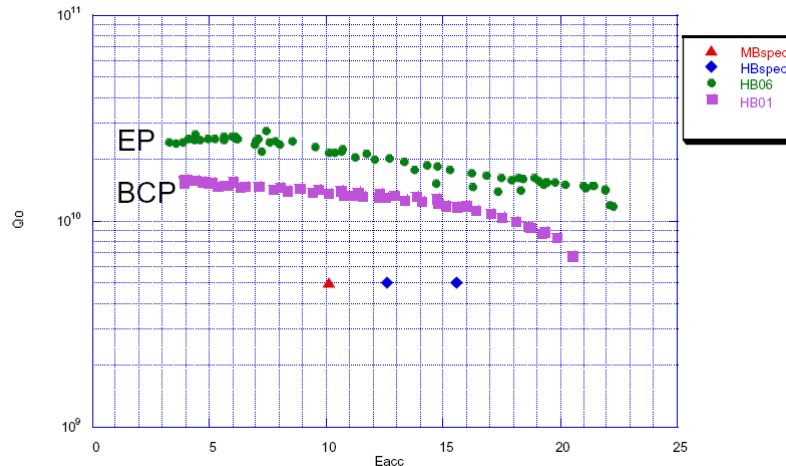

Figure B.3: SNS test results for high beta cavity #1 and #6. x-axis is E_0T in MV/m.

In 130 m one can have 15 cryomodules. Assuming an accelerating gradient (E_0) 30 MV/m, 15 cyromodules can accelerate H^- from 400 MeV to 1435 MeV. The energy can be upgraded to 1533 MeV if the accelerating gradient (E_0) of 33 MV/m (achieved at TESLA) becomes a reality in future for cavities with $\beta \leq 1$.

B.2   Present Linac Upgrade to 400 MeV

B.2.1   Choice of Structure

The present linac is an Alvaraz-type drift-tube linac (DTL) consisting of nine tanks operating at a frequency of 201.25 MHz that accelerates H^- ions to 200 MeV. To achieve 400 MeV in the same length the new structure should have higher accelerating gradients. The choices of technologies are superconducting and warm.

The low velocity superconducting structures which have been primarily developed for heavy ions linacs (half-wave, quarter-wave, spoke resonators, etc) owing to their high accelerating field capabilities. Multi cell elliptical cavities cannot be used for $\beta \leq$0.5 because of their poor mechanical stability and their high peak surface field to accelerating field ratio. The spoke resonators are simple, highly stable mechanically, compact in size and have achieved quite high accelerating gradient corresponding to peak surface field of about 40 MV/m and 100 mT. However, since an excessive longitudinal phase advance must be avoided, we cannot take full advantage of the high gradient available with super conducting cavities at low energy. As

a result, the energy gain per real estate meter in a super conducting linac ($\sim$0.8 MeV/m) is about a factor 2 lower than the normal conducting DTL linac in this energy range.

In order to get higher accelerating gradient in a warm structure, there are two choices: (1) disk and washer and (2) side coupled cavity. The disk and washer has high efficiency and strong coupling, however, its mode structure and construction are very complex. The side-coupled structure is easy to build, and better understood and has a proven history. Our choice is side-coupled structure.

The last choice to be made is the transition energy between the DTL and the CCL. Figure B.4 shows the shunt impedances of these structures as function of the particle velocity (β=v/c). As the particle velocity increases the shunt impedance of the DTL decreases and the shunt impedance of the CCL increases. They cross over about β=0.4 (100 MeV) [56].
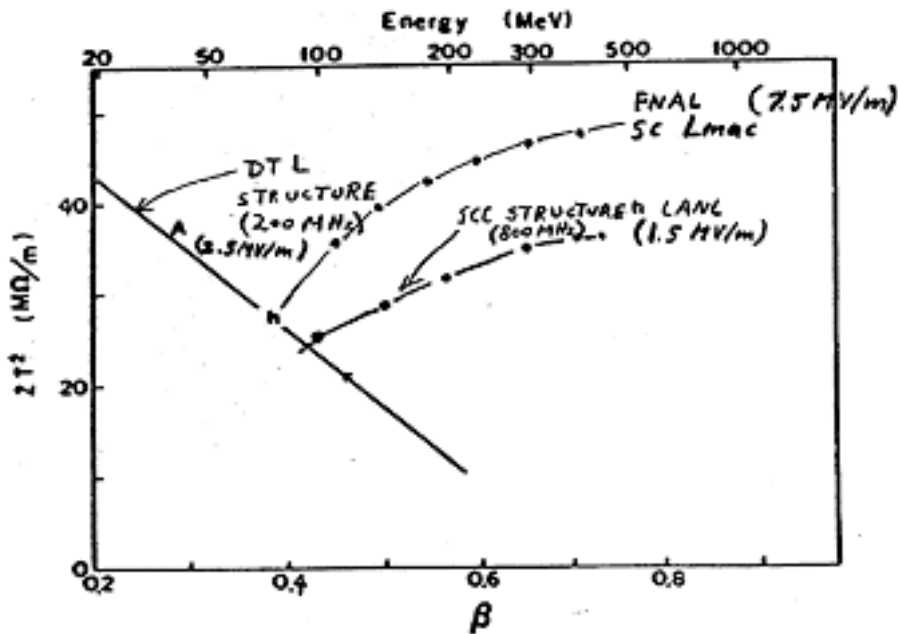

Figure B.4: Shunt impedance of the DTL and the CCL as a function of particle velocity (β).

B.2.2 Coupled Cavity Linac

The coupled cavity structure is a TM-excited circular waveguide. The small drift tubes in the irises prevent direct coupling from cell to cell. Coupling is then provided laterally through resonant cavities alternating diametrically. From field propagation point of view, these coupling cavities play a role similar to the accelerating ones. If they are considered as period, the structure is operated in the $\pi/2$ mode. For accelerating cells, however, the phase shift is π. In standing wave operation, only the accelerating cells are excited and the field is weak in the coupling cells.

A CCL section consists of 12-20 same length ($\beta_g\lambda/2$) cells coupled by side coupling cells. The number of cells in a section is determined by the allowable phase slip per cells since the cell length is the same whereas particle velocity is increasing. One section is coupled to

another section with different cell length by a long coupling cell, called bridge coupler. The bridge coupler is generally put off axis to provide space for the quadruploes, diagnostics and port for rf power. Three to six sections coupled by bridge couplers make a module. The number of sections in a module is determined by the available power source (klystron power) and higher order mode coupling. Generally the maximum number of cells powered by one klystron can be 128.

B.2.3   Design of the CCL

Figure B.5 shows the half-cell of the CCL structure and various cell parameters for the half-cell. Various parameters determining the shape of the cell are important. Shunt impedance increases with decreasing bore radius, web thickness between the neighbor cells and nose thickness.

The maximum surface field, which gives the spark rate in the structure, occurs at the nose corner. The optimized design is a compromise between maximizing shunt impedance, the transit time factor, minimizing the maximum surface field and satisfying other physical requirements. For example the bore radius is determined by the beam size and loss limits; the web thickness and the nose corner is determined by the cooling channels; and the cell radius is kept constant through out the linac to minimize the cost.

The CCL is divided into seven modules, each with four sections of sixteen cells. This solution gives acceptable surface fields, approximately equal power to each module, minimizes mechanical variability and acceptable transverse focusing condition. Table B.1 shows the general parameters of the side coupled cavity linac. Table B.2 shows the parameters for the modules and Table B.3 for the sections.

The achieved sparking rate at Fermilab is about 0.033% with RF pulse length of 50 μs[55]. Since our rf pulse length is about 1 ms, the sparking rate could be higher. It would require some R&D efforts to minimize the sparking rate. In the Fermilab design nose corner is not water cooled. For our 1 ms long rf pulse length this could be a problem.

B.2.4   CCL Beam Dynamics

Beam from the present DTL bunched at 201.25 MHz has to be matched to 805 MHz bucket, and transverse matching into the side coupled cavity linac. This is accomplished by four meter long matching section with two buncher cavities. The transverse matching is achieved using DTL Tank 5 quadrupoles and two quadrupoles in the transition section. The CCL will use constant gradient quadrupoles through out the linac with average phase advance of 79 degrees per FODO cell. The longitudinal phase advance is below stability limit. Figure B.6 shows the TRACE3D out put for the transition section and CCL. Figure B.7 shows the beam envelopes though the CCL and Figure B.8 shows the input and output phase spaces. The emittance growth through the CCL is minimum. Simulations show no losses through the linac.
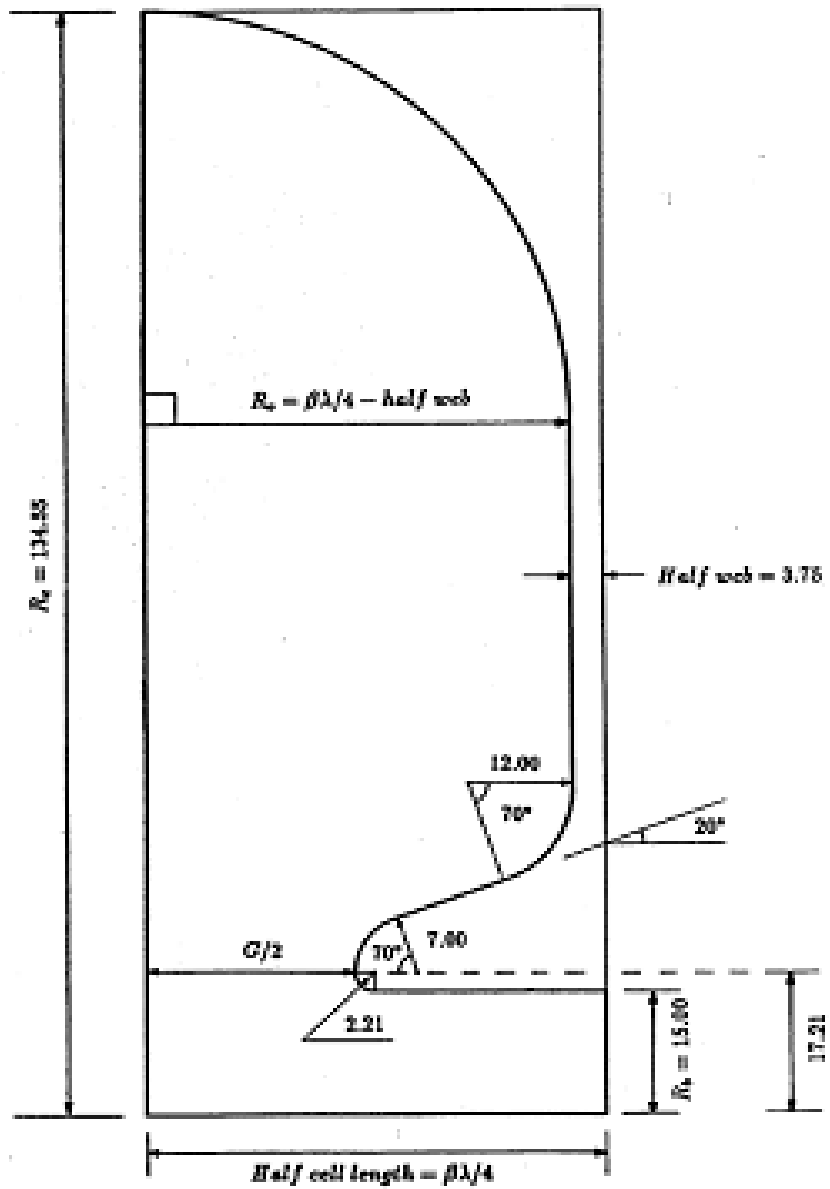
Figure B.5: Half side coupled cavity cell, showing all the cell parameters for the Fermilab CCL.

Table B.1: General parameter of the CCL.

Initial Kinetic Energy (β=0.454)	116.54	MeV
Final Kinetic Energy (β=0.714)	401.56	MeV
Beam Current, Design	50	mA
Repetition Rate	2.5	Hz
Beam Pulse Length, Design	1.0	ms
Length, with Transition Section	63.678	m
Frequency	805.0	MHz
Number Buncher Cavities	2, (16 cells, and 4 cells)	
Number of Modules	7	
Number of Section/Module	4	
Number of Cell/Section	16	
Total number of cell (7x4x16)	448	
Bridge Coupler Length	$3\beta\lambda/2$	
Length between Modules	$3\beta\lambda/2$	
Cavity Bore Radius	1.5	cm
Accelerating Phase	-32.0	deg
Average Axial Field (E_0)	7.09 – 8.07	MV/m
Kilpatrick	1.35	
Maximum Surface Filed	36.8	MV/m
rf Power per Module	< 12	MW
Copper Losses	7.2	MW
Beam Power (@ 50 mA)	2.0	MW
Control and Reserve	2.8	MW
Transverse Focusing	FODO	
Average Phase Advance (Transverse)	79	deg
Quadrupole Length (Magnetic)	8.0	cm
Quadrupole Bore Radius	2.0	cm
Quadrupole Pole Tip Field	4.6	kG
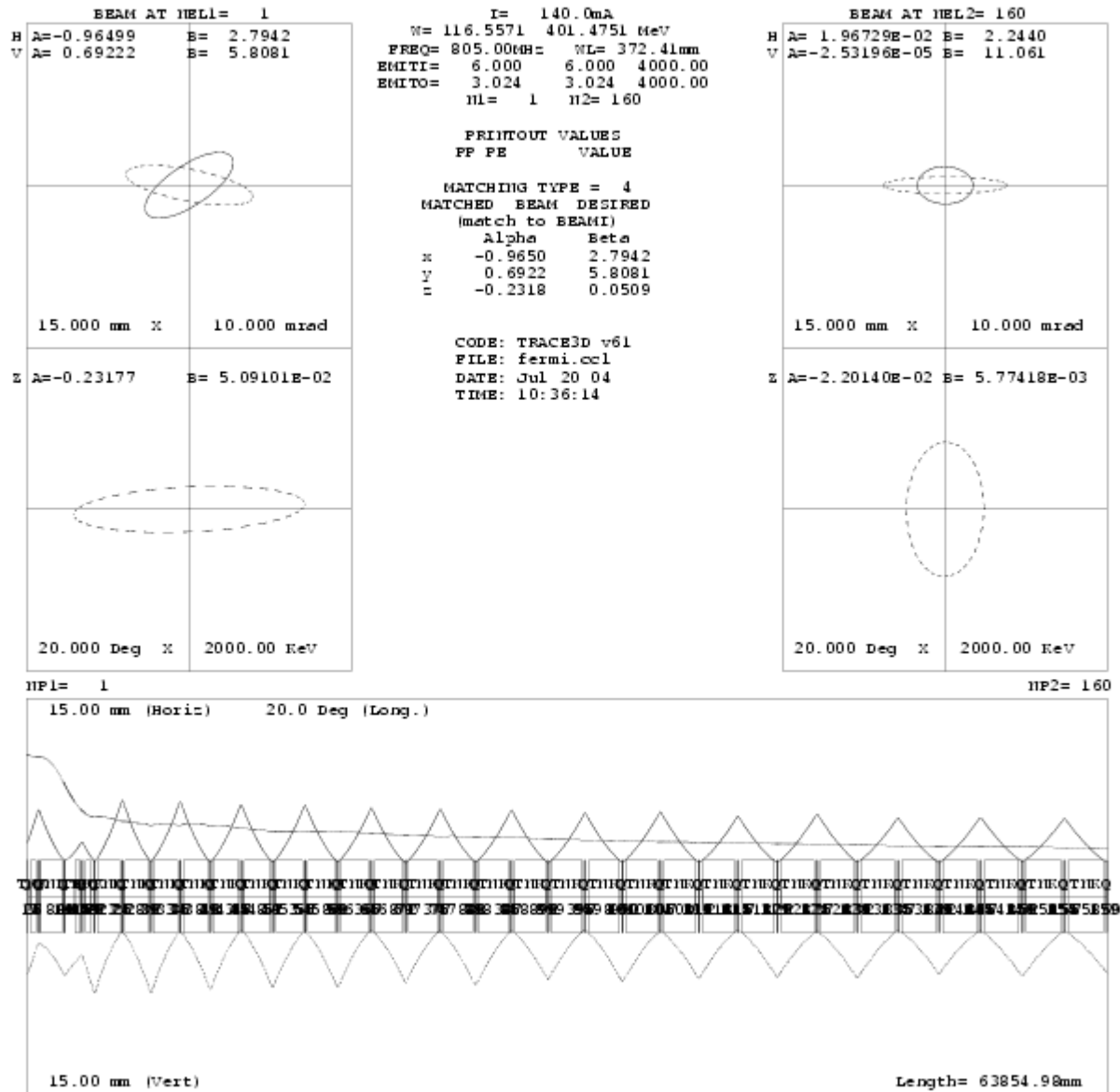
Figure B.6: TRACE3D output for the CCL.

Table B.2: Summary of module's parameters.

Module	Energy In (MeV)	Energy Out (MeV)	Length (m)	Power, Cu (MW)	Power, Beam (MW	Power Total (MW)
B-1	116	116	1.3613	0.13	0.0	0.13
B-2	116	116	0.3403	0.0	0.0	0.0
1	116	152	6.7146	7.47	1.76	9.25

Figure B.7: W-W$_s$, $\varphi - \varphi_s$ and x profiles through the CCL.

Table B.3: Summary section's parameters

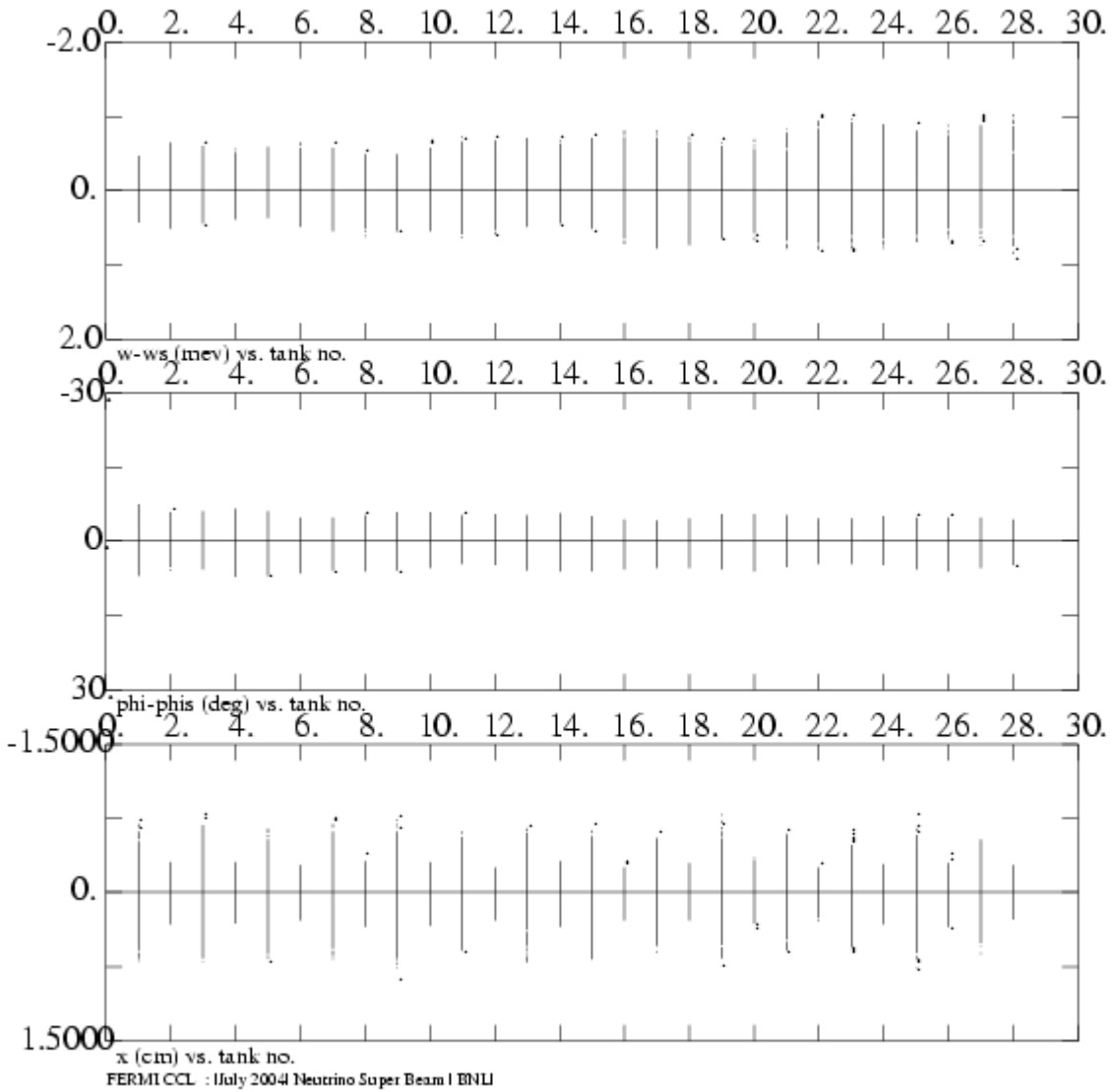| M-S	E (MeV)	G (MV/m)	β_G	L_{rf} (m)	L_d (m)	P_{Cu} (MW)	P_{beam} (MW)
B-1	116.5	2.23	0.456904	1.3613	0.6653	0.13	0.0
B-2	116.5	0.0	0.456904	0.3403	0.7951	0.0	0.0
					0.8381		
1-1	125.1	8.07	0.463663	1.3814	0.1418	1.75	0.43
1-2	133.8	8.07	0.477121	1.4215	0.2628	1.88	0.44
1-3	142.8	8.07	0.490245	1.4606	0.2703	1.93	0.45
1-4	152.1	8.07	0.503034	1.4987	0.2775	1.91	0.46
2-1	161.2	7.85	0.515325	1.5353	0.2846	1.72	0.46
2-2	170.6	7.85	0.527119	1.5704	0.2912	1.85	0.47
2-3	180.2	7.85	0.538009	1.6047	0.2977	1.58	0.48
2-4	190.6	7.85	0.549796	1.6380	0.3044	1.58	0.49
3-1	199.7	7/66	0.560552	1.6700	0.3102	1.70	0.48
3-2	209.5	7.66	0.570889	1.7000	0.3161	1.82	0.49
3-3	219.6	7.66	0.580696	1.7309	0.3218	1.86	0.50
3-4	229.8	7.66	0.590748	1.7600	0.3273	1.85	0.51
4-1	239.9	7.48	0.600174	1.7881	0.3327	1.68	0.51
4-2	250.1	7.48	0.609241	1.8151	0.3379	1.79	0.51
4-3	160.5	7.48	0.618069	1.8414	0.3428	1.84	0.52
4-4	271.1	7.48	0.626662	1.8670	0.3477	1.83	0.53
5-1	181.5	7.34	0.634946	1.8917	0.3524	1.67	0.52
5-2	292.1	7.34	0.642932	1.9155	0.3570	1.78	0.53
5-3	302.8	7.34	0.650708	1.9387	0.3614	1.83	0.53
5-4	313.6	7.34	0.658322	1.9613	0.3657	1.81	0.54
6-1	324.4	7.20	0.665580	1.9830	0.3698	1.66	0.54
6-2	335.2	7.20	0.672619	2.0039	0.3738	1.77	0.54
6-3	346.1	7.20	0.679476	2.0244	0.3777	1.81	0.55
6-4	357.1	7.20	0.680155	2.0443	0.3815	1.79	0.55
7-1	368.1	7.09	0.692611	2.0635	0.3852	1.65	0.55
7-2	379.1	7.09	0.698852	2.0824	0.3887	1.76	0.55
7-3	390.2	7.09	0.704933	2.1002	0.3921	1.80	0.56
7-4	401.5	7.09	0.71086	2.1179	0.3955	1.78	0.56
Total				52.1119	11.5656	50.27	14.25
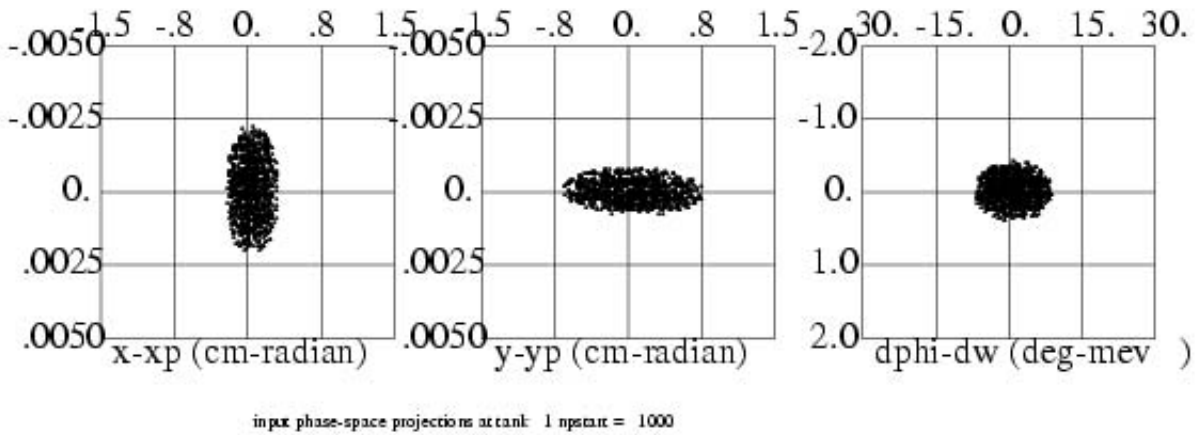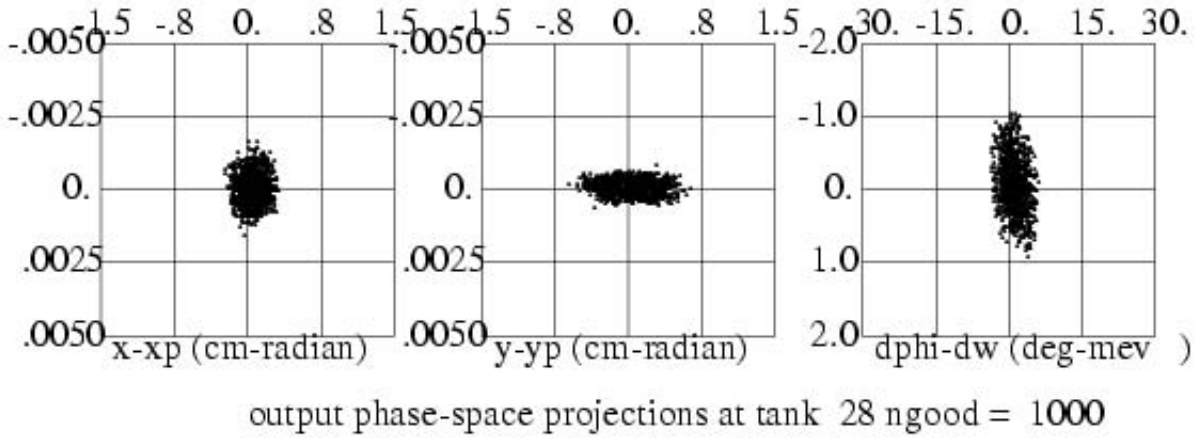
Figure B.8: Input and output phase space plots for CCL.

B.3 Super Conducting Linac (400 MeV − 1500MeV)

B.3.1 Cryomodule

SNS studies show that when accelerating H^- ions from 400 MeV to 1300 MeV the optimized geometric beta for the cavity is 0.81 with an accelerating gradient E_0 of 22 MV/m. The optimized beta for the range of 400 MeV to 1500 MeV will be little higher. For an accelerating gradient of 31 MV/m, the phase slip per cell for the end cavities at 400 MeV is about 90 degrees for a six-cell-cavity, therefore geometric beta cannot be higher than 0.81 at 400 MeV and E_0 of 31 MV/m and six cells section. We could choose to use two geometric beta cavities or six or eight cavity per cryomodule but in the given length and cost minimization, presently our choice is one type of beta cavity with a geometric beta of 0.81. However we are further optimizing the configuration.

B.3.2 Warm Insertion

Each SNS warm insertion is 1.6 m long and has the following elements: (1) quadrupole doublets for transverse focusing and both horizontal and vertical steering dipoles for the equilibrium correction, (2) Beam diagnostics like wire scanner, BPM, current monitors, special diagnostics devices, (3) two bellows in the vacuum beam line and a tee for the a flange to accommodate a pumping port and a valve for the warm section pump down, (4) a precise alignment system and support for quadrupole alignment[57]. We are looking into whether these warm insertions can be cold, so one would have one or two cryomodules rather than 15 cryomodules to save longitudinal real estate, that is occupied by the cold to warm transition in the SNS/CEBAF style configuration. Problems with is configuration could be: (1) diagnostics devices, for example the wire scanner have to move inside the cryomodule , (2) quadrupole alignment becomes more difficult. TESLA cryomodules have twelve 9-cell cavities, BPM and a quadrupole, but no wire scanner. For now, we have chosen the 1.6 m long SNS style warm insertion.

We have also considered a FODO lattice instead of doublet lattice to shorten the warm insertion, and found the beam size is twice as large when compared to the doublet lattice, leading to an aperture to rms beam size ratio of only 6, which is uncomfortable. Therefore we have chosen the doublet lattice leaving the warm section 1.6 m long.

B.3.3 The Design of the SCL

There will be 15 cryomodules, each cryomodule will have four cavities and each cavity will have 6 cells of geometric beta equal to 0.81. Table B.4 shows achievable energies with the given accelerating gradient E_0 for SNS high beta cavities configured as described above. We have chosen the E_0 equal to 31 MV/m for the present design. Table B.5 shows the general parameters for the SCL.

The Cell

The cell design is discussed in Section 2.2.2. The SNS high beta cell design parameter is shown in Table B.6. Figure 2.4 shows the definition of cell parameters. Figure B.9 shows the

Table B.4: Energy vs E_0 for 15 cryomodules, 4 cavities/cryomodules, 6 cell/cavity , SNS high beta cavity.

E_0 MV/m	E_P MV/m	Energy MeV
22.807	37.63*	1180.3
25.0	41.25	1258.1
27.0	44.55	1328.2
29.0	47.85	1397.4
30.0	49.5**	1435.2
31.0	51.2	1461.7
33.0	54.5***	1533.6

* SNS design peak surface field.

** Achieved peak surface field at SNS.

*** Achieved peak surface filed at TESLA.

Table B.5: General parameter of the SCL

Parameter	SCL	Unit
Ave. Incremental Beam Power	39.5	kW
Average Beam Current	36.0	μA
Initial Kinetic Energy	400	MeV
Final Kinetic Energy	1462	MeV
Frequency	805	MHz
Cell / Cavity	6	
Cavity/Cromodule	4	
Slot Length	7.891	m
Warm Insertion Length	1.6	m
Cavities/Klystron	1	
No. of Power Coupler/Cavity	1	
Accelerating Gradient (E_0)	31	MV/m
RF Phase Angle	-19.5	deg
Lattice	doublet	
Number of period	15	
Period length	7.891	m
Phase Advance per Period	70	deg
Total Length	119.7	m
Number of Klystron	60	
Klystron Power	550	kW
Average Dissipated Power/cavity	108	W
Norm. rms Emittance	1.0	πmm rad
Rms Bunch area	1.0	πdeg-MeV (805 MHz)

Superfish output for the SNS high beta (β=0.81) half cell. The static frequency shift Δf is given by

$$\Delta f = K \times (E_0 T)^2 \tag{B.1}$$

where K is the Lorentz force detuning factor, which depends on the cavity shape and construction, and $E_0 T$ is the accelerating gradient. If the rf generator frequency is fixed during detuning, then more power is needed to maintain the cavity voltage constant. The required increase in the generator rf power $P_{\Delta f}$ is given by

$$P_{\Delta f} = P_{\Delta f=0} \times \left(1 + \left(\frac{\Delta f}{f_{1/2}} \right)^2 \right) \tag{B.2}$$

where $f_{1/2}$ the full width half maximum bandwidth of the cavity. With K=-0.43, $E_0 T$=23.87 MV/m , the Δf is 245 Hz. The cavity bandwidth of 1150 Hz requires an increase in rf power about 4.5%.

Table B.6: Cell parameters

Parameter	High Beta	unit
Frequency	805	MHz
Geometric Beta	0.81	
Alpha	7	deg
R isis	4.3	cm
R dome	5.2	cm
R equator	16.41	cm
a/b	0.555	
E peak	50.1	MV/m
E_0	31	MV/m
E_p/E_0	1.65	
M max	101.4	mT
Bmax/E_p	2.14	MT/MV/m
Coupling	1.6	%
Lorentz force Detuing Coef.	-0.43	Hz/(MV/m)^2

Cryomodule

Linac architecture is discussed in section 2.2.3, Figure B.10 show the SNS high cryomodule with slot length of 7.891 m. Cavity temperature is 2.1 ° K.

Beam Dynamics

Figure B.11 shows the TRACE3D out for the SCL, Figures B.12 and B.13 show the beam profile through the SCL, Figures B.14 and B.15 show the input and output phase space plots for the SCL. Simulations show no emittance growth. The error studies for the CCL and SCL have yet to be completed.
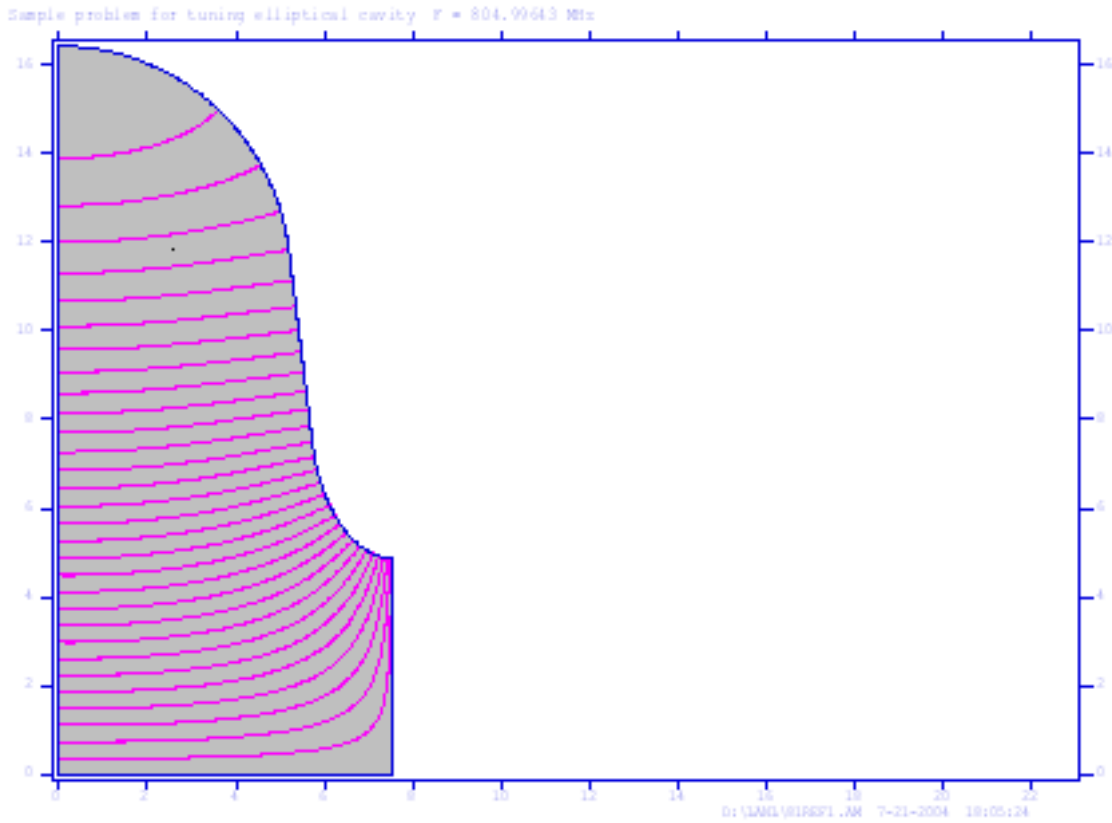
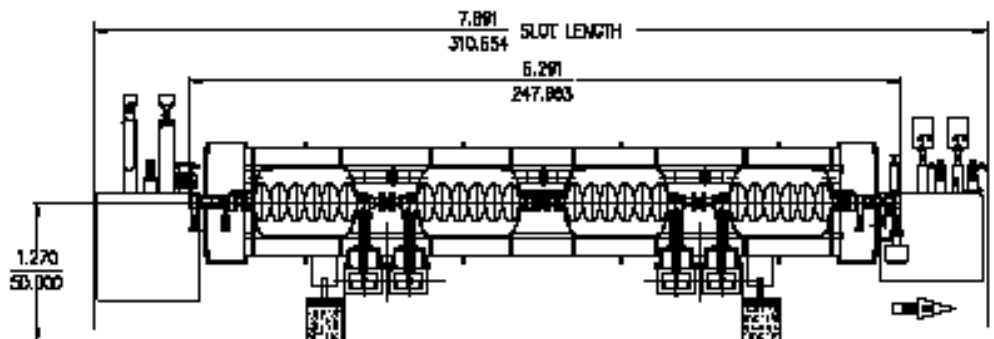Figure B.9: Superfish output for SNS high beta (β=0.81) half cell.

Figure B.10: SNS high beta cryomodule.
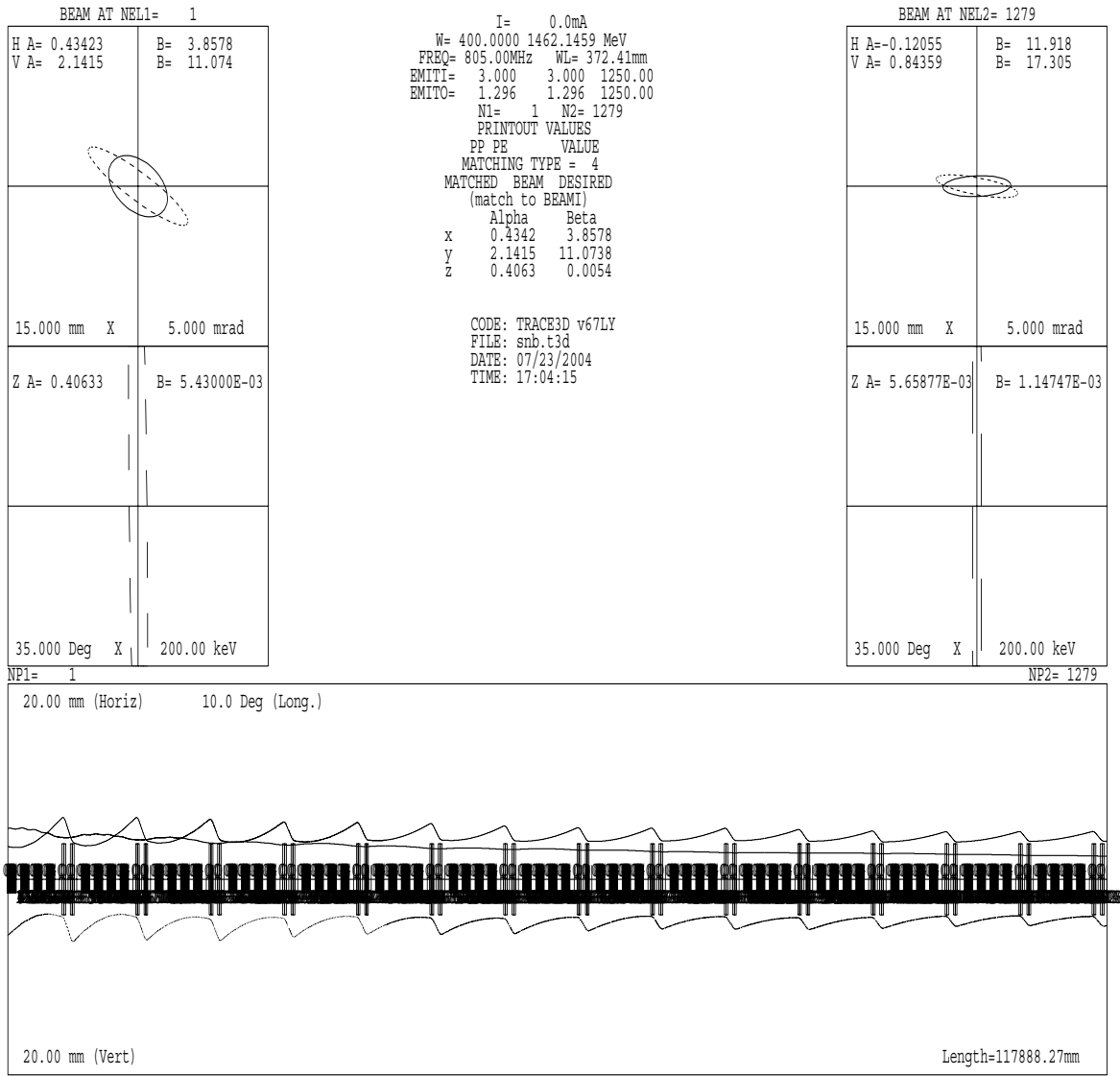
```
     BEAM AT NEL1=    1                          I=      0.0mA                      BEAM AT NEL2= 1279
 ┌──────────────┬───────────────┐      W= 400.0000 1462.1459 MeV        ┌──────────────┬───────────────┐
 │ H A= 0.43423 │ B=  3.8578    │    FREQ= 805.00MHz   WL= 372.41mm     │ H A=-0.12055 │ B=  11.918    │
 │ V A= 2.1415  │ B=  11.074    │   EMITI=  3.000    3.000  1250.00     │ V A= 0.84359 │ B=  17.305    │
 │              │               │   EMITO=  1.296    1.296  1250.00     │              │               │
 │              │               │      N1=    1   N2= 1279              │              │               │
 │              │               │      PRINTOUT VALUES                  │              │               │
 │              │               │      PP PE       VALUE                │              │               │
 │              │               │     MATCHING TYPE =  4                │              │               │
 │              │               │    MATCHED  BEAM  DESIRED             │              │               │
 │              │               │      (match to BEAMI)                 │              │               │
 │              │               │        Alpha    Beta                  │              │               │
 │              │               │   x    0.4342   3.8578                │              │               │
 │              │               │   y    2.1415  11.0738                │              │               │
 │              │               │   z    0.4063   0.0054                │              │               │
 │              │               │                                       │              │               │
 │ 15.000 mm  X │   5.000 mrad  │                                       │ 15.000 mm  X │   5.000 mrad  │
 ├──────────────┼───────────────┤     CODE: TRACE3D v67LY               ├──────────────┼───────────────┤
 │              │               │     FILE: snb.t3d                     │              │               │
 │ Z A= 0.40633 │ B= 5.43000E-03│     DATE: 07/23/2004                  │ Z A= 5.65877E-03│ B= 1.14747E-03│
 │              │               │     TIME: 17:04:15                    │              │               │
 │              │               │                                       │              │               │
 │              │               │                                       │              │               │
 │              │               │                                       │              │               │
 │ 35.000 Deg  X│   200.00 keV  │                                       │ 35.000 Deg  X│   200.00 keV  │
 └──────────────┴───────────────┘                                       └──────────────┴───────────────┘
NP1=    1                                                                                      NP2= 1279
```
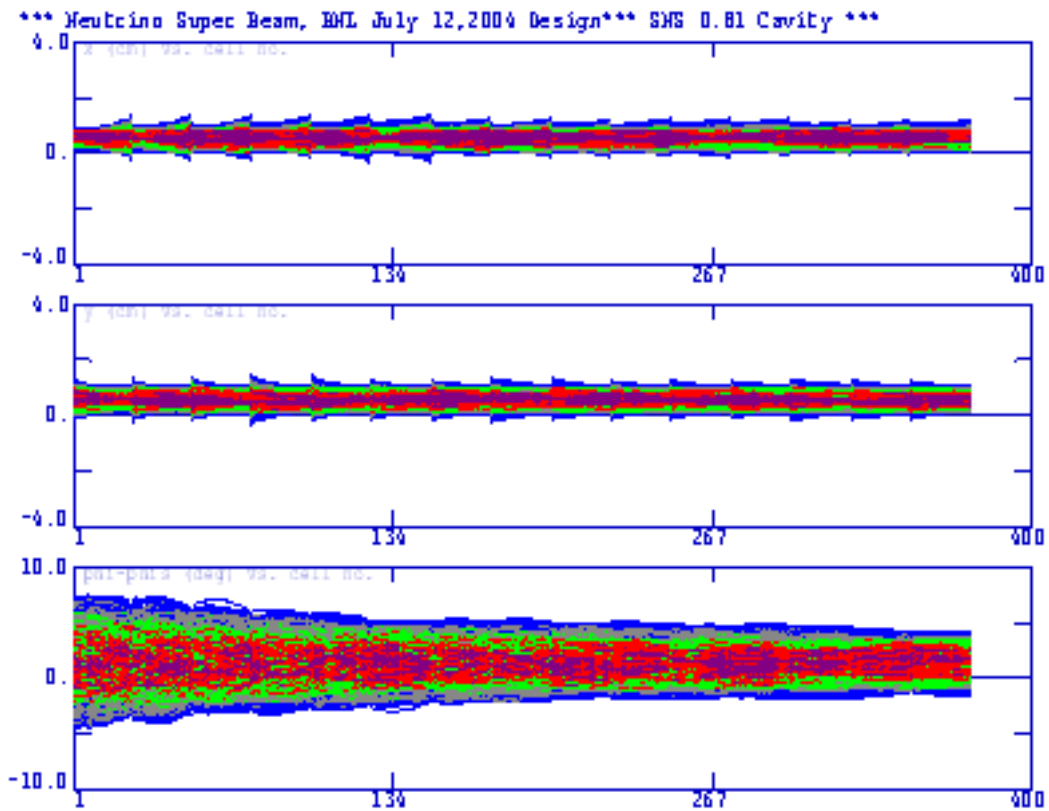

Figure B.11: TRACE3D output for the SCL.

Figure B.12: Beam profiles (x, y, $\varphi - \varphi_s$) through the SCL, Beam offset is artificial due to plotting program of PARMILA.
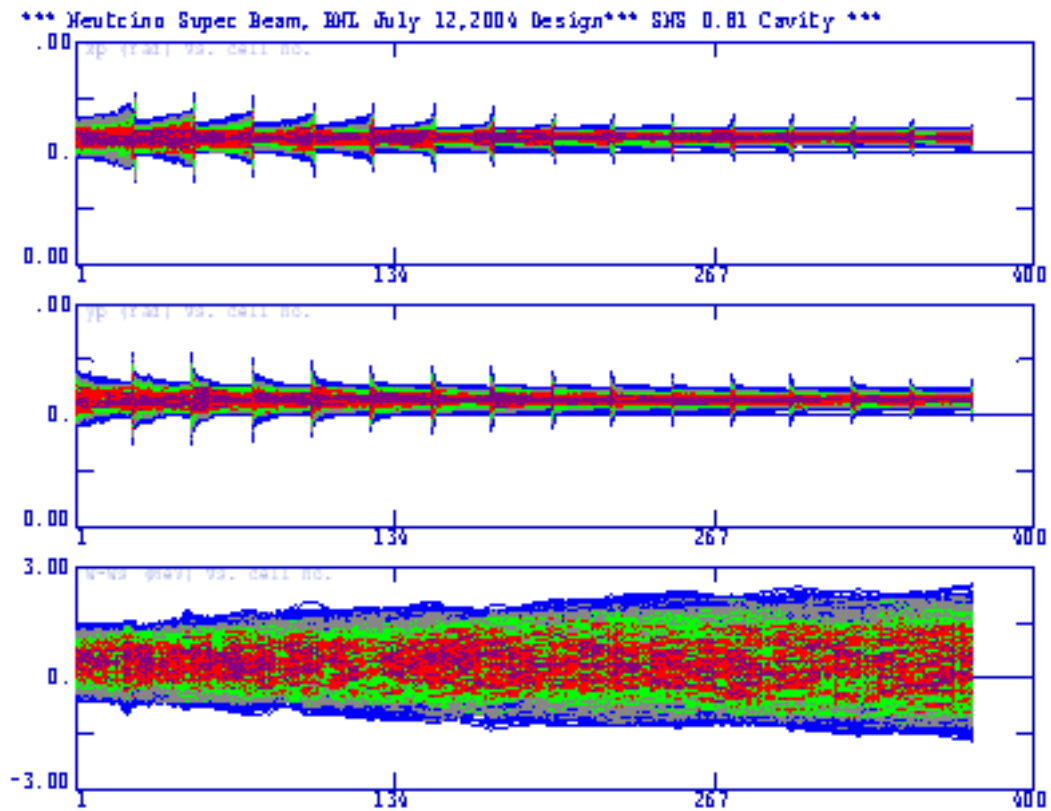
Figure B.13: Beam profiles (XP, YP, W-W$_s$) through the SCL, Beam offset is artificial due to plotting program of PARMILA.
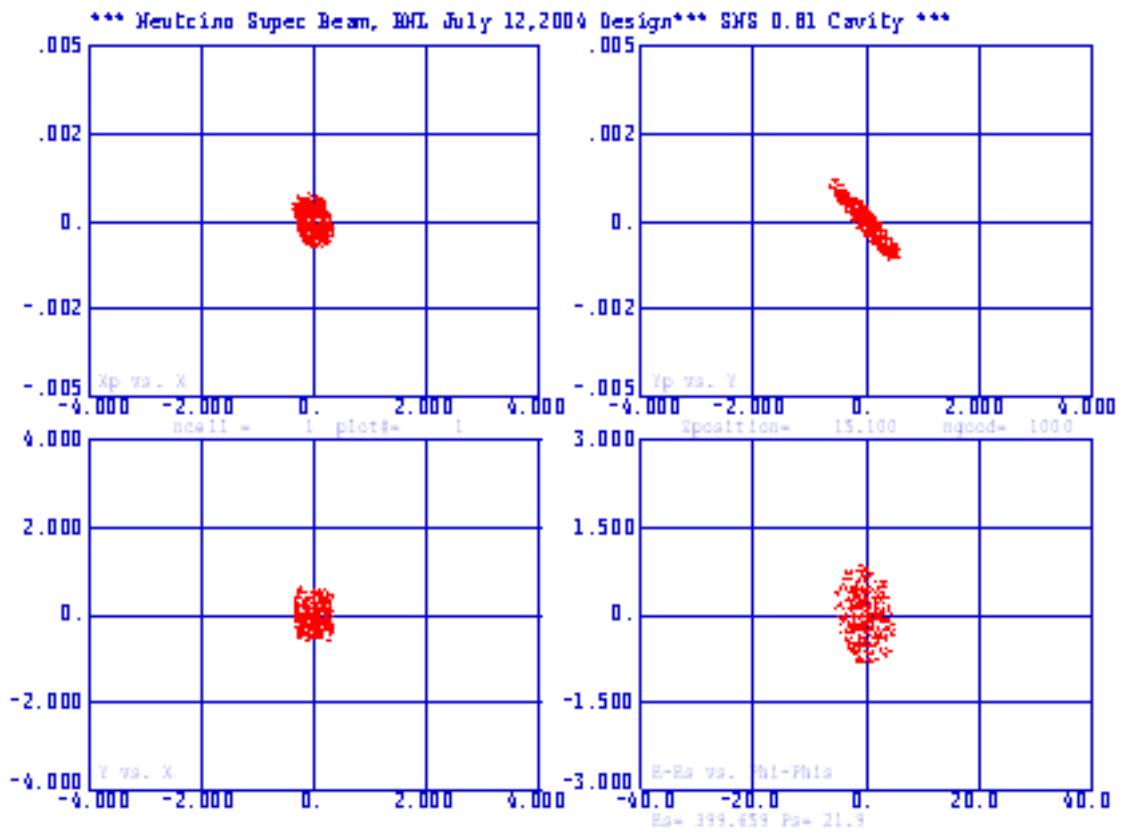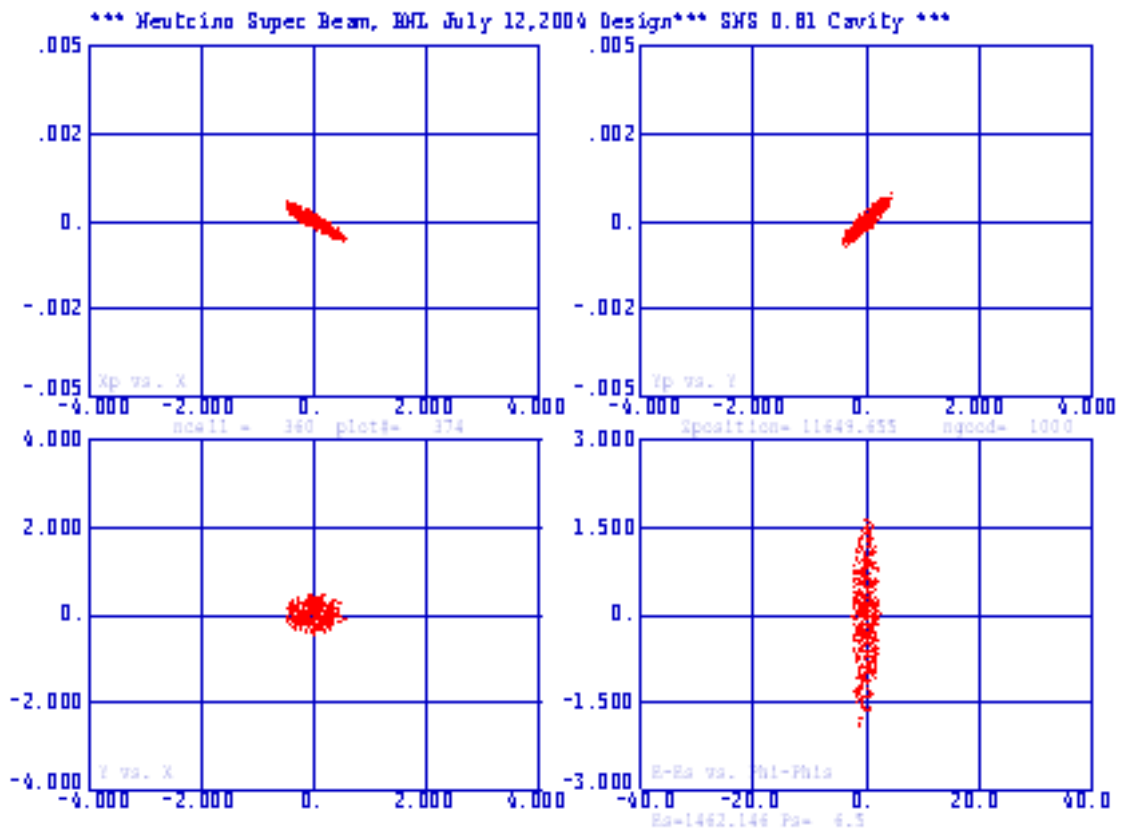
Figure B.14: Phase space plots at entrance of SCL.

Figure B.15: Phase space plots at end of SCL.

B.4   Matching between CCL and SCL

The beam from the CCL linac was matched into the SCL using four additional quads and one dipole. Dipole and quadrupoles strengths are low enough to avoid stripping of H$^-$. Figure B.16 shows the TRANSPORT output.
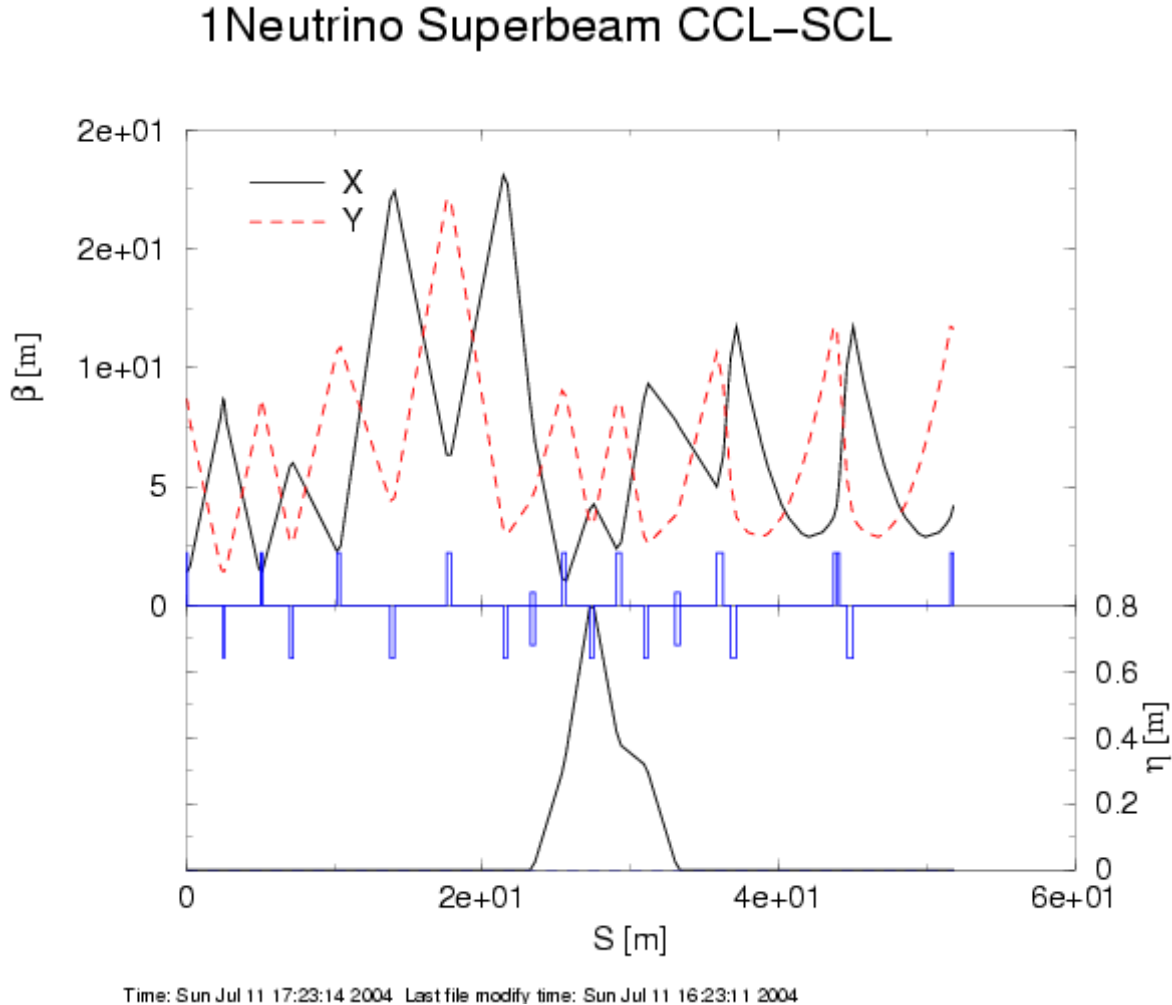
Figure B.16: β and η functions along the matching section between CCL and SCL.

B.5   Matching into the AGS

The Courant-Snyder parameters at the injection point are given in Section 4.1.2. A 30 m long transfer line consisting of eight quadrupoles and an eleven degree bend accomplishes the matching constraints. Dipole and quadrupole strength are low enough to avoid stripping of H$^-$. The matching section is not long enough for efficient momentum collimation and the energy corrector cavity. Further studies are required to accommodate these features. Figure B.17 shows the TRANSPORT output for this transfer line.
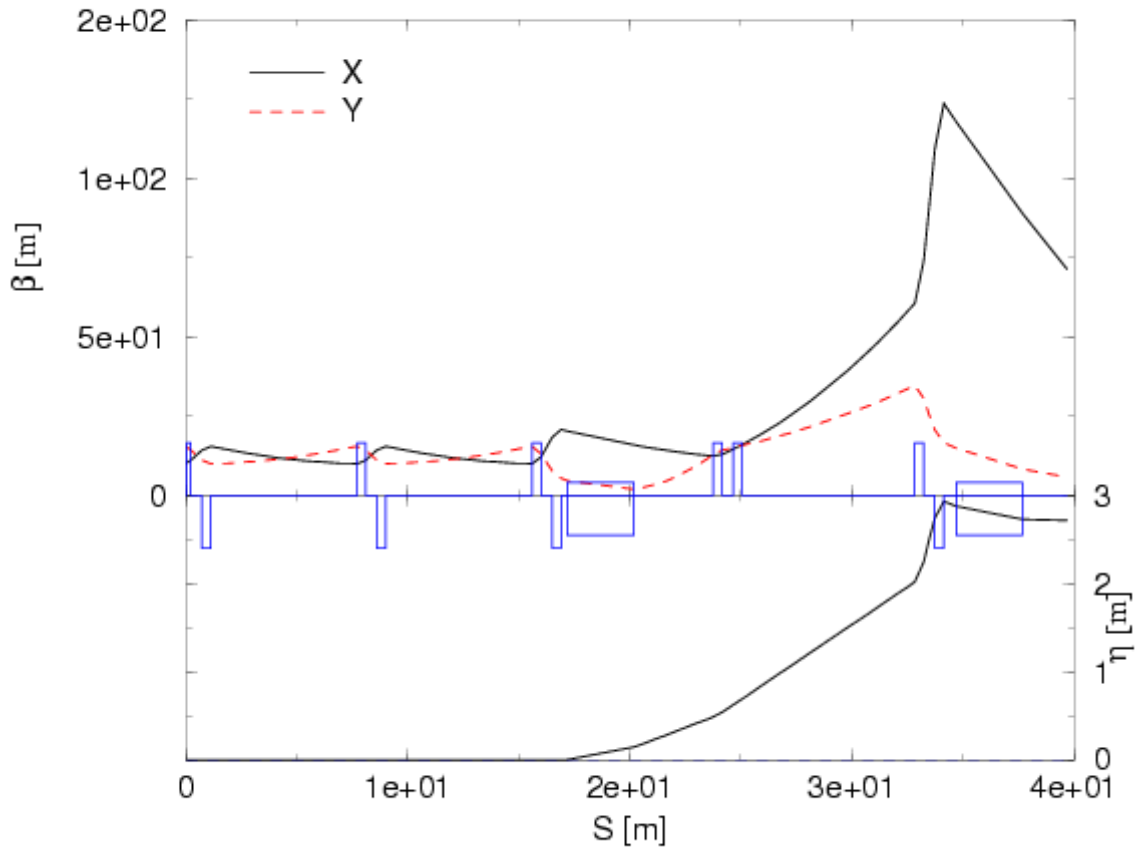
Figure B.17: β and η functions along the matching section between SCL and AGS matching point.

B.6   Cryogenic System

There are 15 cryomodules consisting of one type of cavity in SCL. Because the total length of the Linac is approximately 130 m, it is impractical to adopt a long cryomodule such as that of TESLA. The SNS high beta design is selected as the baseline.

In the SCL, each cryomodule consists of four cavities and each cavity consists of six cells. There is a power coupler for each cavity. The cavities are to be immersed in a helium vessel operating at 2.1 °K and 0.04 bar. The power couplers are to be cooled by 4.5 °K helium flow at 3 bar. The heat shield is to be cooled between 30 and 50 °K. Based on the SNS design, parameters and heat loads of a cryomodule are given in Table B.7. The static heat load consists of heat conduction and thermal radiation. The dynamic heat loads results from rf operation. The dynamic heat load is assumed to be 10% of the SNS because the duty cycle for the SCL is about 5% that of SNS.

Table B.7: Parameters and heat loads of a cryomodule

Parameter	Value	Unit
No. of cryomodule	15	
No. of cavities per module	4	
No. of cells per cavity	6	
Length	7.9	m
2 °K static heat load	28	W
2 °K dynamic heat load(estimate)	3.3	W
4.5 °K static load for couplers	0.2	g/s
4.5 °K dynamic load for couplers	0.1	g/s
Shield heat load including transfer line	200	W

The cryogenic system must provide cooling at 2 °K, 4 °K and 50 °K temperature levels. All 15 cryomodules are cooled in parallel as shown in Figure B.18. Helium refrigerator is located outside the tunnel and is connected to the SCL by a set of transfer lines.

A flow schematic for cooling a cryomodule is given in Figure B.19. Two end boxes are used for interfacing a cryomodule with the transfer lines. A 2 °K subcooler heat exchanger is installed in one of the end boxes. 4.5 °K cold helium is provided to the SCL through the transfer line. The 4.5 °K cold helium is used for the 2.1 °K liquid fill and for cooling the power couplers.

For the 2.1 °K fill, the 4.5 °K helium is cooled to ∼ 3 °K through the subcooler by counter flow heat exchange with the 2.1 °K boil-off. With a reduction in temperature from 4.5 to 3 °K, higher liquid percentage is obtained after Joule Thompson expansion. A small portion of the 4.5 °K helium at 3 bar is used to cool the power couplers of the cavity. The refrigerator also provides 30 °K helium flow to cool the heat shield. Helium returned from the heat shield is kept below 50 °K.
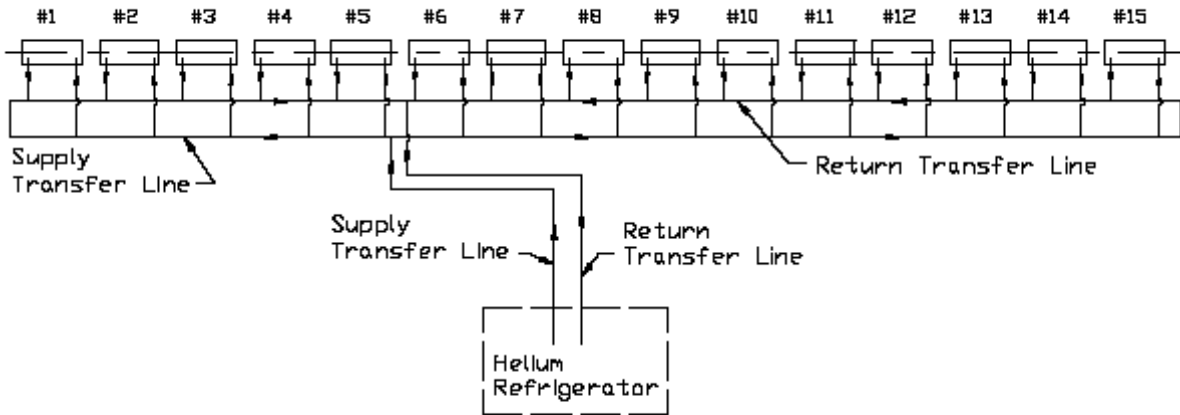
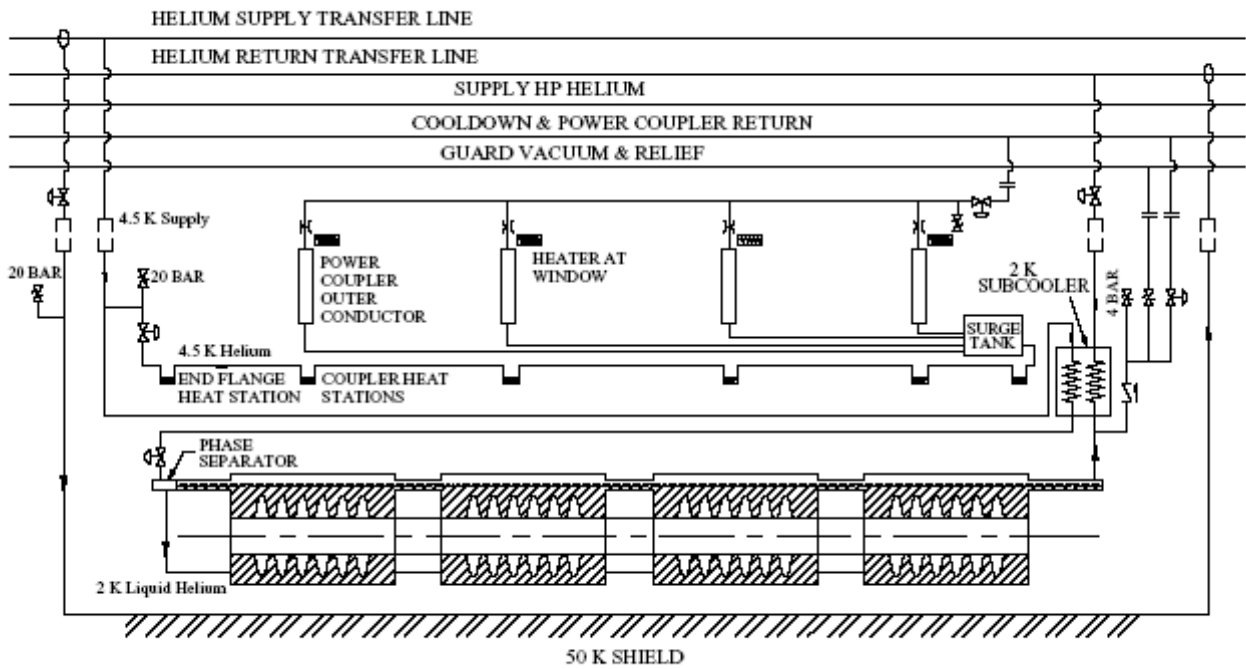Figure B.18: Cryogenic distribution system for AGS SCL.

Figure B.19: Flow schematic for cooling a cryomodule in AGS SCL.

Use of the 2 °K subcooler improves thermodynamic efficiency and simplifies the transfer line. Compared to the case without 2 °K subcooler, one less line is needed. The efficiency is better because the heat load in the supply line is absorbed at 4.5 °K rather than at 2 °K. In the SNS, bayonets and isolation valves are incorporated in the transfer lines. A cryomodule can be replaced without warming up other modules. This feature increases the cost of the distribution system. In the follow up study, we will further justify this feature.

Table B.8: Refrigeration parameters

Temperature	2.1K	4.5 K	35 - 55 K
Pressure	0.04 bar	3.0 bar	$\sim$ 4bar
Static load	420 W	3.0 g/s	3,000 W
Dynamic load	50 W	1.5 g/s	-
Total load	470 W	4.5 g/s	3,000 W
Refrigeration Capacity Margin	950 W $\sim$ 100%	9 g/s $\sim$ 100%	4,000 W $\sim$ 35%

Total heat load, temperature, pressure and flow requirements for the SCL are given in Table B.8. Baseline heat loads are extrapolated from the SNS published literature. Once actual SNS experience becomes available, heat load values will be revised. In the SCL, the 2 °K dynamic load is relatively small due to its low duty cycle. The 4.5 °K dynamic heat loads of the power couplers are assumed to be the same as in the SNS.

In this conceptual design report, capacity margin of the helium refrigerator is chosen to be similar to that used in the SNS. Once the SNS is commissioned, these margins should be revised to values more suitable for the operation. Total equivalent capacity is 1,500 W at 2.1 °K and equals about 40% that of the SNS refrigerator. Refrigerator configuration is expected to consist of a conventional 4 °K cold box and a 2 °K cold box with cold compressors. Redundancy and maintainability will be incorporated to achieve the highest reliability.

C   Appendix C: Target and Horn System R&D

C.1   Target Irradiation

The goal of the R&D effort associated with the neutrino super-beam study is to assess how prone the baseline materials (target and horn) are to experiencing degradation of their properties under irradiation. Recent studies [51] suggest that some alloys that exhibit favorable physical and mechanical properties for use as high power targets, experience dramatic changes to these properties under small irradiation levels. Specifically, in a recent experimental study at BNL, the alloy super-Invar along with Inconel-718 were irradiated and subsequently tested for induced changes. Figure C.1 depicts changes induced on the coefficient of thermal expansion (CTE) for different test samples that received different levels of irradiation. Figure C.2 and C.3 summarize the irradiation-induced change as a function of displacements-per-atom (dpa) for super-Invar and inconel-718 samples under similar irradiation levels. It is clear that super-Invar is seriously affected by irradiation and it ceases to be the wonder material (almost no thermal expansion up to $\sim 150^oC$) after irradiation. Given that inconel-718, also an alloy, does not experience similar changes, should indicate that the dramatic changes are alloy-specific. Figures C.4 and C.5 depict changes in the mechanical properties of super-Invar. For a target material both the CTE and the material strength are important components in choosing which material can survive beam thermal shock.
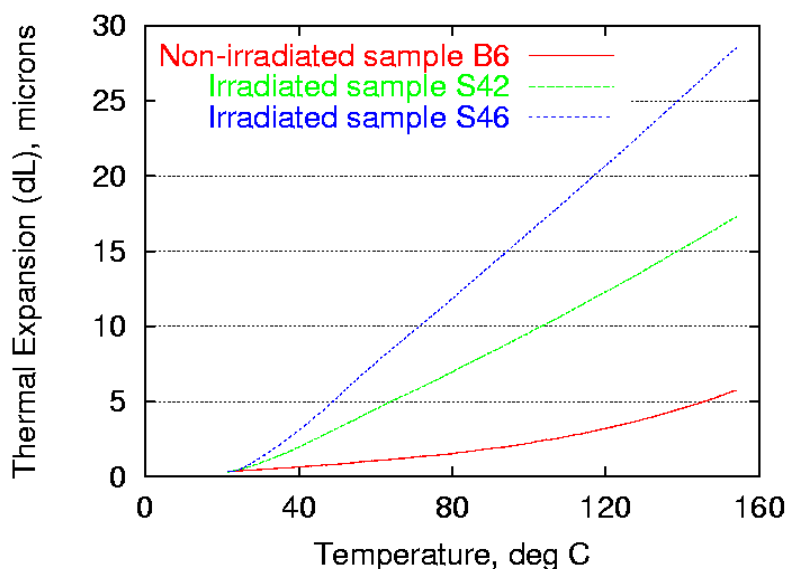
Figure C.1: Irradiation effects on the CTE of super-Invar alloy.

Given that the Carbon-carbon composite has been selected as baseline target material on the basis of its very low CTE up to $\sim 1000^oC$, it is important to assess how well will it respond under irradiation. To answer this important question an experimental effort has been set
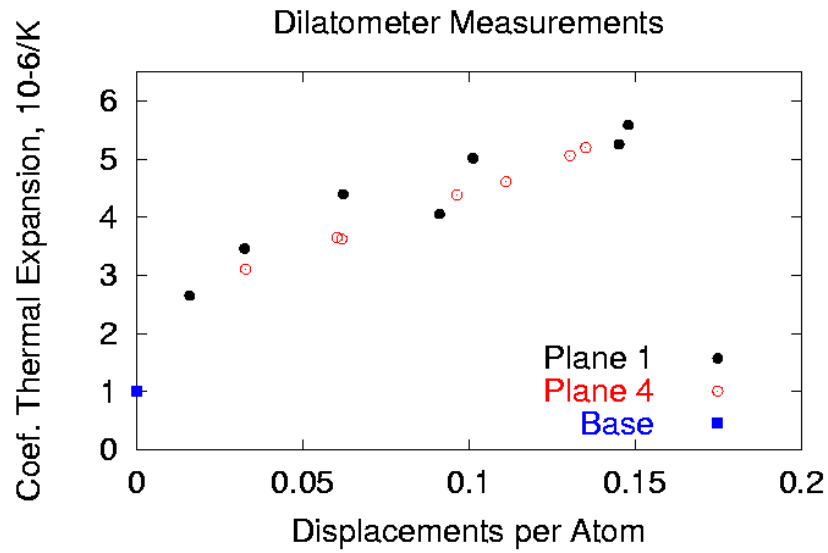
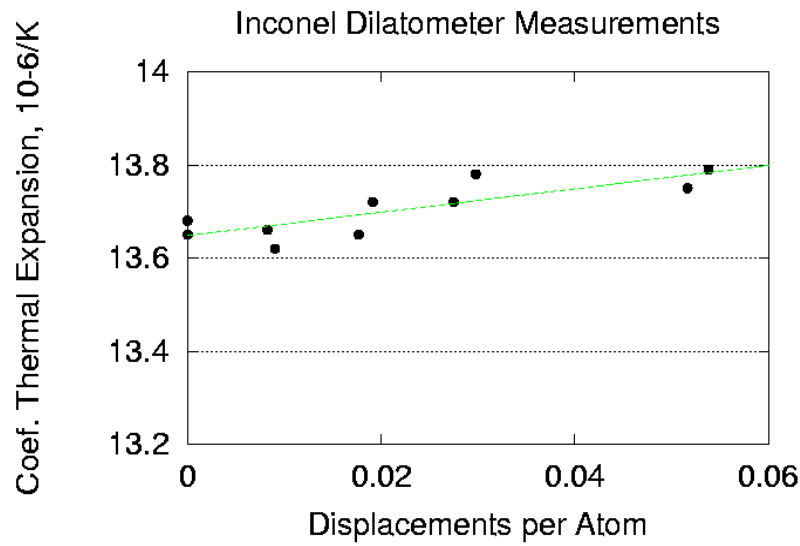Figure C.2: Super-Invar CTE changes vs. dpa levels.

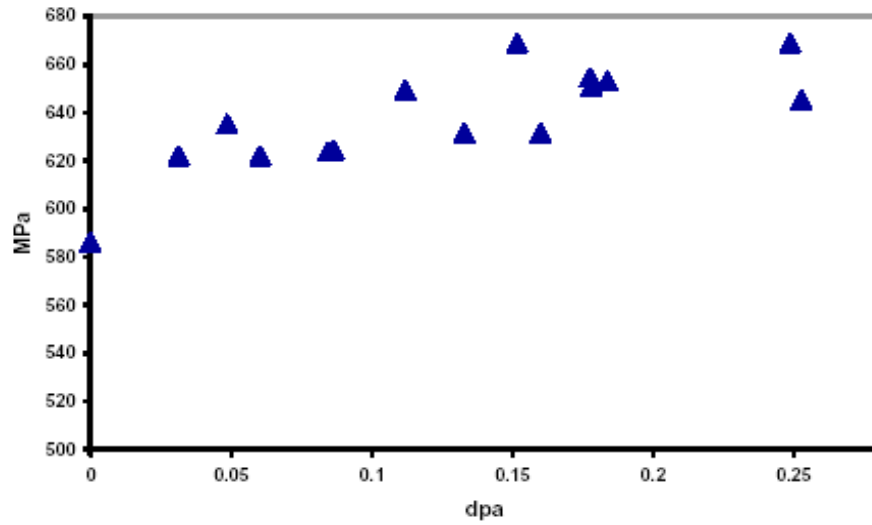Figure C.3: Inconel-718 CTE changes vs. dpa levels.

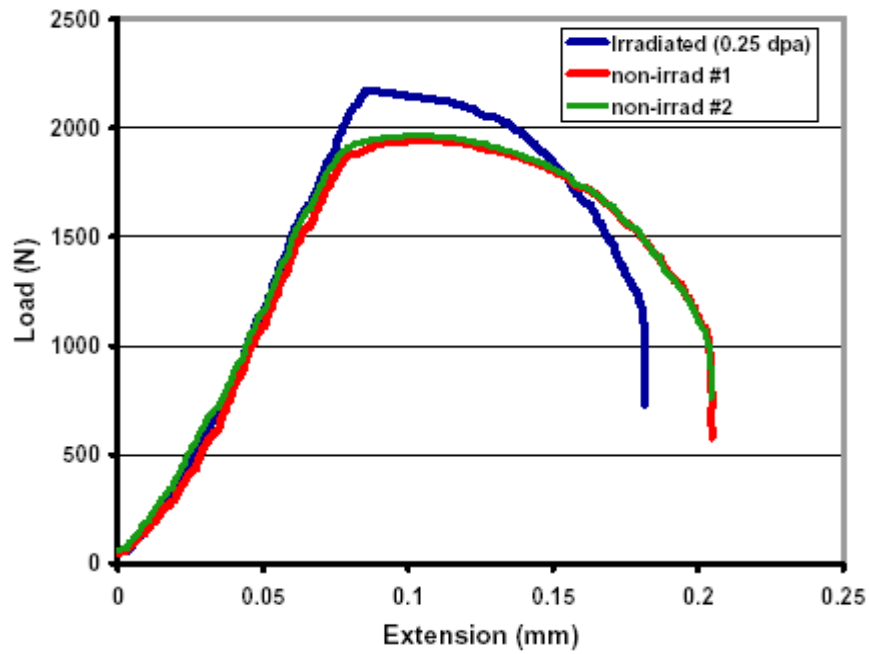Figure C.4: Super-Invar yield strength changes with irradiation.

Figure C.5: Super-Invar elastic property changes with irradiation.

in motion [52] that will allow for the qualitative assessment of the irradiation effects on CC properties (both physical and mechanical) and ensure its longevity as the target material. In addition to the CC composite, the horn material, nickel-plated aluminum 6061 T6, is being tested for potential degradation of the bonding between the protective nickel plating and the base material. Nickel-plating is introduced to reduce the surface degradation due to water corrosion and increase the fatigue resistance.
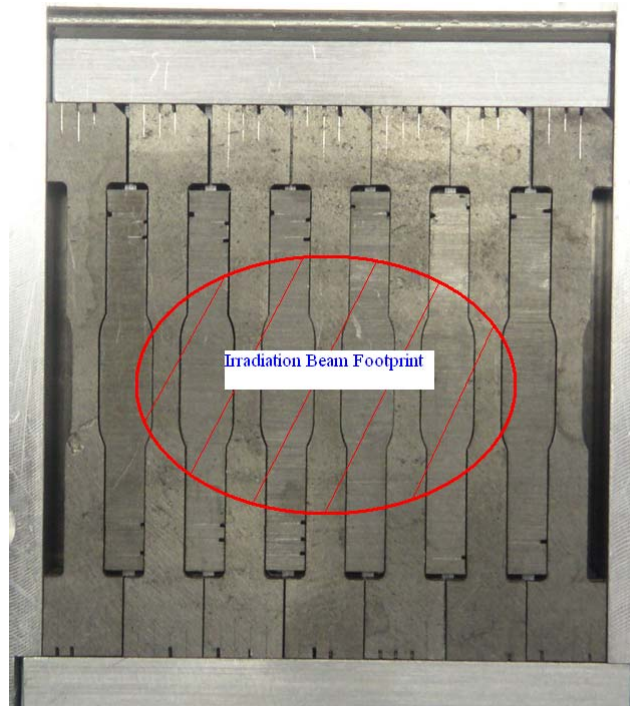
Figure C.6: CTE and tensile specimen arrangement during proton irradiation.

Figure C.6 shows the actual arrangement of test specimens for the irradiation study. The irradiated specimens will be used to assess the CTE and tensile strength changes of the CC composite as well as other materials that formed the experimental matrix. In addition to the CC composite and the nickel-plated aluminum, the material matrix includes IG-43 graphite, Beryllium, AlBeMet, Ti-alloy (6Al-4V), Vascomax and Toyota "Gum Metal" [53].

Figures C.7 and C.8 depict the CTE and tensile specimen design for the CC composite while Figures C.9 and C.10 show the arrangement of the CC and the nickel-plated aluminum specimens in their respective irradiation target assemblies.

During the irradiation, special nickel-foils were integrated into the assembly to allow for beam positioning and activation level measurements. Preliminary results of the radiographic analysis are shown in Figures C.11 and C.12.

In order to establish the irradiation temperature of the specimens, a special experiment was conducted using temperature sensitive paints (TSP), the exact irradiation geometry, cooling flow conditions and proton beam. Figures C.13 and C.14 depict the two surfaces of a 3mm aluminum foil painted with two different grades of TSP. Figures C.15 andC.16 show simulation results of temperature distribution. The goal of the experimental/simulation exercise is to
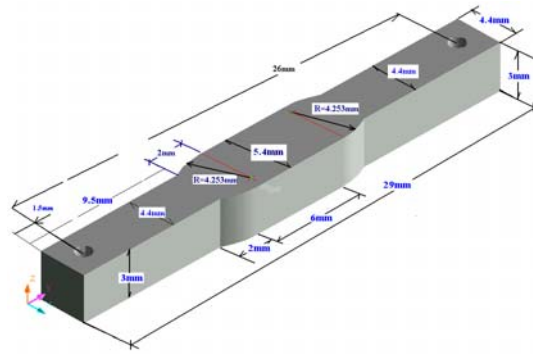
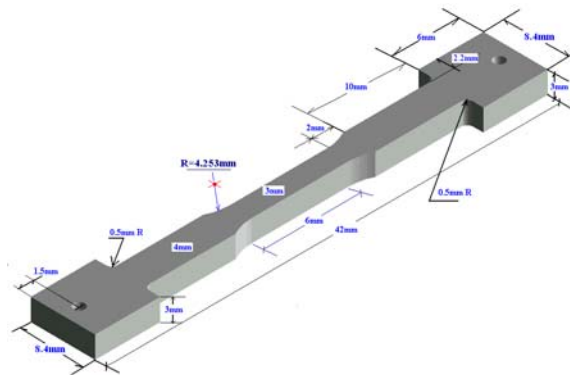Figure C.7: Carbon-Carbon composite CTE specimen design.

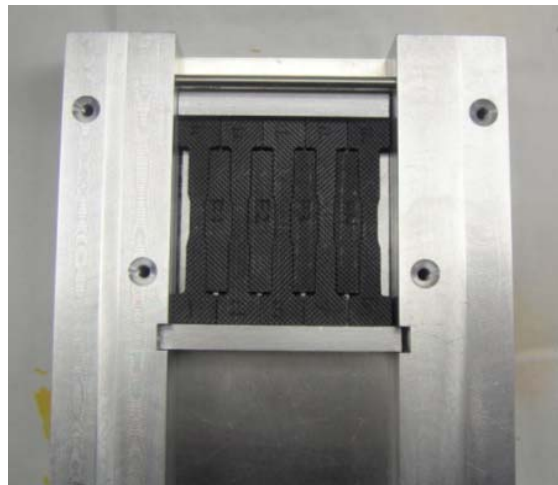Figure C.8: Carbon-Carbon composite tensile specimen design.

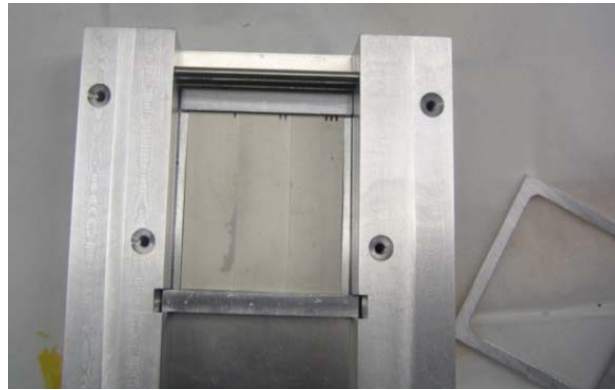Figure C.9: Carbon-Carbon CTE arrangement during proton irradiation.

Figure C.10: Assembly of nickel-plated aluminum specimens (horn baseline material).

benchmark the simulation results and deduce the temperature field during irradiation of the target specimens.
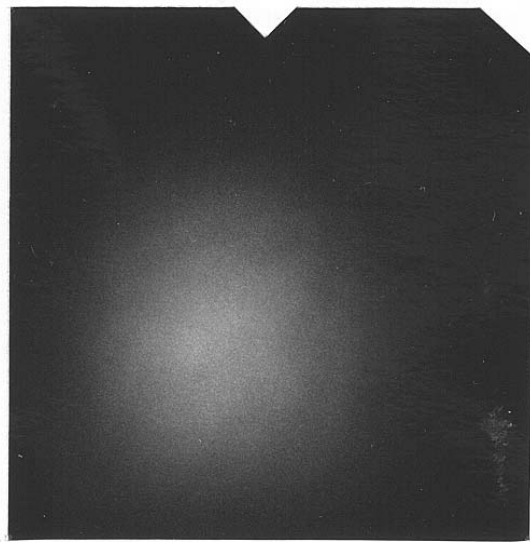

Figure C.11: Radiographic analysis of embedded nickel-foils indicating the beam location and footprint relative to the samples.

Post-Irradiation Target and Horn Material Analysis

Following the irradiation phase of the target and horn materials, the physical and mechanical properties of the irradiated specimens will be measured at the BNL Hot Cell facility. Specifically, the post-irradiation study will focus on assessing changes in the CTE and the mechanical strength of the CC composite. Figures C.18 and C.19 show the remote-controlled mechanical tester and the special dilatometer for CTE evaluation. Given that the CC composite is a 3-D weaved structure there exist strong and weak orientations. To ensure that the composite does not favor any particular orientation during irradiation, the specimens were specially designed so that both orientations were irradiated.
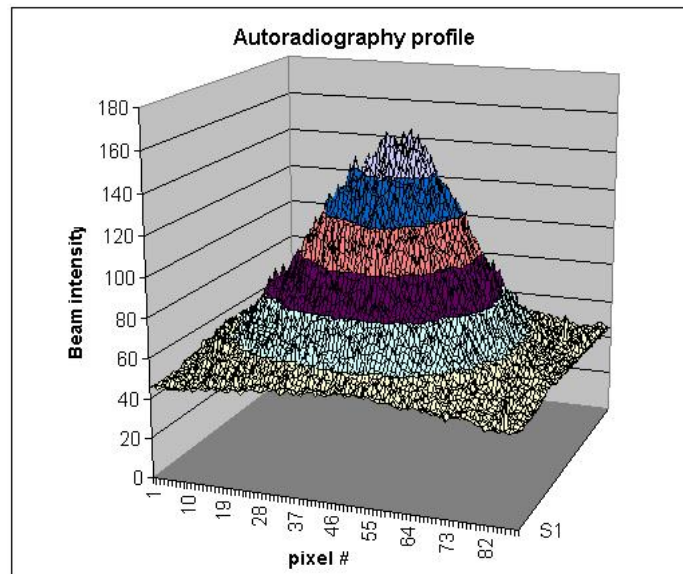
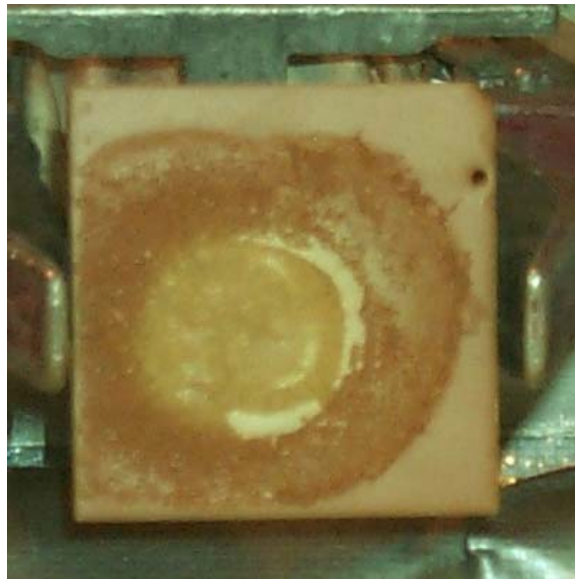Figure C.12: Beam intensity measurement from the activation analysis.

Figure C.13: Temperature profile in a 3 mm aluminum foil after exposure to irradiation beam (two-color TSP).
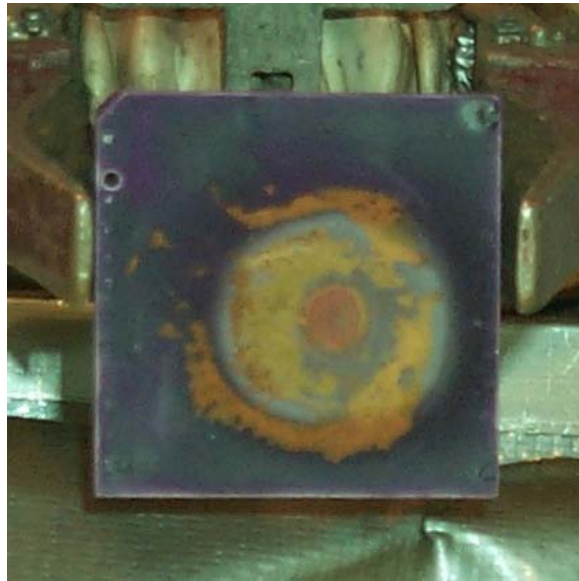
Figure C.14: Temperature profile in a 3mm aluminum foil after exposure to irradiation beam (12-color TSP).
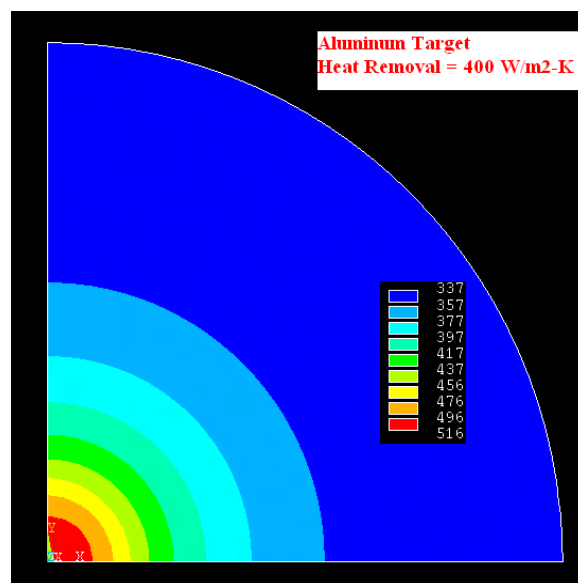

Figure C.15: Temperature profile simulations of irradiation temperatures of Figure C.14
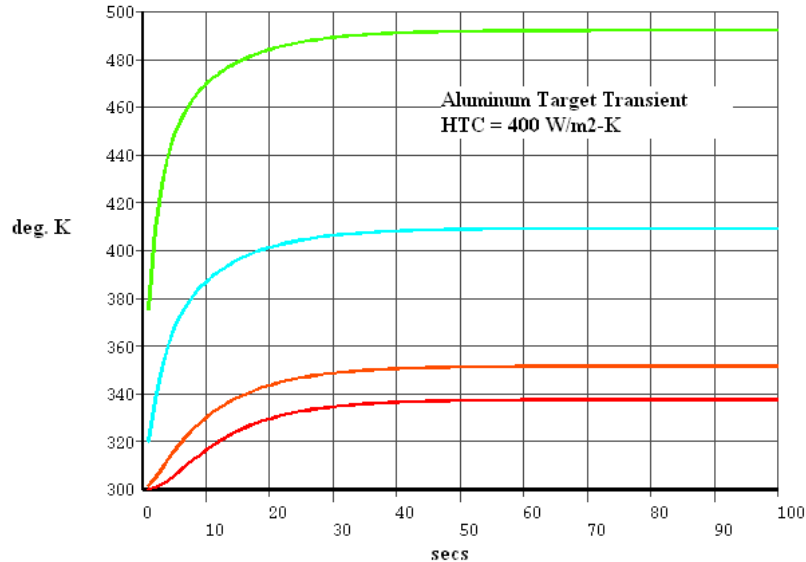
Figure C.16: Temperature profile simulations of irradiation temperatures of Figure C.14

The horn nickel-plated aluminum material will be closely examined for visible or microscopic degradation of the bonding. Irradiation, the effects of irradiation on electrical resistivity, a key parameter of its function, will be assessed. Alternative options to nickel-plating are being entertained in the event that bonding of the nickel layer with the base material is seriously affected by irradiation. These alternative options include (a) nano-structured film deposition and (b) chemical vapor deposition (CVD).

Other irradiated materials of interest to the neutrino superbeam initiative will be evaluated as well. These include Beryllium, AlBeMet and graphite IG-43. AlBeMet, in particular, is a material of interest for the horn as an alternative to aluminum. It is also examined as the baseline material for an alternative target/horn scheme in which the inner horn conductor and the target are merged. In this scheme, there is no annular space or need for a coolant to flow past the target and heat removal is by spraying on the inner conductor alone.

Figure C.17 is a comparative list of AlBeMet properties and other common materials [54].

C.2   R&D Activities Other Than Target Irradiation

A program to validate the concept used in the target/horn system design is number of experimental studies are being formulated. It includes:

Heat transfer experiments. These experiments are designed to validate the heat transfer mechanism of (a) annular helium flow and (b) water spraying.

Non-beam thermal shock experiments. A program To assess the susceptibility of the target and horn materials to laser-induced thermal shocks is being designed. An ultrasonic system is being integrated to enable real time response of the materials. The goal is to assess the fracture potential of the target materials.

Figure C.17: AlBeMet Physical & Mechanical Properties

AlBeMet® Property Comparison

Property	Beryllium S200F/AMS7906	AlBeMet AM16H/AMS7911	E-Material E-60	Magnesium AZ80A T6	Aluminum 6061 T6	Stainless Steel 304	Copper H04	Titanium Grade 4
Density lbs/cuin (g/cc)	0.067 (1.85)	0.076 (2.10)	0.091 (2.51)	0.065 (1.80)	0.098 (2.70)	0.29 (8.0)	0.32 (8.9)	0.163 (4.5)
Modulus MSI (Gpa)	44 (303)	28 (193)	48 (331)	6.5 (45)	10 (69)	30 (205)	16.7 (115)	15.2 (105)
UTS KSI (Gpa)	47 (324)	38 (262)	39.3 (273)	49 (340)	45 (310)	75 (515)	45 (310)	95.7 (660)
YS KSI (Gpa)	35 (241)	28 (193)	N/A	36 (250)	40 (275)	30 (205)	40 (275)	85.6 (590)
Elongation %	2	2	< .05	5	12	40	20	20
Fatigue Strength KSI (Gpa)	37.9 (261)	14 (97)	N/A	14.5 (100)	14 (95)	N/A	N/A	N/A
Thermal Conductivity btu/hr/ft/F (W/m-K)	125 (216)	121 (210)	121 (210)	44 (76)	104 (180)	9.4 (16)	225 (391)	9.75 (16.9)
Heat Capacity btu/lb-F (J/g-C)	.46 (1.95)	.373 (1.56)	.310 (1.26)	.251 (1.05)	.214 (.896)	.12 (.5)	.092 (.385)	.129 (.54)
CTE ppm/F (ppm/C)	6.3 (11.3)	7.7 (13.9)	3.4 (6.1)	14.4 (26)	13 (24)	9.6 (17.3)	9.4 (17)	4.8 (8.6)
Electrical Resistivity ohm-cm	4.2 E-06	3.5 E-06	N/A	14.5 E-06	4 E-06	72 E-06	1.71 E-06	60 E-06

Figure C.18: Hot cell facility set-up for post-irradiation testing.

Figure C.19: Hot cell facility set-up(dilatometer) for post-irradiation CTE measurements.

D   Appendix D: Near Detector

D.1   The Near Detector Facility

Description

The near detector facility will be located 75 m from the back of the beam stop, 21 m below ground level. The facility will consist of welded steel tunnel sections 6 m in diameter, with a 6 m access shaft to the surface. A 9 m wide x 15 m long service building will be constructed over the access shaft with a removable roof to access equipment below. This building will contain electrical distribution, HVAC units, water cooling systems, power supplies & experimental equipment associated with the detector. There will be an elevator provided for accessing the detector from the service building. A unit substation and cooling tower will be provided for utilities in this area.

A near detector facility is planned to be located at 285 m from the target. Although it would be desirable to have the near detector further from the target so that at the near detector the neutrinos appear to come from a point source, the steep 11.3° incline limits the choice of location. The near detector facility is shown in an elevation view in Figure D.1. The facility hall will be 21 m below ground level and the hall will be 9 m wide × 6 m high × 15 m long. There will be an access shaft that is 6 m in diameter with an overhead crane for bringing large equipment into the detector hall. There will also be an elevator for normal access.

Since the facility is located below the water table, installation of the tunnel sections will involve de-watering of the excavation site while the tunnel sections are being installed. The tunnel is then seal welded and back-filled with soil.

Design Basis

The design of the decay tunnel was escalated as a basis for the underground tunnel design but with on-site fabrication. Standard coffer-dam and de-watering techniques were assumed.

Cost Estimate

The cost of the decay tunnel was escalated and per unit costs from standard estimating guides were used for installation of the underground facility, service building and utilities.

The cost estimate follows the same methodology of that used in the accelerator system and are created from bottom up WBS approach. The resultant direct cost for the near detector facility is $ 5.8 M with $ 725k for EDIA, $ 4.9 M for M&S, and $ 200 k for labor. The total estimated cost is $ 8.6 M, including BNL overhead 14.5% of $841 k and contingency 30% of $ 2.0 M.

D.2   The Near Detector Design Concept

The main purpose of the near detector is to provide knowledge of the composition of the neutrino beam:
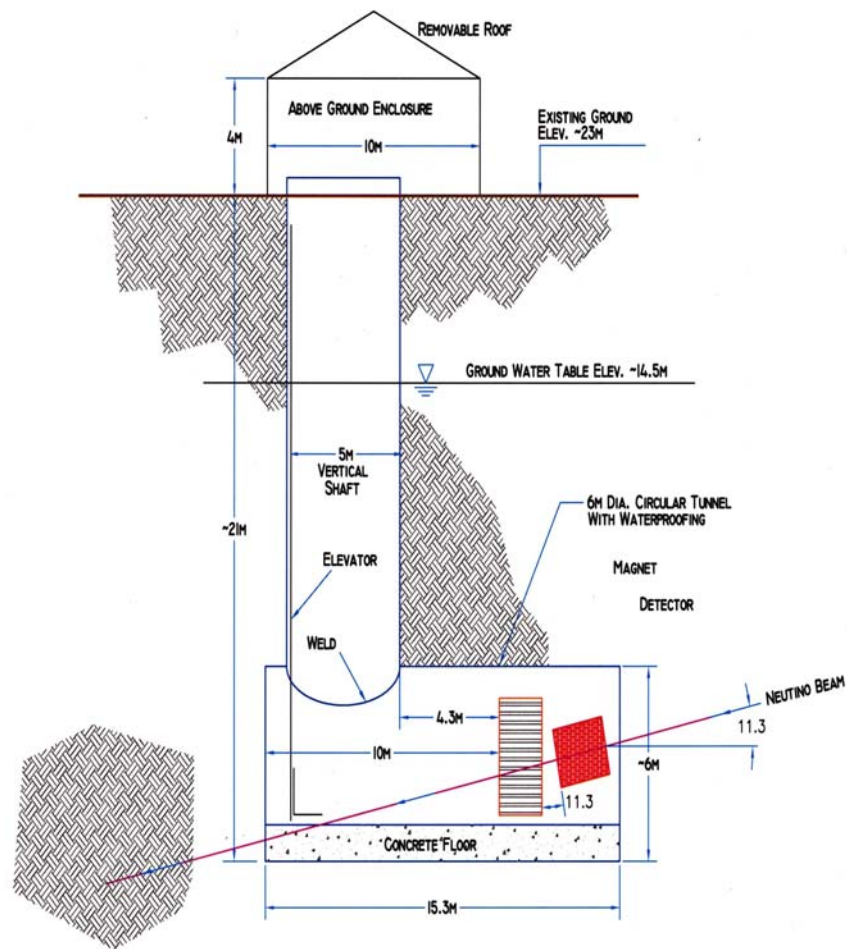
Figure D.1: Near detector vertical section

- The energy spectrum of the dominant ν_μ flux.

- The energy spectrum of the contaminant neutrino species in the beam: ν_e, $\overline{\nu}_\mu$, and $\overline{\nu}_e$.

- The integrated neutrino flux for overall normalization.

- Alignment information from neutrino data.

Since the near detector is very close to the source the flux distribution at the far detector is not related to the near detector flux distribution by a simple scaling with $1/r^2$. Figure D.2 shows the flux distribution at near detector and the flux distribution at the far detector scaled to the near detector position. The near detector flux is peaked at a lower energy than the flux at the far detector. The near detector would have to be located at least 1.5 km from the target for scaling to be reliable. At that distance the detector hall would have to be 300 m below ground level. Because of the large statistics that will be present at the near detector, the flux distribution can be measured as a function of position in the detector to provide information for the extrapolation of the spectrum to the far detector. Also data on the neutrino direction can be extracted from the ν_e elastic events and quasi-elastic events would be valuable for the spectrum extrapolation.

Flux distributions at the near detector can be obtained from a simulation of the target and horn system using both the GEANT and MARS programs. MARS is used to produce a particle production spectrum from the 28 GeV proton beam on the carbon-carbon target. A file of $\pi^\pm$, $k^\pm$, and $\mu^\pm$ produced on the target is generated by MARS. This file is input to the GEANT program which will track these particles through the horn system and allow them to decay to channels that produce neutrinos. The flux of these neutrinos is scored at the detector position. Figure D.3 shows the flux spectrum of the dominant ν_μ species and the contaminant $\overline{\nu}_\mu$ and ν_e species. The ratio of $\overline{\nu}_\mu$ to ν_μ flux at the near detector is about 3%. The ratio of ν_e to ν_μ flux is about 1% at that location.

The number of events of each neutrino species produced at the near detector location can be calculated by integrating the flux with the corresponding neutrino cross-sections. Table D.1 shows the number of events that are expected at the near detector site for a 200 ton detector for a 5×10^7 second running period. A detector of 200 tons was chosen to be large enough to contain the entire event, but small enough not to be excessively priced. The total number of events seen in this running period is 4×10^9 which would be 32 events per pulse in the detector.

The desired attributes that a near detector should include:

- The technology chosen for the near detector should be able to handle this high rate.

- It should be sensitive to and be able to distinguish the different neutrino species. That means that it should have a magnetic field and should be able to distinguish electrons from π°.

- It would be desirable that the interactions be on a similar material as the far detector so that uncertainties about π re-absorption will cancel.
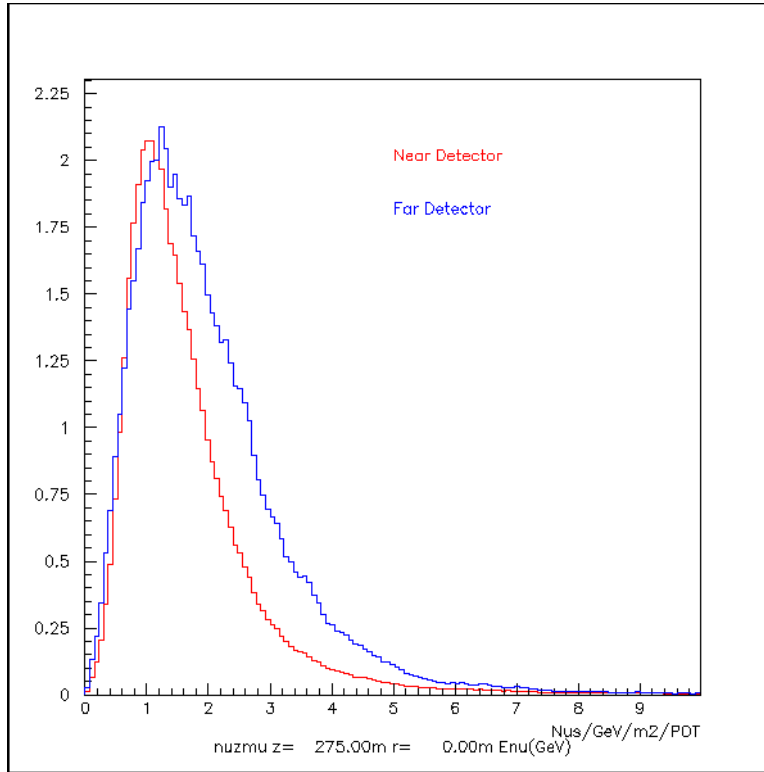
Figure D.2: Comparison of the flux at the near detector (blue) with the flux at the far detector (red) scaled by $(r_{far}/r_{near})^2$, where r is the distance from a point midway in the decay tunnel to the corresponding detector. For this comparison r_{far}=2540 km and r_{near}=175 m.
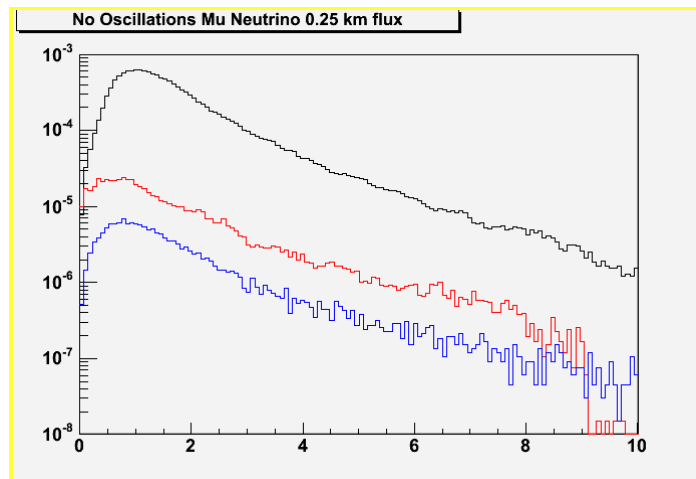

Figure D.3: The neutrino flux distributions at the near detector. The distributions for ν_μ (black), $\overline{\nu}_\mu$ (red), and ν_e (blue) are shown. The flux is in units of neutrinos per m^2 per GeV per proton on target.

Table D.1: Signal events that are expected for a 200 ton detector positioned at 275 m from the target. The event numbers are for a 5×10^7 second running period for a 1 MW proton source.

Species	Quasi-Elastic	Charge Current	Neutral Current
ν_μ	1.33×10^9	3.66×10^9	2.01×10^8
$\overline{\nu}_\mu$	7.70×10^6	7.74×10^7	1.37×10^6
ν_e	1.42×10^7	3.99×10^7	3.10×10^6
$\overline{\nu}_e$	4.89×10^4	3.98×10^5	1.30×10^4

- It should be able to contain enough of the event to be able to distinguish μ from π and to be able to measure the visible neutrino energy.

- The near detector should have its own physics program.

It is not evident that all of these conditions will be met.

Although it is not the purpose of this report to choose the near detector technology, it is instructive to examine whether the choice (or proposed choice) of near detectors for other neutrino oscillation experiments could be used. A water cherenkov detector would not be able to easily separate a pileup of events occurring in the single pulse. However a liquid argon detector, because of its fine resolution, should be able to separate a significant fraction of the events in a single pulse. Typically a neutrino event in liquid argon should occupy about a 6 m^3 volume. Figure D.4 shows a schematic of a 175 ton liquid argon detector with an active volume of 100 tons. This detector could be put into a 0.5 tesla dipole magnetic field to distinguish between positive and negative charged leptons produced in the neutrino interactions. This would allow identification of the neutrino species from its antiparticle. An iron-scintillator range stack should be placed behind the liquid argon detector to distinguish muons from pions. The iron is magnetized to determine the charge of the muon. This particular detector scenario would require increasing the longitudinal dimension to 20 m and increasing the height to 8 m to allow some vertical clearance.
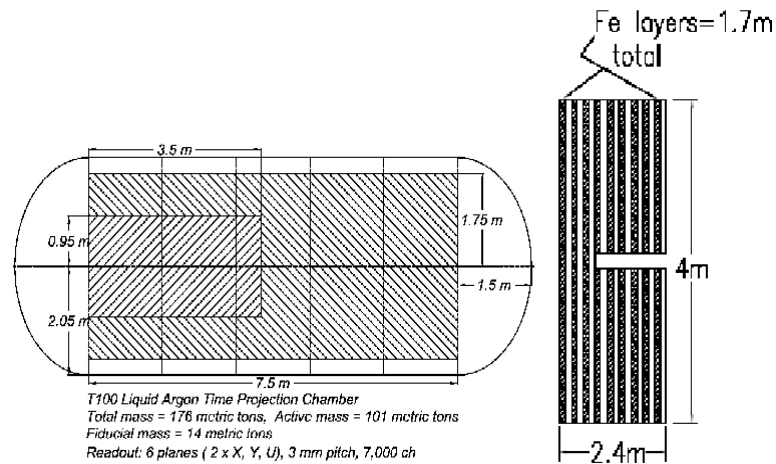
Figure D.4: Schematic of a 176 tons liquid argon TPC detector that could be used as a near detector for the BNL long baseline experiment. An iron scintillator stack is placed behind the argon cryostat as a muon identification device.

References

[1] K. Hagiwara et al., Particle Data Group, Phys. Rev. **D 66**, 010001 (2002), p. 281.

[2] Y. Fukuda et al., Phys. Rev. Lett. **81**, 1562 (1998) S. Fukuda et al., Phys. Rev. Lett. **86** 5656, 2001; E.W. Beier, Phys. Lett. **B283**, 446 (1992); T. Kajita and Y. Totsuka, Rev. Mod. Phys. **73**, 85 (2001). Y. Ashie et al., hep-ex/0404034.

[3] Q. R. Ahmad et al., Phys. Rev. Lett. **87** 071301 (2001). S. Fukuda et al., Phys. Rev. Lett., **86** 5651 (2001).

[4] S. H. Ahn et al., Phys. Lett. **B 511** 178 (2001). M. H. Ahn et al., Phys. Rev. Lett. **90** 041801 (2003).

[5] K. Eguchi, *et al.*, Phys. Ref. Lett. **90**, 021802 (2003). hep-ex/0212021. T. Araki, *et al.*, hep-ex/0406035.

[6] Physics Potential and Feasibility of UNO, UNO collaboration, June 2001. SBHEP01-3.

[7] "Very Long Baseline Neutrino Oscillation Experiment for Precise Measurements of Mixing Parameters and CP Violating Effects", M. V. Diwan, *et al.*, **PRD 68** (2003) 012002.

[8] "The Case for a Super Neutrino Beam," Milind V. Diwan, Talk at Heavy Quarks and Leptons, San Juan, Puerto Rico, June 1-5, 2004. hep-ex/0407047.

[9] W. T. Weng, "Performance and Measurements of the AGS and Booster Beams", AIP Conf. Proc. 377, P. 145-157, 1995.

[10] W. T. Weng and T. Roser, "The AGS High Power Upgrade Plane", AIP Conf. proc. 642, P. 56, 2002.

[11] Superconducting Radio Frequency Linac for the Spallation Neutron Source, SNS-110020300TR0001R000, November 22, 1999.

[12] G. W. Wheeler, K. Batchelor, R. Chasman, P. Grand, J. Sheehan, "The Brookhaven 200-MeV Proton Linear Accelerator", Particle Accelerators 9 (1979) 1-156.

[13] J.G. Alessi, et.al., "Upgrade of the Brookhaven 200 MeV Linac", Proc. 1996 Linear Accel. Conf., CERN 96-07, p. 773, 1996.

[14] D. Raparia, to be pbulished in 2004 linac conference.

[15] A. G. Ruggiero, "Design Considerations on a Proton Superconducting Linac".BNL-Internal Report 62312, August 1995.

[16] G.H. Gillespie, Phys. Rev. A16, 943 (1977).

[17] J. Wei, Ph. D thesis (1990); in *Handbook of Accel. Phys. Eng.*, ed. A. Chao and M. Tigner (World Scientific) p. 285

[18] N. Tsoupas, private communications (2004)

[19] J. Wei and N. Tsoupas, 2004 European Particle Accelerator Conference, Lucerne, 2004

[20] S.Y. Zhang, private communications, 2004

[21] W. Hardt, 9th Intl. Conf. High Energy Acc., Stanford (1974)

[22] P. Yamin et al, PAC 1987, p. 134

[23] M. Syphers et al, AGS/AD/94-5 (BNL-60824, 1994)

[24] H. Grote, F.C. Iselin, CERN/SL/90-13 (1990)

[25] J. Wei, Rev. Mod. Phys. **75** (2003) 1383

[26] W. T. Weng, *et al*, " Effect of the Halo on the AGS Injection from 1.2 GeV linac", AIP
      Conference Proceedings **693**, Montauk, New York, 2003.

[27] N. Tsoupas et al. *Alternative Beam Optics for U-Line for lossless beam transport to the
      neutrino-line*,C-AD Accelerator Physics Note 70, Feb 2002

[28] E889 Collaboration, Physics Design Report, BNL No. 52459, April, 1995.

[29] L. A. Ahrens et al., Phys. Rev. **D 34**, 75 (1986).

[30] N.V. Mokhov, "The MARS Code System User Guide, Version 13 (95)", 1995.
      http://wwwinfo.cern.ch/wwwasd/geant4/geant4.html

[31] "Proposal to Study Production for the Neutrino Factory and for the Atmospheric Neu-
      trino Flux", CERN-SPSC/99-35

[32] "Effects of beam plugs and hadronic hose", B. Viren, NUMI-0719, 2001-07-06. "Neutrino
      Fluxes, Hadron Production and the Hadronic Hose", M. Messier, et al., NUMI-070, 2000-
      12-01.

[33] H. Kirk et al., "Target Studies with BNL E951 at AGS," PAC2001, TPAH137

[34] N. Simos, *et al.*,"Concept Design of the Target/Horn System for the BNL Neutrino Os-
      cillation Experiment", APAC-2003, 2003.

[35] N. Simos, *et al.*," Material Studies for Pulsed High Intensity Proton Beam Targets",
      ICONE12, 2004.

[36] A.J. Chapman, Heat Transfer, 3rd Edition, Macmillan, 1974

[37] H.E. McCoy, Jr and J.R. Weir Jr, " Influence of Irradiation on the Tensile Properties of
      the Aluminum Alloy 6061", Nuclear Science & Engineering, Vol. 25, pp. 319-327, 1966

[38] MCNPx, User Manual, Version 2.1.5., L.S. Waters, Los Alamos National Laboratory, Los
      Alamos, NM. TPO-E83-G-UG-X-00001, (1999).

[39] G. Acquistapace, J.M. Maugain, F. Voelker, "Considerations on a 75 Hz pulsed horn", CERN, 05, 2000.

[40] K. Bourkland, K. Roon, D. Tinsley, "205 kA Pulse Power Supply for Neutrino Focusing Horn", 2002 PMS.

[41] G. Grawer, "Investigation of the possibility to build a 400 kA pulse current generator to drive a magnetic horn", CERN-NUFACT Note 038, July 19, 2000.

[42] J. Sandberg, et.al. "The Neutrino Horn 300 Kiloampere Pulsed Power Supply at Brookhaven National Laboratory", PAC 1987.

[43] K. Bourkland, C. Jensen, D. Tinsley, " High Current Pulse Striplines", 2001 PPPS.

[44] The *Pbeam* program was written by Noel Stanton of Kansas State University and was modified by Wesley Smart of Fermilab and Richard Milburn of Tufts University.

[45] A. J. Stevens, private communication to D. Beavis, "MCNPX 2.1.5 Shielding Estimates in a Simple Tunnel Geometry", 2002.

[46] K. Tesch and H. Dinter, Radiation Protection Dosimetry, Vol. 15 No. 2 pp89-107, 1986.

[47] A. H. Sullivan, "A Guide to Radiation Protection and Radioactivity Levels Near High Energy Particle Accelerators", Nuclear Technology Publishing, 1992.

[48] Kin Yip, private communication to D. Beavis.

[49] D. Beavis, AGS/EP&S/Tech. Note No. 130, 1988.

[50] Design Pratice Specification for Know Beam-Loss Locations, BNL SBMS, http://www.rhichome.bnl.gov/AGS/Accel/SND/EMS/beamLoss.pdf.

[51] H. Kirk, et al., 2002-2003 BNL BLIP Super-Invar Irradiation Experiment.

[52] N. Simos, et al., 2004 BNL BLIP Material Irradiation Experiment.

[53] T. Saito, et al., "Multifunctional Alloys Obtained via a Dislocation-Free Plastic Deformation Mechanism," Science, Vol.300, pp. 464-467, 2003.

[54] APT Materials Handbook, TPO-P00-MDD-X-00001, 2001.

[55] E. S. McCrory, " The Commissioning and initial operation of the Fermilab 400 MeV linac" 1994 International Linac Conference, Tsukuba, Japan, August 1994.

[56] Fermilab Linac Upgrade: Readiness Review, June 1993.

[57] C. Rode, et al., "The SNS superconducting linac system", 2001 Particle Accelerator Conference, Chicago, pp 619-623, 2001.

[58] C. Rode, Talk given in SNS DOE review May 2004.